UNIVERSIDAD COMPLUTENSE DE MADRID
FACULTAD DE CIENCIAS FÍSICAS

TESIS DOCTORAL

Predicción Numérica Aplicada a Meteorología Aeronáutica: estudio de Fenómenos Locales Peligrosos

Numerical Weather Prediction Applied to Aeronautical Meteorology : Study of Local Hazardous Phenomena

MEMORIA PARA OPTAR AL GRADO DE DOCTOR

PRESENTADA POR

Pedro Bolgiani

Directores

María Luisa Martín Pérez
Sergio Fernández González

Madrid

UNIVERSIDAD COMPLUTENSE DE MADRID

FACULTAD DE CIENCIAS FÍSICAS

TESIS DOCTORAL

Predicción Numérica Aplicada a Meteorología Aeronáutica: Estudio de Fenómenos Locales Peligrosos

MEMORIA PARA OPTAR AL GRADO DE DOCTOR
PRESENTADA POR

Pedro Bolgiani

DIRECTORES

Dra. María Luisa Martín Pérez

Dr. Sergio Fernández González

TUTOR

Dr. Francisco Valero Rodríguez

Madrid, 2020

UNIVERSIDAD COMPLUTENSE DE MADRID

FACULTAD DE CIENCIAS FÍSICAS

DOCTORAL THESIS

Numerical Weather Prediction Applied to Aeronautical Meteorology: Study of Local Hazardous Phenomena

REPORT FOR CONSIDERATION FOR A DOCTORAL DEGREE
PRESENTED BY

Pedro Bolgiani

DIRECTORS

Dr. María Luisa Martín Pérez

Dr. Sergio Fernández González

MENTOR

Dr. Francisco Valero Rodríguez

Madrid, 2020

A Tatá,
que fue joven hasta los 96 años.

RESUMEN

Predicción Numérica Aplicada a Meteorología Aeronáutica:
Estudio de Fenómenos Locales Peligrosos

La aviación y la meteorología están intrínsecamente relacionadas. A pesar de que los niveles de seguridad operacional de la industria son indiscutibles, el crecimiento sostenido supone un desafío constante para mantener los estándares asumidos a día de hoy. En esta tarea, los peligros relacionados con la meteorología son una de las prioridades, ya que algunos de ellos todavía suponen un gran riesgo para la operación de aeronaves. El objetivo principal de esta tesis doctoral es mejorar el conocimiento de la predicción numérica aplicada a eventos de meteorología aeronáutica. El mismo se lleva a cabo a través de la evaluación de cuatro eventos peligrosos diferentes: engelamiento en onda de montaña, baja visibilidad, precipitación por convección profunda y *microbursts*. Estos fenómenos están relacionados no solo por la alteración que pueden ocasionar en la operación de aeronaves, sino también por el hecho de que pueden darse en dominios espacio-temporales muy reducidos y locales, lo cual los hace muy difíciles de predecir. Los eventos se analizan usando simulaciones realizadas con un modelo atmosférico mesoescalar, mayormente el modelo *Weather Research and Forecasting* (WRF). Se prueban diferentes parametrizaciones y configuraciones. También se aplican diferentes métodos de validación y criterios de cualificación. La evaluación se complementa con el uso de otras técnicas de *nowcasting*, no basadas en predicción numérica.

Los resultados para el engelamiento en onda de montaña muestran que el modelo es muy competente en la simulación de este fenómeno y la turbulencia asociada. La velocidad vertical del viento y el contenido de agua líquida pueden resultar variables de pronóstico muy útiles, y su uso representaría una mejora considerable en los tiempos de anticipación de la predicción, comparados con el que generan las técnicas actuales de *nowcasting*. En los eventos de baja visibilidad, el modelo WRF presenta una infraestimación de la velocidad del viento en superficie, y genera peores cualificaciones de pronóstico cuando se lo compara con otro modelo mesoescalar. Los resultados también muestran que la predicción numérica no es suficientemente precisa para generar un buen pronóstico de estos eventos, por lo que se requiere una combinación de técnicas para el mismo. El modelo también es capaz de capturar la estructura general de sistemas de convección profunda, aunque generando una infraestimación sistemática de la precipitación. Los resultados de este caso de estudio ponen de relieve la influencia que tienen los diferentes factores en la simulación, presentando diferentes sensibilidades para las parametrizaciones físicas y las condiciones iniciales y de contorno. Además, los datos sugieren un efecto reducido de la resolución de la simulación en los resultados totales. Cuando se aplica a los *microbursts*, el modelo representa adecuadamente la dinámica y las variables características del fenómeno, aunque generando cierta infraestimación. Sin embargo, la sensibilidad de estas variables es muy baja, casi sin respuesta ante las condiciones termodinámicas mesoescalares. Un análisis mayor de este hecho sugiere que la razón puede recaer en la resolución efectiva del modelo y las

incertidumbres del mismo en microescalas. Los resultados muestran que las variables simuladas por el modelo no serían adecuadas para el pronóstico del fenómeno, ya que la disipación de energía cinética a tales resoluciones no es realista.

Un análisis integrado de los resultados previos muestra la relevancia de una configuración adecuada del modelo. Las parametrizaciones físicas son decisivas en la simulación de los eventos seleccionados, generando diferencias significativas en los resultados deterministas, lo cual ha sido ampliamente establecido por otros autores. Las condiciones iniciales y de contorno también afectan al posicionamiento y la coordinación de las simulaciones, y resoluciones mayores no acarrean necesariamente mejores resultados, en línea con la literatura existente. La resolución del modelo se convierte así en uno de los factores principales de esta tesis, ya que los fenómenos evaluados bordean la microescala. Los resultados muestran que la configuración del modelo permite simulaciones microescalares correctas, aunque las variables reproducidas están sujetas a una baja sensibilidad, probablemente debido a las incertidumbres generadas en el espectro energético. Esta falta de sensibilidad genera dudas en la competencia del modelo para pronosticar los fenómenos, y es representativa de la necesidad de producir parametrizaciones adecuadas a esta escala, como ya sostienen otros autores. Los resultados de algunas de las técnicas de *nowcasting* usadas muestran que el modelo puede mejorar notablemente con la asimilación de datos observacionales mejores, los cuales también darían mayor conocimiento de la variabilidad del sistema. Finalmente, los métodos de validación deberían adaptase a los fenómenos en cuestión, y se debería realizar una evaluación integradora para obtener mejores resultados en los eventos particulares de la meteorología aeronáutica.

Las conclusiones de esta tesis se pueden resumir en las siguientes: la predicción numérica puede ser una herramienta muy útil en el pronóstico de los fenómenos en cuestión, mejorando notablemente los tiempos de anticipación. Múltiples técnicas y algoritmos de pronóstico son ya factibles por el estado del arte. Además, estas se podrían mejorar notablemente con las parametrizaciones y configuración microescalar del modelo, lo cual ya está siendo investigado. Sin embargo, las características de los fenómenos evaluados requieren una configuración particular del modelo y la consideración de los múltiples factores que afectan a la simulación. Esto hace casi obligatoria la configuración del modelo a medida. En consecuencia, se requiere más investigación en las parametrizaciones. La variabilidad del modelo también debería ser atendida, para lo que podría ayudar la asimilación de datos observacionales. También sería de utilidad la evaluación de las incertidumbres generadas por el modelo y la aproximación estadística con *ensembles*. La conclusión general es que parece existir un futuro prometedor para la predicción numérica aplicada al campo de la meteorología aeronáutica.

ABSTRACT

Numerical Weather Prediction Applied to Aeronautical Meteorology: Study of Local Hazardous Phenomena

Aviation and meteorology are intrinsically related. Even if the safety level of the industry is indisputable, the sustained growth represents a constant challenge to maintain the standards assumed today. In this task weather hazards are one of the priorities, as some of these still pose a large risk for aircraft operation. The main objective of this doctoral thesis is to improve the knowledge of numerical weather prediction models when applied to aeronautical meteorology events. This is done by means of the evaluation of four different hazards: mountain wave icing, low visibility, deep convective precipitation and microbursts. These phenomena are linked not only by the disruption they may create to aircraft operation, but also by the fact that they can occur in very local and reduced spatiotemporal domains, which renders them very difficult to predict. The events are analysed using simulations run by a mesoscale atmospheric numerical model, mostly the Weather Research and Forecasting (WRF) model. Different parametrizations and configurations are tested. Several skill scores and validation methods are applied, adapted to each phenomenon. Other nowcasting techniques, not based in numerical weather prediction, are used to support the assessment.

The results for the mountain wave icing show that the WRF model is very competent in the simulation of this phenomenon and the associated in-flight turbulence. Vertical wind speed and liquid water content can be very useful as prognostic variables, and their use would represent a notable improvement on forecasting lead times compared with current nowcasting techniques. For low visibility events, the model presents an underestimation of surface wind speed, and yields worse forecasting results when compared with a different mesoscale model. The results also show that numerical weather prediction is not accurate enough to provide a good forecast and a combination of techniques is required. The model is able to capture the general structure of deep convective systems too, although generating a systematic underestimation of precipitation. The results of this case study highlight the influence of the different factors in the simulation, presenting different sensitivities for physics parametrizations and initial and boundary conditions. In addition, the data suggests a reduced effect of the simulation resolution in the total outcome. When applied to microbursts, the WRF model properly represents the dynamics and characteristic variables of the phenomenon, despite underestimating some of them. However, the sensitivity of these variables is very low, being almost unrelated to the mesoscale thermodynamic conditions. Further analysis on this topic suggest that the reason for this may rely on the effective resolution of the model, and the uncertainties in the microscale. The results show that the variables simulated by the model may not be adequate for the forecasting of this phenomenon, as the kinetic energy dissipation generated at these resolutions is not realistic.

An integrated analysis of the previous results shows the relevance of proper model configuration. Physics parametrizations are decisive in the simulation of the events, producing significant differences in deterministic results, which has been profusely established by other authors. Initial and boundary conditions affect the positioning and timing of the simulation too, and higher resolutions do not necessarily produce better results, in line with previous literature. The resolution of the model becomes a principal issue of this thesis, as the phenomena evaluated is verging the microscale. The results show that the model configuration may allow proper microscale simulations, although the variables reproduced are subject to a low sensitivity, most probable due to the large uncertainties introduced by the energy spectrum. This lack of sensitivity casts some doubts on the forecasting competence of the model, and represents the need to produce parametrization schemes adequate to microscale, as stated by other authors. The results of some of the nowcasting techniques used show that the models may also be improved by the assimilation of better observational data, which will yield further insight into the variability of the system. Finally, the validation methods should be adapted to the phenomena in question, and an integrative assessment should be performed for better results in aeronautical meteorology.

The conclusions of this thesis can be summarised in the following: numerical weather prediction can be a very useful tool for the forecasting of the phenomena in question, notably increasing the lead times. Several prediction techniques and algorithms are already possible as per the state of the art. These may be greatly improved by the ongoing research on microscale model parametrization and configuration. Nonetheless, the characteristics of the phenomena evaluated requires particular model configurations and the consideration of the multiple factors affecting the simulation. This renders bespoke configurations almost mandatory. In turn, more research in parametrizations is required. The variability of the model should be addressed, which may be done by assimilating better observational data. Likewise, by the evaluation of the uncertainties generated by the model and a statistical approach with simulation ensembles. The overall conclusion can be that there is a promising outlook for numerical weather prediction applied to aeronautical meteorology.

TABLE OF CONTENTS

INDEX OF FIGURES

INDEX OF TABLES

1. PREFACE

As per its nature, aviation is intrinsically related with meteorology. The natural environment of an aircraft is the atmosphere and, thus, aviators soon learn that the weather is one of the major components in their daily labour. Weather reports are one of the first things to be studied before a flight, and pilots on duty are constantly checking the meteorological conditions at destination and alternative airports. Weather affects almost every aspect of aviation, from the electrical wire isolation specified in the aircraft design to the standardized phraseology used by the air traffic controllers or the landing technique applied by the flight crew. As a consequence, many meteorological phenomena can become a hazard for aircraft in flight and on the ground.

Aviation safety and meteorology

Meteorology has been an important factor in safety since the dawn of aviation, especially when commercial services began operating regularly. Additionally, as soon as professional aviation was born, accident investigation began developing. Some early reports show that the threats of weather were soon understood. In 1933 an Avro Ten aircraft, operated by Imperial Airways, impacted a radio mast in Belgium. The official report concluded the main reason was the low visibility conditions. One year later, a Swissair flight, performed in a Curtiss Condor II aircraft, crashed in Germany while trying to fly through a thunderstorm. The investigation found that the turbulence created by the storm caused a major structural failure. In 1935, an investigation reported the inaccurate weather forecast as one of the causes behind the crash of a Douglas DC-2 operated by Transcontinental and Western Airways in the United States of America. A similar aircraft flying for the same airline crashed two years later. The report is one of the first declaring ice accumulation as the probable cause of the accident. Also in 1937, the Hindenburg airship, operated by the Deutsche Zeppelin-Reederei, burst into flames when mooring. The probable cause was reported to be static electricity accumulated when flying near a frontal system. Other phenomena took longer to associate with aviation safety. In 1959 a Trans World Airlines flight, performed in a Lockheed Starliner, crashed in Italy soon after departure. The investigation is one of the first concluding that the crash was originated by a lightning strike. And not until 1975 were microbursts discovered, due to the accident of an Eastern Airlines operated Boeing 727 in the United States of America. In this way, aircraft accident investigation has been closely related with meteorological research and, in some cases, has been a driver for it.

Professional aviation safety figures are incontestable nowadays. According to the International Air Transport Association, in 2018 approximately 46.1 million flights were performed between more than 2200 city pairs, carrying more than 4400 million passengers (International Air Transport Association, 2019). For the same year, the European Union Aviation Safety Agency reports a worldwide total of 14 fatal accidents with 586 fatalities in the Large Aircraft category (European Union Aviation Safety Agency, 2019). These figures are not exceptional in the industry. Over the 2008-2017 decade there was an annual average of 17.3 fatal accidents in the Large

Aeroplane category, with 512 fatalities per year. Aviation safety parameters become more impressive when it is considered that in the 2009-2018 decade the number of Passenger-Kilometre Performed grew by 84% (International Civil Aviation Organization, 2020). In fact, the fatal accident rate has dropped from 4.2 per million flights in 1977 to less than 0.3 per million flights in 2017 (Figure 1).

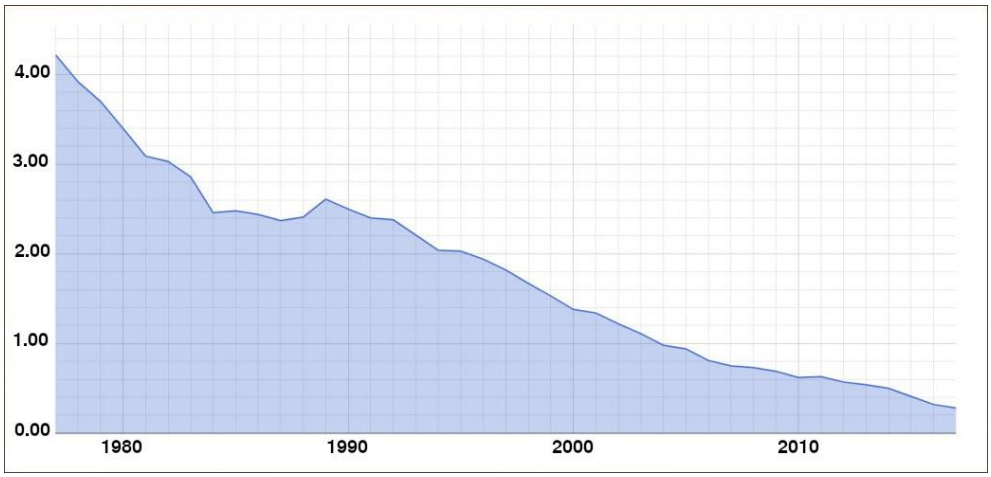

Figure 1: Fatal large aircraft accidents per million flights between 1977 and 2017 (Aviation Safety Network, 2020).

The origin of these figures is in the culture of the aviation industry. Safety has been paramount from the beginning of commercial flights. The whole community has grown and developed around the idea and the objective of safety. It is closely supervised and audited in every possible aspect. Safety panels cover a wide range of specialities, from flying technique to aircraft manufacturing, data processing or psychology. Aircraft accident investigations have been an example of collaboration, independence, science and logical reasoning from the dawn of aviation. Safety culture in aviation is focused on the reasons behind the problems, not in who to blame. The objective always is to evaluate and avoid risks, and, when accidents happen, to identify and correct the problem. Thereby, aviation is a complex and strict activity, very similar to science. Nothing is left to chance, everything is evaluated and there is a reason behind every procedure and ruling; there is a permanent nonconformist attitude about safety. In aviation, there are approved procedures even for the words one can use. That is the only way of achieving the safety figures we are so proud of. Nonetheless, this is a continuous effort. In the next two decades air traffic is expected to duplicate (International Air Transport Association, 2019) and the industry is not willing to accept worse safety rates. Besides, as technology and research develop, the hazards change. Hence aviation is in a constant endeavour to improve knowledge and methods.

The National Transportation Safety Board reported for the 2000-2011 period that 37% of the accidents in Commercial Operations involved meteorological conditions as one of the main causes (Eick, 2014). The resulting 165 accidents are distributed per cause as follows:

- In-flight turbulence: 71%
- Adverse wind: 14%
- Thunderstorms: 6%
- Precipitation: 5%
- Aircraft icing, fog, wind shear, freezing rain: 4%

Nonetheless, this statistic does not take into account the gravity of the accident. According to the European Risk Classification Scheme for 2019 (European Union Aviation Safety Agency, 2019), weather related events represented approximately 15% of the accidents and serious incidents for the Large Aeroplane category. However, convective weather and ice in flight are ranked as the second and third most hazardous type of events (Figure 2). Runway surface condition ranks 12th out of 45, ice on ground is 20th, clear air turbulence and mountain waves is 23rd, and wind shear is 25th. Furthermore, the major risk by this scheme is the monitoring of flight parameters and automation modes, which is particularly critical in low visibility situations.

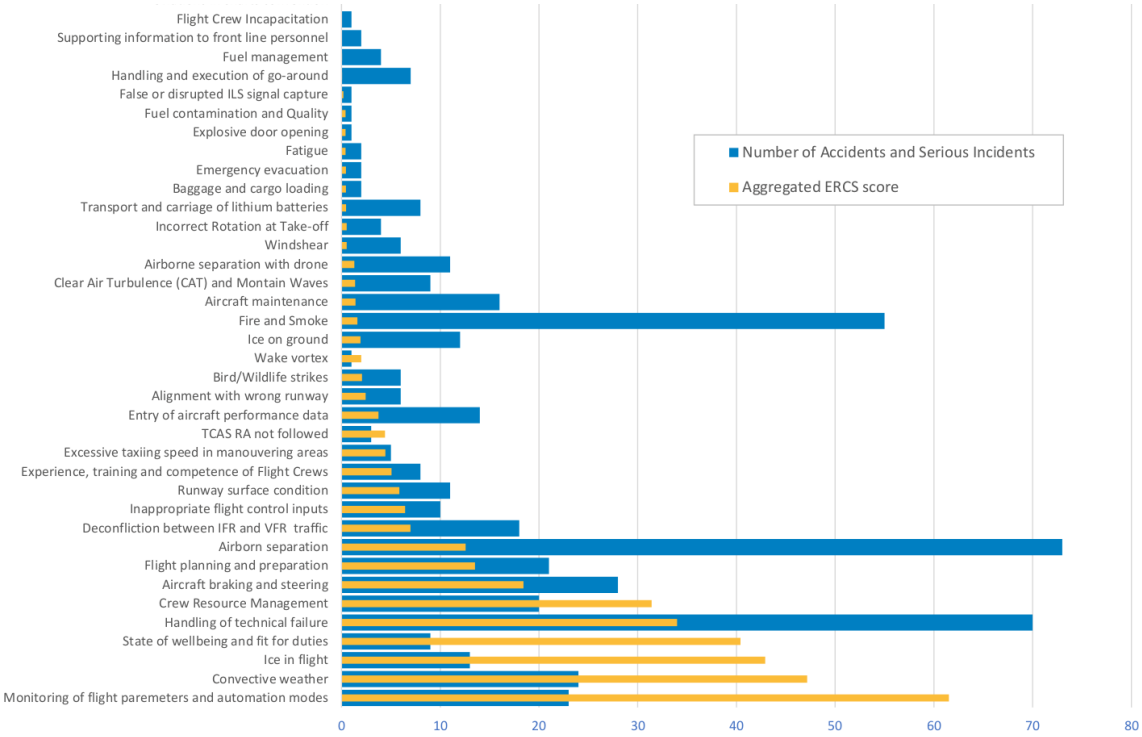

Figure 2: Comparison of number of occurrences and aggregated European Risk Classification Scheme score per safety issue. Adapted from European Union Aviation Safety Agency (2019).

Since the problem of flying with no visual references was solved by radio navigation instruments, the traditional approach to meteorological hazards has been very pragmatic: more training and more power. More thrust allows the aircraft to have a power excess available in case of a degraded performance. This is a tool that the crew can use if the aircraft reaches a dangerous state of low energy or has to deal with extreme meteorological conditions. At the same time, more thrust allows it to climb higher, which provides a larger vertical range to avoid in-flight turbulence, aircraft icing or thunderstorms. More power also enables more powerful aircraft systems, being able to deal with more extreme conditions such as icing (*e.g.*, de-icing and anti-icing systems) or precipitation contaminated runways (*e.g.*, thrust reversers and braking systems). Power is translated into electrical output as well, which enables the installation of more electronics, *e.g.*, meteorological radar, wind shear detection systems or icing detection systems. The human factor has been improved by training. Professional crews are periodically trained and evaluated, and weather hazards is always a part of that. Some of the challenges regularly studied and trained by crews are take-off and landing with crosswind conditions, severe in-flight turbulence events, low visibility operation, aircraft icing conditions, wind shear events or operation in low density atmospheric conditions.

Notwithstanding, there is an important factor in the meteorology related safety which has not kept the same pace of improvement as those aforementioned. That is prediction. Meteorological forecasting has advanced notably for synoptic and mesoscale situations in the last decades. Surface meteorological prediction has been greatly enhanced by observed data assimilation, and the forecasting of extreme situations is relatively reliable nowadays. Despite this, there is a feature of some weather phenomena which renders them particularly hazardous to aviation and very elusive to forecasting: they are very local events.

Forecasting

Numerical prediction models have become a major research instrument in the last decades. The improvement of computational power and the large availability of observational data have turned computers into laboratories. Even more, thanks to broadband internet connections, the instantaneous remote access to computer mainframes and data repositories have largely facilitated the research in meteorology. It should be noted that this has been detrimental to *ad hoc* observation campaigns and field experiments, although this issue is not in the scope of this thesis. Numerical weather models combined with statistics and the myriad of observations assimilated nowadays have notably enhanced the forecasting of many meteorological phenomena (Figure 3). Thus, the general public takes for granted the prediction of regular meteorological events, and sees as a common capability the prediction of extreme events. Even people more literate in meteorology, as professional pilots, often wonder how a certain event cannot be predicted or how a particular prediction failed.

In reality, due to the chaotic character of weather, some complex phenomena are still not fully understood. They can be described as per physics and in laboratory conditions; in spite of that there is not a firm grasp of them in real environments. In turn, common events as precipitation or cloudiness are still subject to large forecasting uncertainties. As a consequence, very local meteorological predictions are far from perfect, being this especially important for aviation. This is a relevant issue in the field, as the constant research efforts prove (Gultepe et al., 2019). Even more, the internal variability derived from the chaotic nature of the atmosphere casts doubts on the plausibility of performing highly accurate predictions. The impossibility of knowing every piece of information with the required exactitude, renders the system stochastic in practice. In fact, in the last decades the deterministic forecasting of meteorological conditions has been left aside in favour of a probabilistic approach. There is still room for improvement, however. Larger computational capacities allow for higher resolutions, which may enable the integration of synoptic, mesoscale and microscale physics. Better deterministic models will create better statistical models, and facilitate the research of particular mechanisms and phenomena.

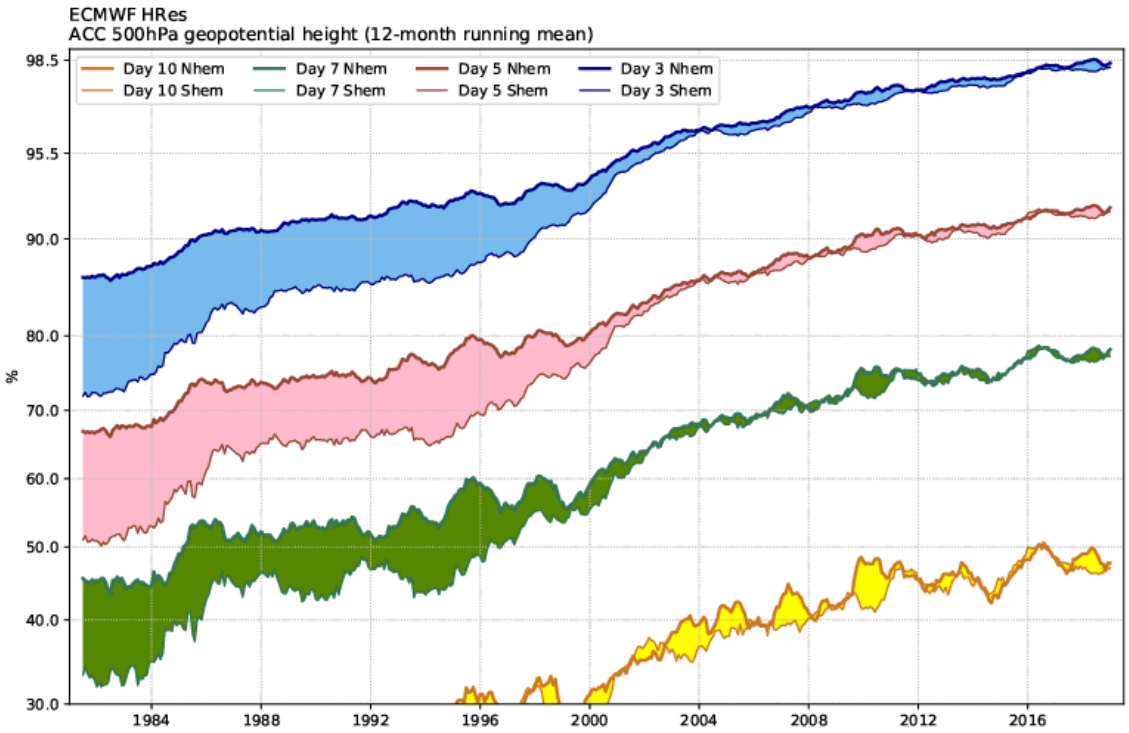

Figure 3: Anomaly correlation skill at three, five, seven and ten day lead times, computed for the 500 hPa *geopotential height over the northern and southern hemispheres (European Centre for Medium-Range Weather Forecast, 2020).*

1.1. Motivation

This doctoral study arises from the motive of improving the simulation and forecasting techniques of several meteorological phenomena hazardous to aviation. It should be noted that this thesis is focused on a practical approach to the issue, based on the robust and widely known theoretical knowledge of aeronautical meteorology. The physics of the phenomena treated are well understood, and it is not the purpose of the author to deepen that knowledge. In fact, the dynamic, microphysics and thermodynamic mechanisms behind these events are far more complex than what is presented here. The intention of the author is to recognise if there is room for development for the numerical weather prediction in the field of aeronautical meteorology and set some bases for future research.

2. OBJECTIVES

The integrated objective of this doctoral thesis is to improve the knowledge on the use of the Weather Research and Forecasting (WRF) numerical model for diagnosing and forecasting meteorological phenomena adverse to aviation safety. As this study is founded on several peer-reviewed publications, the objectives can be detailed for each one, in particular:

- **Mountain wave icing**: This topic is examined by means of a study case near Madrid-Barajas Airport. The target is to demonstrate the ability of the WRF model to reproduce mountain waves and the associated aircraft icing and in-flight turbulence conditions. Observations taken in flight and satellite images are used to evaluate the accuracy of the simulation over the existing forecast.
- **Low visibility**: This phenomenon is evaluated simulating fourteen fog events with the WRF and the HARMONIE-AROME models. The aim is to enhance the fog and low visibility prediction in Tenerife Norte Airport. The simulations are used to produce a categorical forecasting algorithm with the aim of improving the short term prediction. Satellite based products are used to improve the nowcasting reliability.
- **Deep convective precipitation**: A case study near Madrid-Barajas Airport is selected for the analysis of this issue. The target is to study the performance of the WRF model using different boundary conditions, domain resolutions and physics parametrizations. The temporal evolution and geographical distribution of the variables are evaluated to determine the best model configuration. In addition, two time-sensitive skill scores are proposed.
- **Microburst**: The study of this topic is carried out in two different publications.
  - Sensitivity analysis: The objective of the first one is to examine the competence of the WRF model to capture microburst events. Three days with distinct meteorological situations are simulated using different physics parametrizations. The characteristic variables and the dynamics of the events simulated are assessed. The sensitivity of the variables and the best model configuration are established.
  - Effective resolution: The previous results are then used to determine the ability of the model to forecast microburst events. The energy spectrum of the simulations is evaluated to confirm the effective resolution. In accordance with this, three forecasting indices are assessed against climatology.

A secondary objective is to study the plausibility of the application or development of forecasting algorithms and tools based on the simulations.

3. PHYSICAL CONCEPTS

This thesis covers four meteorological phenomena hazardous to aviation: low visibility, deep convective precipitation, icing associated with mountain wave, and microbursts. There are a myriad of meteorological and physics concepts related to these phenomena, and many paths can be followed to present these topics. Nevertheless, all of them originate from a single substance. This is an attempt to thread very different meteorological events not only by the significance to aviation, but also by a physical common denominator: water. To initiate, water vapour must be briefly discussed.

3.1. Water Vapour

One of the gases constituting Earth's atmosphere is water vapour. It is the fifth gas as per concentration, being approximately 99% of it contained in the troposphere and representing approximately 0.4% of the total volume. Nonetheless, water vapour is the thermodynamic working medium for tropospheric processes becoming responsible for a vast number of meteorological phenomena. It is subject to large variations of the local concentration, ranging from 0.01% to 4.24% (McElroy, 2002). Figure 4 presents the average zonal distribution in the atmosphere. Water vapour can condensate into liquid or solid form in the atmosphere, creating **hydrometeors**. The phase changes of water in the troposphere involve the trading of latent heats, which become another factor into meteorological physics (and a large uncertainty factor into forecasting and simulation). Finally, water vapour and hydrometeors affect radiation fluxes, albedo, chemistry, dynamics and other significant processes in the atmosphere as well, although these are not in the range of this study.

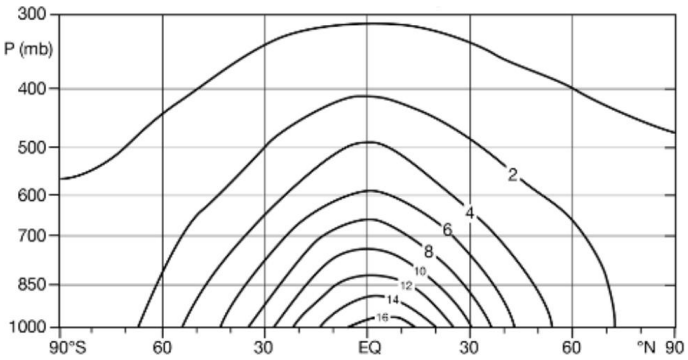

Figure 4: Annual zonal average water vapour mixing (g kg^{-1}) field as a function of latitude and pressure (P. K. Wang, 2013).

At a constant temperature, there is a maximum partial pressure which water vapour can exert in a volume of air. Beyond that, the air becomes saturated and any excess vapour in the air will condensate. Saturation is one of the main atmospheric variables, as it will determine the plausible

processes water can go through. A typical measure of saturation is made via the **relative humidity**, as the percentage of the effective vapour pressure over the saturation vapour pressure. Additionally, as the saturation vapour pressure increases with temperature, a **dewpoint temperature** can be defined as the temperature at which a particular volume of air will saturate, at constant pressure, with the actual quantity of vapour in it (Ahrens, 2009). This leads us to the process by which a parcel of air can change its temperature in the atmosphere, mainly adiabatic expansion and contraction.

Adiabatic processes and stability

Vertical displacements play an important role in meteorology. The vertical movement of a volume of air in the atmosphere can be considered adiabatic, hence it will expand and cool when rising, while a descent will produce the opposed effect. If the adiabatic vertical movement does not generate a phase change of the water content in the air, it is considered unsaturated. The **unsaturated adiabatic rate** (also referred to as dry adiabatic rate) is constant at 9.8 $^{o}C\ km^{-1}$. If the adiabatic vertical movement generates a phase change, the air is considered saturated. Latent heat intercedes notably in the change of temperature of this process. As a consequence, the **saturated adiabatic rate** (also referred to as moist adiabatic rate) is not constant but variable with temperature, eventhough it is always smaller than the unsaturated rate. A commonly accepted reference value near the surface is 5 $^{o}C\ km^{-1}$; this gets closer to the unsaturated rate with altitude, as relative humidity decreases. A volume of air rising adiabatically in the atmosphere will lose temperature as per the unsaturated rate until it reaches the dewpoint temperature and becomes saturated. Beyond that point, it will continue rising following the saturated rate. These temperature rates will create different stability situations for a volume of air in the atmosphere (Figure 5), depending on the environmental lapse rate (González, 2005):

- **Absolute stability**: A vertically forced volume of air will return to its initial position once the forcing disappears. The environmental temperature rate is lower than both adiabatic rates, then the volume of air will always change its density faster than its surroundings. This produces a negative buoyancy in case of a rise or a positive buoyancy in case of a sink, forcing the volume of air towards its original level.
- **Absolute instability**: A vertically forced volume of air will continue moving away from its initial position once the forcing disappears. The environmental temperature rate is higher than both adiabatic rates, then the volume of air will always change its density slower than its surroundings. This produces a positive buoyancy in case of a rise or a negative buoyancy in case of a sink, forcing the volume of air away from its original level.
- **Conditional instability**: A vertically forced volume of air will be stable if unsaturated yet unstable if saturated. The environmental temperature lapse rate is lower than the unsaturated adiabatic rate, but higher than the saturated rate. This condition is interesting as an unsaturated volume of air will be stable as long as the forced rise does not take it to the dewpoint temperature. If this happens, it is said that it has reached the **condensation level** and from there it will become unstable.
- **Neutral stability**: If the environmental temperature rate is coincident with the adiabatic rate (unsaturated or saturated), the volume of air will be displaced for as long as the forcing exists, remaining at the same level once the forcing disappears.

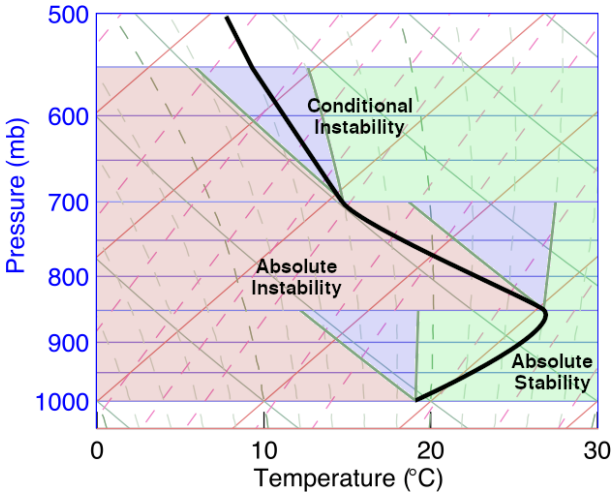

Figure 5: Atmospheric temperature diagram showing different stability conditions.

A stable atmospheric condition does not completely inhibit the vertical movements of air, although some external forcing will be required. On the other hand, an unstable atmospheric condition promotes large vertical movements and, in turn, large changes of temperature for the forced volumes of air. To follow, the main condensation procedures are reviewed.

Condensation mechanisms

As aforementioned, the adiabatic expansion is the most common procedure for air temperature loss in the atmosphere. This cooling will enable the saturation of air, which, in turn, will foster the phase change of water content in it. Temperature loss and the consequent condensation may be generated by several mechanisms (González, 2005):

- **Convection**: A volume of air near the surface is heated and rises as per thermal buoyancy.
- **Orographic forcing**: A volume of air is mechanically forced upslope by wind flows perpendicular to an orographic barrier.
- **Dynamic forcing**: A volume of air is forced to rise by another mass of air with larger density. In this case, the denser air may act as a barrier, forcing upwind warm air to rise upslope of cold air (**warm frontal system**); or may act as a wedge, forcing downwind warm air to rise as cold air pushes from behind (**cold frontal system**).
- **Low level convergence**: Large volumes of air in the lower troposphere converge due to large-scale mechanisms. The air in the centre of the convergence rises as per dynamic processes.
- **Turbulent diffusion**: **Turbulence** is the chaotic change of pressure and velocity of the air flow. In the atmosphere, this implies a vertical displacement of the air. This movement generates a diffusion effect of the particles in it. In this way, turbulent diffusion may raise some air to a point of saturation.

Other physical processes which may produce condensation, not involving an adiabatic expansion, are:

- **Advection**: This is the horizontal movement of air in the atmosphere. It can produce a volume of air to contact a surface or other mass of air with different temperature conditions, enabling a heat transference.
- **Radiation**: Earth's surface cools during the night, due to the radiation loss not counteracted by sunlight. Thus, the lowest layer of air in contact with the surface loses temperature.

3.2. Hydrometeors

Hydrometeors are water particles present in the atmosphere in liquid or solid phase, generated by condensation, solidification or deposition processes of existing water content. These can also be the result of water particles lifted or sprayed from the surface to the troposphere. Hydrometeors are the base of many meteorological features and phenomena, as cloudiness and precipitation. Six types of hydrometeors can be described, where size refers to the diameter of the particle (P. K. Wang, 2013):

- **Cloud drop**: Liquid water droplet suspended in the air. Typical size ranges from a few micrometres to 400 μm, being 10 μm the characteristic size. These hydrometeors do not precipitate, but stay aloft by turbulence and updraughts. In some phenomena, the size of these droplets is an important factor; 50 μm is usually established as the threshold between small and large cloud drops.
- **Raindrop**: Liquid water drop that precipitates from the cloud. Typical size ranges from a few hundred micrometres to 3 *mm*, being 1 *mm* the characteristic size. A subdivision can be made for smaller raindrops, usually called **drizzle drops**, with sizes below 250 μm.
- **Ice crystal**: Solid water crystalline particle suspended in the air. These do not precipitate and may also be referred to as **cloud ice**. Typical size ranges from a few tens to a few hundred micrometres. These particles can take many shapes, *e.g.*, plate, dendrite, column or prism.
- **Snow crystal**: Solid water crystalline particle that precipitates from the cloud. These can take the same shapes as ice crystals. Typical size is a few hundred micrometres. These hydrometeors tend to aggregate into a single piece, named **snowflake**, reaching sizes up to a few centimetres.
- **Graupel**: Solid water precipitating particle generated by the accretion of snow crystals and liquid droplets. The liquid water solidifies over the ice crystal, producing **rime** on it and eventually covering the crystal to generate a grain-like particle. The maximum size of graupel by convection is 5 *mm*.
- **Hail**: Solid water precipitating particles produced by successive rimming processes over a graupel particle. Size ranges from 5 *mm* to several centimetres.

Figure 6 depicts cloud drops, raindrops, graupel and three types of ice crystals, as seen by a cloud, aerosol and precipitation spectrometer probe.

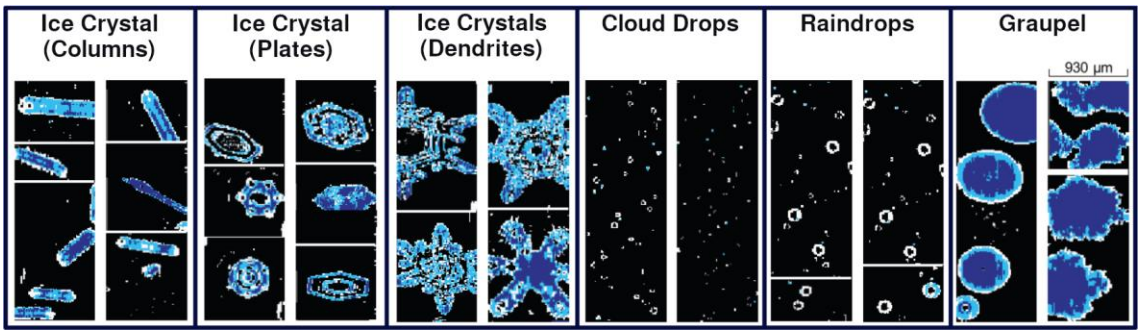

Figure 6: Different types of hydrometeors as captured by a spectrometer. Adapted from Fernández-González (2016).

As we shall see, each of the described hydrometeors may create a particular phenomenon or pose a particular risk to aviation. Likewise, each of them may require different methodologies and considerations for forecasting and simulation.

Genesis of hydrometeors

The generation of hydrometeors necessarily implies a phase change. Every precipitating hydrometeor originates in a cloud drop or ice crystal, as these act as a base for further growth. The fundamental process of condensation, solidification and deposition is **nucleation**, and requires a saturated atmosphere. Nucleation mechanisms do not work in a massive process but in small clusters of particles with similar properties (P. K. Wang, 2013). The mechanisms are two:

- **Homogeneous nucleation**: The hydrometeor forms from particles of a clean substance, attaching to each other and not requiring any other material. Homogeneous condensation will form water droplets of pure vapour, homogeneous solidification will create ice crystals from pure water, and homogeneous deposition will produce ice crystals from pure vapour.
- **Heterogeneous nucleation**: The hydrometeor is generated by the attachment of particles to a foreign nucleus. This nucleus will facilitate different types of hydrometeors depending on its characteristics. Therefore cloud drops require **condensation nuclei** (sometimes referred to as cloud condensation nuclei) while ice crystals require **ice nuclei**.

Homogeneous nucleation is very rare in the atmosphere, as it requires a supersaturated environment (relative humidity above 100%). In the case of homogeneous condensation, as humidity approaches saturation, water vapour particles start a strong interaction with each other, forming clusters of molecules. The number of water molecules interacting in a cluster increases with saturation, and the gas begins to exhibit non-ideal properties (P. K. Wang, 2013). When supersaturation reaches a certain threshold, the collision of clusters forms water drops. Nevertheless, in the free atmosphere this process would require a relative humidity of several hundred percent. Homogeneous solidification and deposition is not as rare, although they require ambient temperatures of $-38\ ^{o}C$ or lower (Lamb & Verlinde, 2011).

Almost every hydrometeor in the atmosphere is created by heterogeneous nucleation. This process, by definition, must involve strange materials other than water. These particles facilitate the production of cloud drops or ice crystals, consequently, the type and concentration of nuclei is one of the principal factors in the hydrometeors nucleation rate, size and concentration.

Aerosols and nuclei

Gases and hydrometeors are not the only contents of the atmosphere, but also particulate matter called **aerosols**. These play an important role in meteorology, organic chemistry and biology at planetary scales. The main source of atmospheric aerosols is Earth's surface, usually particles originated from erosion, ocean waves, combustion by-products, natural phenomena or anthropogenic activity, *e.g.*, dust, marine salt, volcanic ash or industrial emissions. As a result, the maximum vertical concentration of aerosols is located near the surface, being the local concentration highly variable. Aerosols which facilitate nucleation are subdivided per size as (Junge, 1955): **Aitken** particles ($r < 0.1\ \mu m$), large particles ($0.1\ \mu m < r < 1.0\ \mu m$) and giant particles ($r > 1.0\ \mu m$). Figure 7 shows the relative sizes of Aitken particles and liquid hydrometeors.

In the case of condensation nuclei, experimental observations show a variable concentration ranging from 10 to $10^2\ cm^{-3}$ over the ocean and from 10^2 to $10^3\ cm^{-3}$ over the land. This generates clouds with a larger drop concentration but smaller drops sizes over continental areas, while cloud drops are larger yet less concentrated in oceanic clouds. Aerosols prone to become condensation nuclei are hygroscopic and soluble particles (Dusek et al., 2006). This ability depends on air saturation too. As the atmosphere becomes supersaturated, more particles are activated as nuclei. In the case of ice nuclei, the activation of particles with saturation is exponential and becomes clearly patent with the decrease of temperature. Typical concentrations at $-10\ ^oC$ are a few particles per litre, once more, presenting higher concentrations over land. Contrary to condensation nuclei, ice nuclei are hydrophobic and indissoluble particles, mainly minerals, although it is known that some bacteria can facilitate the creation of solid hydrometeors (Lee et al., 1993). Crystal-like structures increase the effectiveness of ice nuclei, as well as large particles or nuclei with contaminants on them. However, as solid hydrometeors can be reached by two different mechanisms, there are different types of heterogeneous nucleation for ice, and thus, different types of ice nuclei: Deposition nuclei facilitate the creation of ice crystals directly from water vapour. Immersion nuclei and contact nuclei promote the solidification of water into ice crystals from inside or outside the droplet, respectively. Finally, some nuclei can serve as a condensation nucleus first, to create a drop which then solidifies into an ice crystal.

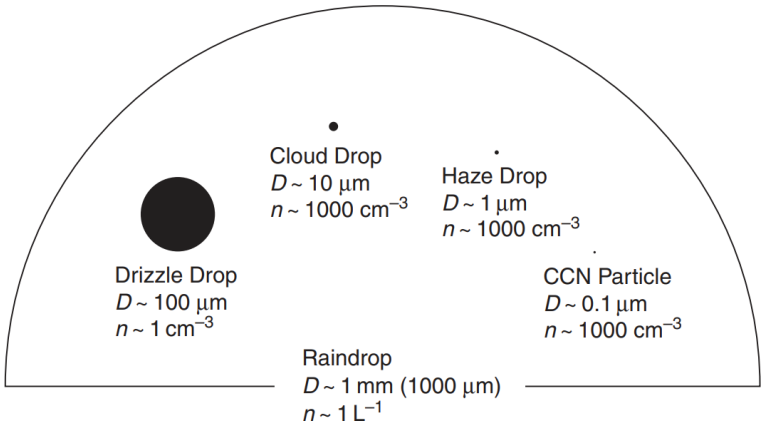

Figure 7: Relative sizes (diameter) and concentrations of various liquid drops found in clouds (Lamb & Verlinde, 2011).

3.3. Clouds

When atmospheric conditions become adequate, a volume of air may achieve the necessary ingredients to produce cloud drops or ice crystals: water vapour, nuclei and cooling. This volume usually has relatively homogenous characteristics, thereby the nucleation process becomes massive, the air is filled with hydrometeors and loses translucency. According to this mechanism, a cloud can be defined as a visible aggregate of cloud drops or ice crystals in the free atmosphere (Ahrens, 2009). Once a cloud particle is suspended in the air, it can evolve by several mechanisms of growth or reduction. To follow, the growth process for smaller particles is presented.

Growth by vapour diffusion

A cloud drop suspended in supersaturated air (with respect to liquid water) will grow by the net condensation of water molecules on its surface. This is a complex mechanism that depends on many microphysics issues, *e.g.*, solute effects of the condensation nuclei, curvature, partial pressure of vapour, dynamics and ventilation effects of the falling droplet, or latent heat trading with the atmosphere (Lamb & Verlinde, 2011). Nonetheless, some basic concepts can be outlined: the rate of addition of water vapour to the droplet is directly related with supersaturation; the excess of vapour concentration depends on the droplet temperature due to the heating derived from condensation; in turn, temperature depends on the growth rate of the cloud drop. As a consequence, this is a partially self-regulated process which performs better for small droplets and loses efficiency for droplets above 40 μm. In the case of ice crystals, vapour diffusion growth is performed via deposition and the supersaturation has to be considered with respect to solid water. This process is predominant for crystal sizes below several hundreds of micrometres. It is a similar mechanism as the aforementioned, even though solute and curvature effects are less important, while atmospheric conditions are more significant. Temperature and supersaturation will affect the shape of the ice crystal, which will have an impact on its growth.

An interesting effect of vapour diffusion arises when ice crystals and cloud drops are present in the same volume of air. The vapour pressure for solid water is lower than for liquid water. This will favour the deposition of vapour in ice crystals, which will decrease the saturation with respect to liquid water and, in turn, will promote the evaporation of cloud droplets. This process, called Bergeron-Findeisen (P. K. Wang, 2013), is most efficient at approximately −15 ^{o}C, when saturation vapour pressure difference for liquid and solid water is larger.

Supercooled liquid water

The attentive reader will have noticed, in the previous section, the mention of liquid water coexisting with solid water and below-freezing atmospheric temperatures. Conventional knowledge will believe this is a mistake, albeit being a fairly common situation. **Supercooled liquid water** is a liquid hydrometeor which temperature is below 0 ^{o}C. Observations estimate that this is the norm in the atmosphere, rather than the exemption, as approximately 40% of cloud particles at −12 ^{o}C are supercooled water (P. K. Wang, 2013). However, as we have seen, supercooled liquid water and ice cannot coexist in equilibrium. The reason that allows this special hydrometeor not to be depleted is in the availability of nuclei. The concentration of cloud condensation nuclei is several orders of magnitude larger that the concentration of ice nuclei (Rogers, 1993). In addition, ice nuclei are less efficient at temperatures above −10 ^{o}C (Huffman

& Norman, 1988). As a result, the process of vapour condensation is more efficient than the process of vapour deposition (Rauber & Tokay, 1991). Ice crystals will be created and will deplete some of the vapour from the ambient, but the consumption is not enough to take the atmosphere below liquid water supersaturation levels. This allows for cloud drops to develop and remain liquid below 0 ^{o}C temperatures. Increasing supersaturation will activate ice nuclei more efficiently than condensation nuclei. As a result, this phenomenon is less common with decreasing temperatures. The lower limit for supercooled liquid water is approximately −40 ^{o}C, when homogeneous freezing becomes efficient.

Icing as an aviation hazard

When supercooled liquid water is present in the atmosphere a risk appears for any body travelling through it. Supercooled water is an unstable hydrometeor which will solidify upon contact. In aviation, this is called aircraft icing*. The performance of an aircraft is highly dependent on the aerodynamic profile of the airfoil and the mass of the airframe. Thus, the uncontrolled loading of ice in flight entails a major hazard.*

Cloud classification

Clouds can be classified depending on several characteristics. A technical categorisation is made by the phase of hydrometeors in the cloud. In this way, there are three groups (Lamb & Verlinde, 2011):

- **Liquid phase clouds**: Clouds where all the hydrometeors are in liquid state. Conventionally, these are considered to be clouds in the lower levels of the troposphere, as per temperature. In fact, these may as well be referred to as warm clouds. Nevertheless, this idea is misleading, as low clouds can have solid phase hydrometeors due to low environmental temperature, or cold clouds can have supercooled hydrometeors.
- **Solid phase clouds**: Clouds where all the hydrometeors are in solid state. Also named cold clouds, conventionally these are clouds in the higher part of the troposphere, which can be misleading as already mentioned.
- **Mixed phase clouds**: Clouds where some hydrometeors are solid and some are liquid. This is usual for clouds with large differences in temperature (bottom and top) or with temperatures between 0 ^{o}C and −15 ^{o}C.

In the early XIX century, clouds were classified by appearance. Four basic characteristics were defined and named. Layer shaped clouds are called ***stratus***; heap-like clouds are named ***cumulus***; clouds shaped like filaments are named ***cirrus***; and rain clouds are named ***nimbus***. These four names were later combined into ten categories, and divided into four primary cloud groups by their height above the ground. Table 1 and Figure 8 summarise this practical classification system, widely used in meteorology.

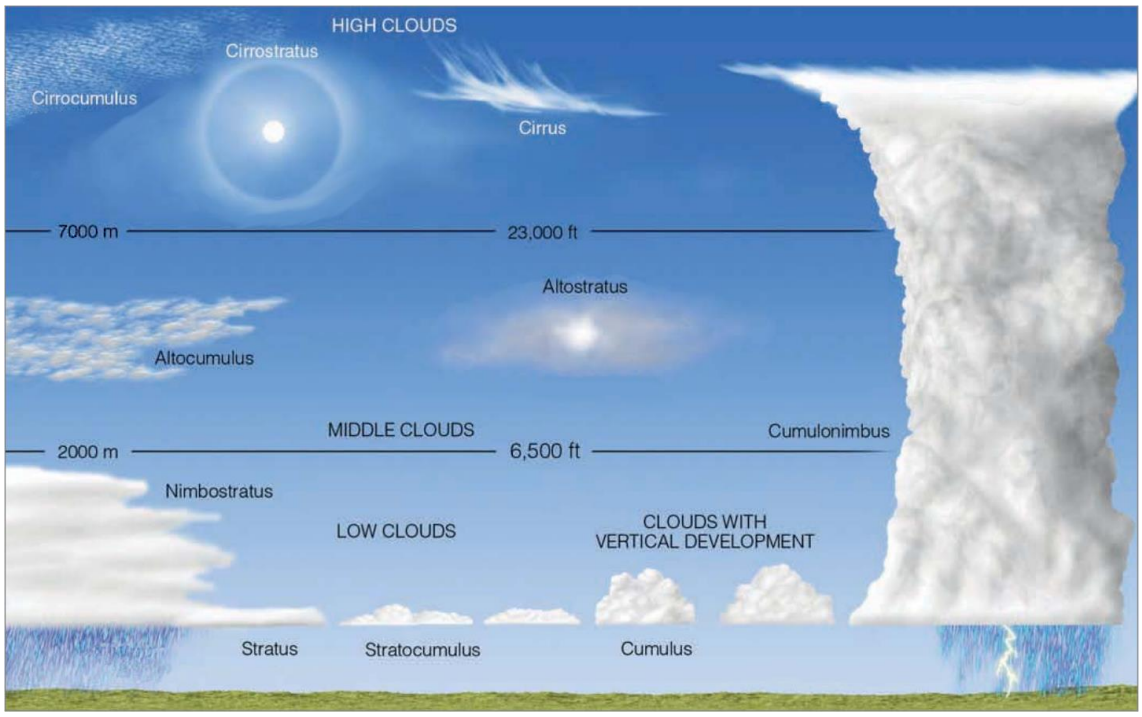

Figure 8: A generalized illustration of basic cloud types based on height above the surface and vertical development. Adapted from Ahrens (2009).

Table 1: Cloud classification as per appearance and altitude.

Cloud Groups	Cloud Types	Altitude (*m* above mean sea level)		
		Tropics	Mid-Latitudes	Polar
High	*Cirrus* *Cirrostratus* *Cirrocumulus*	6000 - 18000	5000 - 13000	3000 - 8000
Middle	*Altostratus* *Altocumulus*	2000 - 8000	2000 - 7000	2000 - 4000
Low	*Stratus* *Stratocumulus* *Nimbostratus*	0 - 2000		
Vertical Development	*Cumulus* *Cumulonimbus*	Large vertical extension		

Fog and mist

According to the American Meteorological Society glossary (American Meteorological Society, 2020), **fog** and **mist** are not different from a cloud other than in the fact that its base is at the surface, therefore it affects visibility near the ground. Both should be differentiated from **haze**, which also obstructs visibility but is composed of suspended aerosols and photochemical effects, and may or may not contain water droplets. According to the conventional definition (World Meteorological Organization, 2019b), mist and haze reduce horizontal visibility below 5000 *m*, while fog decreases below 1000 *m*. These can be discriminated by the relative humidity too, as the upper limit for haze is 80%, while mist requires anything above 95% yet not reaching the 100% of fog. Notwithstanding these considerations, it has to be noted that fog and mist are subject

to a series of interactions with the surface which create some mechanisms different from clouds aloft. Radiation effects, light breezes and shallow thermal inversions can create thin layers of fog during the night (sometimes thinner than 2 *m*). Advection of moist air over cool surfaces can generate saturation, typical over lakes or coastal areas. A similar process can be generated by advection of cold air over warm water.

Low visibility as an aviation hazard

Visibility is an important issue in aviation. Flight plans have to determine if the aircraft will be under Visual Flight Rules or Instrument Flight Rules, and airports have to declare the minimum visibility required to land in their runways. Even if many modern aircraft have the ability to perform almost the entire flight under instrumental procedures, there still are critical parts to be conducted visually. This renders low visibility conditions as a large risk factor in aviation.

3.4. Precipitation

When the mass of a suspended particle is subject to a downward gravitational attraction larger than the displaced volume of air, the particle precipitates. Technically, every hydrometeor is precipitating, even so, many can stay aloft due to atmospheric turbulence or larger updraughts. In meteorology, **precipitation** is referred to those hydrometeors which fall to the earth's surface (American Meteorological Society, 2020). Every hydrometeor has a fall velocity depending on its mass and shape, and when they continue growing beyond cloud drop or ice crystal size their vertical speed increases notably. Figure 9 depicts the dependence of the fall speed on the dimensions of the particle. The masses required for a hydrometeor to become precipitation are usually not achieved by vapour diffusion only, and other growth processes become relevant.

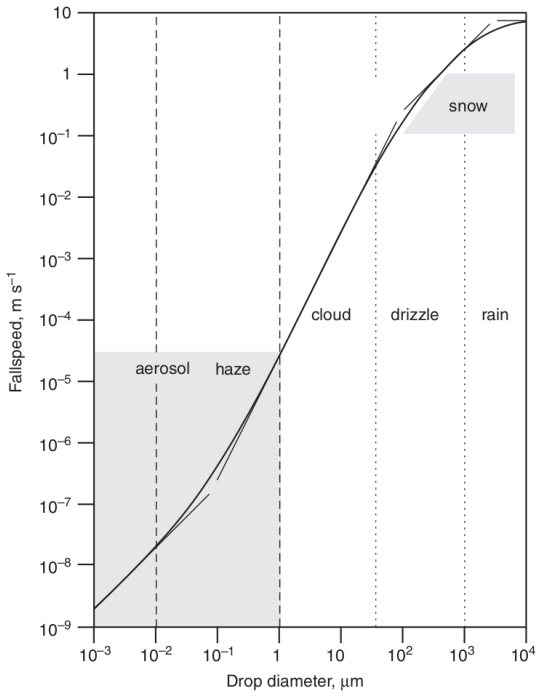

Figure 9: Summary of fall speed as a function of particle diameter for average conditions in the lower troposphere. The shaded region suggests the types of particles suspended by atmospheric turbulence (Lamb & Verlinde, 2011).

Growth by collision-coalescence

Collision-coalescence is the aggregation of two small liquid droplets into a larger drop by means of them making contact. The droplets collide and, as a result, they coalesce into a single hydrometeor. It is predominant between droplets with different sizes travelling at different speeds. Collision-coalescence is a complex mechanism affected by atmospheric turbulence, gravitational forces, aerodynamics and even the electrical forces between the two droplets. It is more efficient than vapour diffusion and generates larger drops, being the main mechanism of precipitation growth in liquid phase clouds. It is estimated that cloud drops require at least 15 *min* of development with collision-coalescence mechanisms to become raindrops. In fact, the **in-cloud residence time** is an important factor in the mass of the drop (Ahrens, 2009). Consequently, the thickness of the cloud and the internal currents of air partially determine the maximum raindrop size.

However, coalescence is not the typical outcome of the collision of two droplets. Observations indicate that only 20% of collisions create a new single drop (List et al., 2009). Coalescence efficiency depends on the size, temperature and velocity of the colliding hydrometeors, and on the relative humidity (P. K. Wang, 2013). It is not unusual for cloud drops below 100 μm to bounce, as the air layer between them cannot drain away during the collision. Larger drops are unstable and tend to break apart; as a consequence, they tend to create a short temporal coalescence which then breaks into two or more droplets.

Growth by accretion and aggregation

Beyond vapour diffusion, the growth of ice crystals into larger hydrometeors can be achieved by two different mechanisms. Accretion (also referred to as **riming**) takes place when a supercooled liquid hydrometeor collides with a solid hydrometeor, freezing upon contact. The efficiency of this process depends on the droplet size and the shape of the crystal (P. K. Wang, 2013). The supercooled drop may solidify immediately or not, according to environmental conditions, generating different types of ice. Accretion is the origin of graupel and hail. It is most intense in clouds with vertical development and at temperatures between 0 and −10 ^{o}C. Moreover, it may produce splinters of ice, which can rapidly multiply the ice crystals in the atmosphere.

A second mechanism is the aggregation of ice crystals after collision, which creates snowflakes. The efficiency of this process is largely dependent on the shape of the crystal and the falling velocity, being higher for more complex structures. It becomes rare below −20 ^{o}C, thus the larger snowflakes are produced at negative temperatures close to 0 ^{o}C.

Deep convection as an aviation hazard

Deep convection are mesoscale convective processes which generate large vertical displacements on massive amounts of air and water. The resulting clouds generate very long in-cloud residence times, which fosters heavy precipitation and every type of hydrometeors. Additionally, deep convection mechanisms are associated with strong winds, gale-force wind gusts, lightning and turbulence. These processes can evolve into large synoptic dimensions as well, creating a widespread hazard which affects many airports and aircraft at the same time.

Evaporation, fusion and sublimation

When precipitation departs its original environment, hydrometeors descend and reach unsaturated layers where they may be affected by evaporation, fusion or sublimation (Figure 10). Solid hydrometeors may be subject to sublimation, becoming vapour, or to fusion, becoming liquid water. Liquid hydrometeors can evaporate partially, reducing the amount of precipitation, or completely, producing ***virga*** (precipitation not reaching the surface). Similar processes can suffer solid hydrometeors through sublimation.

Furthermore, fusion can produce special types of precipitation, as **freezing precipitation**. This is composed of liquid phase hydrometeors which fall to the surface at temperatures below 0 *ºC*. This meteorological phenomenon can have two origins. The first mechanism is solid phase precipitation that melts when falling through an intermediate layer of positive temperatures. It then enters a near-surface thermal inversion with sub-zero temperatures. The second mechanism is the growth of supercooled liquid water by collision-coalescence processes, which precipitates to the surface within a vertical profile with sub-zero temperatures. This type of freezing precipitation is generated in liquid phase clouds with relatively high cloud top temperatures (above −15 *ºC*), does not suffer melting and never finds temperatures above 0 *ºC* in its fall. The result in both cases is that liquid precipitation reaches the surface in a supercooled state (Ahrens, 2009). As it has already been mentioned, these hydrometeors will freeze upon contact.

Finally, evaporation, fusion and sublimation mechanisms have consequences not only for precipitation and water in the atmosphere, but also for cloud dynamics and thermodynamics. The trading of latent heats can have a large impact in density and buoyancy, and may generate new changes of phase and new processes. In turn, the vertical displacement generated by the buoyancy alteration will generate adiabatic temperature changes that can compete with the previous. All these variations have an additional effect on saturation pressure and relative humidity, modifying once more the conditions stability. The final result is a chaotic system where small changes in the hydrometeors can produce very different outcomes.

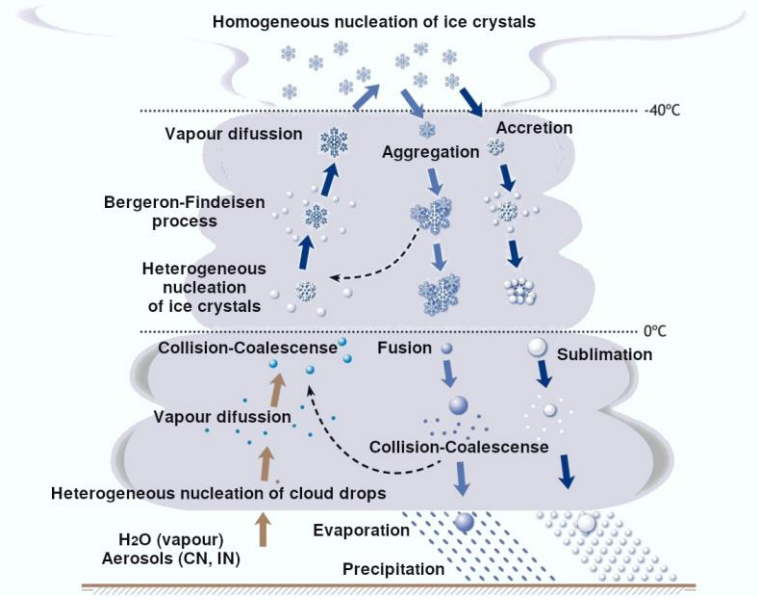

Figure 10: Diagram of the main processes involved in the generation of the different hydrometeors. Adapted from Fernández-González (2016).

Microbursts as an aviation hazard

Microbursts are a relatively unknown phenomenon highly determined by evaporation, fusion and sublimation. The phase change of some solid hydrometeors near the 0 ºC *can create a largely negative buoyant volume of air. This plummets to the surface, assisted by other thermodynamic processes. When a microburst hits the ground it will produce a divergent pattern of high-speed winds. Some microbursts have been observed producing gusts up to 66* $\mathrm{m\ s^{-1}}$ *and generating tornado-like damages on the surface. Needless to say, this is a major hazard for any aircraft flying close to it. In addition, microbursts are very difficult to forecast, rendering it one of the most difficult meteorological situations a pilot can face.*

4. HAZARDS TO AVIATION

Before going into some detail about the hazardous phenomena evaluated in this thesis, it is worth a brief commentary on the meteorological information available in aviation.

Meteorological reports for aviation

There are many weather reports in aviation. These are broadcasted by airports and meteorological offices at regular intervals, and include specific variables relevant to aircraft operation. Wind, visibility, cloudiness, temperature, pressure and severe weather are compulsory to report. Dangerous phenomena must be specifically notified, *e.g.*, severe turbulence, severe icing, thunderstorms, hail, mountain waves or volcanic ash. This information is coded into a standard format and emitted in public regulated messages. Some of these reports are here described (Federal Aviation Administration, 2016b):

- **METAR**: Meteorological Aerodrome Report. This is a routine report of meteorological observations issued for a particular airport. Usually emitted at 30 or 60 *min* intervals.
- **SPECI**: Special meteorological report. This is a report of significant observations issued for a particular airport. It is emitted when the defined criteria is met, usually for hazardous or specific phenomena. A SPECI may also be issued when the conditions reported in the current METAR change notably during the validity period. The formatting is similar to a METAR.
- **TAF**: Terminal Area Forecast. This is a forecast report issued for a particular airport. It must contain the expected conditions for the specified period, including possible significant changes. Validity periods usually are 9, 24 or 30 *h*.
- **SIGMET**: Significant Meteorological report. This is a report of significant observations issued for a particular area or airspace. It is emitted when the defined criteria is met, usually for hazardous or specific phenomena.
- **SIGWX**: Significant Weather map. This is a routine forecast map issued for a particular area or airspace. It is emitted every six hours with a validity period of six hours. It presents hazardous or specific phenomena.
- **AIREP**: Air Report. This is a special message of observed adverse meteorological conditions. It is issued by a flight crew, reporting conditions met in flight, usually for hazardous or specific phenomena.

The coding of these messages is not complex, although it is very specific and follows strict rules for each type. Decoding charts are provided in Figure 11, Figure 12 and Figure 13.

1. Symbols for significant weather

Tropical cyclone		Drizzle	
Severe squall line*		Rain	
Moderate turbulence		Snow	
Severe turbulence		Shower	Hail
Mountain waves		Widespread blowing snow	
Moderate aircraft icing		Severe sand or dust haze	
Severe aircraft icing		Widespread sandstorm or duststorm	
Widespread fog		Widespread haze	
Radioactive materials in the atmosphere**		Widespread mist	
Volcanic eruption***		Widespread smoke	
Mountain obscuration		Freezing precipitation****	

* In-flight documentation for flights operating up to FL 100. This symbol refers to "squall line".

** The following information should be included in a separate text box on the chart: radioactive materials in the atmosphere symbol; latitude/longitude of release site; and (if known) the name of the site of the radioactive source. In addition, the legend of SIGWX charts on which a release of radiation is indicated should contain "CHECK SIGMET AND NOTAM FOR RDOACT CLD". The centre of the radioactive materials in the atmosphere symbol should be placed on significant weather charts at the latitude/longitude site of the radioactive source.

*** The following information should be included in a separate text box on the chart: volcanic eruption symbol; the name of the volcano (if known); and the latitude/longitude of the eruption.

In addition, the legend of SIGWX charts should indicate "CHECK SIGMET, ADVISORIES FOR TC AND VA, AND ASHTAM AND NOTAM FOR VA". The dot on the base of the volcanic eruption symbol should be placed on significant weather charts at the latitude/longitude site of the volcanic event.

**** This symbol does not refer to icing due to precipitation coming into contact with an aircraft which is at a very low temperature.

Note: Height indications between which phenomena are expected, top above base as per chart legend.

2. Fronts and convergence zones and other symbols used

Cold front at the surface		Position, speed and level of maximum wind	
Warm front at the surface		Convergence line	
Occluded front at the surface		0°:100	Freezing level
Quasi-stationary front at the surface		Intertropical concergence zone	
Tropopause high		State of the sea	
Tropopause low		Sea-surface temperature	
Tropopause level		Widespread strong surface wind*	

FL 320
220/400
FL 310

Wind arrows indicate the maximum wind in jet and the flight level at which it occurs. If the maximum wind speed is 60 m/s (120 kt) or more, the flight levels between which winds are greater than 40 m/s (80 kt) is placed below the maximum wind level. In the example, winds are greater than 40 m/s (80 kt) between FL 220 and FL 400.

The heavy line delineating the jet axis begins/ends at the points where a wind speed of 40 m/s (80 kt) is forecast.

Symbol used whenever the height of the jet axis changes by +/–3000 ft or the speed changes by +/–20 kt

* This symbol refers to widespread surface wind speeds exceeding 15 m/s (30 kt).

3. Abbreviations used to describe clouds

3.1 Type

CI = Cirrus	AS = Altostratus	ST = Stratus
CC = Cirrocumulus	NS = Nimbostratus	CU = Cumulus
CS = Cirrostratus	SC = Stratocumulus	CB = Cumulonimbus
AC = Altocumulus		

3.2 Amount

Clouds except CB

FEW = few (1/8 to 2/8)	BKN = broken (5/8 to 7/8)
SCT = scattered (3/8 to 4/8)	OVC = overcast (8/8)

CB only

ISOL = individual CBs (isolated)
OCNL = well-separated CBs (occasional)
FRQ = CBs with little or no separation (frequent)
EMBD = CBs embedded in layers of other clouds or concealed by haze (embedded)

3.3 Heights

Heights are indicated on SWH and SWM charts in flight levels (FL), top over base. When XXX is used, tops or bases are outside the layer of the atmosphere to which the chart applies.
In SWL charts:
(a) Heights are indicated as altitudes above mean sea level;
(b) The abbreviation SFC is used to indicate ground level.

4. Depicting of lines and systems on specific charts

4.1 Models SWH and SWM – Significant weather charts (high and medium)

Scalloped line	=	demarcation of areas of significant weather
Heavy broken line	=	delineation of area of CAT
Heavy solid line interrupted by wind arrow and flight level	=	position of jet stream axis with indication of wind direction, speed in kt or m/s and height in flight levels. The vertical extent of the jet stream is indicated (in flight levels), e.g. FL 270 accompanied by 240/290 indicates that the jet extends from FL 240 to FL 290.
Flight levels inside small rectangles	=	height in flight levels of tropopause at spot locations, e.g. 240. Low and high points of the tropopause topography are indicated by the letters L or H, respectively, inside a pentagon with the height in flight levels. Display explicit FL for jet depths and tropopause height even if outside forecast bounds.

4.2 Model SWL – Significant weather chart (low level)

X	=	position of pressure centres given in hectopascals
L	=	centre of low pressure
H	=	centre of high pressure
Scalloped lines	=	demarcation of area of significant weather
Dashed lines	=	altitude of 0°C isotherm in feet (hectofeet) or metres Note: 0°C level may also be indicated by 0°:060, i.e. 0°C level is at an altitude of 6000 ft.
Figures on arrows	=	speed in kt or km/h of movement of frontal systems, depressions or anticyclones
Figure inside the state of the sea symbol	=	total wave height in feet or metres
Figure inside the sea-surface temperature	=	sea-surface temperature in °C
Figures inside the strong surface wind symbol	=	wind in kt or m/s

4.3 Arrows, feathers and pennants

Arrows indicate direction. Number of pennants and/or feathers correspond to speed.

Example: 270°/115 kt (equivalent to 57.5 m/s)
Pennants correspond to 50 kt or 25 m/s
Feathers correspond to 10 kt or 5 m/s
Half-feathers correspond to 5 kt or 2.5 m/s

* A conversion factor of 1 to 2 is used.

Figure 11: Summary of notifications used in aviation meteorological documentation (International Civil Aviation Organization, 2016).

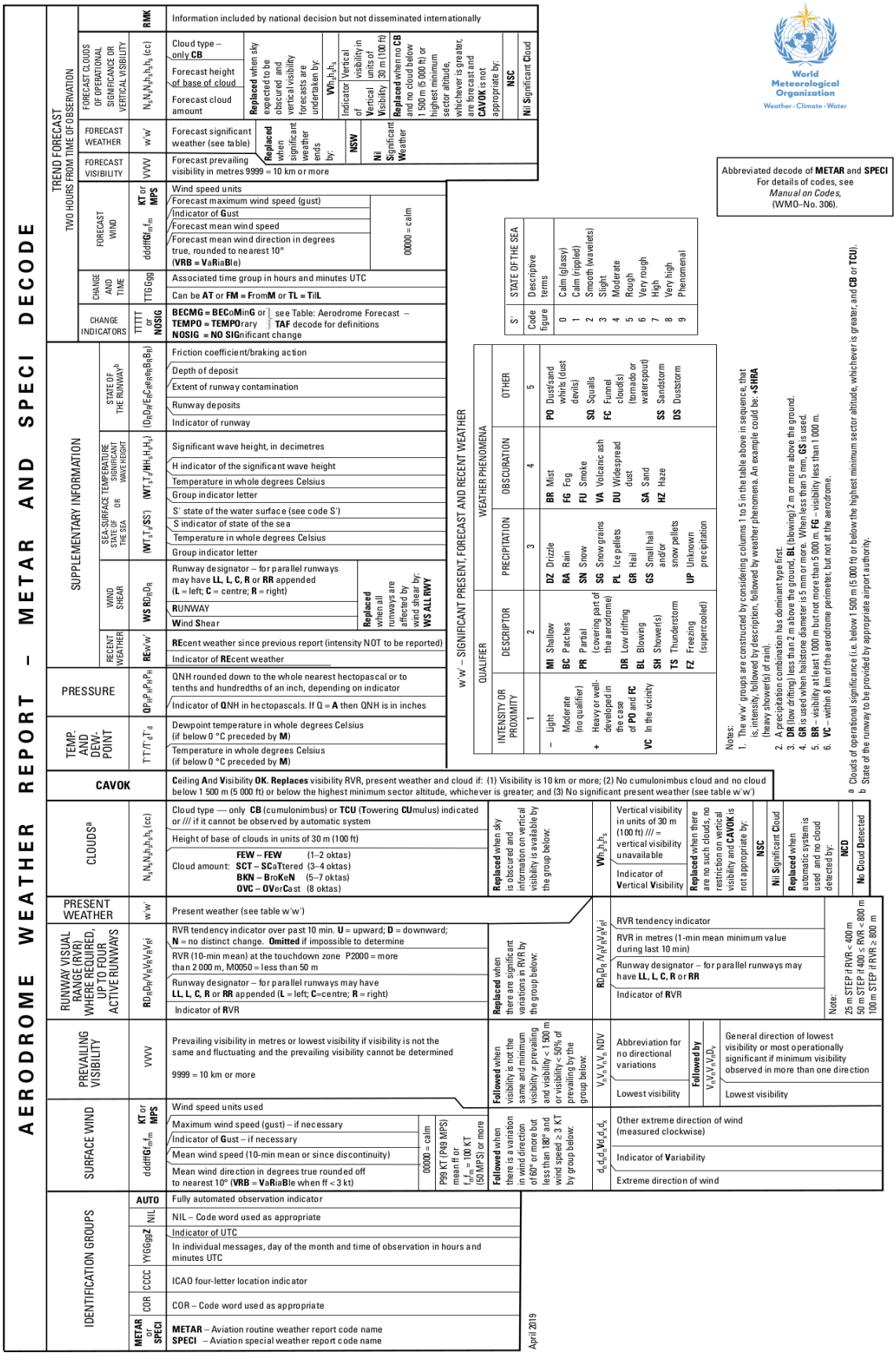

Figure 12: METAR and SPECI decoding reference card (World Meteorological Organization, 2019a).

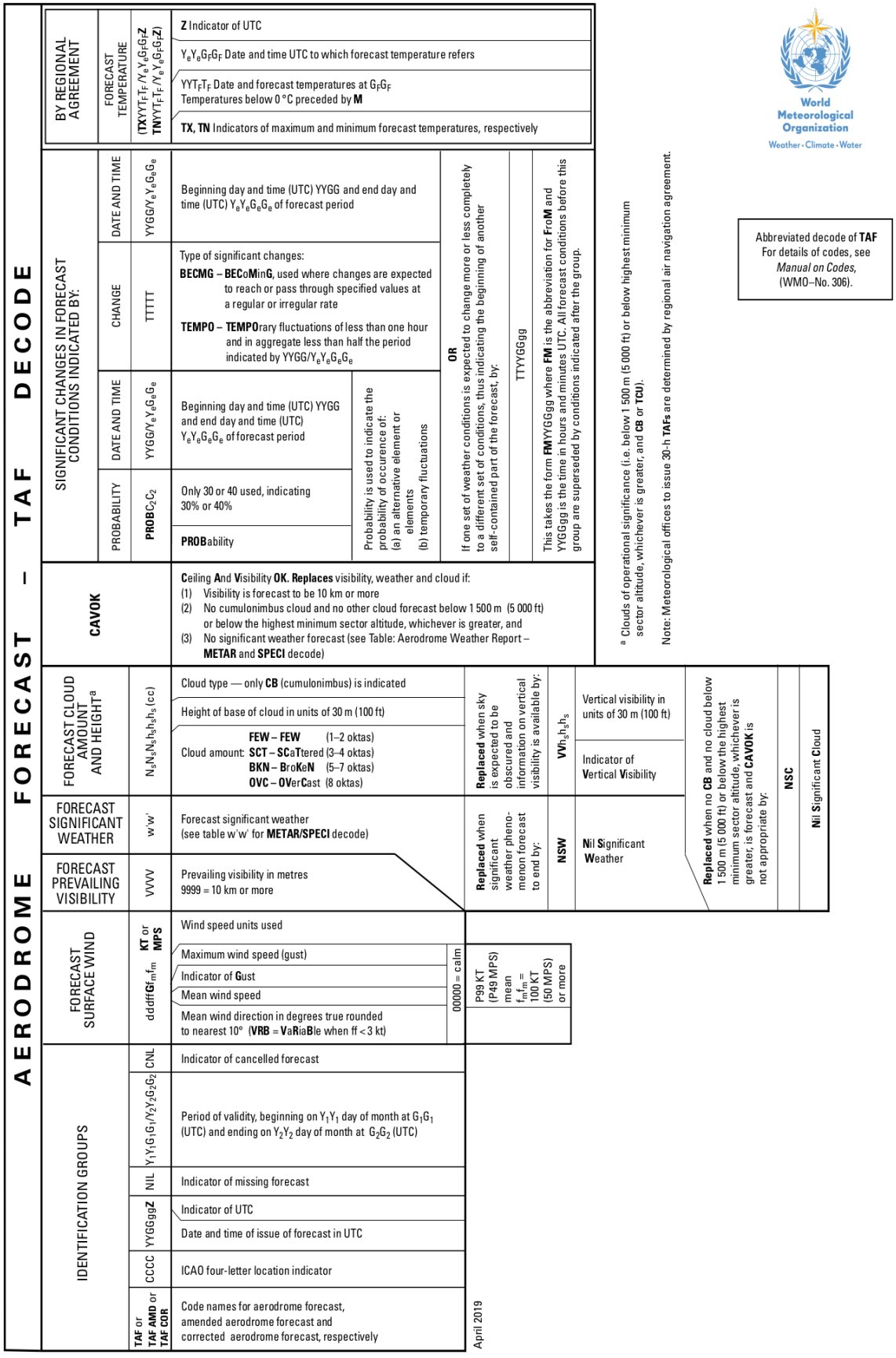

Figure 13: TAF decoding reference card (World Meteorological Organization, 2019a).

If the reader is interested in the full explanation and formatting, it is recommended to consult the International Civil Aviation Organization (2016), the World Meteorological Organization (2019a) and the related documents. Having presented this brief note on aviation meteorological reports, further insight into the physics of the selected phenomena and the implications to aviation safety is to continue.

4.1. Icing

In general terms, icing can be defined as the build-up of ice on an object. The event of **aircraft icing** is simply the accretion of ice on an aircraft in flight. Nonetheless, the actual event of ice accretion should be differentiated from the atmospheric conditions conducive to it. This has been a research issue at least since 1940 (Jeck, 2001), and it is intimately related with the research of hydrometeors. Gent et al. (2000) define aircraft icing as the solidification of supercooled liquid hydrometeors when impinging on the surface of an aircraft flying at temperatures at or below 0 ^{o}C. Thereby aircraft icing conditions does not define the presence of ice phase hydrometeors in the atmosphere, but rather the presence of liquid phase hydrometeors which can cause icing. In this section, only in-cloud icing will be considered, as freezing precipitation is less common and follows a similar mechanism.

Once there are supercooled hydrometeors suspended in the troposphere, two processes have to be considered for aircraft icing. The first one is the rate of collection of hydrometeors by the aircraft. This depends on the liquid water content of the cloud, the diameter of the droplets, the speed of the aircraft, and the shape and size of the collecting surface. Ambient pressure and temperature effects are negligible. When the droplet has impacted the surface, the second process to consider is the rate of solidification. Freezing of the impinged water depends on the dissipation of the fusion latent heat, governed by the convective and evaporative cooling, as well as by the kinetic heating. Consequently, the speed and characteristics of the iced surface, and the temperature and pressure will determine the freezing rate (Gent et al., 2000).

As supercooled liquid water content in the troposphere is the governing factor in the process, icing conditions are predominantly related to vertical movements of air. This is common in areas with deep convective conditions or low level convergence associated with instability, *e.g.*, warm sectors of frontal systems. Also, areas subject to orographic forcing, *e.g.*, orographic clouds or mountain waves. Another tropospheric condition where icing is very common is temperature inversions, *e.g.*, areas ahead of warm fronts, where freezing precipitation can be found (Fernández-González, 2016). According to this, *cumuli congesti* and *cumulonimbi* are major icing hazards. *Altocumuli*, *strati* and *stratocumuli* may produce icing, although not in large amounts. *Nimbostrati* can generate only low amounts of icing, albeit their extension represents a risk. Accounting for the genesis of supercooled liquid water, almost all icing conditions tend to occur between 0 and −20 ^{o}C of atmospheric temperature. In fact, about half of the aircraft icing is reported between −8 and −12 ^{o}C, and altitudes between 1500 and 4000 m (Federal Aviation Administration, 2016a).

Types of aircraft icing and categories

Depending on the characteristics of the hydrometeor and the atmospheric conditions, three types of icing can be produced (Figure 14) as per the Federal Aviation Administration (2016a):

- **Rime ice**: This is produced by supercooled droplets that freeze immediately upon impact. The rapid solidification traps air, creating a rough, white opaque ice. The atmospheric conditions that favour this type of icing are temperatures below −15 ^{o}C, low liquid water content and small droplets (<50 μm). Rime ice is very common in aviation. It accumulates on the forward exposed edges of the airframe.
- **Clear ice**: Also known as glaze ice. This is generated by supercooled droplets that spread over the surface before freezing. The relatively slow solidification efficiency allows the air to escape, thus creating a glossy, clear and translucent ice. High liquid water content, large droplets (>50 μm) and temperatures above −10 ^{o}C are conducive to clear ice. It is not as common as rime ice, although it can be extremely dangerous for aircraft in flight. It can create either a thin smooth layer or streak, spreading beyond the point of impact, or accumulate on a horn, near the top or bottom of the leading edge of the airfoil.
- **Mixed ice**: This type of icing presents mixed characteristics between rime and clear ice.

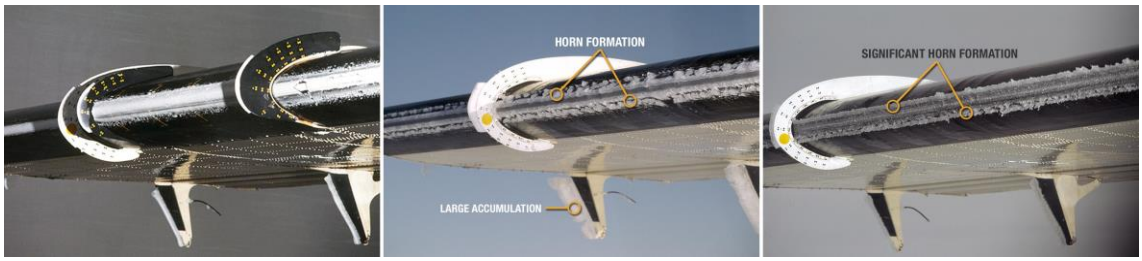

Figure 14: Types of aircraft icing at moderate intensity (National Aeronautics and Space Administration, 2020). Left: rime ice. Centre: mixed ice. Right: Clear ice.

Independent from the type of icing, the variables related with aerodynamics and design of the airframe generate two important points. First, icing behaviour and effects are different for each type of aircraft and can vary with speed. Second, icing is a very local phenomenon. In fact, manufacturers usually reflect in the operating manual which area of the airframe pilots should check first, as it is not uncommon for ice accretion to initiate on very specific parts of the aircraft. These issues render the objective measurement of aircraft icing a very difficult task. In consequence, icing categories used in aviation are subjective, with the following definitions (Jeck, 2001):

- **Trace**: The rate of accretion is slightly superior to the rate of sublimation. Ice is perceptible on the airframe, nevertheless protection systems are not required. It does not alter the flight characteristics nor poses a hazard.
- **Light**: Accretion is clearly perceptible and may pose a risk if exposition lasts over one hour. The use of protection systems is required, at least occasionally.
- **Moderate**: Accretion is clearly perceptible and becomes hazardous even at short expositions. The uninterrupted use of protection systems is required while exposed to the conditions.
- **Severe**: The rate of accretion is superior to the rate of removal/prevention provided by the protection systems. Flight performance is impacted and safety is at risk. Immediate flight diversion from icing conditions is required.

From the meteorological point of view, there have been several attempts to establish an objective measurement. As in situ observations are difficult and expensive to obtain, there is not a widely accepted scale. Nevertheless, Tafferner et al. (2003) use numerical simulations and take into consideration laboratory icing studies to relate the aforementioned categories with supercooled liquid water content, as shown in Table 2.

Table 2: Liquid water content for stratiform and cumuliform clouds and corresponding icing category.

LWC ($g\ m^{-3}$) stratiform	LWC ($g\ m^{-3}$) cumuliform	Icing category
< 0.11	< 0.07	Trace
0.11 - 0.69	0.07 - 0.50	Light
0.69 - 1.33	0.50 - 1.00	Moderate
> 1.33	> 1.00	Severe

Icing in mountain lee waves

When a stratified flow of air is mechanically forced upslope an orographic barrier and the atmospheric conditions are stable, a **mountain lee wave** can be generated. The air reaching the top of the barrier is negatively buoyant as per the adiabatic cooling, hence it descends as soon as the forcing disappears. This descent is assisted by gravity below the neutral level, creating a positive buoyancy which excites the oscillation (Ledesma & Baleriola, 2007). This wave-like motion of air can propagate horizontally and vertically from the orographic barrier. If the relative humidity is in the adequate levels, the upslope of the wave will saturate air, which will be then unsaturated in the downslope. This creates a particular type of stratified cloud along each of the crests, named **wave cloud**. Furthermore, if the temperature is in the appropriate range, the relatively fast variation of vertical velocity creates favourable conditions for supercooled liquid hydrometeors, due to the larger efficiency of condensation nuclei and the reduced in-cloud residence time. This fosters aircraft icing conditions. Mountain waves are also related with turbulence, which will be covered later.

Further remarks about aircraft icing

Icing is usually referred to aircraft in flight, even so, the threat is plausible on ground too. Freezing precipitation poses a large risk for aircraft, as per obvious reasons. Solid hydrometeors can melt over the airframe and then freeze due to temperatures below 0 *ºC*. Also while on the ground, any kind of stagnated water can freeze inside hollow parts of the aircraft, such as engine ducts or pitot probes. Another type of icing not mentioned before is produced due to the cold soak effect. Aviation fuel has a low thermal conductivity and it is in direct contact with the airplane's wing skin. In this way, if an airplane has been cruising at ambient temperatures below 0 *ºC*, the wing surface will retain this temperature during the descent. At positive atmospheric temperatures, non-supercooled liquid droplets impinging on this surface can produce icing. The same may happen when an airplane on ground is refuelled with fuel below 0 *ºC*. A different type of icing can happen to aspirated reciprocating engines. Carburettor icing does not require the presence of hydrometeors in the atmosphere, only water vapour. It is produced by the combination of the Venturi effect and the fuel vaporization, which create a sharp temperature drop. Thereby, when relative humidity is above 50%, carburettor icing is plausible with atmospheric temperatures up to 33 *ºC*.

4.2. Low Visibility

In meteorology, visibility is the greatest distance in a given direction at which it is possible to see and identify, with the unaided eye, a dark object against the sky at the horizon (American Meteorological Society, 2020). In physics terms, low visibility is a relatively simple concept. Any particle, aerosol or hydrometeor, suspended in the atmosphere will produce visibility degradation by reducing transparency or affecting the translucency characteristics of the air.

Notwithstanding the maximum visibility definitions for fog, mist and haze, the hazard for aviation is related to the minimum that can be produced. Low visibility can be found in a myriad of meteorological states and locations, as many phenomena can generate it. Mist, haze or smoke can reduce visibility to a few thousand metres. Suspended dust or sand can hinder the visual range below a thousand metres. Fog, **smog** (mixture of fog and smoke) or **snow blizzards** (snow being blown aloft from the surface by the wind) can degrade visibility to only a few metres. Moderate precipitation (drizzle, rain, snow or hail) can reduce the range below 500 *m*, while heavy precipitation may allow only 50 *m*. Finally, clouds will affect visibility as well, with the following approximate ranges (González, 2005): *cumulus*, 10 to 80 *m*; *cumulonimbus* and *nimbostratus*, 10 to 20 *m*; *stratus* and *stratocumulus*, 30 to 200 *m*; *altocumulus* and *altostratus*, 80 to 300 *m*.

Types of visibility and categories

In aviation, four different types of visibility are relevant (Ledesma & Baleriola, 2007):

- **Horizontal visibility**: This is the horizontal visibility for an observer on the ground. When declared for an airport, this must represent the general condition of the nearby area unless there are significant variations depending on the direction. In the latter case, the minimum visibility must be reported.
- **Runway Visual Range**: This is the horizontal distance at which the runway surface markings of lightning can be seen for an observer at 2.5 *m* over the axis of the referred runway. Day and night conditions for the measurement of Runway Visual Range are established. This variable must be reported by the airport when horizontal visibility is below 2000 *m*.
- **Vertical visibility**: In aviation terms this is referred to as the vertical distance at which a flying observer can see the runway. In meteorological terms, this is the vertical distance at which a tethered balloon can be seen. This must be reported in case of any visibility obscuring phenomena.
- **Oblique visibility**: This is the distance at which the runway surface markings of lightning can be seen by an observer flying the referred runway approach path (vertical and horizontal). This visibility cannot be measured directly. It is derived from horizontal and vertical visibilities, nonetheless, these are not reliable estimations as light scattering and reflection can induce large errors.

Visibility will determine several flying techniques and procedures. The navigation of aircraft can be performed by visual recognition (Visual Flight Rules) or by radio and electronic signals (Instrument Flight Rules). These are very different methods which imply particular rules,

operation, training, aircraft equipment and airport facilities. Therefore, to perform a flight under Visual Flight Rules the following conditions must be met: horizontal distance to clouds, 1500 *m*; vertical distance to clouds, 300 *m*; horizontal visibility below 3050 *m* above mean sea level, 5 *km*; horizontal visibility at or above 3050 *m* above mean sea level, 8 *km*. There are exceptions and special considerations to these, but, as a general rule, any flight performed under worse meteorological conditions has to follow Instrument Flight Rules.

Moreover, instrumental flights are subject to other rules as per the visibility conditions. Take-off and ground movement of an aircraft are crucial parts of the flight due to the proximity of obstacles, and cannot be performed by instruments. International regulations allow normal operating procedures for ground movements and take off down to a visibility of 550 *m*. When visibility is below that threshold, Low Visibility Procedures must apply down to a limit of 75 *m*. The most critical parts of a flight are the approach and landing operations. Under Instrument Flight Rules, the approach is performed by instruments down to a decision point where the landing must be continued by visual references. Depending on the aircraft characteristics, the airport facilities and the operating procedures, each approach must specify the minimum required conditions to land. The most precise techniques will allow continuing an approach with zero visibility down to a height of 15 *m*. Below this height, a horizontal visibility of only 75 *m* is necessary to continue the landing.

Further remarks about low visibility

Visibility can be impaired by optical effects as reflections and refractions, thus humidity, density and turbulence of the air become a factor. Colour, brightness and size of the objects as well, and also the luminosity, natural or artificial. These all are taken into account in aeronautical regulations, with strict rules for signalling, marking and lightning of objects. Finally, physiological phenomena are considered in aviation too, as the human body is subject to many sensory effects which can hinder perception, *e.g.*, vision is affected by hypoxia (possible when flying above 3000 *m* due to oxygen partial pressure), and speed perception is lower when flying in low visibility conditions.

4.3. Deep Convection

Deep convection is defined as the process where thermally driven turbulent mixing creates vertical motions able to raise a volume of air from the low troposphere to higher levels. There are not specific requirements defined, although some commonly accepted features are (National Oceanic and Atmospheric Administration, 2020):

- Low level convergence.
- Triggering mechanism (thermal, orographic, dynamic or turbulent forcing).
- Deep unstable layer.
- Relative humidity in excess of 70% lifted above 500 *hPa*.
- Upper level divergence.

Deep convection conditions are conducive to the generation of vertical development clouds. When these reach considerable dimensions and become susceptible to generating a hazard, they

are usually named **convective cells**. The diameter of these cells can range between 5 and 20 *km*, and the base can range altitudes from 500 to 2500 *m*, depending on the atmospheric humidity. A major characteristic of convective cells is the vertical movement of air. The number and features of convective cells will determine the type of storm generated. A single cell storm will grow in the following phases (González, 2005):

- **Development**: The required ingredients are humidity, instability and a trigger for convection. When these meet, updraughts will take humid air aloft and generate condensation, creating a *cumulus*. The amount of latent heat released will foster more convection, producing ascending velocities around 10 $m\ s^{-1}$. In turn, condensation and hydrometeors will grow. When precipitable sizes are reached, descending movements of cold air will appear inside the cloud. The cell reaches a ***cumulus congestus*** state, with the characteristic towering appearance and cloud tops in the range of 6000 to 8000 *m* of altitude, well below 0 *ºC* temperatures. The time required for this stage is usually 15 to 20 *min*.
- **Maturity**: When a *cumulus congestus* reaches its maximum height, it becomes a *cumulonimbus*. The mature phase is marked by the development of strong descending velocities. These carry cold air and precipitation from the top of the cell, cooling the base and fostering the downdraughts. Equivalent to the ascending velocities, the downward motion of air can reach more than 10 $m\ s^{-1}$. When the downdraughts impact on the ground, they displace the warm air below the cell, creating a **gust front**. As a result, wind gusts and turbulence are observed aloft and on the surface. While this happens, the updraughts have become more intense, reaching velocities larger than 30 $m\ s^{-1}$. When the convective cell reaches the troposphere, the intense wind shear usually caps it, creating the characteristic ***cumulonimbus incus*** shape. This stage typically lasts 15 to 30 *min*. It is a violent and very hazardous phase, associated with strong turbulence, wind gusts, hail, heavy precipitation and lightning.
- **Dissipation**: This stage is denoted by the weakening of the upward forces. Downdraughts dominate the base of the cell, inhibiting convection and growth. Vertical velocities drop below 5 $m\ s^{-1}$, precipitation intensity decreases and the cell slowly dissipates into a stratiform shape. This stage lasts around 30 *min*.

An extreme case of the aforementioned process is the **supercell**. This is a single cell convective storm which acquires very severe characteristics, growing from local to small mesoscale dimensions. Large vertical wind shears promote a rotational motion in the ascending air of the cloud, which may produce a drop of pressure below the cell, creating a **mesocyclone** (Figure 15). This not only fosters surface air convergence, but also allows for ascending and descending air to coexist without interrupting the feedback of humidity and temperature, as convection is not inhibited. Thence, supercells can live for hours, creating strong winds, large hail, heavy precipitation, very severe weather and even tornadoes.

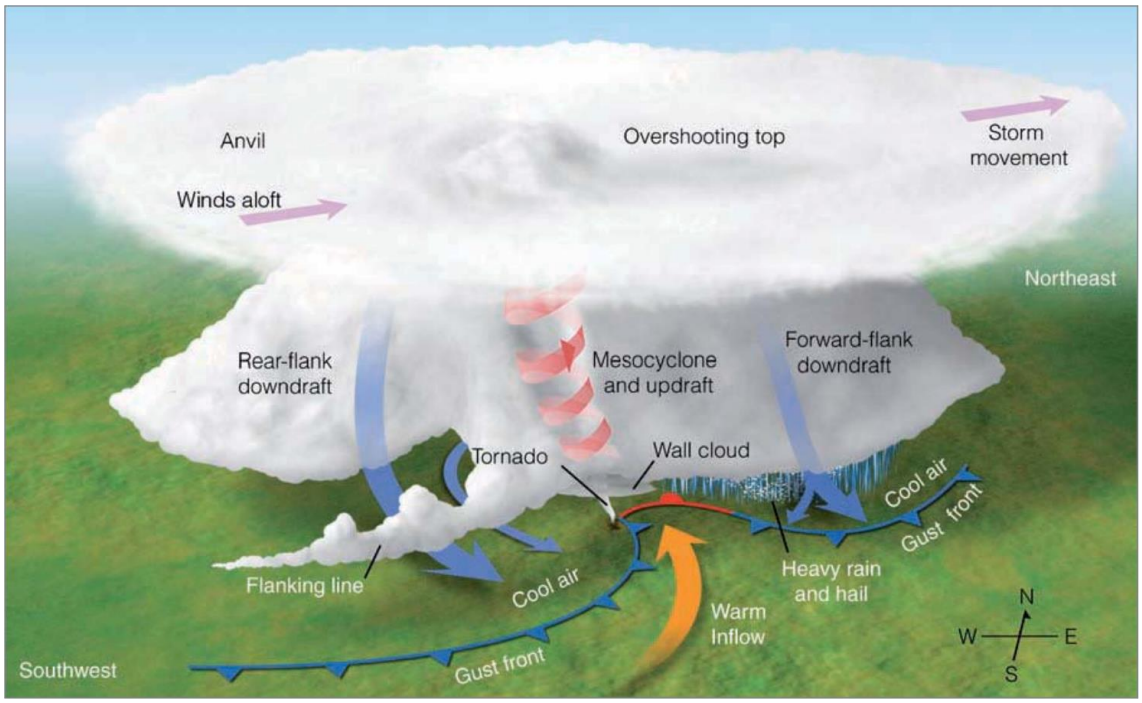

Figure 15: Typical tornadic supercell structure (Ahrens, 2009). A surface anticlockwise rotation is depicted. Cardinal directions are valid for the Northern Hemisphere.

Supercells should not be confused with a **multicellular** storm. This follows the same behaviour as single cell storms with a particularity: the gust front of a parental cell acts as the triggering mechanism in the surrounding areas, creating a child cell. In this way, several cells in different development stages are united in a single storm. The feedback processes of multicellular storms can be very persistent, lasting for hours and creating very large and dangerous clouds. A different type of storm involving multiple cells can be generated by cold frontal systems. As per the dynamic forcing created in the warm sector, they can produce a **squall line**. These are fronts of multiple single convective cells, extending hundreds of kilometres long and tens of kilometres wide. Squall lines are not local phenomena, but require mesoscale features. When deep convection conditions dominate at large mesoscale dimensions, they are referred to as a **mesoscale convective system**. These systems foster an organised and synoptic scale structure of storms, reaching dimensions just below extratropical cyclones.

Due to the characteristics of a convective cell, the processes in it acquire massive dimensions and involve large amounts of air, water and energy. Heavy precipitation is a typical result of deep convection. As per dynamics and hydrometeors in-cloud residence time, convective cells are prone to generate every type and rate of precipitation. Although there is not a standardized description for precipitation intensity, Table 3 presents a widely accepted scale (American Meteorological Society, 2020).

Table 3: Precipitation intensity rates as per hourly average and maximum 6 min *rate.*

Type	Average Rate ($mm\ h^{-1}$)	Maximum Rate ($mm\ 6\ min^{-1}$)
Light	< 2.5	< 0.25
Moderate	2.5 - 7.6	0.25 - 0.76
Heavy	> 7.6	> 0.76

In-flight turbulence and categories

Another hazard directly created by deep convection is turbulence. As aforementioned, the vertical motion of air is a necessary component of convective cells. Thence, atmospheric turbulence is a core feature of them. It is worth here to note the following: in aviation, turbulence is the rapid alternation of the vertical velocity of the aircraft, creating an irregular flight motion. This **in-flight turbulence** should not be mistaken with atmospheric turbulence. Notwithstanding, in-flight turbulence may be the result of the atmospheric type, *e.g.*, convection or wind shear. However, it may also arise from other non-turbulent meteorological phenomena; any which creates an oscillatory vertical movement of air, *e.g.*, mountain waves. In addition, aeronautical meteorology emphasises on a particular type of in-flight turbulence which yields no visual clues: **clear air turbulence** is the in-flight turbulence produced by any phenomena not accompanied by clouds or other visual signatures, rendering it unexpected.

As for aircraft icing, in-flight turbulence depends on the characteristics of the aircraft, flight speed and atmospheric irregularities. Thus, the most used in-flight turbulence categories are subjective (Ledesma & Baleriola, 2007):

- **Light**: Slight and erratic changes in attitude and/or altitude. No particular actions are required.
- **Moderate**: Erratic changes in attitude, altitude and speed. The effective control of the aircraft requires continuous input changes. Loose light objects may be displaced. The use of seat belts is required for comfort.
- **Severe**: Large, abrupt changes in attitude, altitude and speed. There may be brief periods where the effective control of the aircraft is impossible. Loose heavy objects may be displaced. The use of seat belts is required for safety.
- **Extreme**: Complete loss of control of the aircraft. Possible structural damage of the airframe.

There have been several attempts to create objective turbulence categories. Aircraft manufacturers use the vertical acceleration (±0.2 *g*, ±0.5 *g*, ±1.0 *g* and >1.0 *g*, respectively) or a combination of the load factor and the maximum equivalent wind gust, which are defined as design requisites. The International Civil Aviation Organization recommends the use of the Eddy Dissipation Rate (González, 2005). This is based in Kolmogorov's hypothesis to calculate the rate at which atmospheric turbulent kinetic energy dissipates into heat. This objective measure of the atmospheric conditions can be applied to the aircraft weight and speed to produce an objective scale of intensities. Nevertheless, this is used in technical reports and scientific analyses, yet is not a usual categorization method in aeronautical meteorology.

Further hazards of deep convection

Initially, heavy precipitation is not a direct hazard to aircraft. Even so, flying through an area with heavy hail can badly damage the skin of the aircraft. Heavy precipitation will degrade visibility as well. The impact on flight performance is only small, despite this, the runway friction will be affected, reducing the braking performance and even generating hydroplaning. A convective cell will also produce icing conditions at some point, while turbulence and wind shear are almost ubiquitous. Lightning strikes become another possibility. These may pierce the metal skin of the aircraft and be seriously harmful to composite surfaces; the electronic equipment may result damaged, and electrostatic charges impair the radio signals used for communications and navigation. As a result, convective cells are to be avoided every time possible, and heavy precipitation is an early and useful warning for it. As an operational standard, no commercial aircraft will fly through or close to a convective cell, changing the flight route or even diverting to a different airport if required.

4.4. Microburst

Convective cell downdraughts in the maturity stage of *cumulonimbi* can generate damage on the ground due to the wind gusts produced. For this reason, it was not until the late 1970s that **microbursts** were discovered as a different phenomenon. Microbursts are extreme downdraughts of air which impinge the ground, generating a divergent surface wind pattern with high radial velocities. The surface winds are in fact a gust front, named **outflow**. Figure 16 shows the diagram of a microburst and Figure 17 presents the observed behaviour of surface wind for a particularly extreme microburst. For qualifying as a microburst, the outflow must present a wind speed differential across the centre of the divergence of, at least, 20 $m\ s^{-1}$ (Fujita, 1985). These are very local events, in space and time; the maximum diameter and lifespan of the outflow is 4 *km* and 15 *min* (Fujita, 1981). If the phenomenon extends beyond those dimensions they are named **macrobursts**. Moreover, microbursts can be subdivided in two categories (Wakimoto, 2001):

- **Low-reflectivity** (dry) **microbursts**: The convective cell producing this microburst generates less than 0.25 *mm* of precipitation and shows a radar reflectivity below 35 *dBZ*.
- **High-reflectivity** (wet) **microbursts**: The convective cell producing this microburst generates more than 0.25 *mm* of precipitation and shows a radar reflectivity above 35 *dBZ*.

This subdivision is the main evidence of microbursts not being of the same nature as convective cell downdraughts. Both phenomena share some thermodynamic mechanisms, but originate and develop according to different processes. Microbursts initiate close to the 0 *ºC* level and are highly conditioned by the phase change of hydrometeors (Srivastava, 1985). The triggering mechanism can be **precipitation loading** (air is dragged downward by the weight of precipitation) or a small latent heat cooling (usually promoted by the entrainment of environmental unsaturated air) at the mid-levels of a developing or mature convective cell. Any of these processes generate a descent of the volume of air, which rapidly enters an unstable layer of positive temperatures. Phase changes accelerate and the enhanced latent heat cooling renders the volume of air negatively buoyant. As the air descends to the base of the cloud, it enters an environment with increasing virtual temperature, due to a higher relative humidity. As a result, the negative buoyancy is increased, meaning that the volume of air accelerates as it descends. Once the descending air breaks through the base of the cloud, it enters a **superadiabatic** layer

(lapse rate higher than unsaturated adiabatic). This enhances the vertical velocity towards the ground and completes a differential characteristic of microbursts: the downdraught accelerates toward the surface, achieving the minimum vertical speed between 1000 and 500 *m* above the ground (Proctor, 1989; Srivastava, 1987). It is also worth noting that there is no scientific agreement on the minimum vertical speed required for a microburst to happen. More details of the microburst genesis are found in the results section of this thesis, not reproduced here to avoid redundancy.

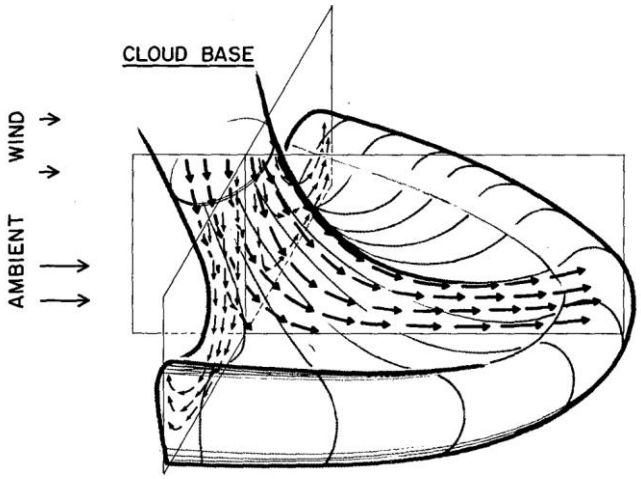

Figure 16: Schematic microburst structure at maximum intensity (Hjelmfelt, 1988).

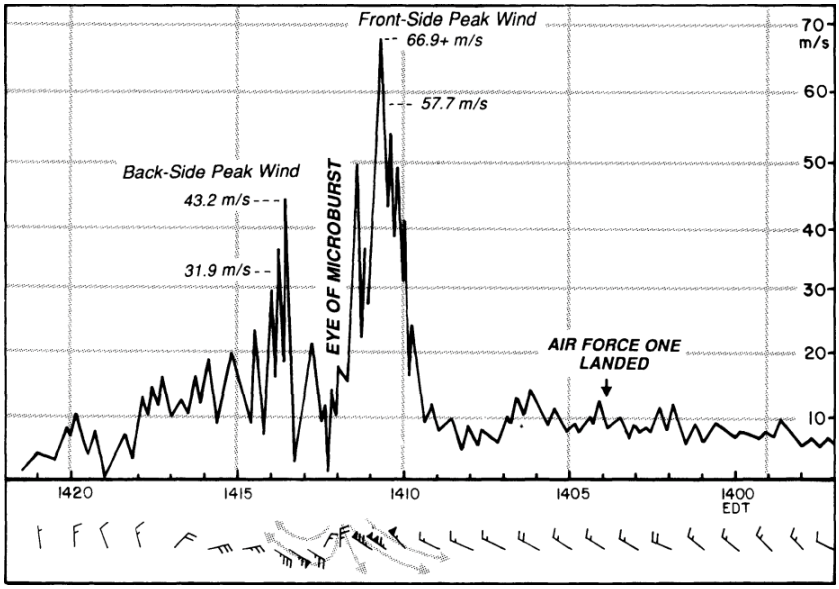

Figure 17: Wind speed and direction trace recorded by an anemometer located near the runway at Andrews Air Force Base on 01 August 1983 (Fujita, 1985).

As per the aforementioned process, microbursts do not necessarily require a strong convective cell to happen. Low-reflectivity microbursts have been observed from virga generating *altocumuli* (Proctor, 1988). Cooling due to phase changes is the primary forcing factor in low-reflectivity microburst. Fusion and sublimation generate larger latent heat cooling than evaporation, as a result, solid phase hydrometeors are optimal for microburst generation. Hail may generate strong high-reflectivity microbursts, while snow may generate strong low-reflectivity microbursts. Nonetheless, sensitivity studies show that sublimated snow can produce downdraughts twice as

intense as those generated by hail (Wakimoto, 2001). For this to occur, the sub-cloud environmental lapse rate is determinant. If it is superadiabatic, the rate of phase changes loses weight as a factor. Even a light precipitation can generate a negative temperature anomaly that will maintain a strong downdraught. The mechanism intensifies with the depth of the superadiabatic layer. All this renders low-reflectivity microbursts even more dangerous; not only because they can create wind gusts as intense as high-reflectivity microbursts, but because they may generate form an innocuous-looking cloud, becoming completely unexpected.

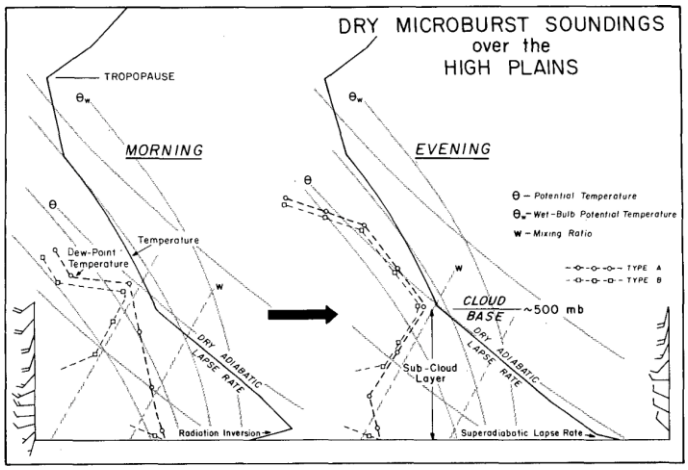

Figure 18: Thermodynamic diagram of the environmental conditions conducive to low-reflectivity microburst in high plain regions (Wakimoto, 1985).

Microburst detection

As per their nature, microbursts are very difficult to detect with ordinary observation instruments. Needless to say that they are almost impossible to forecast accurately. Field campaigns using mesoscale observation arrays have been able to detect and study the phenomenon. The results show that microbursts are associated with characteristic thermodynamic diagrams (Wakimoto, 2001). Figure 18 shows the thermodynamic profile for low-reflectivity microbursts (Wakimoto, 1985), and Figure 19 for high-reflectivity microbursts as observed by Atkins and Wakimoto (1991). The presence and distribution of solid phase hydrometeors just above the 0 *ºC* level has also been related to microbursts, as well as the cloud base height. However there is not enough knowledge of the phenomenon to define a complete set of meteorological conditions conducive to low-reflectivity nor high-reflectivity microbursts.

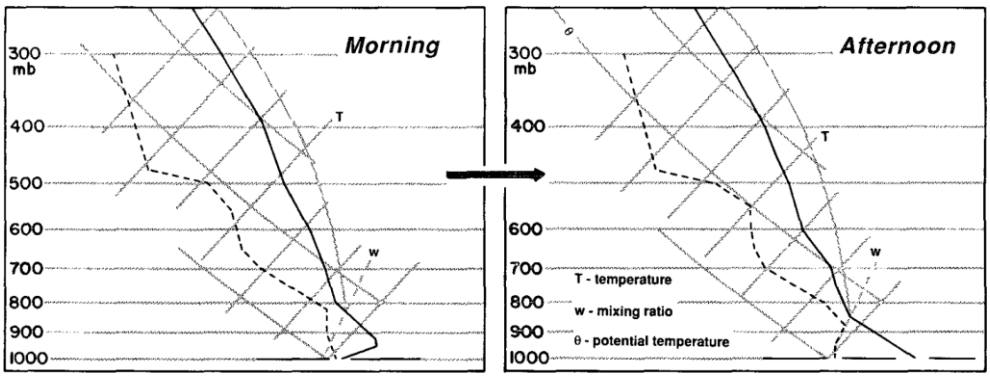

Figure 19: Thermodynamic diagram of the environmental conditions conducive to high-reflectivity microburst in humid regions (Atkins & Wakimoto, 1991).

Up to date, the best detection and nowcasting mechanisms rely on Doppler-radar instruments. A well trained operative radar meteorologist is able to detect the descent of the nucleus of a high-reflectivity microburst. This rapid descent of the precipitation core and large horizontal velocity differentials are the two distinctive features left by the phenomenon in radar images. These have been used to create automated microburst nowcasting systems, which use radar data and assimilated observations to provide a warning with a few minutes lead (Wolfson et al., 1994).

Figure 20: Photographic sequence of a microburst reaching the surface (Peter Thompson, 2015).

In-flight encounter with a microburst

Microbursts are a major hazard for aviation (Figure 20). Every professional pilot has been trained in the simulator for a microburst event, as the situation usually allows for only a few seconds for recognising and taking action. Even so, not even applying the best technique will guarantee a positive outcome. The flying performance of an aircraft depends on airspeed, relative to the volume of air it is flying into. Thus, a sudden change in the speed of the volume of air will create a change of the aircraft's airspeed. This may be compensated for by aerodynamic effects or by the crew taking action (*e.g.*, increasing thrust), yet, if the change is very rapid, the compensation may be insufficient. If airspeed decreases enough, the effective angle of attack of the aircraft will increase to a critical point, reaching a stall condition and losing lift. One simple solution would be to always fly with sufficient airspeed to avoid any stall due to unexpected gusts of air. If the minimum microburst speed differential (20 $m\ s^{-1}$) was to be accounted for, large aircraft would need to add at least a 25% to the typical landing airspeed. This, as per obvious reasons, creates more risks than those it may statistically avoid.

We face an energy trading problem. Aircraft flying low and slow (*e.g.*, landing or taking off) are in a low energy status. Kinetic energy is just enough to fly safely and there is only a small amount of potential energy we can trade into speed. Besides, the thrust delivery of aircraft engines is not immediate. In this situation, an aircraft penetrating a microburst outflow will first encounter a headwind. This will increase airspeed and performance, taking the aircraft above its intended vertical flight path, and increasing the energy condition as a result (Figure 21). If the crew does not recognise the microburst at this point, they will correct the power setting and attitude, taking the aircraft to a lower energy state to compensate the departure from the intended configuration. In a few seconds, the aircraft will enter the downdraught shaft, facing a decrease of flight

performance and a negative vertical speed, pushing it towards the ground. The aircraft, already in a low thrust configuration, will reduce the available potential energy, hence no airspeed can be gained. In this situation, the flight crew has no other choice than to apply maximum thrust and aim for the critical angle of attack, keeping the aircraft airspeed just above the stall and trying to use the power excess to climb away from the ground. Nevertheless, shortly after this, the tailwind will appear. The aircraft now has to deal with a decreased flight performance induced by the outflow, hindering the climbing and accelerating efforts. For these reasons, the outcome of an encounter with a microburst depends on the early identification and action by the crew.

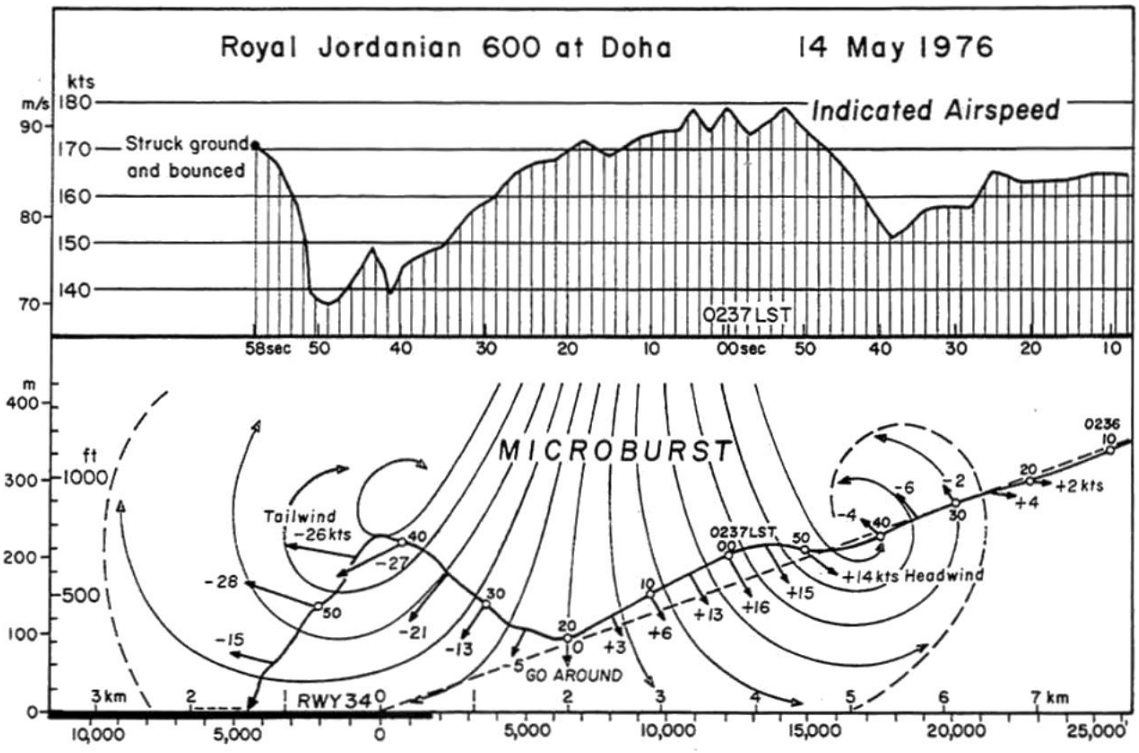

Figure 21: Final approach path of flight Royal Jordanian 600. After encountering with a microburst, the aircraft crash landed at Doha Airport, Qatar, on 14 May 1976 (Fujita, 1985). Lower panel: the dashed line represents the intended vertical flight path; the irregular solid line represents the actual vertical path; the small arrows along the actual path represent the wind direction and speed relative to the horizontal path (assumed to be a straight line extending from the runway); the small numbers along the actual path represent the seconds from the marked times.

5. EXPERIMENTAL RESOURCES

The specific methods and experimental design for each article are adequately explained in the publications. For a better understanding of these, some basic notions about numerical weather models, observations and data processing are presented here.

5.1. Numerical Weather Prediction Models

The base of a numerical weather model is a **dynamical core** that performs the computation of the **primitive equations** of fluid dynamics and thermodynamics, namely (Lauritzen et al., 2011):

- Conservation of energy (First Principle of Thermodynamics):

$$Q = C_p \frac{dT}{dt} - \alpha \frac{dp}{dt} \qquad \text{(Eq. 1)}$$

- Conservation of momentum (Navier-Stokes):

$$\frac{dv}{dt} = -2\Omega \times v - \frac{1}{\rho}\nabla p - \nabla\Phi + F \qquad \text{(Eq. 2)}$$

- Conservation of mass:

$$\frac{\partial \rho}{\partial t} = -\nabla \cdot (\rho v) \qquad \text{(Eq. 3)}$$

- Equation of State (Ideal Gas Law):

$$p = \rho R T \qquad \text{(Eq. 4)}$$

- Conservation of mixing ratio:

$$\frac{\partial \rho q}{\partial t} = -\nabla \cdot (\rho v q) + \rho(E - C) \qquad \text{(Eq. 5)}$$

This produces seven equations with seven unknowns: three velocity components (u, v, w), density (ρ), pressure (p), temperature (T) and water vapour mixing ratio (q). The equation of state is a diagnostic equation that can be resolved from the other variables. The other six equations are prognostic, therefore they can be derived from time with an initial set of values. These values, named **initial conditions**, are necessary to initiate the model. Nevertheless, the equations are non-linear partial differential equations, have no analytic solutions and must be solved by numerical analysis (usually by means of finite differences, finite volumes or spectral representation methods). As a result, the solutions require some approximations, *e.g.*, spherical geoid, quasi-hydrostatic, anelastic or shallow atmosphere. This gives a hint on the importance of accuracy and computational power for numerical weather models. The basic equations and variables are complemented with many other computations and parametrizations to produce a complete set of atmospheric microphysics variables. These are solved for every grid point and time step to create

a spatiotemporal description of the meteorological conditions. Depending on the geographical domain the model is designed to run, there are two main types of numerical weather models:

- **Global model**: Also referred to as General Circulation models. These cover the complete planet and require only initial conditions. They are used to create medium or long term forecasts, although only at a synoptic scale.
- **Limited area model**: These cover a limited domain of the planet, *e.g.*, hemispheric or mesoscale models. They are used to create regional short term forecasts, being able to reach high spatiotemporal resolutions. However, these models need to periodically assimilate the synoptic conditions by a set of external values named **boundary conditions**. Initial and boundary conditions are usually generated from observations or runs of global models.

When using limited area models, its configuration is a very important process in the experiment design. The geographical domains and spatiotemporal resolutions should be adapted to the phenomenon to evaluate (Figure 22), considering the possible influence of atmospheric general circulation, synoptic processes and possible boundary anomalies. If several domains are nested the interaction between them should be contemplated. Regarding the timespan simulated, forecasting lead times can affect the accuracy of the model, as well as the rate of refresh of boundary conditions. Moreover, as not every atmospheric variable can be inputted as initial conditions, a **spin up time** is required when initiating a model. This allows for the different variables to interact until the all the atmospheric features are created and a meteorologically coherent balance is reached. An initiation from the basic unbalanced variables, usually a global model based analysis, is called **cold start**. A **warm start** uses a previous output of the same model as initial conditions, sometimes corrected by assimilated observations, minimizing the spin up time. Finally, research models usually admit various different parametrizations and configurations. These must be carefully chosen and evaluated to achieve the best model configuration for the phenomenon under study.

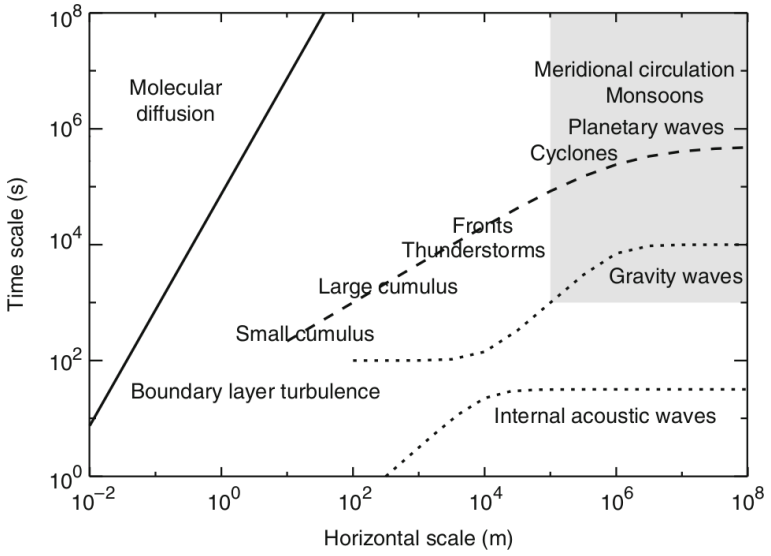

Figure 22: Temporal and spatial ranges of some atmospheric phenomena (Lauritzen et al., 2011).

Weather Research and Forecasting model

The WRF model is a finite-differences mesoscale numerical prediction system designed for both operational forecasting and atmospheric research. It is a very flexible model that can be optimised for specific applications. The model has been developed since 2004 by a collaboration of many United States of America administrations and universities, with the National Center for Atmospheric Research, the National Oceanic and Atmospheric Administration and the Federal Aviation Administration among them. In this thesis, the Advanced Research core of the model is used. Some of the technical features are (Skamarock et al., 2008):

- Fully compressible non-hydrostatic Euler equations with hydrostatic option.
- Prognostic variables are wind velocity components, perturbation potential temperature, perturbation geopotential and perturbation surface pressure of dry air. Turbulent kinetic energy and other scalars (*e.g.*, water vapour, rain or ice mixing ratios) are an option. Scalar-conserving flux form for prognostic variables.
- Vertical coordinates are mass-balanced sigma pressure levels. Variable spacing with height.
- Horizontal Arakawa C-grid staggering.
- Time-split integration with a smaller step for acoustic and gravity-wave modes.
- Second to sixth order advection options in horizontal and vertical.
- Adaptive time stepping.
- Two and three dimensional data for initial conditions.
- Lateral boundary conditions can be periodic, open, symmetric or specified.
- Constant pressure level at top boundary conditions, with gravity wave absorption and Rayleigh damping.
- Complete Coriolis and curvature terms for Earth's rotation.
- Map-scale factors for several projections.
- One-way and two-way nesting with multiple levels possible. Moving nests allowed.
- Global simulation capability.
- Full physics options for microphysics, *cumulus* convection, surface physics, planetary boundary layer physics and atmospheric radiation physics.
- Stochastic parametrization schemes.

The WRF model has been developed with a single-source code and with modular software that can be adapted to many hardware specifications. This makes it possible to efficiently run the software in a wide range of computing platforms, from supercomputer mainframes to common personal computers. Thus the WRF model has been extensively used, tested and validated by many users in a large number of situations, rendering it as a reference for many researchers in the field of meteorology.

HARMONIE-AROME model

The HARMONIE-AROME is a non-hydrostatic convection-permitting mesoscale model. This is a spectral numerical prediction system, with a semi-Lagrangian advection scheme and a semi-Implicit two-time-level scheme (Bengtsson et al., 2017). It is designed as an operational system, in consequence, it is normally nested in the European global model, warm started and assimilates data from multiple sources. In addition, it uses surface and soil schemes provided by external models.

The model is based in the dynamical core of a previous one, which has been improved by an international joint venture of the national meteorological services of 26 countries in the European area. Nonetheless, as per its operational nature, HARMONIE-AROME is more rigid and less adaptable than WRF, offering only a few parametrization options. However, it can be used for research assuming the possible constraints.

5.2. Reanalysis

Global operative models are constantly producing outputs with mid-term forecasts. These analyses are used as initial conditions for future runs of the same model, but can also be used to feed limited area models. In the United States of America, the National Centers for Environmental Prediction operative branch uses the Global Forecasting System, while the European Centre for Medium-Range Weather Forecasts uses the Integrated Forecast System for the production of analyses. These are two of the most important sources of data available to the meteorological community. Furthermore, analyses are used to create reanalyses. These products are usually composed by the combination of the analysis of a global model, with the analysis of a long-term coupled model (*e.g.*, sea or ice) and assimilated observations. The assimilation of observed data represents a large advantage. Satellite radiance, aircraft observations and data from radiosondes, surface stations, ships and drifting buoys are usually fed to the reanalysis. This provides information on surface pressure, wind, temperature and relative humidity, upper-air temperature, wind and humidity, and brightness temperature (Dee et al., 2011). Thereby reanalyses are robust, continuous, balanced and bias-corrected datasets; optimal for the use as initial and boundary conditions for simulations. Unfortunately, they are not immediately available at the current date and cannot be used operationally, however they should always be the dataset of choice to feed a numerical model. The reanalyses produced from the Global Forecasting System and the Integrated Forecast System have been used in this thesis.

The National Centers for Environmental Prediction generates the Climate Forecast System Reanalysis. This is a global, high resolution, coupled atmosphere-ocean-land surface-sea ice system, which assimilates satellite radiances (Saha et al., 2014). It covers the period from 1979 to 2010 with a temporal resolution of six hours. The horizontal resolution of the atmosphere is approximately 0.35^{o} and 64 vertical levels. The ocean is provided at a resolution of 0.25^{o} at the equator, extending to 0.50^{o} beyond the tropics, with 40 levels. The land surface model has four soil levels and the sea ice model has three levels. The reanalysis contains observed variations in carbon dioxide, aerosols and solar variations. There are plans to extend and improve this reanalysis to create a near real-time product.

The European Centre for Medium-Range Weather Forecasts have recently released their fifth generation reanalysis. This uses forecasts from the global atmospheric model coupled to soil and ocean models (European Centre for Medium-Range Weather Forecast, 2019). It provides data from 1979 to 2020 with one hour temporal resolution. The atmosphere spatial horizontal resolution is approximately 0.25^{o} while the vertical resolution is 37 levels. The surface model has four vertical levels, a horizontal soil resolution of approximately 0.10^{o} and an ocean resolution of approximately 0.50^{o}. The assimilation system takes into account the exact timing of the observations to integrate these into the reanalysis. This dataset is available five days behind real-time, with plans to reduce that lag to a near real-time product.

5.3. Observational Instruments

Meteosat satellites

Artificial satellites are a major instrument for meteorology today. Meteorological satellites are passive observation systems which receive the electromagnetic radiation emitted or reflected by the Earth. From the brightness temperature of the planet several data can be obtained and images can be composed. Satellites can be placed in several types of orbits; the geostationary orbit is a geosynchronous orbit, following the same direction of rotation as the planet, at approximately 36000 *km*. Meteosat are the geostationary satellite family deployed by the European Organisation for the Exploitation of Meteorological Satellites since 1977. The second generation is currently in use, which will be gradually decommissioned from 2022 and replaced by the third generation. The Meteosat Second Generation constellation consists of four units. One of them, placed over the intersection of the Equator and the Greenwich prime meridian, provides the principal data coverage at a temporal resolution of 15 *min*. It is assisted by two rapid scanning and gap filling units (five minutes resolution), at different latitudes. A fourth unit is stationed over the Indian Ocean for additional services. The Meteosat Second Generation satellites are spin-stabilized, providing an enhanced image in 12 different channels with a spatial resolution of three kilometres and different tasks (Schmetz et al., 2002):

- Visible (0.6 and 0.8 μm): Cloud and aerosol detection. Land surface and vegetation monitoring.
- High-resolution Visible (broadband: 0.4-1.1 μm): Visible channel with a one kilometre resolution at nadir.
- Near Infrared (1.6 μm): Discrimination of snow from cloud, and solid phase clouds from liquid phase clouds.
- Infrared (3.9 μm): Low cloud and fog detection. Supports other near-surface data.
- Water Vapour (6.2 and 7.3 μm): Water vapour monitoring and wind data. Supports cloud height data.
- Infrared (8.7 μm): Thin *cirri* clouds. Supports other cloud data.
- Infrared (9.7 μm): Ozone data.
- Infrared (10.8 and 12.0 μm): Surface and cloud top temperature. Supports *cirrus* and aerosol data.
- Infrared (13.4 μm): Carbon dioxide data. Supports cloud height data.

The numerical data of each channel can be combined to create additional products as well. These use different colours to identify each band used, creating images for specific meteorological phenomena, *e.g.*, convective cells, fog and cloud composition.

Sounding

Another important instrument for meteorology are atmospheric soundings, as they are the most detailed source of vertical data. There are multiple observations at different heights in the atmosphere, but most of them are performed at single levels (*e.g.*, aircraft data) or have low vertical resolutions (*e.g.*, satellite derived soundings). Soundings produce a complete image of the vertical thermodynamic profile. For obvious reasons, it is local data, nonetheless, this is counterbalanced by the regular execution of soundings in multiple places. The National Oceanic

and Atmospheric Administration declares approximately 1000 different locations distributed globally. Most of these are coordinated and release a sounding every day at 00:00 and 12:00 Universal Time Coordinated. Airports add two more at 06:00 and 18:00 Universal Time Coordinated. Soundings are usually performed using radiosondes. These are small observing stations carried by a helium or hydrogen inflated balloon. The sensors transmit pressure, temperature, relative humidity and position every second. Wind data can be derived from the time and position data. A radiosonde can reach altitudes exceeding 15 *km*, which takes from one to two hours to travel. Consequently, the latest data assimilation techniques aim to account for spatial and temporal drift in the sounding observations. Soundings can also be performed using satellite and microwave radiometer data, however, these are still far from achieving the precision of a radiosonde.

Thermodynamic diagrams and wind are enough information to have an idea of the mesoscale situation. Useful data can be computed from these variables: 0 *ºC* level, stability, convective condensation level, convection temperature, level of free convection, lifting condensation level, equilibrium level, Convective Available Potential Energy and many other indices.

6. RESULTS

The results of this doctoral thesis are composed of the five peer-reviewed publications to follow. These are the condensate of a continuous learning and research process by the author. All of them are published in journals included in the Meteorology & Atmospheric Sciences category as per the Web of Science Group 2018 Journal Citation Report, which observes a total list of 86 journals.

6.1. Mountain Wave Icing

Bolgiani, P., Fernández-González, S., Martin, M. L., Valero, F., Merino, A., García-Ortega, E., & Sánchez, J. L. (2018). **Analysis and numerical simulation of an aircraft icing episode near Adolfo Suárez Madrid-Barajas International Airport**. *Atmospheric Research*, *200*, 60–69.

The following article was published in February 2018 in the Atmospheric Research journal. This is ranked 13th in the Meteorology & Atmospheric Sciences category as per the 2018 Journal Citation Report. The Journal Impact Factor is 4.114.

Atmospheric Research 200 (2018) 60–69

Contents lists available at ScienceDirect

Atmospheric Research

journal homepage: www.elsevier.com/locate/atmosres

Analysis and numerical simulation of an aircraft icing episode near Adolfo Suárez Madrid-Barajas International Airport

Pedro Bolgiani[a], Sergio Fernández-González[a,*], María Luisa Martin[b], Francisco Valero[a], Andrés Merino[c], Eduardo García-Ortega[c], José Luis Sánchez[c]

[a] Department of Earth Physics, Astronomy and Astrophysics II, Faculty of Physics, Complutense University of Madrid, Madrid, Spain
[b] Department of Applied Mathematics, Faculty of Computer Engineering, University of Valladolid, Segovia, Spain
[c] Atmospheric Physics Group, IMA, University of León, León, Spain

ARTICLE INFO

Keywords:
Aircraft icing
Turbulence
METEOSAT
Mesoscale modeling

ABSTRACT

Aircraft icing is one of the most dangerous weather phenomena in aviation security. Therefore, avoiding areas with high probability of icing episodes along arrival and departure routes to airports is strongly recommended. Although such icing is common, forecasting and observation are far from perfect. This paper presents an analysis of an aircraft icing and turbulence event including a commercial flight near the Guadarrama Mountains, during the aircraft approach to the airport. No reference to icing or turbulence was made in the pre-flight meteorological information provided to the pilot, highlighting the need for additional tools to predict such risks. For this reason, the icing episode is simulated by means of the Weather Research and Forecasting (WRF) model and analyzed using images from the Meteosat Second Generation (MSG) satellite, with the aim of providing tools for the detection of icing and turbulence in the airport vicinity.

The WRF simulation shows alternating updrafts and downdrafts ($> 2\ m\ s^{-1}$) on the lee side of the mountain barrier. This is consonant with moderate to strong turbulence experienced by the aircraft on its approach path to the airport and suggests clear air turbulence above the mountain wave cloud top. At the aircraft icing altitude, supercooled liquid water associated with orographic clouds and mountain waves is simulated. Daytime and nighttime MSG images corroborated the simulated mountain waves and associated supercooled liquid water. The results encourage the use of mesoscale models and MSG nowcasting information to minimize aviation risks associated with such meteorological phenomena.

1. Introduction

Adverse weather conditions are the cause of several aircraft accidents every year, and aircraft icing is one of the most dangerous weather phenomena to aviation safety (Caliskan and Hajiyev 2013). This icing has undesirable effects on aerodynamic performance, causing a loss of speed. According to Dillingham (2010), 730 commercial aircraft incidents caused by icing were reported during the period 1998–2007. Therefore, icing has become a major concern in aviation safety.

The vast majority of aircraft are not equipped with icing sensors, so pilots must determine the ice accretion ratio by visual examination. The ice load is largely on protruded surfaces of the aircraft, such as the leading edge of the wing, nose, engine fairing (for jet engines), and propellers. This generates a lift decrease and increase of friction and weight, which causes an immediate loss of flight performance. Finally, this can pose risks by reducing cabin visibility if there is ice accumulation on windshields, or by causing erroneous altitude, pressure and airspeed measurements (Cober et al. 2001). Deicing and anti-icing equipment usually bleeds hot air from the engine onto the wings or inflates pneumatic boots to remove ice accumulation. However, ice can sometimes accumulate in parts of the airframe unprotected against icing, especially when there are supercooled large droplets (SLD) (Lynch and Khodadoust 2001).

Therefore, the best option is to avoid regions where icing conditions are expected through accurate forecasts produced by numerical models. Nevertheless, numerical models tend to overestimate water in the solid phase and underestimate the presence of supercooled water (Fernández-González et al. 2014a). Departure and arrival are the flight phases most exposed to icing conditions in commercial aviation, so high-quality icing forecast should be mandatory, at least in the vicinity of major airports.

Before modeling aircraft icing episodes, processes associated with the presence of supercooled water must be known. There are two

* Corresponding author.
E-mail address: sefern04@ucm.es (S. Fernández-González).

http://dx.doi.org/10.1016/j.atmosres.2017.10.001
Received 12 July 2017; Received in revised form 6 September 2017; Accepted 2 October 2017
Available online 06 October 2017

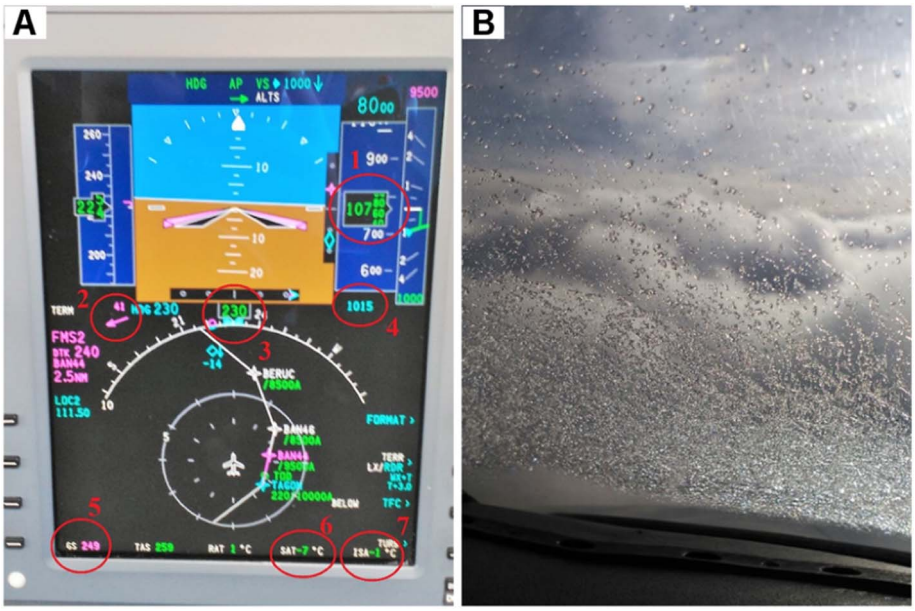

Fig. 1. Photograph of aircraft screen during aircraft icing episode (A), with numbered information as follows. 1 → altitude (feet); 2 → wind speed (knots) and direction (magnetic degrees) with respect to heading; 3 → magnetic heading; 4 → sea level pressure (hPa); 5 → airspeed with respect to the ground (knots); 6 → static air temperature (°C); 7 → temperature deviation relative to International Standard Atmosphere (°C). Photograph of ice loading on windshield (B).

possible mechanisms in the formation of such water. The first appears when hydrometeors in solid phase enter a region with above-freezing temperatures, causing them to melt. Subsequently, the hydrometeors fall into a region of freezing temperatures, producing icing conditions. This mechanism is related to warm fronts and resulting thermal inversion layers (Carrière et al. 2000). With the second mechanism, supercooled water droplets are generated through condensation at temperatures < 0 °C, and then grow by collision–coalescence. It is estimated that this mechanism of supercooled water formation is dominant, making up ~ 75% of supercooled water conditions (Kochtubajda et al. 2017). If the collision–coalescence process persists, it can lead to the formation of SLD, which have a size larger than 50 μm and remain in liquid phase at temperatures below 0°C (Fernández-González et al. 2014a).

Several variables favoring the generation of supercooled water should be taken into consideration. One is humidity, which is required for the development of supercooled water droplets (Pobanz et al. 1994). Mixing increases the efficiency of collision–coalescence. Such mixing can be caused by updrafts (Rasmussen et al. 2002) or wind shear, since it induces droplet growth (Bernstein et al. 1998). Supercooled water content is increased when an inversion layer is present above the cloud top, because this favors wind shear since the updraft is interrupted when reaching the inversion later (Korolev and Isaac 2000). Because warmer temperatures reduce the efficiency of ice nuclei (Hoose and Mohler 2012), supercooled water is prevalent in clouds with tops above the − 15 °C isotherm (Korolev et al. 2003). Moreover, the concentration of cloud condensation nuclei (CCN) is several orders of magnitude higher than those of ice nuclei (IN) (Wang 2013), so the liquid water content from condensation is much greater than liquid water content removal by nucleation into frozen hydrometeors (Pinsky et al. 2015). Thus, the CCN and IN concentration are important factors that should be taken into consideration in the setting of the numerical models (Rasmussen et al. 2002). These factors cause almost half of icing pilot reports to be registered at temperatures between − 8 and − 12 °C and altitudes between 1500 and 4000 masl (FAA Flight Standards Service, 2016).

The processes above are strongly affected by orography, so the use of high horizontal resolution mesoscale models is mandatory. The reason is that orographic features are softened in coarse models, being its representation much more realistic in high resolution models. This type of model has been used in the study area (Fernández-González et al. 2015a) with satisfactory results. Wind flow near mountain ranges is forced to ascend on the windward side and over the orographic barrier (Reinking et al. 2000). On the leeward side of the range, air descends sharply, causing a cloud-free area because of the Föehn effect. In this flow are alternating updrafts and downdrafts, generating conditions appropriate for regions with a high concentration of supercooled water droplets (Geerts et al. 2015).

The objective of the present work was to evaluate the causes of an icing episode near the Adolfo Suárez Madrid-Barajas International Airport (MAD-Airport hereafter). This airport is at the center of the Iberian Peninsula (IP), near the Central System, a mountain range just several tens of kilometers northwest of the airport. Thus, during westerly-northwesterly wind events, air flow ascends over the Central System, and then abruptly descends to generate a cloudless zone. This situation arose near MAD-Airport on 28 February 2017 and affected a commercial aircraft. Data related to the aircraft icing episode was reported by the pilots for the development of this paper. To achieve our aim, high-resolution simulation was carried out with the Weather Research and Forecasting (WRF) model. In addition, images from the Meteosat Second Generation (MSG) satellite were analyzed.

The paper is organized as follows. A detailed description of the aircraft icing event is provided in Section 2. Peculiarities of MAD-Airport and the region where it is located are described in Section 2.1. Meteorological information provided to the pilots is treated in Section 2.2. Section 3 explains in detail characteristics of the mesoscale model and satellite images. Principal results are addressed in Section 4, and are accompanied with reference to previous research. Finally, conclusions are summarized in Section 5.

2. Description of aircraft icing event

As mentioned above, we analyzed an aircraft icing event affecting a commercial flight. The analysis of such events is imperative because of a scarcity of research flight campaigns in the IP (Fernández-González et al. 2014a). Pilot reports have been used in research related to aircraft icing (Belo-Pereira 2015). The aircraft that experienced the icing was a Cessna Citation Jet 3 (C525B). This aircraft is equipped with several deicing and anti-icing systems; deicing boots are installed on the horizontal stabilizer, and a hot air engine bleed is used for anti-icing on the windshields and wings. Measurement instruments (such as the pitot tube) are heated by electrical resistance. The icing was noted during the approach to MAD-Airport during a flight from Barcelona. Takeoff was at 15:54 UTC and landing at 16:59 UTC on February 28, 2017. When

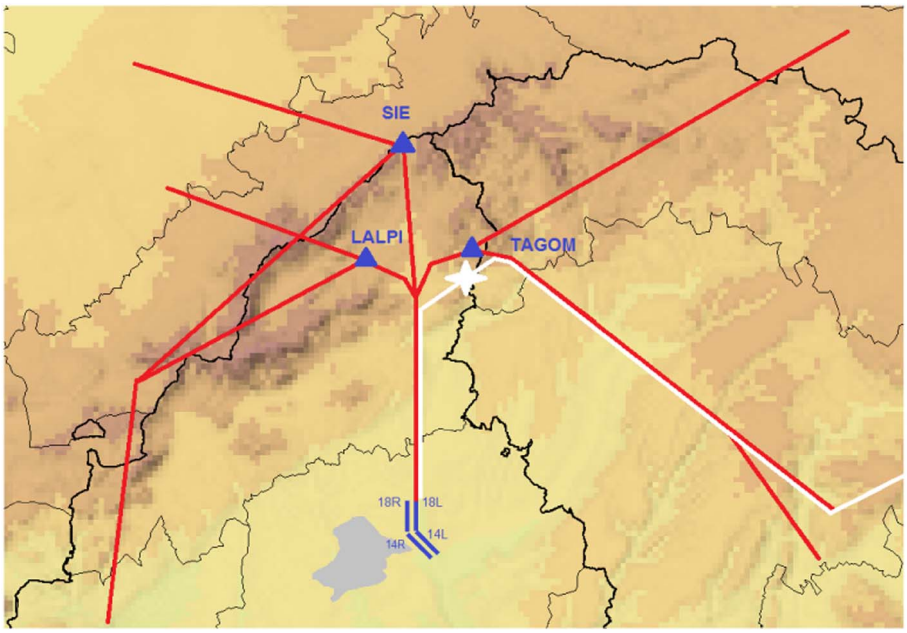

Fig. 2. Arrival and approach procedure chart for runway 18 of MAD-Airport in southern configuration. The four airport runways can be seen with respective orientations. Currently used arrival routes (red) are indicated. Route followed by the aircraft during the case study is marked in white, with location of the aircraft icing incident shown by white star. City of Madrid is indicated in gray, southwest of the airport. (For interpretation of the references to color in this figure legend, the reader is referred to the web version of this article.)

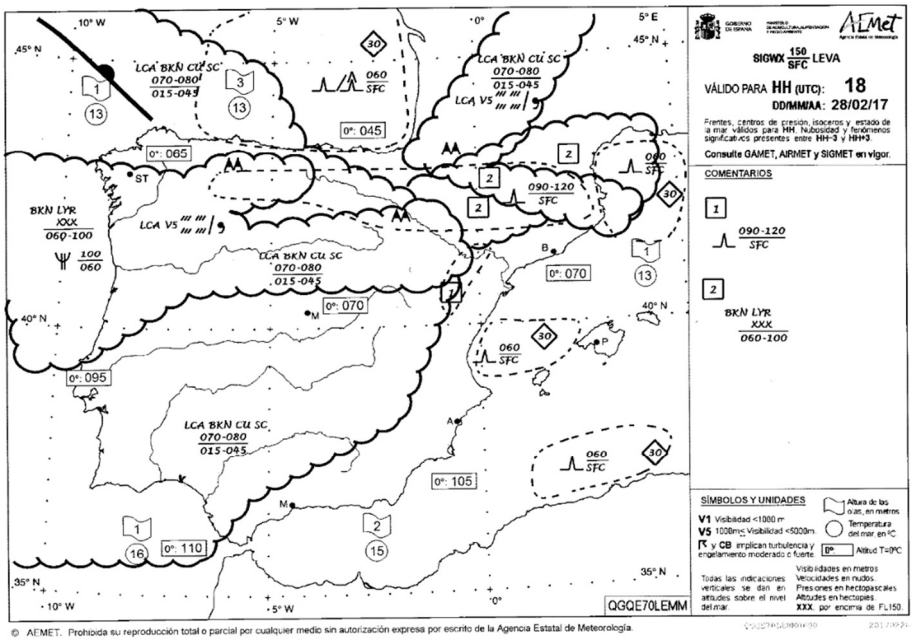

Fig. 3. SIGWX at low levels for IP at 18:00 UTC on 28 February 2017.

the aircraft was at an altitude of 3300 masl, moderate icing (according to specifications in Tafferner et al. 2003) was registered at a temperature of −7 °C. The wind was 21.1 m s^{-1} from the west-northwest (Fig. 1A). Under these conditions, ice loading was almost instantaneous, especially on the windshield and wings (see Fig. 1B).

2.1. MAD-airport surrounding area

MAD-Airport is near the center of the IP, a few km northeast of Madrid, at an altitude of 609 masl. The Guadarrama mountain range (within the Central System) is about 50 km northwest of the airport, with elevations higher than 2400 masl and a southwest-northeast orientation. Given this proximity to the orographic barrier, wind flow is markedly perturbed (especially with northwest winds) along the airport approach path. However, this fact appears not to have been considered in the design of standardized arrival procedures to the airport (Fig. 2). Air traffic is strictly regulated near airports (especially those with heavy traffic), because it is necessary to anticipate and order flight trajectories long before arrival. This ordering is controlled by the wind direction.

The present case study is particularly interesting because orographic blockage produced southwesterly surface winds near MAD-Airport (so the southern configuration was used for approach), although northwest winds were predominant at 3000 masl. During episodes like this, the aircraft has to execute landing and taking off procedures over areas of high ground elevation which leads to higher risk of turbulence and aircraft icing. In the results section, areas with greater risk for aviation safety are analyzed to determine if the approach procedure chart of the airport is optimal during the southern configuration.

2.2. Pre-flight meteorological information

We first examined the forecast information available prior to the flight. The Terminal Aerodrome Forecast (TAF) issued for MAD-Airport at the time of the aircraft icing event estimated a surface wind of

7.2 m s^{-1} and 230° (approximately southwesterly). Visibility was categorized as unlimited, and 3–4 oktas of sky covered by clouds with a base at 600 magl was forecast. Maximum temperature was estimated at 16 °C and minimum temperature at 5 °C.

During the aircraft icing episode, there was no Significant Meteorology Information report (SIGMET) in the study area, so there was no forecast of adverse weather (aircraft icing, turbulence, mountain waves). In addition, the Significant Weather chart (SIGWX) for low levels (up to 4500 masl) for the IP (Fig. 3) indicated that the 0 °C isotherm level over the center of the IP was ~2100 masl. The SIGWX also indicated broken cumulus and stratocumulus at 2100–2400 masl, but clear skies were expected at the level where the aircraft icing was registered (~3000 masl). Furthermore, the forecast estimated a temperature of −3 °C and wind of 18 m s^{-1} and 280° (northwesterly) at 3000 masl. No turbulence, mountain waves, or icing were expected in the study area.

Observation reports from the day in question are described as follows. The Meteorological Terminal Air Report (METAR) at approximately the same time of the aircraft icing event indicated surface wind at 6.7 m s^{-1} and 250°, unlimited visibility and 1–2 oktas of sky coverage by clouds with base at 900 magl. Temperature was ~ 13 °C and the dew point temperature 6 °C. Observed sea level pressure was 1015 hPa. Before the airport arrival procedure, the pilots received local airport reports via a VHF radio system, in which there were no alerts of icing conditions.

In summary, the TAF for the aerodrome was very consistent with subsequent observations in the METAR, with the exception of cloud cover (overestimated in the TAF prediction). However, none of the products predicted the possibility of icing, turbulence or mountain waves in the study area. Moreover, it is remarkable that compared with data measured in situ, the temperature was overestimated in the TAF by > 3 °C at 3000 masl.

3. Methodology

This section presents a complete description of the methods used to achieve the results. First, WRF model characteristics are described in Section 3.1. This mesoscale model was used for short-term estimation of mountain waves and icing conditions. Subsequently, properties of the MSG channels, which are useful for observation of mountain waves and supercooled liquid water, are explained in Section 3.2. MSG images are proposed for the nowcasting of mountain waves and icing conditions.

3.1. Weather research and forecasting (WRF) model

The aircraft icing episode of 28 February 2017 was numerically simulated using the non-hydrostatic WRF mesoscale model version 3.5.1. (Skamarock and Klemp 2008). Initial and boundary conditions were extracted from Global Forecasting System reanalysis, with a horizontal grid spacing of 1° and temporal resolution of 6 h. This reanalysis database is developed and maintained by the National Oceanic and Atmospheric Administration and National Centers for Environmental Prediction.

The simulation was initialized at 00:00 UTC of 28 February 2017, with a forecast period of 24 h. The first 6 h are considered as the model spin-up, but it does not alter the simulation of the aircraft icing event since it occurs approximately at 17:00 UTC, with a lead time of 17 h. The simulation run was for four nested domains (Fig. 4A), each with 100 × 100 grid points in the south–north and west–east directions and 40 sigma levels (with progressive resolution, higher in the low troposphere). The horizontal resolution of domains 1, 2, 3 and 4 was 27, 9, 3 and 1 km, respectively. Domain 1 covers southwestern Europe and North Africa, with the aim of modeling boundary-layer conditions that led to the aircraft icing episode. Domain 2 approximately covered the IP. Domains 3 and 4 were centered over the location of the aircraft icing, providing a high resolution for adequately simulating orographic forcing. The high performance of WRF in modeling terrain-induced flows has been demonstrated (Hari Prasad et al. 2017).

Regarding the WRF model physics configuration, the Dudhia (1989) scheme was used for shortwave radiation and the Rapid Radiative Transfer Model (Mlawer et al. 1997) parameterization for longwave radiation. The parameterization of Thompson et al. (2008) was chosen for microphysics, since it behaves like a 2-moment bulk microphysics scheme for the liquid phase. The parameterization described by Smirnova et al. (2000) was selected for the land surface model, whereas the Nakanishi and Niino (2006) scheme was used for modeling the planetary boundary layer (PBL). Finally, the Kain-Fritsch (Kain 2004) parameterization was used as the cumulus scheme in domains 1 and 2; for domains 3 and 4, the WRF model was run with explicit resolution of cumulus. Fig. 4B displays the orography of domain 4. In this image, a cross section used in the results section is marked by a black line. This WRF model configuration was chosen based on a sensitivity analysis developed for distinct weather phenomena of the IP (Fernández-González et al. 2015b; García-Ortega et al. 2017).

3.2. METEOSAT second generation (MSG)

The MSG is a geostationary satellite that enables the continuous observation (its temporal resolution is 15 min) of meteorological conditions. The MSG is composed by 12 spectral wavelength channels, providing multispectral images. The horizontal resolution is 3 km at nadir for all spectral channels except the high-resolution visible channel, which provides images with 1-km sampling at nadir. With regard to the aims of the present work, the MSG can be used for observing mountain waves and icing conditions by using distinct spectral channels and color schemes. In the following, several tools are described for nowcasting meteorological hazards to aviation safety. First, the high-resolution visible channel is proposed for the detection of clouds related to mountain waves during the diurnal period. However, during nighttime, visible images are not available, so other MSG channels must be used for detecting mountain waves. For this reason, the 7.3-μm MSG channel was also selected. This channel allows the user to differentiate between high and low humidity areas at low and mid levels of the troposphere. Mountain waves can thereby be identified, because lower humidity is expected in their downdrafts and higher humidity in their updrafts.

In addition, the red-green-blue (RGB) color scheme known as “day natural colors,” described by Lensky and Rosenfeld (2008), was used to detect icing conditions. This RGB composite is constructed by combining the 1.6-μm MSG channel in the red beam, 0.8 μm in the green, and 0.6 μm in the blue. This color scheme allows determination of cloud-top phase, depending on distinctive hydrometeor optical properties. Thus, cloud tops in liquid phase will appear in white and those in the ice phase in blue. This is because of strong absorption of ice in the 1.6-μm band (red in the RGB), giving a bluish or cyan color, whereas clouds in liquid phase have strong reflection in the three bands, producing a white color.

4. Results and discussion

In this section, we analyze several meteorological fields simulated by the WRF model. In addition, information acquired with several MSG spectral channels is presented. Finally, the results are contrasted with those of other researchers in the field.

4.1. Synoptic situation

Meteorological conditions at synoptic scale will be described to show the environment during the aircraft icing episode. Fig. 5 depicts temperature and geopotential fields at the 500 and 700 hPa levels in domain 1 of the WRF model simulation. These levels were selected because 500 hPa is representative of the mid troposphere and 700 hPa

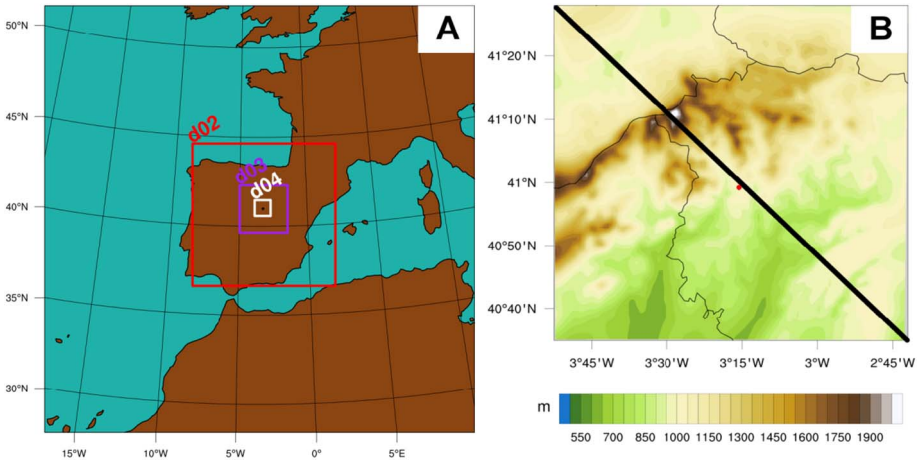

Fig. 4. (A) WRF model domain configuration. (B) Domain 4 with orography. Black and red dots in (A) and (B) respectively indicate location of aircraft icing incidence. (For interpretation of the references to color in this figure legend, the reader is referred to the web version of this article.)

nearly coincides with the height at which the aircraft icing was detected. The mid and lower troposphere configuration at synoptic scale was dominated by a deep trough over France. The impact of this cyclonic wave was accentuated over the northeastern IP, although the influence of a ridge associated with a subtropical anticyclone over the Atlantic Ocean began to be noticeable over the southwestern IP. This configuration fosters northwesterly flow at 500 hPa and west-northwesterly at 700 hPa, producing cold and moist air advection over the study area. Isohypses at 700 hPa (slightly above the peaks of the Guadarrama mountain range) are not close, indicating moderate winds at this level. This pattern favors flow approximately perpendicular to the orographic barrier. Moreover, a temperature of -6 °C at 3040 masl was estimated by WRF (domain 1) in the study area. This synoptic configuration provides the ingredients required for the development of icing conditions in the area (Fernández-González et al. 2014a). Indeed, Bernstein et al. (1998) linked this synoptic pattern to in-flight icing mentioned in pilot reports.

The information provided the WRF model in domain 1 is very similar to meteorological data measured by the aircraft. Although wind direction was adequately forecast in the aforementioned pre-flight meteorological information provided to the pilots, the temperature at 3000 masl was markedly overestimated; values estimated by WRF in domain 1 were much more accurate. However, the meteorological fields must be studied at a higher horizontal resolution to determine risks to aviation safety.

4.2. Short-term diagnosis

In this paper, the use of WRF model simulations is proposed to complement pre-flight meteorological information. In the following, several meteorological fields connected with the aircraft icing episode are analyzed to determine the causes of icing conditions.

First, temperature and wind at 3300 masl were analyzed in domain 3 of WRF model (Fig. 6A). This altitude nearly coincides with that where aircraft icing was detected. The temperature and wind speed simulated by WRF at the location of aircraft icing were -8.1 °C and 22.1 m s^{-1}. The wind was west-northwesterly across the entire domain and very stable. This is because this altitude is above the Guadarrama mountain peaks, so there is no orographic blockage. The above values are very similar to those observed in situ (-7 °C and 21.1 m s^{-1}), and much more accurate than those in the pre-flight meteorological information. The efficiency of ice nucleation processes is low at temperatures > -10 °C (Huffman and Norman, 1988), such as those in the area where the icing occurred. In fact, supercooled liquid droplets are

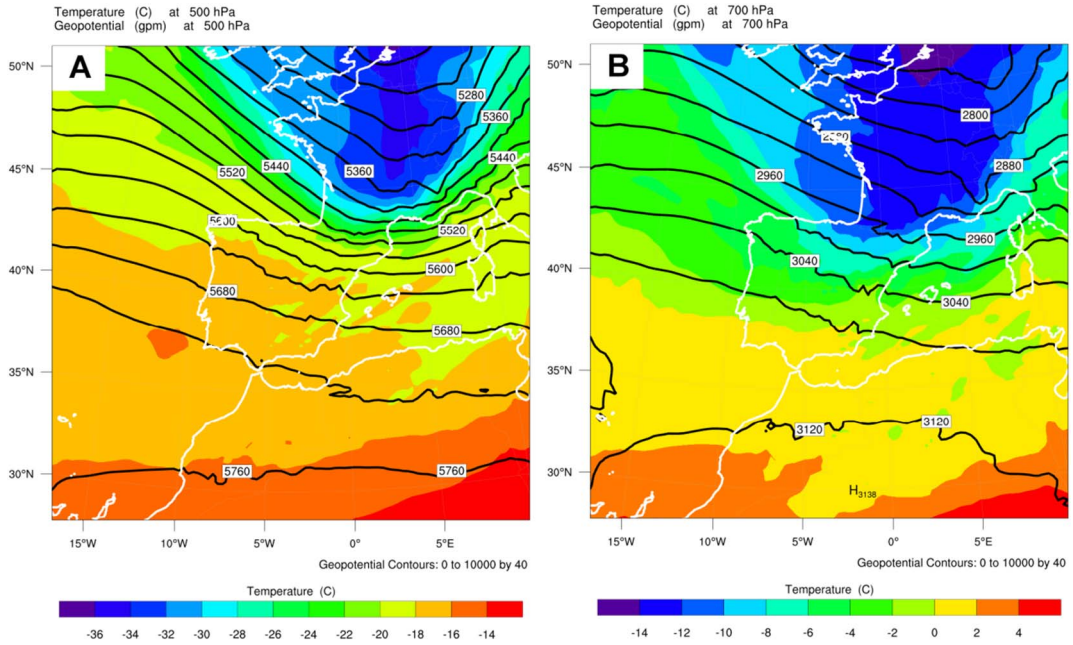

Fig. 5. Temperature (shaded) and geopotential (contour) at 500 hPa (A) and at 700 hPa (B) estimated by WRF model at 18:00 UTC on 28 February 2017.

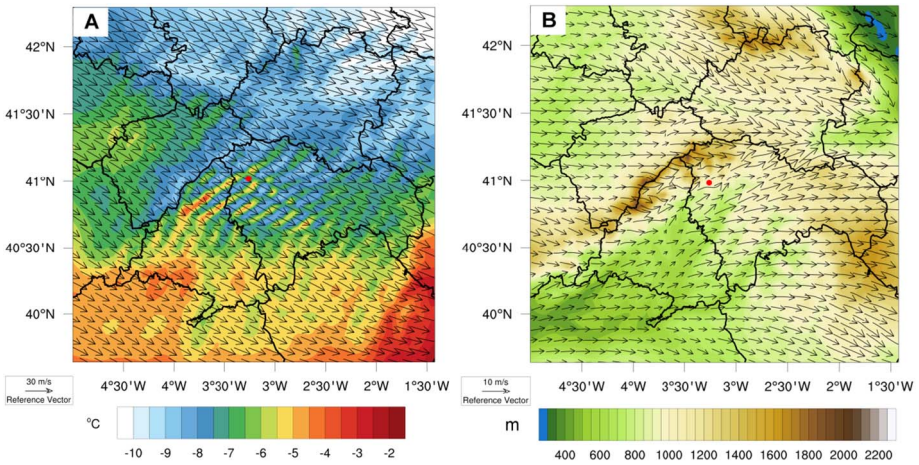

Fig. 6. For 17:00 UTC on 28 February 2017: (A) Wind and temperature at 3300 masl in domain 3. (B) Orography and wind at 10 magl in domain 3. In both panels, red dot indicates location of aircraft icing incident. (For interpretation of the references to color in this figure legend, the reader is referred to the web version of this article.)

present > 50% of times at temperatures above −10 °C (Yoshida et al., 2010). This is consistent with Sand et al. (1984), who asserted that > 95% of aircraft icing episodes develop at temperatures > −20 °C. In the region around the aircraft icing location (red dot in Fig. 6A), alternate bands of higher and lower temperatures are seen. These are likely caused by mountain waves. These cause higher temperatures in their downdrafts and lower temperatures in their updrafts, which is attributable to adiabatic processes of compression and expansion, respectively (Smith et al. 2002).

Fig. 6B shows wind at 10 magl in domain 3 of the WRF simulation at the time of the incident. There are west winds on the windward side of the Guadarrama range, but southwesterlies on the lee side. That was why MAD-Airport was operating with the southern configuration. The surface wind speed at MAD-Airport estimated by WRF was 6.5 m s^{-1}, almost identical to those in the METAR (6.7 m s^{-1}). The WRF output also agrees with the southwesterly winds observed at the airport. This configuration shows that surface wind was at least partially blocked by the orographic barrier. This is consistent with Petersen et al. (2005), who asserted that mountain ranges can block the prevailing wind flow and cause eddy shedding on the lee side. At the aircraft icing location, surface wind convergence appears in the simulation. This is attributable to westerly flow that crossed the Guadarrama range and southwesterlies originating from the valley on the lee side of the orographic barrier. This is consistent with Rowe et al. (2012), who demonstrated that terrain-driven convergence can be caused by weak winds perpendicular to a mountain range. Through moisture advection, this convergence may have contributed to the formation of cloudiness on the lee side of the Guadarrama range. This is critical because high humidity is indispensable to icing formation (Bernstein et al. 2005).

Now we analyze atmospheric stability and the wind profile in detail by describing the vertical atmospheric profile forecast of WRF in the study area at the time of the incident. First, the forecast at MAD-Airport is shown in Fig. 7A. In the vertical profile of horizontal wind, strong wind shear is clearly evident in the lowest 2500 masl (approximately the altitude of the Guadarrama mountain peaks). The profile shows weak southwesterly winds in the PBL and moderate–strong west-northwesterlies above 3000 masl. Moreover, there is a conditionally unstable and almost saturated layer around 2000 masl. It is very likely that this layer was associated with clouds forecast in the pre-flight meteorological information. Above this layer, the atmosphere is more stable and drier, so cloud formation was less likely.

The vertical profile forecast by the WRF at the aircraft icing location is shown in Fig. 7B. There, wind shear is much weaker, varying from west-southwest in the PBL to west-northwest around 3000 masl. The wind speed increase with height is not as great as above MAD-Airport. The reason for this is seen at higher altitudes at the icing location, where the orographic blockage was not pronounced. There was a conditionally unstable layer between 1000 and 2000 masl. In addition, the humidity is very high around 2000 masl, so the formation of low clouds is likely, as indicated in the pre-flight information. Nevertheless, because the freezing level was around 2000 masl, icing conditions were not expected in this layer from the pre-flight information.

The most interesting layer was between 2000 and 4000 masl. In this layer, neutral to stable conditions prevailed, and humidity was high at lower levels, decreasing with altitude. Above the aforementioned layer, low humidity inhibited the formation of clouds. There was a moist layer at altitudes between 8000 and 10,000 masl, but this layer posed no risk to aviation because its low temperatures (< −40 °C) facilitated nucleation processes, causing nearly all hydrometeors to be in the ice phase (Dorsi et al. 2015).

Finally, vertical wind speed and liquid water content estimated by WRF at 3300 masl in domain 4 at 17:00 UTC (essentially the altitude and time at which aircraft icing was recorded) are portrayed in Fig. 8A and B. In the first panel, warm colors reflect downdrafts and bluish colors updrafts. Fig. 8A shows a mountain wave pattern composed of alternating updrafts and downdrafts on the lee side of the Guadarrama range. As discussed above, wind perpendicular to the orographic barrier and neutral or stable conditions favor the formation of mountain waves in the region of aircraft icing. Updrafts reached speeds greater than ± 2 m s^{-1}, which are capable of causing moderate or even strong turbulence effects on aircraft on departure or arrival at MAD-Airport. The magnitude of simulated updrafts is in accord with that reported by Ikeda et al. (2007), who stated that vertical motions are amplified over and on the lee side of orographic barriers when air flow is perpendicular to them.

As seen in Fig. 8B, liquid water content appears to be associated with the updrafts generated by the mountain waves. Liquid water content is also present on the windward side of the Guadarrama range, linked to the formation of orographic clouds. Because the freezing level was ~2000 masl (Fig. 8C or D), all liquid water content estimated by WRF at that level is associated with supercooled liquid water, which poses an aircraft icing risk. Supercooled liquid water content of values ~0.5 g kg^{-1} were reached in both the mountain waves and orographic clouds. According to Tafferner et al. (2003), these values can cause moderate or severe aircraft icing, depending on aircraft characteristics.

The same meteorological fields are shown in Fig. 8C and D for the cross section of Fig. 4B in the lowest 6500 masl. This cross section was selected because it is nearly perpendicular to the Guadarrama mountain range and because it traverses the aircraft icing location. In Fig. 8C and D, the northwest corner of domain 4 is at the right of the image, and the southeast corner is at its left. Fig. 8C shows an updraft on the windward side of the Guadarrama range, caused by orographic forcing. Associated with mountain waves, successive downdrafts and updrafts appear on the lee side of the barrier, in agreement with the results of Kim and

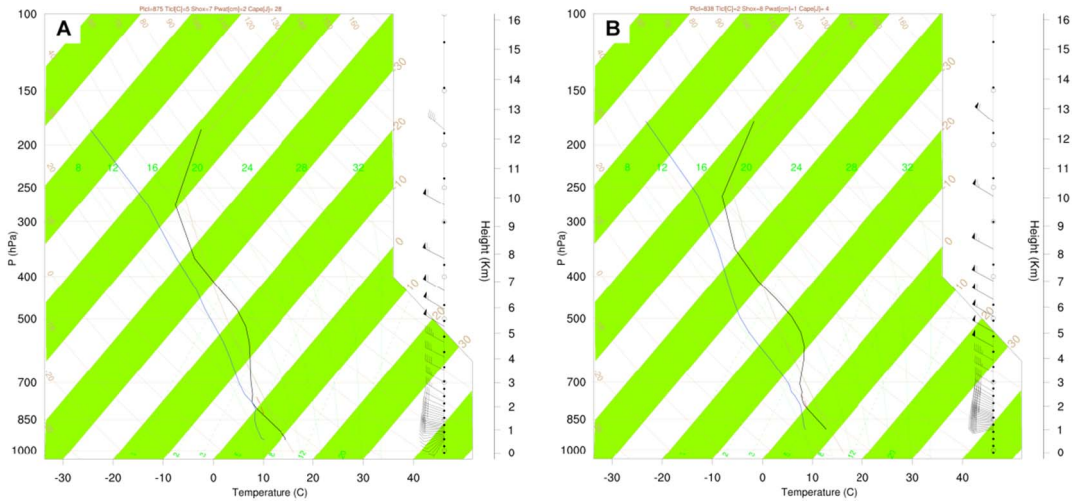

Fig. 7. For 17:00 UTC on 28 February 2017: (A) Vertical atmospheric profile at MAD-Airport estimated by WRF model; (B) vertical atmospheric profile at location of aircraft icing.

Kang (2007). As in Fig. 8B, orographic clouds are evident in Fig. 8D on the windward side of the barrier, with successive mountain waves on the lee side. The greatest liquid water content is at altitudes ~2500 masl, reaching maxima of ~1 g kg^{-1} in the orographic cloud and 0.5 g kg^{-1} in the mountain waves. This is consistent with Geresdi and Rasmussen (2005), who stated that collision and coalescence processes are favored in updrafts, which increase the concentration of large liquid drops in regions affected by mountain waves. In fig. 8C and D, temperature oscillations can be seen, with higher temperatures just behind the downdrafts (owing to adiabatic compression) and lower temperatures in the updrafts (caused by adiabatic expansion). Fig. 8B demonstrates that mountain wave clouds developed in association with the updrafts and lower temperatures. Comparing Fig. 8C and D reveals that updrafts and downdrafts extend to altitudes above 6000 masl, so clear air turbulence (CAT) can be expected above the mountain wave cloud top. This is a major risk to aviation safety because there are no visual indicators of CAT. However, the image demonstrates that it can be forecast by mesoscale models (Ellrod et al. 2015).

4.3. Nowcasting

Finally, the use of MSG images for the nowcasting of turbulence and/or aircraft icing is proposed in order to minimize aviation risks associated with those meteorological phenomena. In this regard, the high-resolution visible channel was used for determining the existence of clouds associated with mountain waves. Fig. 9A indicates the reflectance measured in this channel at the time of the incident, clearly showing the mountain wave system on the lee side of the Guadarrama mountain range. This figure demonstrates the efficiency of this approach to alert for the presence of clouds associated with mountain waves, where turbulence is expected. This information can be used to alert pilots and select safer flight zones. However, images from the

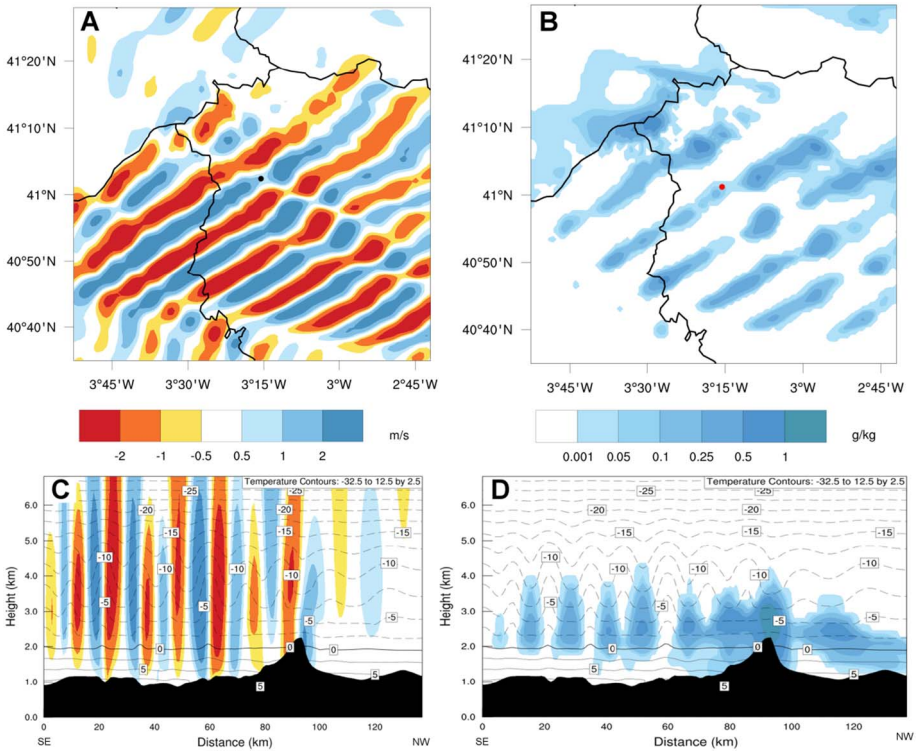

Fig. 8. WRF simulations for domain 4 at 17:00 UTC on 28 February 2017: (A) Vertical wind and (B) liquid water content at 3300 masl; (C) vertical wind and (D) liquid water content on cross section shown in Fig. 4B.

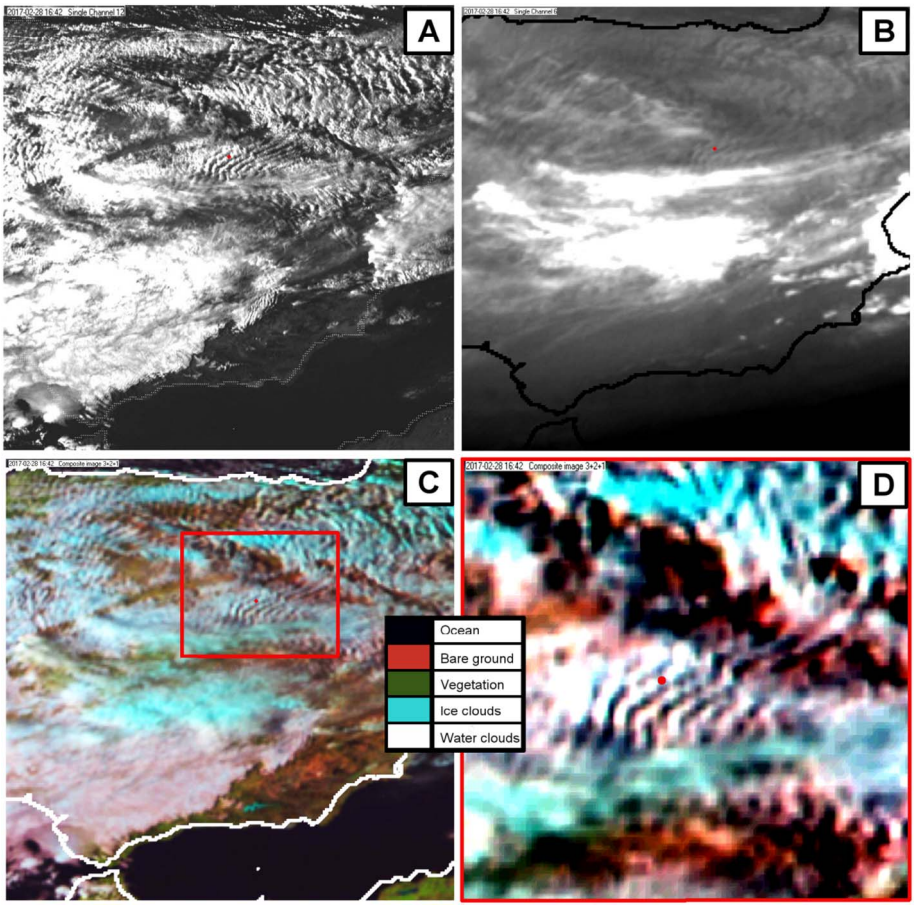

Fig. 9. Meteosat Second Generation (MSG) images at 16:42 UTC on 28 February 2017 over center of Iberian Peninsula: (A) High-resolution visible channel; (B) water vapor 7.3-μm channel; (C) day natural colors scheme; (D) zoom of day natural colors scheme centered on study area. Red dot indicates location of aircraft icing incident. (For interpretation of the references to color in this figure legend, the reader is referred to the web version of this article.)

high-resolution visible channel are only available during daytime. Therefore, use of the 7.3-μm MSG channel is also proposed, in order to detect mountain waves at night. An image constructed with data from this channel is shown in Fig. 9B, from which a mountain wave system over the study area is inferred. Although cloud images related to mountain waves are sharper from the high-resolution visible channel, the 7.3-μm MSG channel can even be used for detecting CAT. Thus, parallel bands of higher/lower humidity are an indicator of updrafts and downdrafts caused by mountain waves, even when the humidity is not sufficiently high to allow the formation of mountain wave clouds.

In addition, the day natural colors scheme (described in Section 3) that combines the 1.6, 0.8 and 0.6 μm visible MSG channels was used because it allows visualizing the cloud top phase during the diurnal period. A general view of the IP using this color scheme is shown in Fig. 9C, with a zoomed view centered on the study area given in Fig. 9D. In these figures, it can be clearly distinguished that the mountain wave system is almost entirely formed by hydrometeors in liquid phase, whereas other clouds colored in blue indicate a high concentration of ice-phase hydrometeors (coinciding with clouds whose tops are at higher altitude). The skill of this color scheme in the detection of supercooled liquid water has been tested with satisfactory results in the study area (Fernández-González et al. 2014b).

5. Concluding remarks

Adverse weather and particularly icing conditions can cause aircraft accidents, especially for commercial aircraft not well equipped with icing sensors. Thus, most pilots must decide on actions when ice accretion becomes visible. In this situation, circumventing icing-prone regions is the best option, although sometimes this may be too late. Furthermore, icing forecasts for aviation are not precise because of numerical weather model underestimation (overestimation) of supercooled (solid) water. In addition, the poor resolution of operational numerical models does not permit forecasting of icing conditions generated by mesoscale or even microscale processes. In the present work, icing experienced by an aircraft on 28 February 2017 near MAD-Airport was analyzed using satellite images and WRF model simulation.

The pre-flight meteorological information provided to the pilot did not contain any significant reports, and indicated the 0 °C isotherm level around 2100 masl in a cloudless area around MAD-Airport. Thus, neither icing nor mountain waves were expected in the area.

Results of the WRF simulation of the aircraft icing event lead us to propose the methods described herein to supplement information pilots receive in the pre-flight meteorological reports. In this respect, we reached the following conclusions.

- Temperature, wind speed and direction simulated by the WRF model at the location of the icing incident were more similar to those recorded by the aircraft than indicated by the pre-flight meteorological information.
- Near the icing location, alternating higher and lower temperature bands were observed along the aircraft path. These bands were caused by mountain waves with adiabatic processes of compression and expansion in the downdrafts and updrafts, respectively. These bands were also well simulated by WRF.
- The vertical atmospheric profile estimate by WRF at MAD-Airport indicated strong wind shear up to 3000 masl. The model also indicate a conditionally unstable and saturated layer around 2000 masl in the study area, which was linked to cloudiness reported to the aircraft pilots.
- The vertical profile simulated by WRF at the icing location shows weaker wind shear than over MAD-Airport, with a conditionally

unstable layer around 1500 masl and high humidity. These data suggest low cloud formation in the area. However, there is a notable neutral-to-stable layer near 3000 masl, with high humidity.

- Simulated alternating updrafts and downdrafts on the lee side of the mountain barrier ($> 2\ m\ s^{-1}$) coincided with moderate-to-strong turbulence experienced by the aircraft on its approach path to MAD-Airport. These vertical drafts also suggest CAT above the mountain wave cloud top.
- Supercooled liquid water associated with orographic clouds and mountain waves were reasonably well simulated by WRF at the altitude of the aircraft icing incident.
- Daytime and nighttime satellite images corroborate the mountain waves and associated clouds simulated by WRF, and thus constitute a very useful tool for alerting pilots.

In the same way that meteorological information would allow pilots to better manage the flight, it would be advisable that mesoscale modeling and satellite remote sensing be considered when planning aviation arrival and departure routes. In view of the results presented herein, it would be advisable to develop arrival routes so as to avoid areas where adverse weather is common. In the southern configuration of MAD-Airport, all the approach procedure routes cross the Guadarrama Mountains. Therefore, it is mandatory to cross mountainous terrain to start the approach, so it is very likely to encounter turbulence and wind shear with any wind direction. This is especially so with a northwesterly wind over the mountain barrier. In future studies, a greater number of aircraft icing episodes should be analyzed to redefine the approach procedure chart for MAD-Airport, in order to minimize aviation safety risks. In this regard, the use of mesoscale models and satellite image monitoring is recommended. In addition, scientific flights are necessary to accurately measure the liquid water content associated to aircraft icing events, and thus develop quantitative validation of the numerical models.

Acknowledgements

This work was partially supported by research projects METEORISK (RTC-2014-1872-5), PCIN-2014-013-C07-04 and PCIN2016-080 (UE ERA-NET Plus NEWA Project), ESP2013-47816-C4-4-P, CGL2010-15930, CGL2016-78702-C2-1-R and CGL2016-78702-C2-2-R, and by the Instituto de Matemática Interdisciplinar (IMI) of the Universidad Complutense. Special thanks go to Roberto Weigand, Steven Hunter, and Analisa Weston.

References

Belo-Pereira, M., 2015. Comparison of in-flight aircraft icing algorithms based on ECMWF forecasts. Meteorol. Appl. 22 (4), 705–715. https://doi.org/10.1002/met.1505.

Bernstein, B.C., Omeron, T.A., Politovich, M.K., McDonough, F., 1998. Surface weather features associated with freezing precipitation and severe in-flight aircraft icing. Atmos. Res. 46 (1–2), 57–73.

Bernstein, B.C., McDonough, F., Politovich, M.K., et al., 2005. Current icing potential: algorithm description and comparison with aircraft observations. J. Appl. Meteorol. 44 (7), 969–986.

Caliskan, F., Hajiyev, C., 2013. A review of in-flight detection and identification of aircraft icing and reconfigurable control. Prog. Aerosp. Sci. 60, 12–34. https://doi.org/10.1016/j.paerosci.2012.11.001.

Carrière, J.-M., Lainard, C., Le Bot, C., Robart, F., 2000. A climatological study of surface freezing precipitation in Europe. Meteorol. Appl. 7 (3), 229–238.

Cober, S.G., Isaac, G.A., Strapp, J.W., 2001. Characterizations of aircraft icing environments that include supercooled large drops. J. Appl. Meteorol. 40 (11), 1984–2002.

Dillingham, L., 2010. Aviation safety, preliminary information on aircraft icing and winter operations. In: GAO, United States Government Accountability Office Testimony Before the Subcommittee on Aviation. Committee on Transportation and Infrastructure.

Dorsi, S.W., Shupe, M.D., Persson, P.O.G., Kingsmill, D.E., Avallone, L.M., 2015. Phase-specific characteristics of wintertime clouds across a midlatitude mountain range. Mon. Weather Rev. 143 (10), 4181–4197. https://doi.org/10.1175/MWR-D-15-0135.1.

Dudhia, J., 1989. Numerical study of convection observed during the winter monsoon experiment using a mesoscale two-dimensional model. J. Atmos. Sci. 46 (20), 3077–3107.

Ellrod, G.P., Knox, J.A., Lester, P.F., Ehernberger, L.J., 2015. Aviation meteorology: clear air turbulence, reference module in earth systems and environmental sciences. Enc. Atmos. Sci. 177-186. https://doi.org/10.1016/B978-0-12-382225-3.00104-3.

FAA Flight Standards Service, 2016. AC: 00-6B. Aviation Weather, Federal Aviation Administration. US Department of Transportation.

Fernández-González, S., Sánchez, J.L., Gascón, E., López, L., García-Ortega, E., Merino, A., 2014a. Weather features associated with aircraft icing conditions: a case study. Sci. World J. 2014.

Fernández-González, S., Valero, F., Sánchez, J.L., Gascón, E., López, L., García-Ortega, E., Merino, A., 2014b. Observation of a freezing drizzle episode: a case study. Atmos. Res. 149, 244–254. https://doi.org/10.1016/j.atmosres.2014.06.014.

Fernández-González, S., Valero, F., Sánchez, J.L., Gascón, E., López, L., García-Ortega, E., Merino, A., 2015a. Analysis of a seeder-feeder and freezing drizzle event. J. Geophys. Res. 120 (9), 3984–3999. https://doi.org/10.1002/2014JD022916.

Fernández-González, S., Valero, F., Sánchez, J.L., Gascón, E., López, L., García-Ortega, E., Merino, A., 2015b. Numerical simulations of snowfall events: sensitivity analysis of physical parameterizations. J. Geophys. Res. 120 (19), 10130–10148. https://doi.org/10.1002/2015JD023793.

García-Ortega, E., Lorenzana, J., Merino, A., Fernández-González, S., López, L., Sánchez, J.L., 2017. Performance of multi-physics ensembles in convective precipitation events over northeastern Spain. Atmos. Res. 190, 55–67. https://doi.org/10.1016/j.atmosres.2017.02.009.

Geerts, B., Yang, Y., Rasmussen, R., Haimov, S., Pokharel, B., 2015. Snow growth and transport patterns in orographic storms as estimated from airborne vertical-plane dual-Doppler radar data. Mon. Weather Rev. 143 (2), 644–665. https://doi.org/10.1175/MWR-D-14-00199.1.

Geresdi, I., Rasmussen, R., 2005. Freezing drizzle formation in stably stratified layer clouds. Part II: the role of giant nuclei and aerosol particle size distribution and solubility. J. Atmos. Sci. 62, 2037–2057. https://doi.org/10.1175/JAS3452.1.

Hari Prasad, K.B.R.R., Srinivas, C.V., Narayana Rao, T., Naidu, C.V., Baskaran, R., 2017. Performance of WRF in simulating terrain induced flows and atmospheric boundary layer characteristics over the tropical station Gadanki. Atmos. Res. 185, 101–117. https://doi.org/10.1016/j.atmosres.2016.10.020.

Hoose, C., Mohler, O., 2012. Heterogeneous ice nucleation on atmospheric aerosols: a review of results from laboratory experiments. Atmos. Chem. Phys. 12, 9817–9854.

Huffman, G.J., Norman Jr., G.A., 1988. The supercooled warm rain process and the specification of freezing precipitation. Mon. Weather Rev. 116 (11), 2172–2182.

Ikeda, K., Rasmussen, R.M., Hall, W.D., Thompson, G., 2007. Observations of freezing drizzle in extratropical cyclonic storms during IMPROVE-2. J. Atmos. Sci. 64 (9), 3016–3043.

Kain, J., 2004. The Kain-Fritsch convective parameterization: an update. J. Appl. Meteorol. 43 (1), 170–181.

Kim, J., Kang, H.S., 2007. The impact of the Sierra Nevada on low-level winds and water vapor transport. J. Hydrometeorol. 8, 790–804. https://doi.org/10.1175/JHM599.1.

Kochtubajda, B., Mooney, C., Stewart, R., 2017. Characteristics, atmospheric drivers and occurrence patterns of freezing precipitation and ice pellets over the prairie provinces and Arctic territories of Canada: 1964–2005. Atmos. Res. 191, 115–127. https://doi.org/10.1016/j.atmosres.2017.03.005.

Korolev, A.V., Isaac, G.A., 2000. Drop growth due to high supersaturation caused by isobaric mixing. J. Atmos. Sci. 57 (10), 1675–1685.

Korolev, A.V., Isaac, G.A., Cober, S.G., Strapp, J.W., Hallett, J., 2003. Microphysical characterization of mixed-phase clouds. Q. J. Roy. Meteor. Soc. 129 (587), 39–65.

Lensky, I.M., Rosenfeld, D., 2008. Clouds-aerosols-precipitation satellite analysis tool (CAPSAT). Atmos. Chem. Phys. 8 (22), 6739–6753.

Lynch, F.T., Khodadoust, A., 2001. Effects of ice accretions on aircraft aerodynamics. Prog. Aerosp. Sci. 37 (8), 669–767.

Mlawer, E., Taubman, S., Brown, P., Iacono, M., Clough, S., 1997. Radiative transfer for inhomogeneous atmospheres: RRTM, a validated correlated-k model for the longwave. J. Geophys. Res. 102 (14), 16663–16682.

Nakanishi, M., Niino, H., 2006. An improved Mellor–Yamada level-3 model: its numerical stability and application to a regional prediction of advection fog. Bound.-Layer Meteorol. 119, 397–407.

Petersen, G.N., Kristjánsson, J.E., Ólafsson, H., 2005. The effect of upstream wind direction on atmospheric flow in the vicinity of a large mountain. Q. J. Roy. Meteor. Soc. 131 (607), 1113–1128.

Pinsky, M., Khain, A., Korolev, A., 2015. Phase transformations in an ascending adiabatic mixed-phase cloud volume. J. Geophys. Res. 120 (8), 3329–3353. https://doi.org/10.1002/2015JD023094.

Pobanz, B.M., Marwitz, J.D., Politovich, M.K., 1994. Conditions associated with large-drops regions. J. Appl. Meteorol. 33 (11), 1366–1372.

Rasmussen, R.M., Geresdi, I., Thompson, G., Manning, K., Karplus, E., 2002. Freezing drizzle formation in stably stratified layer clouds: the role of radiative cooling of cloud droplets, cloud condensation nuclei, and ice initiation. J. Atmos. Sci. 59 (4), 837–860.

Reinking, R.F., Snider, J.B., Coen, J.L., 2000. Influences of storm-embedded orographic gravity waves on cloud liquid water and precipitation. J. Appl. Meteorol. 39 (6), 733–759.

Rowe, A.K., Rutledge, S.A., Lang, T.J., 2012. Investigation of microphysical processes occurring in organized convection during NAME. Mon. Weather Rev. 140, 2168–2187. https://doi.org/10.1175/MWR-D-11-00124.1.

Sand, W.R., Cooper, W.A., Politovich, M.K., Veal, D.L., 1984. Icing conditions encountered by a research aircraft. J. Clim. Appl. Meteorol. 23 (10), 1427–1440.

Skamarock, W., Klemp, J., 2008. A time-split nonhydrostatic atmospheric model for weather research and forecasting applications. J. Comput. Phys. 227 (7), 3465–3485. https://doi.org/10.1016/j.jcp.2007.01.037.

Smirnova, T.G., Brown, J.M., Kim, D., 2000. Parameterization of cold-season processes in the MAPS land-surface scheme. J. Geophys. Res. 105, 4077–4086. https://doi.org/10.1029/1999JD901047.

Smith, R.B., Skubis, S., Doyle, J.D., Broad, A.S., Kiemle, C., Volkert, H., 2002. Mountain waves over Mont Blanc: influence of a stagnant boundary layer. J. Atmos. Sci. 59 (13), 2073–2092.

Tafferner, A., Hauf, T., Leifeld, C., Hafner, T., Leykauf, H., Voigt, U., 2003. ADWICE: advanced diagnosis and warning system for aircraft icing environments. Weather Forecast. 18 (2), 184–203. http://dx.doi.org/10.1175/1520-0434(2003)018<0184:AADAWS>2.0.CO;2.

Thompson, G., Field, P., Rasmussen, R., Hall, W., 2008. Explicit forecasts of winter precipitation using an improved bulk microphysics scheme. Part II: implementation of a new snow parameterization. Mon. Weather Rev. 136 (12), 5095–5115. https://doi.org/10.1175/2008MWR2387.1.

Wang, P.K., 2013. Physics and Dynamics of Clouds and Precipitation. Cambridge Univ. Press, New York, pp. 467.

Yoshida, R., Okamoto, H., Hagihara, Y., Ishimoto, H., 2010. Global analysis of cloud phase and ice crystal orientation from Cloud-Aerosol Lidar and Infrared Pathfinder Satellite Observation (CALIPSO) data using attenuated backscattering and depolarization ratio. J. Geophys. Res. 115, D00H32. http://dx.doi.org/10.1029/2009JD012334.

6.2. Low Visibility

Fernández-González, S., Bolgiani, P., Fernández-Villares, J., González, P., García-Gil, A., Suárez, J. C., & Merino, A. (2019). **Forecasting of poor visibility episodes in the vicinity of Tenerife Norte Airport**. *Atmospheric Research*, *223*, 49–59.

The following article was published in July 2019 in the Atmospheric Research journal. This is ranked 13th in the Meteorology & Atmospheric Sciences category as per the 2018 Journal Citation Report. The Journal Impact Factor is 4.114.

Atmospheric Research 223 (2019) 49–59

Contents lists available at ScienceDirect

Atmospheric Research

journal homepage: www.elsevier.com/locate/atmosres

Forecasting of poor visibility episodes in the vicinity of Tenerife Norte Airport

Sergio Fernández-González[a,*], Pedro Bolgiani[b], Javier Fernández-Villares[a], Pino González[a], Alejandro García-Gil[a], Juan Carlos Suárez[a], Andrés Merino[c]

[a] State Meteorological Agency (AEMET), Spain
[b] Department of Earth Physics and Astrophysics, Faculty of Physics, Complutense University of Madrid, Spain
[c] Atmospheric Physics Group, Environmental Institute, University of León, Spain

ARTICLE INFO

Keywords:
Aviation safety
Fog
Poor visibility
Mesoscale modelling
MSG

ABSTRACT

Aviation safety is a priority that may be compromised by adverse weather conditions. This is the case for poor visibility in the vicinity of airports, which can pose a risk during takeoff and landing. For airports that are prone to fog because of their location, an accurate forecast of poor-visibility episodes is vital. However, the forecasting of low clouds is still a challenge in numerical weather prediction, especially when an airport is near complex terrain for which the use of non-hydrostatic mesoscale models is mandatory. All these factors are present at Tenerife Norte Airport, which is commonly affected by poor visibility from low clouds related to persistent trade winds and moist flows from the Atlantic Ocean.

In this paper, several methods for estimating visibility based on mesoscale model outputs are tested. Use of the HARMONIE-AROME model is encouraged because of its excellent performance in the detection of poor-visibility episodes (False Alarm Ratio = 0.34–0.38; Frequency Of Misses = 0.22–0.38, depending on the model version and method used). In addition, the use of satellite application facilities is proposed for the nowcasting of low clouds affecting the airport area. Specifically, we used products that estimate cloud type, cloud top altitude, and integrated water vapor content in the boundary layer. Finally, an application is presented for the monitoring of weather conditions in real time to estimate poor-visibility risk.

1. Introduction

Air traffic management can be affected by adverse weather conditions such as icing, wind shear, poor visibility and turbulence (Dey, 2018). Particularly, poor visibility around airports affects flight operations by reducing runway and taxiway capacities, which causes flight delays, diversions to other airports, or even cancellations (Bergot et al., 2007). The impact of poor-visibility events has increased in recent decades because of an increase in air traffic (Gultepe et al., 2007).

Poor-visibility events are defined as fog when surface horizontal visibility is < 1000 m, and as mist when that visibility is between 1000 and 5000 m (WMO, 2011). These episodes are caused by the suspension of cloud droplets (of radii 1–40 μm) near the surface. According to Pagowski et al. (2004), the most common fog types are radiation (caused by thermal radiation cooling during clear sky nights), advection (which can occur during warm air advection over a colder surface), and orographic (when air cools adiabatically when lifted by orographic forcing over a mountain slope). Poor visibility can also be related to precipitation (Fedorova et al., 2013).

When visibility falls below a certain threshold, poor-visibility procedures must be activated by airport managers to ensure aviation safety. During fog events, air traffic controllers may reduce taxiway occupation, prolong periods between takeoffs and landings, or even suspend airport operations to avoid runway incursions and other possible incidents or accidents (Guijo-Rubio et al., 2018). Also, missed approach rates are higher, which adds workload and stress to the personnel involved. Therefore, an accurate forecast of poor-visibility episodes affecting airports is vital because of their impacts on flight planning and aviation safety (da Rocha et al., 2015). In this regard, it is crucial to have visibility forecasts as accurate as possible 24 h in advance in order to issue a Terminal Aerodrome Forecast (TAF).

However, the estimation of visibility remains a challenge for numerical weather prediction models. This challenge is greater for airports in complex terrain areas, where the use of mesoscale models with high resolution is indispensable. Fog formation and dissipation depends mainly on microphysical processes, wind, humidity and temperature in

* Corresponding author at: Delegación Territorial de AEMET en Cantabria, C/ Ricardo Lorenzo, 0, CP 39012 Santander, Spain.
E-mail address: sfernandezg@aemet.es (S. Fernández-González).

https://doi.org/10.1016/j.atmosres.2019.03.012
Received 1 February 2019; Received in revised form 22 February 2019; Accepted 6 March 2019
Available online 07 March 2019
0169-8095/

the planetary boundary layer (PBL) (Stolaki et al., 2012; Payra and Mohan, 2014). Some of these variables must be parameterized, so the main sources of error in numerical models are initial conditions and physical parameterizations (Fernández-González et al., 2017). The most common method to evaluate uncertainty associated with a forecast is the perturbation of initial conditions. However, perturbations require time to grow, so they are used mainly for medium-range forecasts (Buizza et al., 1999). For short-term forecasts, it is advisable to use different models or parameterizations to evaluate prediction uncertainty, because this facilitates adequate spread in a short lead time (Stensrud et al., 2000).

Forecasts from mesoscale models can be complemented by the use of satellite products for the nowcasting of fog episodes (Ahmed et al., 2015). Fog detection with satellite imagery has been attempted in recent decades using various approaches (Nilo et al., 2018). For instance, fog and low clouds can be detected by their reflectance characteristics in the visible band. During nighttime, the difference between brightness temperatures in the 10.8 and 3.7 μm channels allows the detection of low clouds, because fog droplets produce less emissivity in the 3.7 μm channel than at 10.8 μm (Gultepe et al., 2007). During daytime, information provided by infrared channels can be compared with visible channels for the detection of fog (Cermak and Bendix, 2008).

The aim of the present research was to provide a categorical forecast of the risk of poor-visibility conditions near Tenerife Norte Airport (hereafter, GCXO, the airport's International Civil Aviation Organization code). This was done using mesoscale models with a lead time of 24 h to improve TAF reliability. In addition, several products of the Nowcasting Satellite Application Facilities (NWC SAF, nwc-saf.eumetsat.int) are proposed to confirm/correct the mesoscale forecasts in real time, improving on information within Meteorological Terminal Air Reports (METAR), special reports (SPECI), and trend reports (TREND). GCXO was selected because of recurring fog; it is the most affected by this phenomenon among all the airports in the Canary Islands, with consequent great impact on flight operations. With over 4.7 million passengers in 2017, GCXO funnels most of the Spanish national air traffic to the island of Tenerife. The airport is also known for one of the worst accidents in aviation history. On 27 March 1977, two Boeing 747 jets collided on the runway, causing 583 fatalities. One of the key factors in this accident was poor visibility caused by dense fog. This event stresses the importance of investigating this type of weather phenomenon at GCXO, especially for its impacts on aviation safety.

2. Study area

GCXO is in the northeast of Tenerife, part of the Canary Islands (Fig. 1). The airport runway is oriented NW–SE at an elevation about 600 m above sea level (masl). It is between two mountain ranges whose elevations are higher than 1000 masl. Depending on wind direction, flights use Runway 12 (R12, northwestern part of the airport) or Runway 30 (R30, in its southeast). One of the key features of this orographic setting is efficient channeling of flow from either the NW or SE, with a clear dominance of the first because of prevailing trade winds (northeasterly) in the area, which occur > 70% of the year.

The state meteorological agency (AEMET) of Spain has the capability to provide aeronautical meteorological services within the national airspace. Therefore, the staff of AEMET issue TAFs, which are forecasts of conditions at airports over the next 24 h. Moreover, routine METARs are produced every half hour using observations at the airport. SPECI reports can be issued when observed meteorological conditions change suddenly. In addition, TREND reports must be issued when significant changes are expected in the next two hours. The purpose of our research was to help AEMET staff revise these reports, improving their reliability by making available more detailed information from mesoscale models and satellite products.

3. Experimental design

3.1. Database

We selected 14 poor-visibility episodes (Table 1) registered at GCXO during 2017 for validation. At least one episode per month was chosen to have events representative of all seasons of the year. In order to cover all the different types of poor visibility episodes that affect the GCXO airport, 4 episodes of SE wind and 10 of NW wind were selected, of which 2 the visibility was reduced by the passage of a cold front. According to several works, this sample number is sufficient for validating mesoscale models (Evans et al., 2012; Johnson and Wang, 2012).

In the validation, we used several instruments near R30, which is the representative runway of the airport. The instrumentation is composed of the following: an anemometer with Vaisala WAA15 wind speed (WSP) sensor and Vaisala WAV15 direction sensor; a Vaisala FD12 front dispersion sensor for measuring visibility and runway visual range; a Vaisala HMP155 thermo-hygrograph measuring temperature (T), dew point (Td), and relative humidity (RH).

3.2. Mesoscale models

We tested various mesoscale models. First, version 3.7.1. of the Weather Research and Forecasting (WRF) model was used to simulate the 14 episodes. WRF is a three-dimensional, nonhydrostatic model

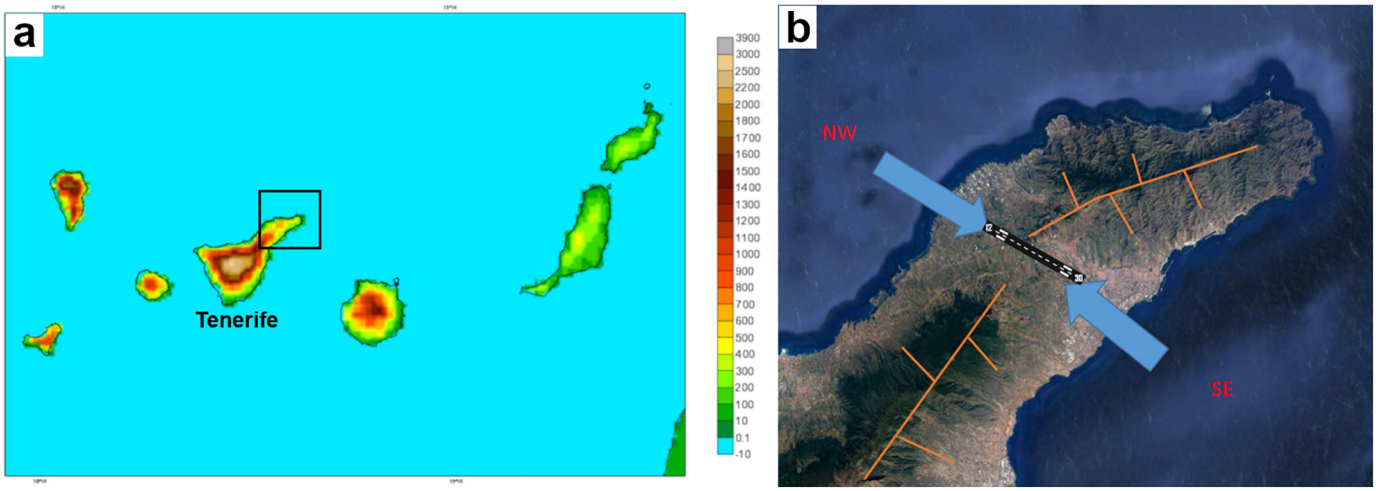

Fig. 1. Orography of Canary Islands (a). Location of GCXO on Tenerife (b).

Table 1
Dates of the fourteen low visibility episodes in GCXO selected for the validation.

2017 01 21	2017 02 19	2017 03 24	2017 04 02	2017 04 26	2017 05 31	2017 06 15
2017 07 05	2017 07 14	2017 08 31	2017 09 07	2017 10 17	2017 11 24	2017 12 02

described by Skamarock and Klemp (2008). This model has been used in the forecasting of visibility near airports (Bang et al., 2008). Its simulations were initialized using initial conditions provided by the NCEP–GFS analysis with $1^0 \times 1^0$ global grid and temporal resolution of 6 h (Saha, 2010). Simulations of each of the 14 days were run individually, initialized at 00:00 UTC with a hindcast period of 24 h. Four nested domains were defined following a two-way nesting strategy. Spatial resolutions were 27 km for the outer domain (D01), 9 and 3 km respectively for D02 and D03, and 1 km for the inner domain (D04), centered over GCXO. Each domain had 100 × 100 grid points in the N–S and E–W directions. We defined 60 sigma levels for the atmosphere, with increasing resolution approaching the surface (8 vertical levels for the first 120 m above ground level (m AGL) and 20 for the first 1000 m AGL). For physical parameterizations, the Thompson six-class microphysics (Thompson et al., 2008), New Goddard long and short wave radiation (Chou et al., 2001), and Mellor-Yamada-Janjic PBL (Janjic, 1990) schemes were used.

Furthermore, two versions of the HARMONIE-AROME model were tested, namely, HARMONIE-AROME 38 h1.2 (H38), which was the operational mesoscale model of AEMET until June 2017, and HARMONIE-AROME 40 h1.1 (H40), which is the agency's current operational mesoscale model. These models have a nonhydrostatic formulation and spectral representation (Seity et al., 2011). A detailed description of the configuration of these models is in Bengtsson et al. (2017). The operational forecasts of each poor-visibility episode, initialized at 00:00 UTC, were used in the validation procedure. These simulations had a lead time of 48 h but only the first 24 h were used. The models had a 2.5-km horizontal grid resolution for the area around the Canary Islands, with 65 vertical levels and a model top of 10 hPa. The domain defined for models H38 and H40 are seen in Fig. 1a.

In the case of H38, descriptions of the assimilation component are in Fischer et al. (2005) and Brousseau et al. (2011). The assimilated observations are equivalent to those used by the European Centre for Medium Range Weather Forecasts ERA-Interim reanalysis (Dee et al., 2011). The surface parameterization scheme was version 7.2 of SURFEX (Masson et al., 2013).

Several changes were made to H40. The SURFEX surface scheme was updated to version 7.3 (Masson, 2016). The assimilation of H40 included Global Navigation Satellite System data for improving humidity observations (Sánchez Arriola et al., 2016). Following the recommendations of Nielsen et al. (2014), the cloud-inhomogeneity factor was changed from 0.7 to 1.0, meaning that the cloud optical thickness was no longer reduced by 30% before cloud transmittance was computed (Nielsen and Gleeson, 2018). In addition, the Cuxart, Bougeault and Redelsperger turbulence scheme (Cuxart et al., 2000) was replaced by the turbulence scheme from the RACMO model (Lenderink and Holtslag, 2004).

3.3. Validation methodology

The validation period spanned 06:00 to 24:00 UTC on each of the 14 days of the study period. The first 6 h of each day were not considered in order to avoid errors from the spin-up period of the WRF model, because it was executed from a cold start. The first 6 h of H38 and H40 were also discarded to validate identical periods, although the warm start from a previous run cycle of HARMONIE-AROME allowed model outputs to be valid from the simulation start. As a result, the database used in the multi-category validation consists of a sample of 252 h. Considering the high horizontal resolution of the mesoscale models and in order to avoid interpolation errors, the validation was performed using data of the grid point nearest the locations of the observations. A preliminary validation was carried out to confirm that the nearest grid point was the most representative of the weather at GCXO.

Model performance was first evaluated for the forecasting of meteorological variables most associated with fog formation. A validation based on continuous statistics was developed for T, Td, T − Td, RH, WSP and wind direction. Validation indexes selected for this task were the Bias, Mean Absolute Error (MAE), and correlation coefficient (r), calculated as follows.

$$Bias = \sum_{i=1}^{n} (M_i - O_i)$$

$$MAE = \frac{1}{n} \sum_{i=1}^{n} |M_i - O_i|$$

$$r = \frac{\sum_{i=1}^{n} (M_i - \overline{M})(O_i - \overline{O})}{\sqrt{\sum_{i=1}^{n} (M_i - \overline{M})^2} \sqrt{\sum_{i=1}^{n} (O_i - \overline{O})^2}}$$

M_i are modelled values, O_i observed values, and n is the number of hours in the study period. Bias compares modelled and observed values with the aim of determining if the model overestimates (Bias > 0) or underestimates (Bias < 0) a certain variable. On the other hand, the MAE evaluates the magnitude of simulation error, regardless of whether the model overestimates or underestimates. Finally, r allows analysis of model performance over time, which is very important during fog episodes affected by the diurnal cycle.

Then, values obtained for the various indexes were normalized in order to compare them. We thereby determined a normalized index (NI). The ultimate purpose of this normalization was to develop a total index (TI) that summarized the results of the validation, thereby objectively determining the best model. The normalization was done by subtracting the average Bias/MAE/r from the obtained values, and then dividing the result by the same average. In the case of Bias, it is necessary to work with absolute values. To obtain a normalized r we must also multiply by −1 because, opposite to the cases of Bias and MAE, values closer to 0 are poorer. Finally, the TI is computed by adding the values of normalized Bias, MAE and r for each model. Negative TI values mean that the model has above average performance, i.e., the smaller the TI, the better the performance.

Subsequently, a multi-category validation for fog/mist/OK visibility events was carried out using contingency tables. According to definitions of the World Meteorological Organization (WMO, 2011), three categories were used for validation: fog (visibility < 1000 m), mist (1000 m ≤ visibility < 5000 m), and OK (visibility ≥ 5000 m).

Visibility in GCXO airport can vary sharply in a few minutes, being one of the most difficult variables to predict by the numerical models. This is the reason why we used two methods to estimate visibility using the mesoscale models. The first estimates visibility (VISRH) using T, Td and RH as predictive variables, by means of an empirical algorithm defined by Doran et al. (1999). The second method gave an additional measure of visibility (VISHD) based on the hydrometeor concentration estimated by the model, following methods in Kunkel (1984), Stoelinga and Warner (1999), and Petersen and Nielsen (2000).

$$\text{VISRH (m)} = 9654000 \times \frac{T - T_d}{RH^{1.75}}$$

$$\text{VISHD (m)} = \frac{-\ln(0.02)}{(\beta_{clean} + \beta_{cloud} + \beta_{ice} + \beta_{rain} + \beta_{snow} + \beta_{graupel} + \beta_{aerosols})}$$

Table 2
Thresholds of the selected variables for defining fog/mist/OK conditions.

	Algorithm 1			Algorithm 2			Algorithm 3		
	T-Td (°C)	RH (%)	WSP (kt)	T-Td (°C)	RH (%)	WSP (kt)	T-Td (°C)	RH (%)	WSP (kt)
Fog	≤0.5	≥96	≥3	≤0.3	≥97.5	≥4	≤0.1	≥99	≥6
Mist	< 1.5	> 90	> 1.5	< 1	> 94	> 2	< 0.5	> 96	> 3
Clear	> 1.5	< 90	< 1.5	> 1	< 94	< 2	> 0.5	< 96	< 3

where β is the volume extinction coefficient of clean air (constant), cloud droplets, ice, rain, snow, graupel (depends on the concentration of each hydrometeor) and aerosols (based on the concentration of cloud condensation nuclei and RH at 2 m).

Finally, an additional method for evaluating poor-visibility risk is proposed, which is based on an algorithm that determines if certain thresholds are exceeded. Given the particular characteristics of fog events at GCXO, variables to develop the algorithm were selected ad hoc for that specific location. These were T − Td, RH, and WSP. Three algorithms were tested, using thresholds in Table 2. These thresholds are linked to Algorithm 1 (A1), Algorithm 2 (A2), and Algorithm 3 (A3).

Then, the contingency table defined in Table 3 was used to contrast the frequencies of forecast fog, mist and OK visibility episodes against observed ones (capital letters signify the sum of the corresponding row/column).

Based on the methodology of Baldwin and Kain (2006) and López et al. (2007), the following skill scores were used. First, the Frequency Bias Index (FBI) was calculated. The FBI estimates the ratio of forecast vs. observed poor-visibility episodes. This score indicates whether the method has a tendency to over-forecast (FBI > 1) or under-forecast (FBI < 1) poor-visibility events. A value of 1 is the perfect score.

Additionally, the False Alarm Ratio (FAR) was estimated to evaluate the fraction of fog and mist episodes that were forecast but did not occur. A value of 0 is the perfect score.

Finally, the Frequency Of Misses (FOM) assesses the fraction of fog and mist episodes that were not forecast but did occur. A value of 0 is the perfect score.

$$\text{FBI} = \frac{M+N}{J+K} \quad \text{FAR} = \frac{g+h}{M+N} \quad \text{FOM} = \frac{c+f}{J+K}$$

3.4. Satellite products

Based on our research, the use of satellite products is encouraged to complement the fog forecast provided by mesoscale models. We used several products from the Meteosat Second Generation, which is a geostationary satellite that provides continuous coverage of the study area. Specifically, we used the products “Cloud Type,” “Cloud Top Altitude,” and “Precipitable Water in Boundary Layer” from the NWC SAF. The Cloud Type product allows discernment of the cloud type and estimation of cloud thickness. By complementing this product with the Cloud Top Altitude, it is possible to estimate cloud top height. In cloud-free regions, the Precipitable Water in Boundary Layer product is able to estimate precipitable water (in mm) integrated from the surface to 850 hPa level. This product permits the estimation of moisture content in the stratum in which the cloudiness producing poor visibility at GCXO develops. A more detailed explanation of the above products is in Rípodas et al. (2016).

Table 3
Contingency table used in the validation process.

		Forecasted			
		Fog	Mist	OK	
Observed	**Fog**	a	b	c	**J**
	Mist	d	e	f	**K**
	Clear	g	h	i	**L**
		M	**N**	**O**	**T**

The best results are highlighted in bold.

4. Results and discussion

4.1. Conceptual model of fog development at GCXO

GCXO is located on a mountain pass between two mountain ranges, which favors wind channeling from the NW or SE, depending on the location of the semi-permanent subtropical high. Thus, the geomorphological configuration is essential to the occurrence of such ageostrophic flow, which differs from the prevailing trade winds. The flow is forced to ascend the slope of a hill, adiabatically cooling so that saturation can be reached when there is substantial moisture. Sometimes, saturation is reached at an altitude lower than the elevation of GCXO, causing poor visibility at the airport. The uplift is often sharply interrupted by a trade wind inversion, limiting the cloud top to the same altitude as the base of the temperature inversion.

Poor-visibility events are frequent throughout the year but are particularly influential during summer, especially in June and July. A diurnal cycle is commonly observed, with the poor-visibility episodes more likely from sunset to dawn, when T and Td approach each other. The presence of the semi-permanent subtropical high generates anticyclonic subsidence in the Canary Island region, forming a thermal inversion that produces low stratocumulus. An example of a radiosonde profile over the island of Tenerife (a few kilometers SW of GCXO) is shown in Fig. 2, in which a strong trade wind inversion is evident around 1000 masl.

In winter, when the inversion is at an average altitude between 1200 and 2000 masl, the cloud base is usually above the runway and visibility does not tend to be much of a problem. However, during drizzle or moderate precipitation events, especially those associated with fronts from mid-latitude systems approaching from the NW, the formation of fog banks is not uncommon, and even the drizzle itself can reduce visibility. These events are not usually strongly dependent on the daily cycle but rather on the front arrival (AEMET, 2019).

In summer, the thermal inversion is normally at lower altitudes (often between 500 and 1000 masl), with a strong diurnal variability that presents the main obstacle to accurately predicting reduced visibility events. It is also in summer when trade winds from the NE are stronger and more frequent (~90% of the time), with the aforementioned orography consistently channeling the flow to be mostly from the NW (Fig. 3a). This flow initiates moisture convergence in the PBL north of Tenerife island (Fig. 4a) and may produce low clouds (Fig. 5a) that are responsible for poor visibility at GCXO. In this scenario, poor visibility first reaches at R12 and later at R30.

Another meteorological situation, less frequent, occurs when the subtropical high becomes very weak or even dissipates. This scenario often weakens the pressure gradient around the Canary Islands. When this occurs, it is common to have a weak flow from the ENE–E that is channeled from SE by the terrain (Fig. 3b). This flow favors low-level moisture pooling south of Tenerife island (Fig. 4b) and cloud development from the southern side of the island to the airport (Fig. 5b). This causes poor visibility to occur earlier at the R30 threshold than at R12.

The conceptual model described in this paper is similar to the fog elucidated by Fedorova et al. (2013), which was also related to a

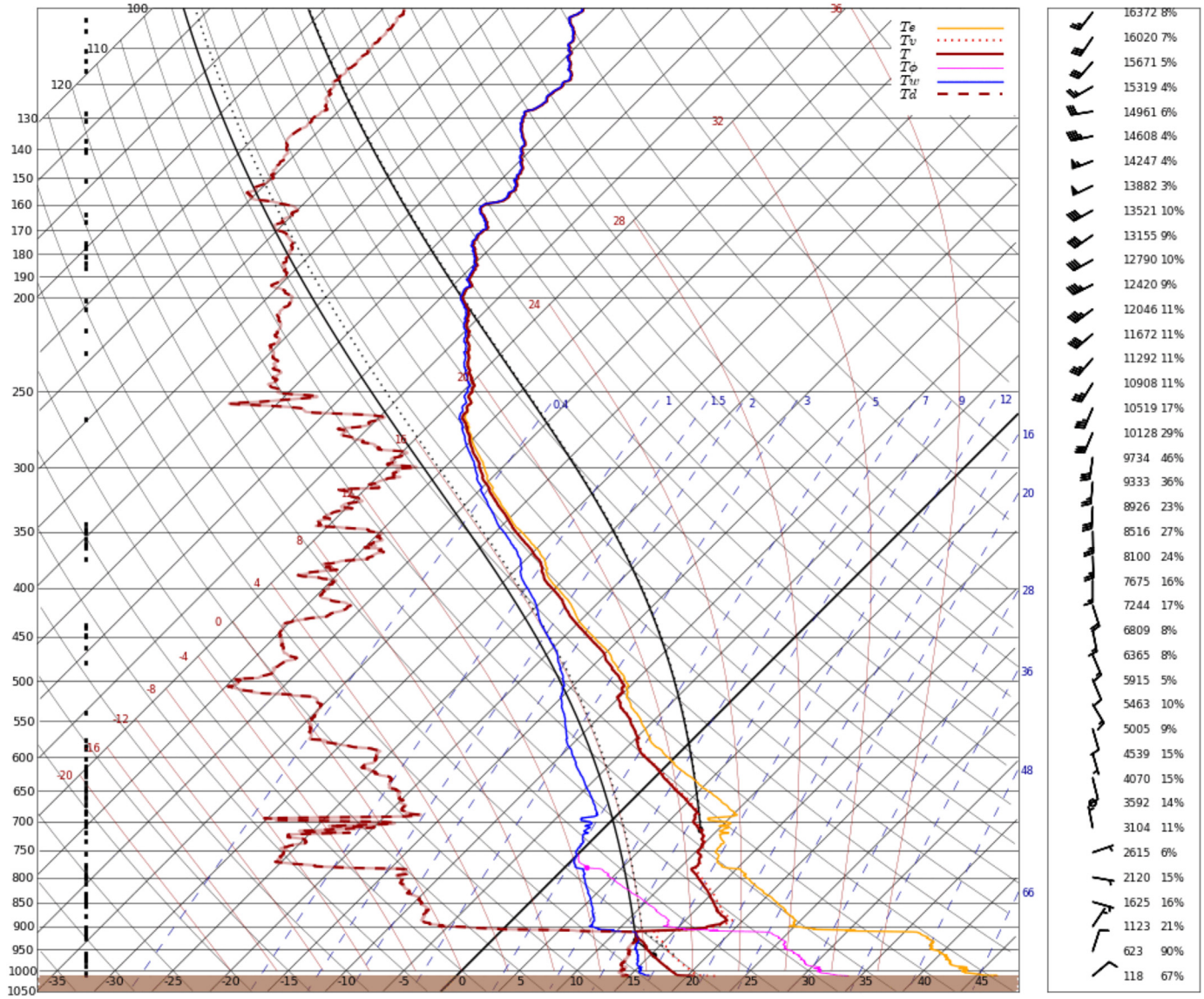

Fig. 2. Radiosonde data from island of Tenerife showing typical trade wind inversion.

thermal inversion above the trade winds. This shows that the products addressed in the following sections could be adapted to other locations with the same visibility problems.

4.2. Validation of mesoscale models

Before defining the products developed to forecast poor-visibility episodes, we validated the variables most associated with fog formation. In this validation, values of the variables estimated by the mesoscale models were compared with those observed at GCXO. The sample used in the validation is composed by observed visibility data from the 14 selected episodes during 2017, with a temporal resolution of 1 h. During the study period, fog was recorded 16.2% of the time, whereas mist was present 27.4% of the time. Visibility was categorized as OK during the remaining hours examined in the validation (56.4%).

4.2.1. Quantitative validation

First, we performed a quantitative validation for the variables T, Td, RH and WSP. The averages for the 14 episodes in the study period are shown in Table 4. Regarding T validation, all models showed slight underestimation ($-0.3 \leq$ BIAS ≤ -0.2), with MAE about 1 °C. The temporal correlation of T throughout the diurnal cycle is satisfactory, as shown by values of $r \geq 0.92$. Comparing the models, H38 and H40 were slightly better than WRF in the estimation of T at GCXO. Maximum temperature was simulated early during certain episodes by both H38 and H40, possibly causing earlier fog dissipation in the simulations than in reality.

From the validation of Td, BIAS values indicate moderate underestimation was detected for all the mesoscale models, with MAE = 1.6 °C for H38 and H40, and slightly larger for the WRF (MAE = 1.8 °C). The temporal correlation is very good for all cases ($r \geq 0.84$), although slightly weaker than that of T. Similar results were obtained for RH, with general moisture underestimation by the mesoscale models for GCXO. MAE values of 9%–10% were obtained, and temporal correlation was very disappointing ($0.43 \geq r \geq 0.54$). The most accurate model in the estimation of Td and RH near GCXO was H38, closely followed by H40. The best temporal correlation in Td estimation with respect to RH suggests the use of Td output by the mesoscale models as a moisture indicator for GCXO.

Regarding WSP, there was slight underestimation from the H38 model and moderate underestimation by the WRF. In contrast, the H40 model appeared to correct the WSP underestimation and was even characterized by slight overestimation (BIAS = 0.8 m/s), especially for strong wind episodes. Consequently, the MAE was smaller for H40 and

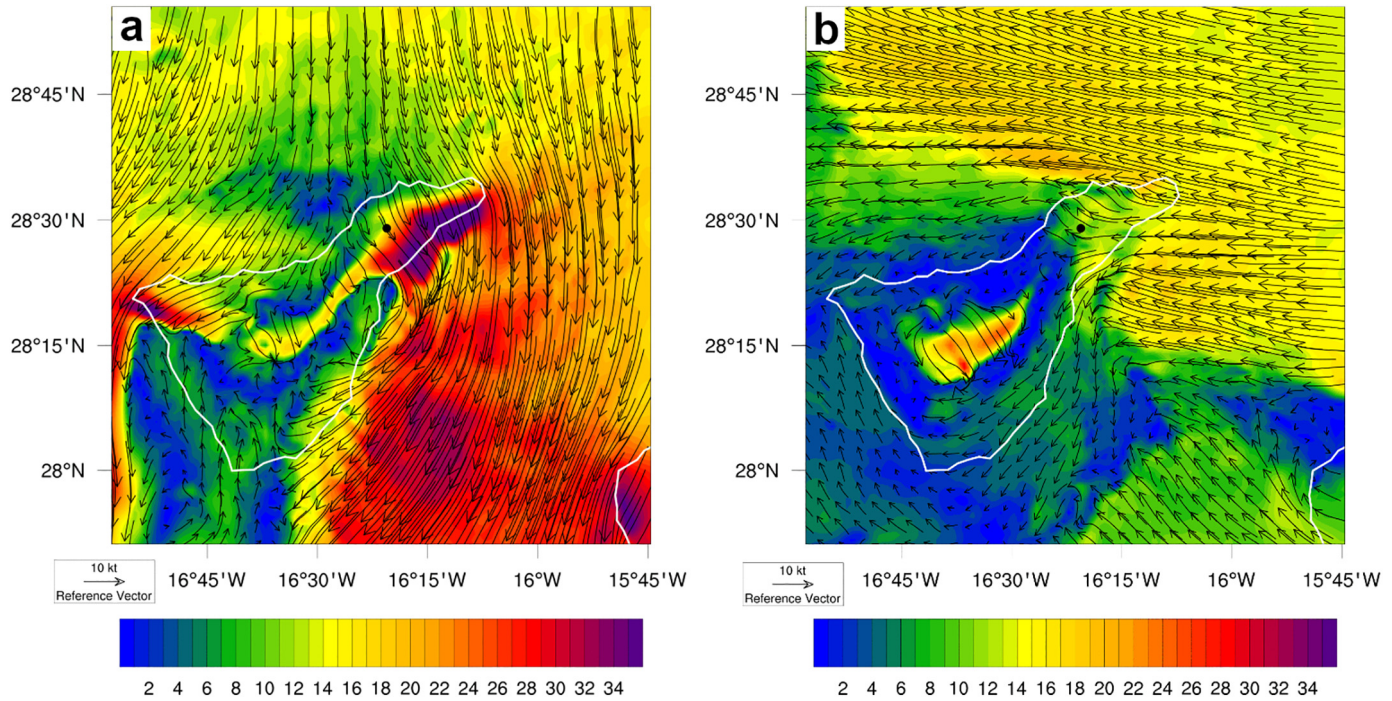

Fig. 3. Wind at 10 m above ground level (magl) estimated by WRF model in D03 during poor-visibility episodes with NW flow (a) and SE flow (b). Location of GCXO is represented by a black dot.

larger for the WRF. The temporal correlation was satisfactory for both the H38 and H40 models (r = 0.86 and 0.90, respectively), with poorer results from WRF. In general, predictability was greater for W and NW flows, which are characterized by strength and stability. However, the models were less reliable in estimating southerly component winds, because these are less strong. The models struggled with simulating changes in wind direction, especially when there was no marked pressure gradient. In the case of WSP, the H40 model clearly achieved the best results, followed closely by H38. The results of WRF are very disappointing.

Considering the TI, which considers all the variables as a whole, the H38 and H40 models stand out for their satisfactory results (with H40 slightly better). Those of the WRF are not very accurate. The poorer figures for the WRF model may be related to the cold-start used in its initialization and use of the GFS analysis for initial and boundary conditions. The better results for H38 and H40 may be attributed to a more complete assimilation system, in which observational data from a multitude of sources are considered. This corrected deviations from the previous model cycle to produce an analysis used as initial conditions in the warm start of the model.

4.2.2. Multi-categorical validation

Next, it was decided to execute a multi-categorical validation for testing model performance in estimating visibility. This decision was made after verifying that the results of a classical validation of a variable such as visibility gave results that were difficult to interpret.

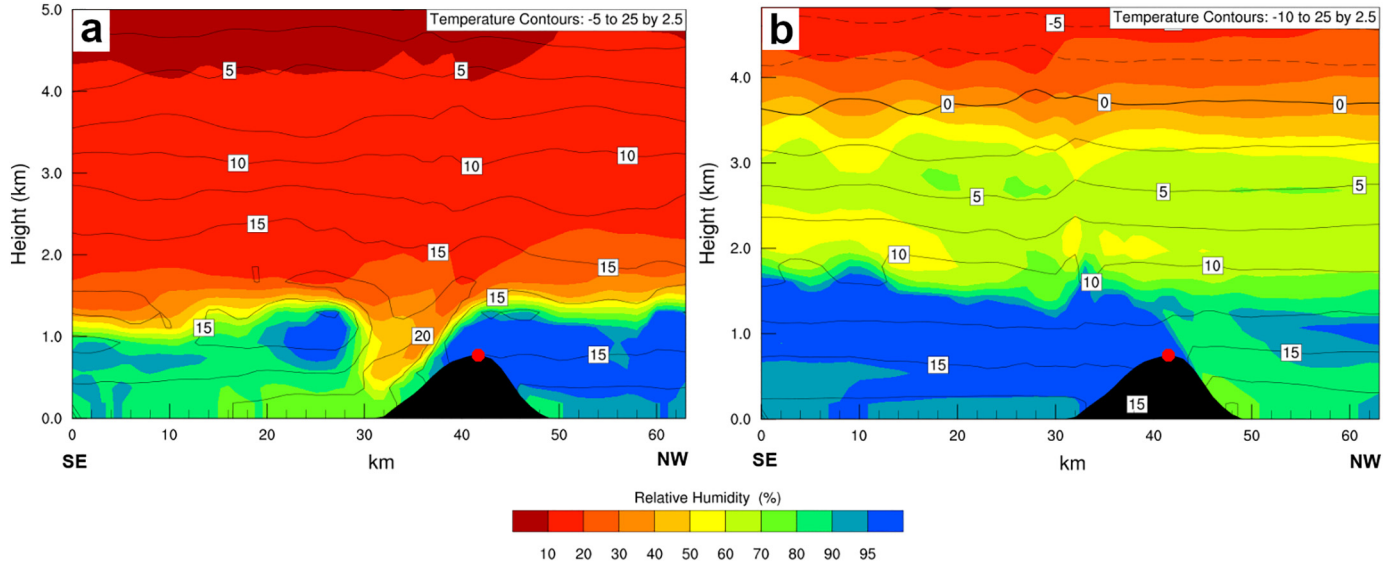

Fig. 4. RH estimated by WRF model in a D03 cross section oriented SE–NW across GCXO (red dot), during poor visibility episodes with NW (a) and SE flow (b). (For interpretation of the references to color in this figure legend, the reader is referred to the web version of this article.)

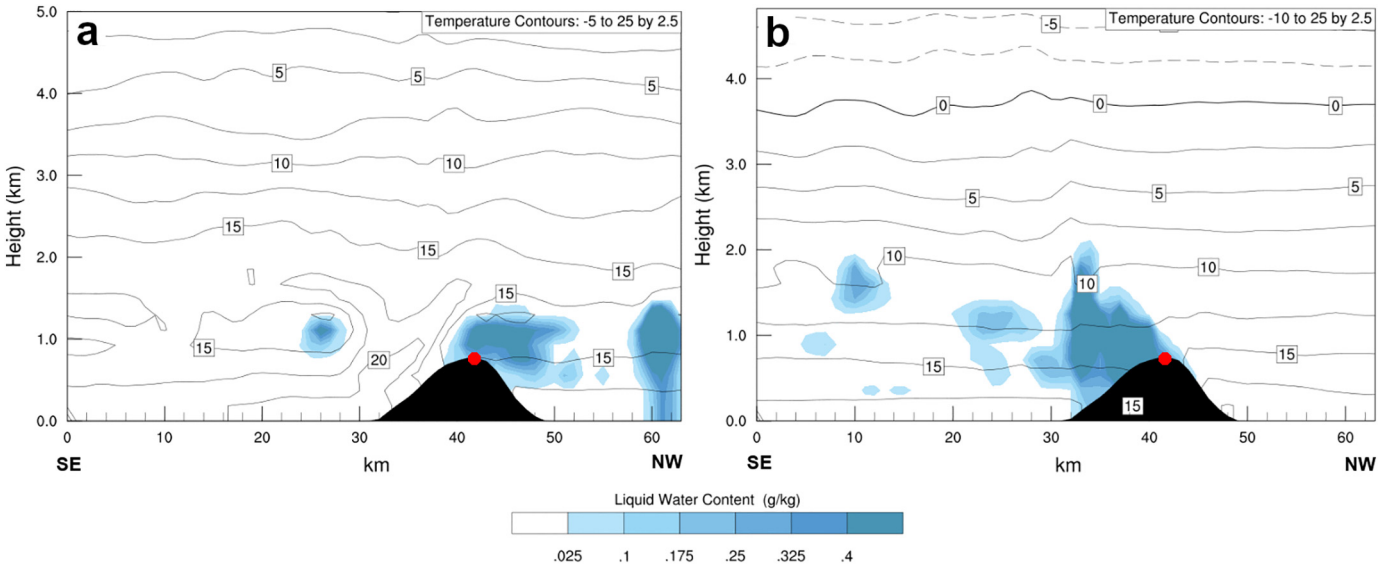

Fig. 5. Liquid water content estimated by WRF model in a D03 cross section, oriented SE–NW across GCXO (red dot), during poor visibility episodes with NW (a) and SE flow (b). (For interpretation of the references to color in this figure legend, the reader is referred to the web version of this article.)

Visibility has drastic variations that can lead to large errors in numerical models, even though observed and forecast visibilities are not problematic for aviation operations. As previously mentioned, three categories were defined, depending on observed and model-estimated visibility values (fog, mist and OK). After developing respective contingency tables, the FBI, FAR and FOM were calculated. Table 5 shows results of the three mesoscale models and two methods of estimating visibility, i.e., using the algorithm based on moisture (VISRH) or that based on hydrometeor concentration (VISHD). Results of the WRF model are disappointing, especially for the large number of false alarms. The FOM was good when using the VISRH method, but showed substantial overestimation of poor-visibility episodes.

Regarding results of the two versions of the HARMONIE-AROME model, the outcomes were very similar when considering the VISRH method. The forecasts were balanced (FBI around 1.05), with FOM and FAR about 0.30 and 0.35, respectively. For the VISHD method, we observed moderate overestimation of poor-visibility episodes from H38, but this led to a very favorable FOM (0.22). In contrast, H40 slightly underestimated poor-visibility events, thereby increasing the number of such events that were observed but not adequately predicted (FOM = 0.38). The FAR was similar for both versions of HARMONIE-AROME and both methods (0.34–0.38), markedly improving the results of WRF.

Because the present work focused on providing operational forecasters tools to maximize aviation safety during poor-visibility episodes, the aim was to minimize the FOM, because unforeseen fog events can pose a risk to aviation. Although it is also necessary to minimize the FAR, a greater number of false alarms would activate the poor-visibility protocol of GCXO and not pose an immediate risk to air safety. Nilo et al. (2018) obtained similar results (FAR = 0.31, FOM = 0.30) for a nowcasting system based on satellite observations, but our forecasting system is able to predict fog 24 h in advance. This demonstrates that the results of H38 and H40 are satisfactory, especially considering the challenge of forecasting localized meteorological phenomena such as mist and fog in complex terrain. The validation was developed exclusively using data of poor-visibility episodes, which pose a greater challenge.

Analyzing the forecasts for each day of the study period individually, it was detected that the performance of both versions of the HARMONIE-AROME model was case-dependent, because on some days the H38 was more accurate in visibility estimation, whereas for other episodes H40 yielded superior results. For this reason, and taking into account that the validation results of both versions of HARMONIE-AROME are similar, it was decided to use both models and the two methods in the operational forecasting system. Thus, the operational forecaster would have four different visibility estimates from which to infer the risk of poor visibility at GCXO, as well as having a measure of

Table 5
Results of the multi-categorical validation for the visibility based on T and RH (VISRH) and visibility based on hydrometeors concentration (VISHD).

	WRF		H38		H40	
	VISRH	VISHD	VISRH	VISHD	VISRH	VISHD
FBI	1.64	1.17	1.05	1.26	1.06	0.98
FAR	0.56	0.51	0.34	0.38	0.36	0.37
FOM	0.28	0.42	0.31	0.22	0.32	0.38

Table 4
Results of the model validation for the variables T, Td, RH and WSP.

	WRF				H38				H40			
	T	Td	RH	WSP	T	Td	RH	WSP	T	Td	RH	WSP
BIAS	−0.3	−1.6	−6.0	−2.0	−0.2	−1.3	−5.2	−1.0	−0.2	−1.4	−5.9	0.8
MAE	1.1	1.8	9.9	3.7	1.1	1.6	9.2	2.4	1.0	1.6	9.6	2.2
r	0.93	0.84	0.43	0.61	0.92	0.84	0.54	0.86	0.92	0.85	0.52	0.90
NI	0.3	0.2	0.2	2.2	−0.2	−0.2	−0.2	0.2	−0.2	−0.1	0.0	−0.3
TI	3.10				**−0.50**				**−0.54**			

The best results are highlighted in bold.

Table 6
Results of the multi-categorical validation for the algorithms based on distinct thresholds of T-Td, RH and WSP.

	OBSERVED			WRF			H38			H40		
	A1	A2	A3	A1	A2	A3	A1	A2	A3	A1	A2	A3
FBI	1.47	1.24	0.85	1.45	1.35	1.17	1.10	0.95	0.83	1.11	0.85	0.61
FAR	0.36	0.28	0.22	0.55	0.52	0.48	0.38	0.33	0.29	0.37	0.32	0.30
FOM	0.06	0.11	0.34	0.35	0.35	0.39	0.31	0.36	0.41	0.30	0.42	0.57

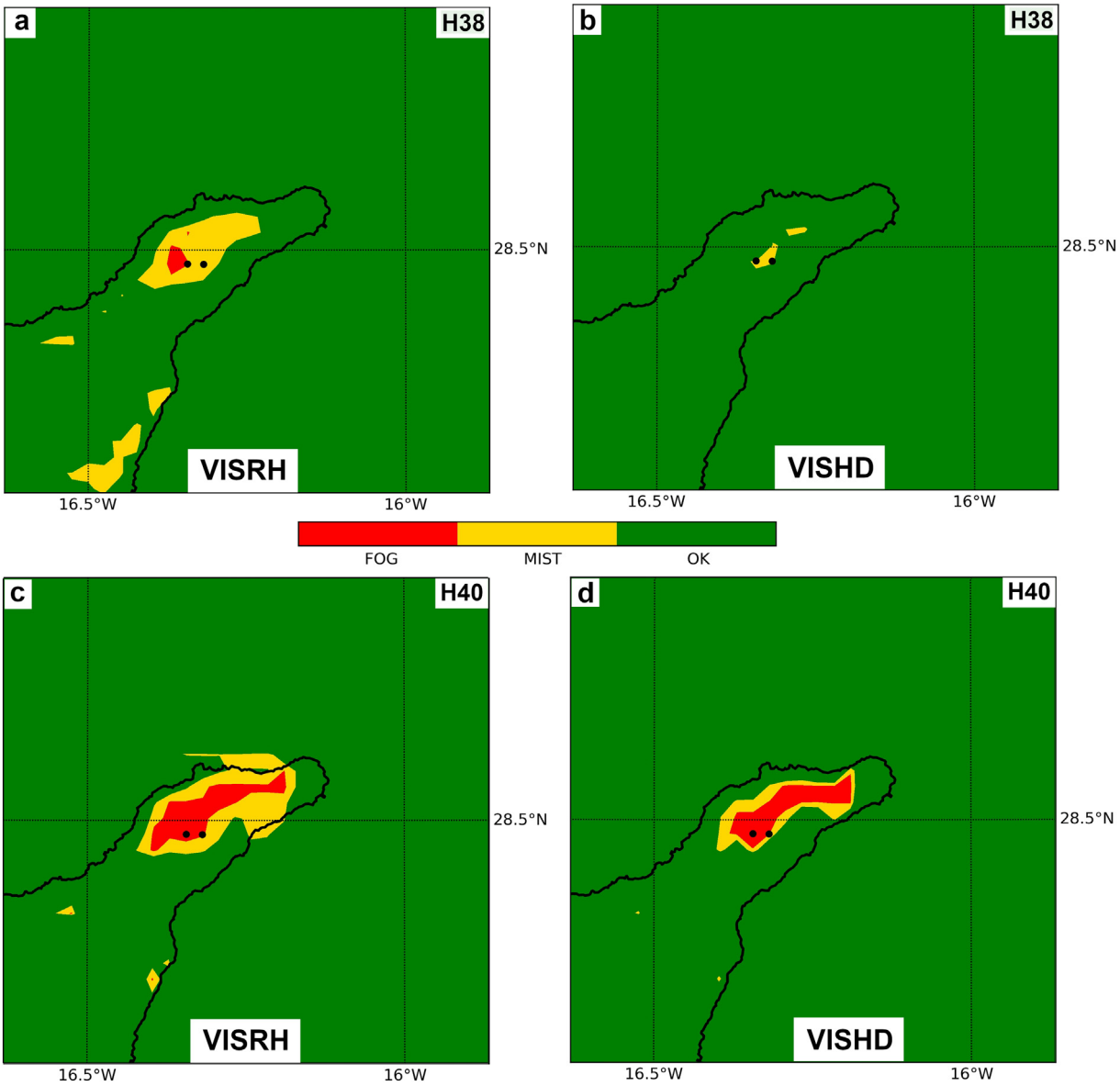

Fig. 6. Visibility estimated by H38 (a, b) and H40 (c, d) models using VISRH (a, c) and VISHD (b, d) methods at 09:00 UTC on 13 December 2018. Black dots indicate grid points nearest the locations of GCXO R12 (left) and R30 (right).

forecast uncertainty according to the ratio of products that consider whether fog will form in the study area.

In addition to considering the VISRH and VISHD products, we validated three algorithms based on the exceedance of certain thresholds of T − Td, RH and WSP. Results of the algorithms are listed in Table 6. Visibility varied sharply in a few minutes at GCXO. This is the reason we also tested the algorithms with observed values, with the aim of applying them to the nowcasting of visibility.

As expected, best results were achieved using the observational data. In this case, A2 produced the best results, with a FOM of only 0.11. This algorithm slightly overestimates poor-visibility episodes (FBI = 1.24), leading to FAR = 0.28. The other algorithms were discarded because A1 markedly overestimated the number of such episodes, whereas A3 showed notable underestimation. A2 results are outstanding compared with similar nowcast products (Guijo-Rubio et al., 2018).

Regarding the algorithms applied to mesoscale models, the worst results were once again obtained by the WRF model because of excessive overestimation of poor-visibility events, yielding for every algorithm a FAR around 0.50. To prioritize air safety, it was decided to

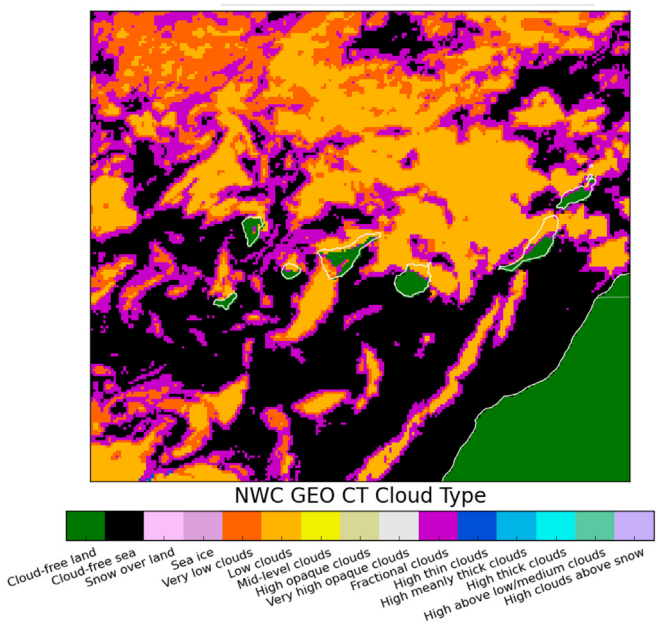

Fig. 7. Image of Cloud Type product of NWC SAF during poor-visibility episode characterized by NW flow. Copyright 2018 EUMETSAT.

choose the algorithm that minimized FOM. As a result, A1 was chosen for both versions of the HARMONIE-AROME model. This algorithm had slight overestimation of poor-visibility episodes, with very satisfactory values of FAR and FOM (around 0.37 and 0.30, respectively). The results of A1 for H38 and H40 are similar to those obtained by the VISRH and VISHD products from the same mesoscale models, so its use can be complementary, with the performance of each method superior for certain episodes or circumstances (e.g., wind direction and season).

Per the validation results, the use of A2 is recommended for the system based on observational data, and A1 is proposed for the H38 and H40 versions of the HARMONIE-AROME model. The WRF setting used in this research is not capable of simulating accurately poor visibility episodes in this emplacement, but further research would be convenient to find out if the results improve by using other physical parameterizations.

Because visibility forecasts are sensitive to both moisture quantity and the predicted mass concentrations of hydrometeors (Bang et al., 2008), all methods described in this paper are valid. Because the validation results are similar (and very accurate) for VISRH, VISHD and the algorithms based on thresholds, all those methods are adequate for forecasting poor visibility episodes at GCXO.

4.3. Forecast system

A poor-visibility episode on 13 December 2018 was selected to show the potential of the forecast applications developed in our research. First, information provided by mesoscale models was used to elaborate the products for a short-term forecast. These forecast products are oriented to the creation of TAF reports, with a lead time out to 24 h. Then, several satellite products were used to aid the development of TREND reports and potentially inform about errors in the model forecasts.

4.3.1. Short-term forecast

According to the validation results, use of the WRF model was rejected for operational forecast. Because the validation results for the H38 and H40 models are very similar, it was decided to use both. Likewise, we considered the two methods to estimate visibility (VISRH and VISHD). Thus, a greater amount of information is made available and our prediction system therefore more robust.

Fig. 6 shows visibility estimated by the H38 and H40 models using the VISRH and VISHD methods for a poor-visibility episode characterized by a NW wind. In this example, the airport had reduced visibility especially at R12 but also affecting R30. Unlike the H40 model, H38 did not reproduce the drastic reduction of visibility in this case, simulating only a risk of mist in the vicinity of GCXO.

Regarding differences between the two methods, the visibility reduction was sharper in the case of VISHD, going from visibility OK to fog, with almost no areas of mist. The reduction was progressive using the VISRH method.

The spread between models and methods to estimate visibility can be interpreted as a measure of the predictability of an episode. For instance, when fog is forecast by both models and methods, the forecaster can be reasonably sure that poor visibility will occur. However, when there are discrepancies between the various visibility estimates (as in the case of Fig. 6), the reliability of the predictive system is poorer and associated forecast uncertainty is greater.

In addition to the short-term forecast products, T − Td, RH, wind direction and WSP fields estimated by H38 and H40 were also generated for supporting the decision-making process for constructing TAF and TREND reports. Vertical profiles of T, Td and wind forecasts by the HARMONIE-AROME model at the nearest grid point to each of the GCXO runways are also available to the operational forecaster to provide information equivalent to radiosonde observations.

4.3.2. Nowcasting

Ultimately, the use of satellite products is proposed for the nowcasting of poor-visibility episodes at GCXO. It is thereby possible to complement the information from the mesoscale models or have another source of information when the models are not accurate. In addition, the product obtained from the algorithm based on thresholds is described.

An image of the Cloud Type product is presented in Fig. 7, which allows differentiation between low, medium, and high clouds, as well as between thin and thick clouds. The accuracy of this product was substantiated by the verification of Karlsson and Dybbroe (2010). The product can be complemented by the Cloud Top Altitude product (Fig. 8), which furnishes information about cloud-top altitude in feet (ft). Poor-visibility episodes at GCXO are related to stratocumulus, which are identified as low or very low clouds in the Cloud Type product, commonly with cloud-top altitude below 6000 ft. When the trade

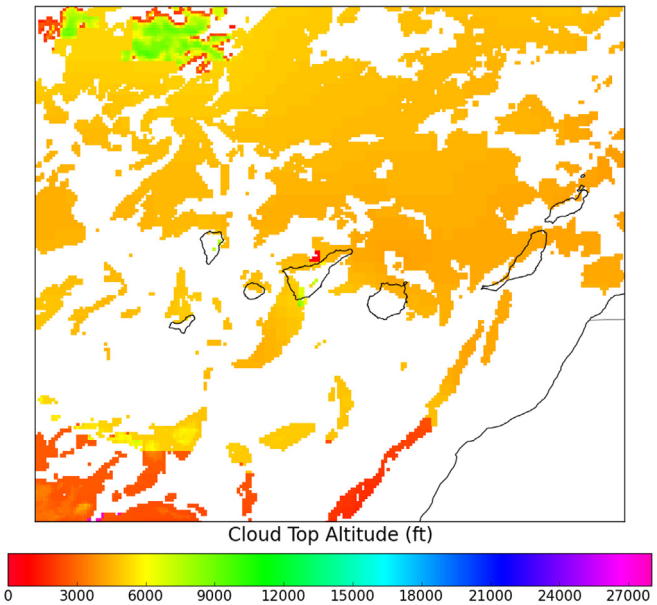

Fig. 8. Image of Cloud Top Altitude product of NWC SAF during poor-visibility episode characterized by NW flow. Copyright 2018 EUMETSAT.

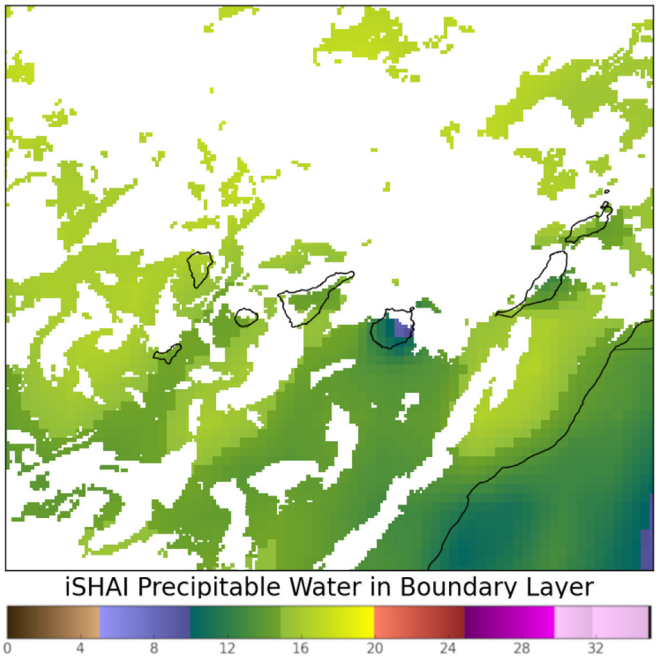

Fig. 9. Image of Precipitable Water in Boundary Layer product of NWC SAF during poor-visibility episode characterized by NW flow. Copyright 2018 EUMETSAT.

winds prevail as in the case shown by Figs. 7–9, low clouds usually form north of Tenerife island, which may affect visibility at GCXO. The altitude estimated by the aforementioned product is very reliable because it was tested following the methodology in Karlsson and Johansson (2013).

Finally, Fig. 9 shows an example of images generated by the Precipitable Water in Boundary Layer NWC SAF product over the Canary Islands. In accord with monitoring during the months of the project, precipitable water in the PBL in excess of 10 mm is necessary for low cloud development in the study area, which can lead to episodes of poor visibility at GCXO. The risk of such episodes increases when precipitable water in the PBL is > 15 mm. The main limitation of the product is that it is not available for areas covered by clouds. However, because variations of precipitable water in the PBL are slight over large regions, the product can reliably estimate water content in the study area and in air masses approaching the Canary Islands, even when there are large areas covered by cloudiness.

Finally, a tool was developed for indicating inferred visibility by color-coding the runway threshold (OK: green; mist: yellow; fog: red) based on if certain values of the variables T, Td, RH and WSP defined in Table 2 are exceeded. In this way, an algorithm is developed to decide the color-coding of each runway threshold on the application developed for the operational forecasters. Owing to the particular characteristics of fog, it requires sufficient kinetic energy provided by the wind, which is transformed into potential energy during air mass ascent along the slope of the hill on which GCXO is situated. A large moisture amount is also needed so that the adiabatic cooling experienced during the ascent condenses the water vapor contained in the air mass. The tool was developed to complement the mesoscale models and satellite products, with a focus on nowcasting. Because visibility in the study area changes very rapidly, this tool is intended to anticipate such changes on a short scale of a few minutes. For this reason, the monitoring of real-time observations can facilitate anticipation of a change in weather that forms fog in the study area.

The aim of the above application is to alert regarding the risk of mist or fog when certain observed conditions are fulfilled. For observed conditions, A2 was selected in the validation, so this was used in development of the application. As seen in Fig. 10, the risk of poor

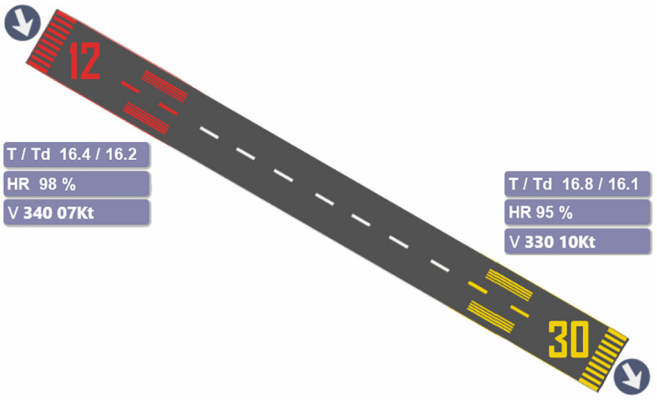

Fig. 10. Application for inferring visibility from algorithm based on observed thresholds of T − Td, RH and WSP.

visibility at R12 was indicated by the algorithm, because a NW wind stronger than 4 kt was driving a moisture flow (RH ≥ 97.5%) that reduced T − Td to < 0.3 °C. In this example, as is usually the case during NW wind episodes, visibility conditions were better at R30, where only the risk of mist was indicated by the algorithm.

5. Conclusions

Visibility forecasts in the vicinity of airports are vital to maximize aviation safety. However, this task is not easy for numerical weather prediction models, especially for airports in complex terrain such as GCXO. In such cases, the use of high-resolution mesoscale models is essential to attain accurate visibility forecasts. The main conclusions of our research are as follows.

- Poor visibility episodes in the vicinity of GCXO are related to trade winds and a thermal inversion favored by the semi-permanent subtropical high. At the mesoscale, trade winds are channeled through a mountain pass where the airport is located, and the air mass (which is typically moisture-laden after crossing the Atlantic Ocean) is forced to ascend and cool adiabatically. When all factors are favorable, condensation is reached, forming low clouds in the study area.
- Validation results of the H38 and H40 versions of HARMONIE-AROME are satisfactory, especially for the variables T and WSP. The models struggled with predicting variables related to humidity, but Td values were accurately predicted. The performance of the methods proposed herein for estimating visibility was outstanding, especially considering the local scale at which the analyzed meteorological phenomenon develops, the complex terrain in which the airport is located, and the poor predictability of the episodes selected as samples in the validation.
- Using the numerical weather prediction models, there is no single method for estimating visibility that is clearly optimal at GCXO for every poor-visibility episode. Consequently, a combination of information provided by several methods may be useful, facilitating the evaluation of uncertainty associated with the forecast of a specific episode.
- For nowcasting, the use of products based on satellite images is greatly encouraged, because they can provide information on moisture content in the PBL and alerts of the formation of low clouds around the Canary Islands.
- The application developed from the algorithm based on observed variables may allow the monitoring of realtime observations, enabling forecasters to anticipate weather conditions favorable to fog development.

In conclusion, the short-term and nowcasting products proposed in this research may improve safety at GCXO and be applied to other airports affected by low-visibility episodes, after analyzing specific characteristics of the fog that develops at each location. This could be the objective of future work, examining which airports are also affected by poor visibility and adapting the tools developed herein to the needs of each aerodrome.

Acknowledgements

This work was supported by the Aeronautics Annual Plan 2018 of AEMET. Special thanks go to projects SAFEFLIGHT (CGL2016-78702-C2-1-R and CGL2016-78702-C2-2-R) and UE ERA-NET Plus NEWA (PCIN2016-080).

References

AEMET, 2019. Climatología aeronáutica del aeropuerto de Tenerife Norte/Los Rodeos. http://ama.aemet.es/documents/19/48901/GCXO.pdf.

Ahmed, R., Dey, S., Mohan, M., 2015. A study to improve night time fog detection in the indo-gangetic basin using satellite data and to investigate the connection to aerosols. Meteorol. Appl. 22, 689–693. https://doi.org/10.1002/met.1468.

Baldwin, M.E., Kain, J.S., 2006. Sensitivity of several performance measures to displacement error, bias, and event frequency. Weather Forecast. 21 (4), 636–648. https://doi.org/10.1175/WAF933.1.

Bang, C.H., Lee, J.W., Hong, S.Y., 2008. Predictability experiments of fog and visibility in local airports over Korea using the WRF model. J. Korean Soc. Atmos. Env. 24, 92–101.

Bengtsson, L., Andrae, U., Aspelien, T., Batrak, Y., Calvo, J., de Rooy, W., Gleeson, E., Sass, B.H., Homleid, M., Hortal, M., et al., 2017. the harmonie–arome model configuration in the ALADIN–HIRLAM NWP system. Mon. Weather Rev. 145, 1919–1935. https://doi.org/10.1175/MWR-D-16-0417.1.

Bergot, T., Terradellas, E., Cuxart, J., Mira, A., Liechti, O., Mueller, M., Nielsen, N.W., 2007. Intercomparison of single-column numerical models for the prediction of radiation fog. J. Appl. Meteorol. Climatol. 46, 504–521. https://doi.org/10.1175/JAM2475.1.

Brousseau, P., Berre, L., Bouttier, F., Desroziers, G., 2011. Background-error covariances for a convective-scale data-assimilation system: AROME-France 3DVar. Q. J. R.Meteorol. Soc. 137, 409–422. https://doi.org/10.1002/qj.750.

Buizza, R., Miller, M., Palmer, T., 1999. Stochastic representation of model uncertainties in the ECMWF Ensemble Prediction System. Q. J. R. Meteorol. Soc. 125 (560), 2887–2908. https://doi.org/10.1002/qj.49712556006.

Cermak, J., Bendix, J., 2008. A novel approach to fog/low stratus detection using Meteosat 8 data. Atmos. Res. 87, 279–292. https://doi.org/10.1016/j.atmosres.2007.11.009.

Chou, M.-D., Suárez, M.J., Liang, X.-Z., Yan, M.-H., 2001. A thermal infrared radiation parameterization for atmospheric studies. In: NASA Tech. Rep. Series on Global Modeling and Data Assimilation. vol. 19 Goddard Space Flight Center (NASA/TM-2001-104606, 56 pp).

Cuxart, J., Bougeault, P., Redelsperger, J.L., 2000. A turbulence scheme allowing for mesoscale and large-eddy simulations. Q. J. R. Meteorol. Soc. 126, 1–30. https://doi.org/10.1002/qj.49712656202.

Dee, D.P., Uppala, S.M., Simmons, A.J., Berrisford, P., Poli, P., Kobayashi, S., Andrae, U., Balmaseda, M.A., Balsamo, G., Bauer, P., et al., 2011. The ERA-Interim reanalysis: Configuration and performance of the data assimilation system. Q. J. R. Meteorol. Soc. 137, 553–597. https://doi.org/10.1002/qj.828.

Dey, S., 2018. On the theoretical aspects of improved fog detection and prediction in India. Atmos. Res. 202, 77–80. https://doi.org/10.1016/j.atmosres.2017.11.018.

Doran, J.A., Roohr, P.J., Beberwyk, D.J., Brooks, G.R., Gayno, G.A., Williams, R.T., Lewis, J.M., Lefevre, R.J., 1999. The MM5 at the Air Force Weather Agency-New products to support military operations. In: The 8th Conference on Aviation, Range, and Aerospace Meteorology, Dallas, Texas.

Evans, J.P., Ekström, M., Ji, F., 2012. Evaluating the performance of a WRF physics ensemble over south-East Australia. Climate Dyn. 39, 1241–1258. https://doi.org/10.1007/s00382-011-1244-5.

Fedorova, N., Levit, V., da Silva, A.O., dos Santos, D.M.B., 2013. Low visibility formation and forecasting on the northern coast of Brazil. Pure Appl. Geophys. 170 (4), 689–709. https://doi.org/10.1007/s00024-012-0565-6.

Fernández-González, S., Martín, M.L., Merino, A., Sánchez, J.L., Valero, F., 2017. Uncertainty quantification and predictability of wind speed over the Iberian Peninsula. J. Geophys. Res. Atmos. 122, 3877–3890. https://doi.org/10.1002/2017JD026533.

Fischer, C., Montmerle, T., Berre, L., Auger, L., Stefanescu, S.E., 2005. An overview of the variational assimilation in the ALADIN/France numerical weather-prediction system. Q. J. R. Meteorol. Soc. 613, 3477–3492. https://doi.org/10.1256/qj.05.115.

Guijo-Rubio, D., Gutiérrez, P.A., Casanova-Mateo, C., Sanz-Justo, J., Salcedo-Sanz, S., Hervás-Martínez, C., 2018. Prediction of low-visibility events due to fog using ordinal classification. Atmos. Res. 214, 64–73. https://doi.org/10.1016/j.atmosres.2018.07.017.

Gultepe, I., Tardif, R., Michaelides, S.C., Cermak, J., Bott, A., Bendix, J., Müller, M.D., Pagowski, M., Hansen, B., Ellrod, G., Jacobs, W., Toth, G., Cober, S.G., 2007. Fog research: a review of past achievements and future perspectives. Pure Appl. Geophys. 164 (6–7), 1121–1159. https://doi.org/10.1007/s00024-007-0211-x.

Masson, V., 2016. The Externalized Surface User's Guide v7.3; Tech. Report; Meteo France: Toulouse, France. Available online. http://www.umr-cnrm.fr/surfex/spip.php?rubrique10 (accessed on 4 December 2018).

Janjic, Z.A., 1990. The step-mountain coordinate: physics package. Mon. Weather Rev. 118, 1429–1443.

Johnson, A., Wang, X., 2012. Verification and calibration of neighborhood and object-based probabilistic precipitation forecasts from a multimodel convection-allowing ensemble. Mon. Wea. Rev. 140, 3054–3077. https://doi.org/10.1175/MWR-D-11-00356.1.

Karlsson, K.G., Dybbroe, A., 2010. Evaluation of Arctic cloud products from the EUMETSAT Climate Monitoring Satellite Application Facility based on CALIPSO-CALIOP observations. Atmos. Chem. Phys. Discuss. 9, 16755–16810. https://doi.org/10.5194/acp-10-1789-2010.

Karlsson, K.G., Johansson, E., 2013. On the optimal method for evaluating cloud products from passive satellite imagery using CALIPSO-CALIOP data: example investigating the CM SAF CLARA-A1 dataset. Atmos Meas. Tech. 6, 1271–1286. https://doi.org/10.5194/amt-6-1271-2013.

Kunkel, B.A., 1984. Parameterization of droplet terminal velocity and extinction coefficient in fog models. J. Clim. Appl. Meteorol. 23, 34–41. https://doi.org/10.1175/1520-0450(1984)023<0034:PODTVA>2.0.CO;2.

Lenderink, G., Holtslag, A., 2004. An updated length-scale formulation for turbulent mixing in clear and cloudy boundary layers. Q. J. R. Meteorol. Soc. 130, 3405–3427. https://doi.org/10.1256/qj.03.117.

López, L., García-Ortega, E., Sánchez, J.L., 2007. A short-term forecast model for hail. Atmos. Res. 83, 176–184. https://doi.org/10.1016/j.atmosres.2005.10.014.

Masson, V., Le Moigne, P., Martin, E., Faroux, S., Alias, A., Alkama, R., Belamari, S., Barbu, A., Boone, A., Bouyssel, F., et al., 2013. The SURFEXv7. 2 land and ocean surface platform for coupled or offline simulation of earth surface variables and fluxes. Geosci. Model Dev. 6, 929–960. https://doi.org/10.5194/gmd-6-929-2013.

Nielsen, K.P., Gleeson, E., 2018. Using Shortwave Radiation to Evaluate the HARMONIE-AROME Weather Model. Atmosphere 9 (163), 1–16. https://doi.org/10.3390/atmos9050163.

Nielsen, K.P., Gleeson, E., Rontu, L., 2014. Radiation sensitivity tests of the HARMONIE 37h1 NWP model. Geosci. Model Dev. 7, 1433–1449. https://doi.org/10.5194/gmd-7-1433-2014.

Nilo, S.T., Romano, F., Cermak, J., Cimini, D., Ricciardelli, E., Cersosimo, A., Di Paola, F., Gallucci, D., Gentile, S., Geraldi, E., Larosa, S., Ripepi, E., Viggiano, M., 2018. Fog detection based on Meteosat Second Generation-Spinning enhanced visible and infrared imager high resolution visible channel. Remote Sens. 10 (4), 541. https://doi.org/10.3390/rs10040541.

Pagowski, M., Gultepe, I., King, P., 2004. Analysis and modeling of an extremely dense fog event in southern Ontario. J. Appl. Meteorol. 43 (1), 3–16. https://doi.org/10.1175/1520-0450(2004)043<0003:AAMOAE>2.0.CO;2.

Payra, S., Mohan, M., 2014. Multirule based diagnostic approach for the fog predictions using WRF modelling tool. Adv. Meteorol. 2014, 456065. https://doi.org/10.1155/2014/456065.

Petersen, C., Nielsen, N.W., 2000. Diagnosis of visibility in DMI-HIRLAM. In: DMI Scientific Report 00-11, pp 37. DMI, Copenhagen, Denmark Available from.

Rípodas, P., Legleau, H., Kerdraon, G., Moisselin, J.M., Autones, F., García Pereda, J., Martínez, M.A., Marcos, C., Jann, A., Wirth, A., Calbet, X., Alonso, O., Ariza, C., 2016. NWC SAF GEO v2016. New products, changes and improvements. Proceedings for the 2016 EUMETSAT Meteorological Satellite Conference, Darmstadt, Germany.

da Rocha, R.P., Gonçalves, F.L., Segalin, B., 2015. Fog events and local atmospheric features simulated by regional climate model for the metropolitan area of São Paulo. Brazil. Atmos. Res. 151, 176–188. https://doi.org/10.1016/j.atmosres.2014.06.010.

Saha, S., et al., 2010. The NCEP climate Forecast System Reanalysis. Bull. Amer. Meteor. Soc. 91, 1015–1057. https://doi.org/10.1175/2010BAMS3001.1.

Sánchez Arriola, J., Lindskog, M., Thorsteinsson, S., Bojarova, J., 2016. Variational bias correction of GNSS ZTD in the HARMONIE modeling system. J. Appl. Meteorol. Climatol. 55 (5), 1259–1276. https://doi.org/10.1175/JAMC-D-15-0137.1.

Seity, Y., Brousseau, P., Malardel, S., Hello, G., Benard, P., Bouttier, F., Lac, C., Masson, V., 2011. The AROME France convective-scale operational model. Mon. Wea. Rev. 139, 976–991. https://doi.org/10.1175/2010MWR3425.1.

Skamarock, W.C., Klemp, J.B., 2008. A time-split nonhydrostatic atmospheric model for weather research and forecasting applications. J. Comput. Phys. 227, 3465–3485. https://doi.org/10.1016/j.jcp.2007.01.037.

Stensrud, D., Bao, J.-W., Warner, T., 2000. Using initial condition and model physics perturbations in short-range ensemble simulations of mesoscale convective systems. Mon. Weather Rev. 128, 2077–2107. https://doi.org/10.1175/1520-0493(2000)128<2077:UICAMP>2.0.CO;2.

Stoelinga, M.T., Warner, T.T., 1999. Nonhydrostatic, mesobeta-scale model simulations of cloud ceiling and visibility for an East Coast winter precipitation event. J. Appl. Meteorol. 38, 385–404.

Stolaki, S., Pytharoulis, I., Karacostas, T., 2012. A study of fog characteristics using a coupled WRF-COBEL model over Thessaloniki Airport, Greece. Pure Appl. Geophys. 169 (5–6), 961–981. https://doi.org/10.1007/s00024-011-0393-0.

Thompson, G., Field, P.R., Rasmussen, R.M., Hall, W.D., 2008. Explicit forecasts of winter precipitation using an improved bulk microphysics scheme. Part II: Implementation of a new snow parameterization. Mon. Wea. Rev. 136, 5095–5115. https://doi.org/10.1175/2008MWR2387.1.

WMO, 2011. Manual on Codes, International Codes. Technical Report. World Meteorological Organization.

6.3. Deep Convective Precipitation

Bolgiani, P., Fernández-González, S., Valero, F., Merino, A., García-Ortega, E., Sánchez, J., & Martín, M. (2018). **Numerical Simulation of a Heavy Precipitation Event in the Vicinity of Madrid-Barajas International Airport: Sensitivity to Initial Conditions, Domain Resolution, and Microphysics Parameterizations**. *Atmosphere*, *9*(9), 329.

The following article was published in August 2018 in the Atmosphere journal. The journal is ranked 45th in the Meteorology & Atmospheric Sciences category as per the Web of Science Group 2018 Journal Citation Report. The reported Journal Impact Factor is 2.046.

atmosphere

MDPI

Article

Numerical Simulation of a Heavy Precipitation Event in the Vicinity of Madrid-Barajas International Airport: Sensitivity to Initial Conditions, Domain Resolution, and Microphysics Parameterizations

Pedro Bolgiani [1], Sergio Fernández-González [2], Francisco Valero [1,3], Andrés Merino [4], Eduardo García-Ortega [4,*], José Luis Sánchez [4] and María Luisa Martín [3,5]

1 Department of Earth Physics, Astronomy and Astrophysics II, Faculty of Physics, Complutense University of Madrid, 28040 Madrid, Spain; pbolgiani@gmail.com (P.B.); valero@ucm.es (F.V.)
2 State Meteorological Agency (AEMET), 28040 Madrid, Spain; sfernandezg@aemet.es
3 Institute of Applied Mathematics, Complutense University of Madrid; 28040 Madrid, Spain; mlmartin@eii.uva.es
4 Atmospheric Physics Group, IMA, University of León, 24071 León, Spain; amers@unileon.es (A.M.); jl.sanchez@unileon.es (J.L.S.)
5 Department of Applied Mathematics, Faculty of Computer Engineering, University of Valladolid, 47002 Valladolid, Spain
* Correspondence: eduardo.garcia@unileon.es; Tel.: +34-987-293-192

Received: 2 July 2018; Accepted: 18 August 2018; Published: 22 August 2018

Abstract: Deep convection is a threat to many human activities, with a great impact on aviation safety. On 7 July 2017, a widespread torrential precipitation event (associated with a cut-off low at mid-levels) was registered in the vicinity of Madrid, causing serious flight disruptions. During this type of episode, accurate short-term forecasts are key to minimizing risks to aviation. The aim of this research is to improve early warning systems by obtaining the best WRF model setup. In this paper, the aforementioned event was simulated. Various model configurations were produced using four different physics parameterizations, 3-km and 1-km domain resolutions, and 0.25° and 1° initial condition resolutions. Simulations were validated using data from 17 rain gauge stations. Two validation indices are proposed, accounting for the temporal behaviour of the model. Results show significant differences between microphysics parameterizations. Validation of domain resolution shows that improvement from 3 to 1 km is negligible. Interestingly, the 0.25° resolution for initial conditions produced poor results compared with 1°. This may be linked to a timing error, because precipitation was simulated further east than observed. The use of ensembles generated by combining different WRF model configurations produced reliable precipitation estimates.

Keywords: deep convection; heavy precipitation; WRF model; validation; parameterization schemes; domain resolution

1. Introduction

Heavy precipitation poses a significant risk to human activities in several parts of the world [1]. Meteorological phenomena related to deep convection cause thousands of casualties and huge economic losses worldwide every year [2]. The main risks associated with this type of atmospheric phenomena are heavy precipitation, gale-force wind gusts, hail, and lightning [3,4]. In particular, the Iberian Peninsula is a region favourable for the development of deep convection systems during the warm season [5]. Some heavy precipitation events of the Iberian Peninsula have been analysed because of their associated hazards and risks [6].

Early warning systems may decrease the damage caused by deep convection, and are mainly based on an accurate weather forecast [7]. Nevertheless, the forecasting of heavy precipitation episodes is still a challenge for numerical weather prediction models [8]. The reason is linked to the fact that these events are strongly affected by mesoscale processes (such as convection and radiation) that must be parameterized by numerical models [9]. These parameterizations are case-dependent, so it is convenient to consider the use of an ensemble composed of different physical parameterizations [10].

When evaluating model performance, precipitation is an interesting field because it is unlikely to easily achieve accurate verification [11]. Risky situations caused by heavy precipitation are not only related to large amounts of accumulated precipitation (that can be obtained by persistent precipitation over long periods) but also to strong precipitation intensities over a few hours [12]. Therefore, different validation methods must be used to evaluate both accumulated precipitation and the temporal evolution of precipitation rate. Both mean absolute error (MAE) and root mean square error (RMSE) are adequate for testing the accumulated precipitation estimated by a numerical weather prediction model, by comparing it to precipitation measured in a region during a specific period [13]. Nevertheless, these validation indices do not provide information about the accuracy of the temporal evolution of precipitation. As a result, good verification scores can be obtained in spite of modelled precipitation being forecast in a different time interval than the observed precipitation. In this regard, the Pearson's correlation coefficient is commonly used for the evaluation of the similarity of precipitation temporal evolution between forecast and observed precipitation time series [14]. However, strong correlation can be obtained when modelled and observed precipitation maxima are acquired at the same time, despite their magnitudes (and consequently accumulated precipitation) being very distinct. Therefore, it seems most appropriate to evaluate both total accumulated precipitation and temporal evolution of the precipitation rate together, using indices that integrate both types of validation.

This paper analyses a deep convection episode at the centre of the Iberian Peninsula on 7 July 2017, causing widespread heavy precipitation. This event was linked to a cut-off low at mid-levels over the southwestern part of that peninsula. This low was originated by an extratropical cyclone in the North Atlantic that was isolated from the general circulation of the atmosphere (characterized by westerlies at those latitudes), forming a closed cyclonically circulating eddy in the middle and upper troposphere, where the air is colder than the surroundings. In addition, warm temperatures on the surface and at low levels of the troposphere caused strong instability, generating ideal conditions for the development of deep convection. As a result, dozens of flights were diverted or cancelled at the Adolfo Suárez Madrid-Barajas International Airport (LEMD hereafter, per the airport's International Civil Aviation Organization code). In addition, there were dramatic traffic jams on the main highways of Madrid.

With the aim of improving the forecast of future heavy precipitation episodes, the aforementioned event was simulated by the weather research and forecasting (WRF) model. Several initial conditions, model resolutions, and physics parameterizations were tested to discover which setup was optimal for forecasting this type of episode in the study area. Accumulated precipitation was not only analysed, but also the temporal evolution and geographic distribution of precipitation, by comparing the precipitation rate estimated by the model and observed values from multiple weather stations within the study area. Thus, two validation indices are proposed, which take into account both accumulated precipitation and its temporal evolution.

The paper is organized as follows. The experimental design is detailed in Section 2, including a description of the study area, the model setup, and information about observational data. Section 3 explains the main results of this investigation, followed by Section 4, in which results and an integrating discussion are presented.

2. Experiment

2.1. Area of Study

This work focused on the area close to LEMD. The airport is near the centre of the Iberian Peninsula, a few kilometres northeast of the city of Madrid at an elevation of 609 m above sea level (m.a.s.l.). The main orographic feature in the surrounding area is the Guadarrama mountain range (within the Central System), which runs in a southwest-northeast direction approximately 50 km northwest of the airport, with elevations higher than 2300 m.a.s.l. (Figure 1b). To the southeast of this range, a small plateau extends up to the Tajo Valley, which runs from east to west approximately 50 km south of the airport, with elevations lower than 500 m.a.s.l. The climatology of the airport in July is marked by two predominant wind directions, north and southwest, both with similar frequencies, but the southwesterlies are more intense [15]. Owing to the terrain configuration, orographic blocking protects the area from precipitation during northerly winds, but enhances precipitation during southerly winds. The mean maximum temperature in July is 33.5 °C, and the mean minimum is 16.8 °C. Mean monthly precipitation is 9 mm for the month [15]. On the day of the event, 44.7 mm was measured at the airport.

The LEMD is the busiest airport in Spain, with more than daily 1000 operations (take-offs and landings). It is one of the major gateways of air traffic into Europe and ranks among the 50 busiest airports in the world. With regard to aviation safety, heavy precipitation events generate reduced visibility, contaminated runways, reduced braking action, and reduced aerodynamic performance of aircraft. Sudden and strong precipitation can result in substantial disruption of airport operation, affecting arriving and departing aircraft many hours after the precipitation has disappeared.

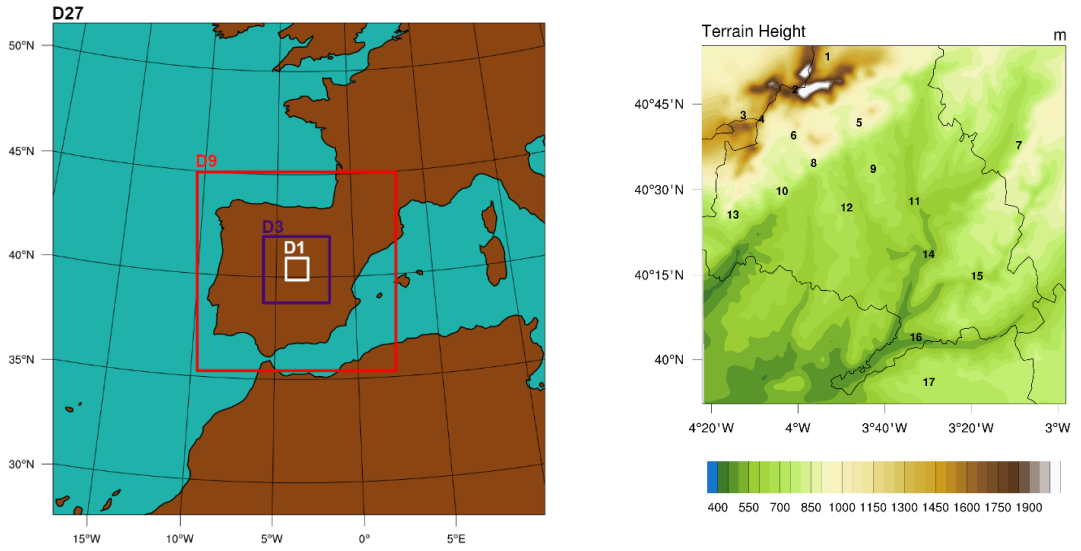

Figure 1. (**a**) Nested domains used in WRF simulations with 1° × 1° initial conditions' grid resolution. Outer frame corresponds to domain D27. Only D9, D3, and D1 were used for simulations with 0.25° × 0.25° initial conditions' grid resolution. (**b**) D1 with terrain elevation metres above sea level (m.a.s.l.), location, and assigned number of observation data stations. Station #11 corresponds to the Adolfo Suárez Madrid-Barajas International Airport (LEMD).

2.2. Model Configuration

The experiment consisted of several numerical simulations of the studied event and their validation against observational data. The simulations were performed with the advanced research WRF model version 3.7.1. This is a non-hydrostatic model with several parameterization options, which

has been extensively proven and validated for weather prediction and research [16]. All simulations were conducted from 00:00 to 24:00 UTC, 7 July 2017. Initial and boundary conditions were taken from the Global Forecast System (GFS) reanalysis developed by the National Centers for Environmental Prediction (NCEP). It was decided to use this database because of free access. Grid resolutions $1^\circ \times 1^\circ$ and $0.25^\circ \times 0.25^\circ$ were used (GFS1 and GFS025 hereafter), providing data at 6 and 3 h intervals, respectively. For GFS1, WRF was configured in 4 domains, 120×120 grid points each, with 27, 9, 3, and 1 km grid resolutions (D27, D9, D3, and D1 hereafter). All domains were approximately centred on LEMD (Figure 1a). Only D9, D3, and D1 were used for GFS025. This time and domain configuration was chosen to allow for spin-up time (validation began at 10:00 UTC) but minimizing lead time to the event, and to use relatively small outer domains. Both conditions have been proven to perform better statistically with long lead times and large outer domains [17].

A two-way nesting strategy was chosen. Sixty sigma levels were defined with a progressive resolution, greater in the lower levels of the troposphere. All other parameters not mentioned were identical for every simulation.

Model results were produced every hour for D3 and every 10 min for D1. For standardization and validation comparison, only hourly results were considered for D1. For grid point data, the closest grid point to the geographic location was used for D3. For D1 results, an average value was determined from data in a 3×3 grid from the nearest grid point. Thus, the validated areas in D1 and D3 are equivalent and the results of validation are comparable.

2.3. Physics Parameterizations

The simulated precipitation during deep convection episodes depends mainly on microphysics schemes used in the model [8,17,18]. In this experiment, we assessed the sensitivity of the model to three microphysics parameterizations:

1. Thompson scheme [19]: This is a single-moment scheme but adds a double moment (mass of hydrometeors and number concentration are independently predicted) for rain and cloud ice. It determines the hydrometeor mixing ratio and the number concentration for rain and cloud ice. Snow size was controlled by ice water content and temperature. Snow shape was non-spherical and density varied inversely with diameter. It considered six types of hydrometeors: water vapour, cloud water, rain water, cloud ice, snow, and graupel.
2. Milbrandt–Yau scheme [20,21]: This is a double-moment scheme (although it allows up to three moments). Mixing ratio and number concentration was predicted for cloud and hydrometeors. Radar reflectivity as predicted for some hydrometeors. It considered seven types of hydrometeors: water vapour, cloud water, rain water, cloud ice, snow, graupel, and hail.
3. Morrison scheme [22]: This is a double-moment scheme that includes predicted mixing ratios and number concentrations for cloud water, cloud ice, rain, and snow. It also includes a predicted rain size distribution and different rates of rain evaporation for convective and stratiform clouds. It considered six types of hydrometeors: water vapour, cloud water, rainwater, cloud ice, snow, and graupel.

For these three microphysics schemes, the same physics parameterizations are used: New Goddard as long and short wave radiation schemes [23], Unified Noah as the surface scheme [24], Eta Similarity as the clay scheme [25], and Mellor–Yamada–Janjic (MYJ) as planetary boundary layer (PBL) scheme [25]. Cumulus were explicitly computed for D3 and D1. All were chosen according to studies that already validated these parameters for similar precipitation events over Spain [8].

In addition to microphysics, precipitation can be also affected by radiation (both long and short wave), surface, and PBL parameterizations [8,25]. Therefore, in other simulations, the Thompson microphysics scheme was combined with a different set of physics parameterizations, so sensitivity to other than microphysics could be evaluated: Dudhia as long and short wave radiation schemes [26], the Rapid Update Cycle (RUC) as surface scheme [27], and Mellor-Yamada-Nakanishi-Niino (MYNN)

scheme as clay and PBL schemes [28]. This combination has been validated for snowfall events over the Iberian Peninsula [29] and tested in the vicinity of LEMD [30]. Table 1 shows the names given to every physics combination.

This made two sets (GFS1 and GFS025) of four physics simulations, composing eight deterministic simulations. Also, several ensembles were created for evaluation, i.e., two ensembles combining all microphysics schemes for each GFS resolution configuration (physics ensembles), and one ensemble combining all microphysics schemes and both GFS resolutions (initial conditions ensemble). Five additional ensembles were defined by combining both GFS resolutions and several (but not all) parameterizations. Four of these ensembles were obtained by combining three of the physics schemes but excluding one each time. The fifth ensemble was composed by the simulations that included the Milbrandt–Yau and Morrison microphysics schemes. Table 2 shows all the physics scheme combinations. For each model configuration and ensemble (16 different ones), 3 and 1 km domains were assessed, resulting in a total of 32 datasets.

Table 1. Physics combinations used for deterministic simulations.

Name	Microphysics	Radiation Long & Short Wave	Surface	Surface Clay	PBL
D	Thompson	Dudhia	RUC [1]	MYNN [2]	MYNN
T	Thompson	New Goddard	Unified Noah	Eta Similarity	MYJ [3]
Y	Milbrandt–Yau	New Goddard	Unified Noah	Eta Similarity	MYJ [3]
M	Morrison	New Goddard	Unified Noah	Eta Similarity	MYJ [3]

[1] Rapid Update Cycle; [2] Mellor-Yamada-Nakanishi-Niino; [3] Mellor–Yamada–Janjic.

Table 2. Model ensemble combinations [1].

	Physics Ensemble	Initial Conditions Ensemble	Additional Ensembles				
GFS025	DTYM	DTYM	TYM	DYM	DTM	DTY	YM
GFS1	DTYM						

[1] Ensemble names are given by the adding of names assigned in Table 1 to each physics combinations used in the ensemble.

2.4. Observational Data

Each simulated dataset was evaluated against observed precipitation. The observed precipitation data were taken from 17 rain gauge stations in the region of Madrid, which are certified by the Spanish State Meteorological Agency (Agencia Estatal de Meteorología, AEMET). Only stations inside D1 were selected. Data were recorded every 10 minutes, but aggregated to hourly data for compatibility with model data. Figure 1b shows the location and number assigned to each station (numbered from north to south). Table 3 shows the measured precipitation between 10:00 and 22:00 UTC, 7 July 2017; there was no precipitation registered outside these hours on that day. At 9 of 17 stations, more than 90% of the accumulated precipitation was registered between 12:00 and 16:00 UTC. The 17 stations recorded more than 90% of the daily precipitation during 10:00 to 18:00 UTC. Therefore, this period was selected for validation.

Table 3. Observed precipitation (mm) by hour and total accumulated for 7 July 2017 at stations in study area.

Station Number	Hour UTC												10:00–18:00 Accumulated
	10–11	11–12	12–13	13–14	14–15	15–16	16–17	17–18	18–19	19–20	20–21	21–22	
1	0	0	0	10.6	7.2	4.2	5.2	0.4	0.2	0	0	0	27.6
2	0	2.6	2.2	13.4	20.0	0.8	0.4	0.4	0	0.2	0	0.2	39.8
3	0	1.6	13.0	11.6	5.2	0.8	0.2	0	0	0	0	0	32.4
4	0.2	1.4	6.3	17.4	12.6	0.3	0	0	0	0	0	0	38.2
5	0	0	0.3	14.0	3.7	5.7	4.8	0	0	0	0	0	28.5
6	0	1.0	1.4	15.0	18.8	3.0	0	0	0	0	0	0	39.2
7	0	0.2	0	0	2.2	0.2	7.2	12.4	1.6	0	0	0	22.2
8	0.1	1.2	1.7	11.0	5.5	0.6	0.1	0	0	0	0	0	20.2
9	0	0	0.2	21.2	7.0	8.0	2.8	0.2	0	0	0.2	0	39.4
10	0.2	4.4	7.2	8.6	1.2	0	0	0	0.2	0	0	0	21.6
11	0	0	0	16.6	9.7	13.0	5.4	0	0	0	0	0	44.7
12	0	0.2	7.2	3.0	0.6	4.4	0.2	0.2	0	0	0	0	15.8
13	0.3	16.4	10.9	1.0	0.2	0.3	0	0	0	0	0	0	29.1
14	0	0	0	5.6	14.8	10.4	4.6	0	0	0	0	0.2	35.4
15	0	0	0	0	1.0	0.2	3.8	1.0	0	0	0	0	06.0
16	0	0	0	4.7	13.8	0.6	0.2	0	0	0	0	0	19.3
17	0	0	0	7.8	7.4	0.2	0	0	0.2	0	0	0	15.4

Also, images from the Madrid radar station (certified by AEMET) were used for spatial evaluation of the accumulated precipitation estimated by the WRF simulations. Raw images every 10 min at the lowest elevation of the radar scan (0.5° above the horizontal plane) were analysed and a composite image produced for assessment of total accumulated precipitation.

2.5. Validation Indices

Attending to the spin-up time and observed precipitation times, the event was evaluated between 10:00 and 18:00 UTC. To evaluate the performance for total accumulated precipitation for every model setup, the following validation indices were used.

$$Bias = \sum_{i=1}^{n} (M_i - O_i) \tag{1}$$

$$MAE = \frac{1}{n} \sum_{i=1}^{n} |M_i - O_i| \tag{2}$$

$$RMSE = \sqrt{\frac{1}{n} \sum_{i=1}^{n} (M_i - O_i)^2} \tag{3}$$

where M_i is the modelled value, O_i is the observed value, and n is the number of stations used.

The MAE and RMSE are effective tools to evaluate the magnitude of the simulations' error, because each emphasizes different aspects of the error [13]. In this paper, they were divided by the mean accumulated observed precipitation, yielding relative values (hereafter relative MAE (RMAE) and relative RMSE (RRMSE)). In particular, the RRMSE is useful to highlight simulations with large errors, because it penalizes those more than the RMAE. Bias is converted to relative values by dividing it by the total accumulated observed precipitation (hereafter relative bias (RBias)).

Nevertheless, after analysing the initial results with these indices, it was clear that some information was missing. The RBias, RMAE, and RRMSE may be suitable for assessing the total results of the model (they show a snapshot of the accumulated precipitation at the end of the validation period), but they do not provide any information about the performance over time. We believe that during a heavy precipitation event, knowing the precipitation dynamics and pattern is as valuable as its total. This is the reason that the following complementary indices are proposed.

- Pearson's correlation coefficient (r): we used r to evaluate similarity between the temporal evolution of precipitation estimated by the simulations and observed values at each meteorological station.

$$r = \frac{\sum_{i=1}^{n} (M_i - \overline{M})(O_i - \overline{O})}{\sqrt{\sum_{i=1}^{n} (M_i - \overline{M})^2} \sqrt{\sum_{i=1}^{n} (O_i - \overline{O})^2}} \tag{4}$$

- Number of stations with r statistically significant: r values were computed at the 17 stations, but not all were statistically significant. Thus, two different model configurations may have similar r values, but the number of valid stations may vary. This had to be taken into account in the validation, as it may be a differentiating tool when very similar correlations are found. In this paper, we considered results statistically significant using a confidence level of 95% ($\alpha = 0.05$).

Finally, two indices are proposed to complete the information provided by the indices defined previously. These indices are able to integrate in a single value both the evaluation of total accumulated precipitation and its temporal evolution:

- Relative area under error curve (RAEC): This index consists of the time integration of the bias as defined before. The error curve was drawn along the considered time span for validation and the resulting area was computed using numerical integration methods. The total result was divided

by the mean accumulated observed precipitation, $\bar{O}$, and by the time span (eight hours in this case) to get a relative value.

$$RAEC = \frac{1}{(t_e - t_i)\overline{O}} \int_{t_i}^{t_e} Bias(t)\, dt \quad (5)$$

where t_i is the initial time of the event and t_e is the ending time.

- Relative area under absolute error curve (RAAC): This index consists of the time integration of the MAE. The method was the same as for RAEC but using the absolute error. It is also presented in relative values.

$$RAAC = \frac{1}{(t_e - t_i)\overline{O}} \int_{t_i}^{t_e} MAE(t)\, dt \quad (6)$$

Because of the calculation method, RAEC must always be smaller than or equal to RAAC. Thus, if RAAC is close to zero, it means that there is a small total error (both the error related to the accumulated precipitation and that associated with the temporal distribution of precipitation). If RAAC is considerable, then RAEC must be taken into account. Small values of RAEC are not only associated with a perfect forecast but might also be achieved when positive and negative errors compensate over time. In that case, the accumulated precipitation estimated by the model was very similar to the observed one, but its temporal distribution differed. If this compensation did not occur, RAEC would have large absolute values, closer to RAAC. In addition, RAEC values would be positive when the model overestimates the accumulated precipitation over the study period, and negative if the simulation underestimates.

It is important to understand that these indices give information about the persistence of error over time and how the error behaves during the period of the event, but do not yield information about the temporal correlation between the simulated and observed precipitation. Nevertheless, the correlation can be assessed by representing the error and absolute error curves. If they tend to be parallel to zero, the simulation will have a strong correlation with observations. If the error curves tend to converge or diverge from zero, the correlation will be weaker. However, in any case, RAEC and RAAC should be supplementary indices, and they do not replace information provided by *r*, Bias, MAE or any other scoring index.

The ensemble mean precipitation was chosen for validation to evaluate the performance of the distinct ensembles generated by combining different initial and boundary conditions, plus physics parameterizations of the WRF model. However, it is important to state that the rest of the information contained in the probability distribution function of the ensemble should not be rejected when using the model for warning systems during heavy rain episodes.

3. Results

Results were divided into several types of validations to evaluate various aspects of the model. Also, specific results for LEMD are shown.

3.1. Accumulated Precipitation Validation

In the evaluation of deterministic model configuration results, RBias (Table 4) shows that every physics scheme tended to underestimate total accumulated precipitation, except for the Y scheme. In the case of Y, precipitation was underestimated for GFS025, but overestimated when initialized with GFS1. It is notable that the T scheme yielded the worst performance for every GFS and domain combination, underestimating precipitation by as much as 62%. Best RBias results were achieved by the M scheme in the GFS1 configuration. Among the ensemble configurations, only the D1-GFS1-DTYM and D3-GFS1-DTYM physics ensembles outperformed the best deterministic configuration. Also, comparing the different physics ensembles, there was a clear difference between GFS resolutions. The RBias for GFS1 was substantially smaller than the results of GFS025. There was little difference

between domains for the same GFS resolution. These findings were also true for the D, T, and M deterministic configurations. The difference between GFS resolutions became smaller when both were combined for the initial conditions ensemble and additional ensembles. Thus, these model configurations showed very little difference between domains, with D1 slightly poorer than D3.

Considering RMAE, again the M physics scheme initialized with GFS1 achieved the best results, and was not outperformed by any ensemble. The T scheme, although not always the poorest, was always outperformed by some other deterministic configuration. Once again, there was a difference between GFS resolutions, but not between domain resolutions (except for the Y scheme), with GFS1 better than GFS025. For this index, D1 performed slightly better than D3 when the initial conditions ensemble and additional ensembles were evaluated. Regarding, the best results were achieved by the D3-GFS1-DTYM physics ensemble. Moreover, RRMSE values were much larger than RMAE for the T deterministic simulations and those initialized with GFS025. This finding indicates large errors in these simulations, because RRMSE penalizes them much more than RMAE.

It is important to note how poorly the T physics scheme performed. Also, among the additional ensembles, the DYM configuration (i.e., the one excluding T) produced better results than the initial conditions ensemble for both D1 and D3 for every validation index, which is a sign that the T scheme produced the poorest results. There appeared to be a clear advantage for the M scheme, but considering the additional ensembles, the only combination that never improved on the initial condition ensemble's results was the one excluding Y (i.e., the DTM ensemble). Since it was the only microphysical parameterization that did not underestimate the precipitation with GFS1, the ensemble noticeably underestimated the precipitation when not considering the Y parameterization.

Regarding spatial precipitation distributions, total accumulated precipitation maps for deterministic model configurations (Figure 2) confirmed some of the results already mentioned. Considering the domain resolution, almost no difference was seen between D1 and D3 for the same physics scheme and GFS resolution. D3 appeared to produce slightly less precipitation than D1 (some red spots in D1 are smaller than in D3) and generated coarser rain fields, as may be expected because of grid size, but both domains were virtually the same. However, notable differences were observed for GFS resolutions. For the same domain resolution, GFS1 produced heavier precipitation than GFS025 (clearly observable in the D and M schemes). There was also a notable location/timing difference, as GFS025 produced rain fields to the east of GFS1 (clearly observable in the Y and M schemes). This displacement appears to be the main reason for the poorer results of GFS025.

Table 4. Validation for accumulated precipitation, including Relative Bias, Relative Mean Absolute Error and Relative Root Mean Square Error. All 32 model configurations are shown for domain resolution, initial conditions resolution, microphysics parameterization, and ensembles chosen. The best three performers for each index are shaded.

		Deterministic				Physics Ensemble	Initial Conditions Ensemble	Additional Ensembles				
		D	**T**	**Y**	**M**	**DTYM**	**DTYM**	**TYM**	**DYM**	**DTM**	**DTY**	**YM**
RBias												
D1	GFS025	−0.486	−0.621	−0.286	−0.402	−0.449	−0.261	−0.246	−0.181	−0.352	−0.266	−0.118
	GFS1	−0.117	−0.399	0.308	−0.095	−0.076						
D3	GFS025	−0.491	−0.625	−0.277	−0.377	−0.442	−0.254	−0.238	−0.173	−0.346	−0.259	−0.108
	GFS1	−0.121	−0.423	0.291	−0.107	−0.090						
RMAE												
D1	GFS025	0.528	0.644	0.548	0.576	0.518	0.414	0.425	0.387	0.444	0.417	0.393
	GFS1	0.442	0.486	0.546	0.351	0.397						
D3	GFS025	0.535	0.645	0.526	0.597	0.527	0.429	0.430	0.406	0.460	0.426	0.404
	GFS1	0.442	0.500	0.541	0.345	0.393						
RRMSE												
D1	GFS025	0.631	0.782	0.638	0.663	0.633	0.497	0.501	0.455	0.550	0.502	0.456
	GFS1	0.573	0.611	0.687	0.450	0.442						
D3	GFS025	0.648	0.783	0.664	0.672	0.641	0.509	0.511	0.473	0.562	0.515	0.473
	GFS1	0.574	0.623	0.672	0.443	0.438						

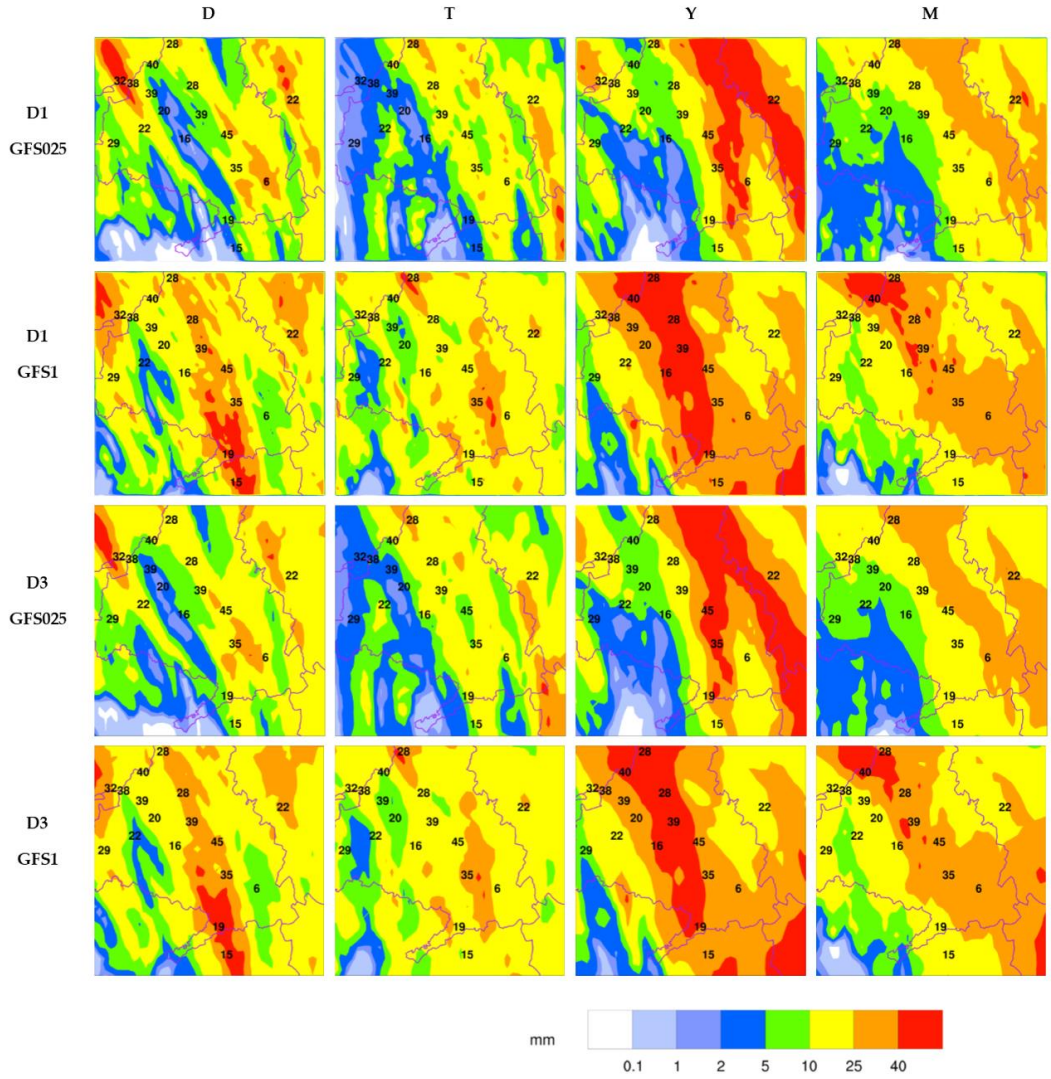

Figure 2. Accumulated precipitation (mm) between 10:00 and 18:00 UTC for GFS025 and GFS1, D1, and D3 deterministic model configurations. Observed accumulated precipitation (mm) for each station is shown at station locations. D3 figures are cropped to match D1.

When the simulated rainfall was compared to the observed accumulated precipitation values at each station (Figure 2), the results were somewhat coincidental with RBias values (Table 4). T underestimated the precipitation. T and M are the schemes that yielded fewer differences in rainfall between resolutions, and many simulations formed a bow-shaped heavy precipitation field (Figure 2). This was aligned in a north–south direction across the centre of the domain, with values dependent on the performance of the physics scheme; this is very evident from the Y scheme (red band). These figures also allow us to put in perspective the validation indices already assessed. The Y scheme always overestimated precipitation. Nevertheless, RBias for Y at the GFS025 resolution was negative (Table 4). Because of the validation indices calculated at the selected stations, the aforementioned displacement of the simulated rain fields radically altered RBias values depending on GFS resolution, with even RMAE and RRMSE very similar for all model configurations in the Y scheme.

Total accumulated precipitation for ensemble model configurations (Figure 3) show similar results for the physics ensembles. For both D1 and D3, precipitation was simulated to the east and in lesser quantities for GFS025-DTYM than for GFS1-DTYM, producing a poorer validation of GFS025 configurations. No large differences were seen between domains for the same GFS resolution, but a coarser structure. When the initial conditions ensemble and additional ensembles merge the two GFS

resolutions, the rain field location difference disappears, but the error in precipitation accumulation is reflected in the domains. D3 showed heavier precipitation than D1 for the same model configuration. This proves that, although negligible, there were small differences between domains, which can also be observed in the validation indices (Table 4). Because of the heavy precipitation simulated by the Y physics scheme (Figure 2), the model ensembles using it tended to reproduce a sharper bow pattern across the study area. A heavy precipitation core was consistently over the northern and central study area, whereas the southwestern corner showed little to no precipitation. The rest of the domain shows variable precipitation amounts but similar patterns, almost always displaying the bow shape seen in the deterministic configurations.

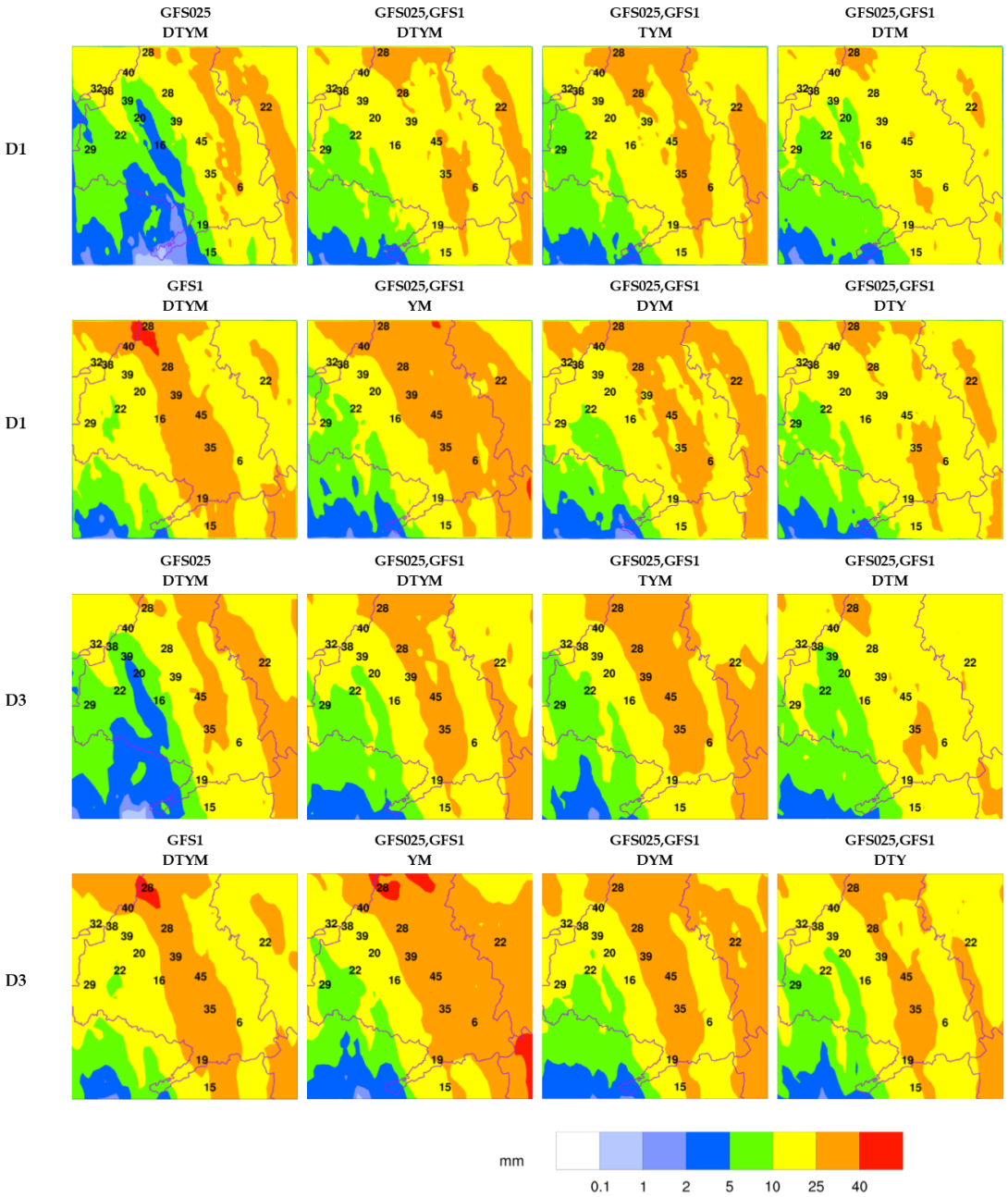

Figure 3. Accumulated precipitation (mm) between 10:00 and 18:00 UTC for ensemble model configurations. Observed accumulated precipitation (mm) for each station is shown at station locations. D3 figures are cropped to match D1.

3.2. Validation of Temporal Evolution

The validation of *r* and number of statistically significant stations for the deterministic model configurations provided conclusive results (Table 5). The M scheme outperformed every other scheme. Even when compared with the ensemble configurations, the D3-GFS1-M and D1-GFS1-M achieved the best results for both *r* and number of statistically significant stations. Once again, GFS1 gave better results than GFS025 and there was little difference between D1 and D3. When initial conditions and additional ensembles were evaluated, the differences between domains were larger. Every *r* value was statistically significant and ensembles tended to perform better than deterministic configurations, clearly influenced by the M physics scheme. This was evident when the DTY ensemble results were compared to every other additional ensemble. Also, when the T scheme was removed (i.e., the DYM additional ensemble), results improved.

Considering the number of statistically significant stations (Table 5), similar results were obtained. Again, the M scheme produced the best results (up to 14 of the 17 stations with satisfactory results), and was not improved by any other deterministic configuration. Only some ensembles yielded better values than the GFS025-M configurations, but not better than GFS1-M configurations. The value of *r* index can be seen with the D1-GFS025-DTYM and D1-GFS1-DTYM physics ensembles. The produced *r* values were very similar, but GFS025 had 13 valid stations while GFS1 had only 11. Although the time correlation was slightly less, a model configuration with 13 valid stations was more robust and spatially consistent than one with 11 statistically significant stations out of 17. Similar results were obtained by ensembles D1-DTYM, D1-DYM, and D3-DTM, but never improving on the results of the deterministic D1-GFS1-M and D3-GFS1-M configurations.

Table 5. Temporal validation: *r* and number of statistically significant stations. All 32 model configurations are shown for domain resolution, GFS resolution, microphysics parameterizations, and various ensembles chosen. All *r* values are statistically significant. Best three performers for each index are shaded.

		Deterministic				Physics Ensemble	Initial Conditions Ensemble	Additional Ensembles				
		D	**T**	**Y**	**M**	**DTYM**	**DTYM**	**TYM**	**DYM**	**DTM**	**DTY**	**YM**
						r						
D1	GFS025	0.465	0.340	0.430	0.533	0.541	0.592	0.598	0.616	0.565	0.544	0.632
	GFS1	0.269	0.386	0.501	0.645	0.554						
D3	GFS025	0.444	0.328	0.299	0.498	0.462	0.554	0.541	0.581	0.552	0.500	0.570
	GFS1	0.265	0.400	0.513	0.652	0.562						
		Number of statistically significant stations										
D1	GFS025	11	9	8	12	13	13	11	13	12	11	12
	GFS1	6	8	10	14	11						
D3	GFS025	11	9	4	12	11	11	10	11	13	9	11
	GFS1	6	8	10	14	11						

3.3. Integrated Validation

Evaluating the integrated indices RAEC and RAAC (Table 6), results were in accordance with the previous indices. The RAEC correlates well with RBias results (Table 4), and almost all RBias conclusions can be assumed. Best deterministic results were achieved by the D1-GFS1-M configuration, only outperformed by the physics ensemble initialized with GFS1. There was no significant difference between domain resolutions, but when initial conditions were evaluated, GFS1 performed better than GFS025. Nevertheless, some considerations must be made. It is remarkable that the D physics scheme overestimated precipitation when initialized with GFS1. This is contradictory to the RBias results for the same model configuration (Table 4), but it is the outcome of RAEC accounting for the entire

validation period and not only for the results at its end. Also, when initial conditions and additional ensembles were considered, differences became smaller than those shown by RBias (Table 4).

The RAAC correlated well with RMAE results (Table 4), and once again almost all RMAE conclusions can be assumed as valid, with the M scheme initialized by GFS1 the best performer. The only remarkable difference with RMAE results was found for the D scheme. This physics scheme achieved better RMAE results with GFS1 initial conditions (Table 4), but RAAC gave a better outcome for GFS025. As was stated for RAEC, this was the product of evaluating the complete period of the simulation.

Overall, the best results were generated by the D1-GFS1-M deterministic configuration, which had the smallest error (RAAC) and was very well compensated (RAEC very close to 0). Although some ensemble configurations can improve RAEC, their RAACs were larger than the best deterministic configuration.

Table 6. Integrated validation: RAEC and RAAC. All 32 model configurations are shown for domain resolution, GFS resolution, microphysics parameterizations, and various ensembles chosen. Best three performers for each index are shaded.

		Deterministic				Physics Ensemble	Initial Conditions Ensemble	Additional Ensembles				
		D	**T**	**Y**	**M**	**DTYM**	**DTYM**	**TYM**	**DYM**	**DTM**	**DTY**	**YM**
RAEC												
D1	GFS025	−0.220	−0.307	−0.140	−0.208	−0.219	−0.113	−0.121	−0.073	−0.150	−0.108	−0.065
	GFS1	0.053	−0.169	0.136	−0.042	−0.006						
D3	GFS025	−0.229	−0.313	−0.154	−0.195	−0.233	−0.114	−0.122	−0.074	−0.150	−0.111	−0.065
	GFS1	0.050	−0.183	0.129	−0.050	−0.013						
RAAC												
D1	GFS025	0.279	0.354	0.345	0.325	0.298	0.254	0.259	0.242	0.260	0.261	0.243
	GFS1	0.310	0.299	0.319	0.208	0.252						
D3	GFS025	0.287	0.355	0.293	0.337	0.302	0.260	0.263	0.250	0.270	0.264	0.247
	GFS1	0.310	0.305	0.317	0.210	0.249						

3.4. Spatial Assessment of Validation

For the spatial assessment of precipitation, three model configurations were selected, considering the overall best performers per the indices already presented. These are the deterministic D1-GFS1-M, physics ensemble D1-GFS1-DTYM, and additional ensemble D1-DYM. Upon initial analysis it was seen that the rainfall simulated by the selected configurations are similar (Figure 4), with three main features already mentioned. Those were a heavy precipitation bow-shaped band across the domain, a very heavy precipitation core to the north of the domain (not seen in the D1-DYM ensemble), and a light or zero precipitation area to the southwest. The largest differences between configurations were in the very heavy precipitation core and east of the domain, where the intensity of precipitation varied and even the bow-shaped band was duplicated by the D1-DYM ensemble.

Upon comparing the accumulated precipitation simulated values with observed values at the stations (Figure 4), it was evident that there were notable differences in RAEC and RAAC results for the same station, even when the station was within the same precipitation range (same colour in the rainfall image) for every selected configuration. This was a feature of the sensitivity of these indices. Evaluating RAEC results for a spatial assessment of precipitation, the most remarkable aspect was that every station near the mountains and west of the bow-shaped band (orange) tended to underestimate precipitation, whereas stations under or west of that band tended to overestimate (with two or three exceptions). Considering the RAAC results, it was seen that the area where stations tended to underestimate was also one with major error values. Also, the stations under the very heavy precipitation core have smaller RAAC values than those underestimated near the western part of the mountain range. This large underestimation error in the vicinity of the Guadarrama mountain

range was possibly linked to an underestimation of the orographic enhancement of precipitation during this episode by the WRF model. The performance at station #11 was also remarkable, where the largest amount of precipitation of the event was observed. Here, the model underestimated with every selected configuration, even though we have seen that stations under the heavy precipitation bow-shaped band tended to overestimate. This location corresponds to LEMD and was analysed in the next section. Comparing RAEC and RAAC results, most of the stations did not compensate errors (the RAEC absolute value is similar to RAAC instead of near zero). This means that the errors at these stations were persistent over the period of validation, and the underestimation or overestimation of precipitation continued over time.

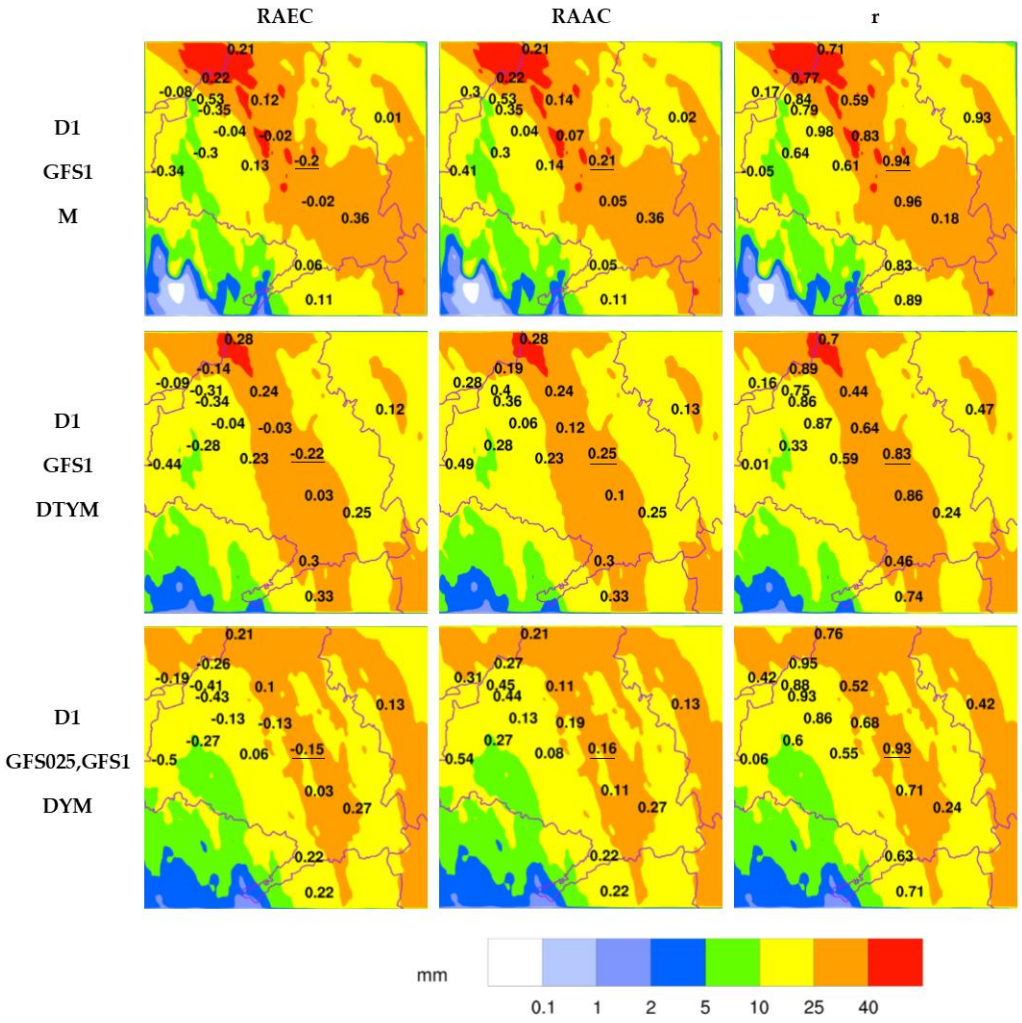

Figure 4. Accumulated precipitation (mm) between 10:00 and 18:00 UTC for the best performing model configurations. RAAC, RAEC and *r* values for each station are shown at station locations.

Concerning *r* values, there was good performance by the selected configurations. Most of the stations' results were well above 0.5, with the deterministic D1-GFS1-M the best performer. Also, from *r* results, there was a consideration that can be extended to a complete spatial assessment. That is, owing to the nature of the event, a thorough interpretation of the data among the geographic domains must be performed, even on an individual station basis, for an integral validation of a model.

Not as an objective validation tool, but for comparison purposes, the radar reflectivity images were compared to the model simulations (Figure 5). The radar images show a convective system in a bow shape, entering the study area at ~10:00 UTC. It moved across the domain from southwest to

northeast. At 14:00 UTC, the system reached the centre of the domain, over the city of Madrid, and remained there after 16:00 UTC. The persistence of rainfall in this area was estimated very accurately by most of the simulations, as shown by the bow shape of maximum accumulated precipitation (coloured in orange), which was repeatedly noted by Figures 2 and 3. At 18:00 UTC, the system was well east of D1 and exiting the domain.

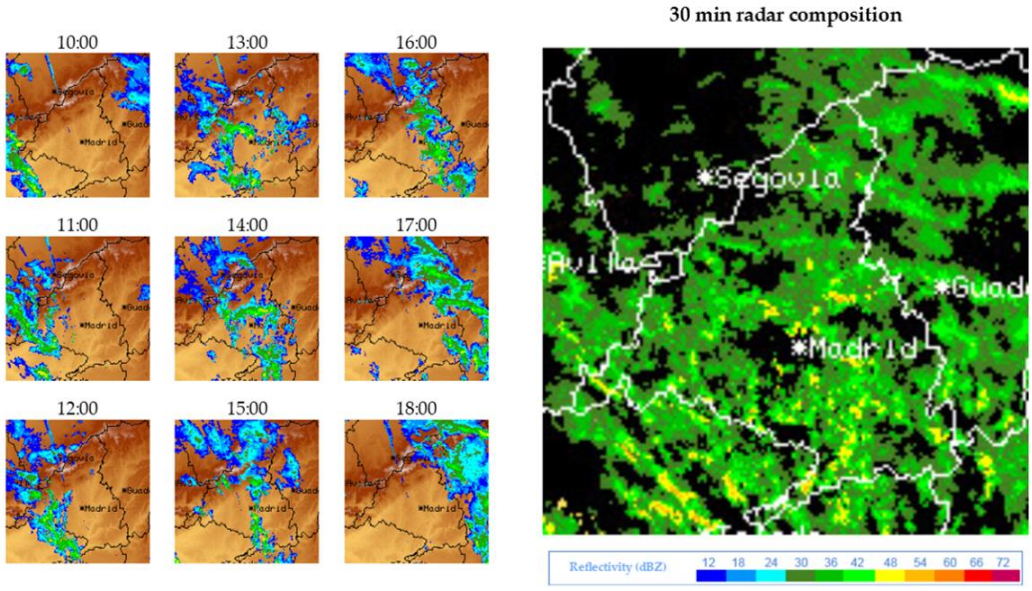

Figure 5. (**a**) Madrid radar reflectivity hourly images from 10:00 to 18:00 UTC and (**b**) composite image of radar reflectivity every 30 min in the same period. Images have been cropped. For the composite, terrain and reflectivity <30 dBZ were removed, and reflectivity values were divided into three ranges (30–42, 48–60, and 66–72 dBZ), prioritizing those of greater reflectivity. Thus, each grid point shows the largest reflectivity value shown over the period.

When the 30-min composite was analysed, three aspects were noted. There is an intense reflectivity core to the southwest of the domain, not captured by precipitation from any model configuration. There were no signs of high reflectivity to the north of the domain, where some model simulations tended to show a heavy precipitation core (although shadowing by terrain elevation should be considered in this case). There was a concentration of high reflectivity points in the centre of the domain, from the city of Madrid southward, which makes the bow shape in the model simulations consistent with reflectivity data. This proves that, as has already been stated, the simulations initialized by GFS025 displaces the bow-shaped maximum accumulated precipitation to the east, and that the model did not properly capture the precipitation near complex terrain and southwest of the domain. These may be the reasons why the validation of GFS025 model configurations gave poorer results and why the stations west of the domain had poor performance.

When 10-min images were analysed from 13:30 to 14:10 UTC (not shown), the development of an intense reflectivity cell (54 dBZ) that crossed LEMD was seen. In Figure 5, at 14:00 UTC this core had just passed over the airport. Later, two more cells traversed the area through 16:50 UTC, but with weaker reflectivity values. This is consistent with the observed precipitation at station #11 and was the cause for the disruption of airport operations during the day of the event.

3.5. LEMD Assessment

On the day studied, there were wind records suggestive of a wet microburst event over LEMD (not shown), which is a weather phenomenon very relevant to aircraft safety. Because this phenomenon

depends largely on convective precipitation [31], there is a need to validate the precipitation simulation before attempting to simulate a microburst. Despite the marginal improvements and validation problems resulting from increasing model horizontal resolution, grid resolutions of 1 km and smaller may be required for the WRF to capture a microburst. Also, because the Thompson scheme is not the most suitable for convective precipitation, mid-altitude snow is an important factor for dry microbursts [32]. This is the reason for validating these model configurations over the area.

As presented in the previous section, although the general weather pattern or dynamics may be captured by a model, results cannot be generalised to every station. Because of scarce observed data, evaluation on individual basis should be performed for closer study, because this may be required for investigating a microburst. For this purpose, LEMD was chosen because it is the most important station for aviation safety in the study area (#11 in Figure 1b). In the evaluation of LEMD, additional ensembles were not considered.

Studying every physics scheme performance for deterministic model configurations (Figure 6), several aspects were noted. Observations showed two precipitation maxima over the station, one at 14:00 and the second at 16:00 UTC, the first one with a slightly greater precipitation amount. GFS025 model configurations tended to simulate the precipitation onset at 13:00 UTC, whereas GFS1 configurations already simulated some rain at 12:00 UTC. The D, T, and M schemes generated more precipitation with the GFS1 configurations than with GFS025, with very little difference between domains. The Y scheme produced more precipitation with GFS025 than with the GFS1 configurations, and there were notable differences between domains when initialized by GFS025. The D physics scheme consistently produced a single maximum of hourly precipitation at 14:00 UTC. It captured very well the first maximum of observed precipitation, but did not reproduce the second, resulting in total accumulated precipitation underestimation. The T scheme showed a single maximum at 15:00 UTC, not coinciding with any of the maxima in observed values and with severe underestimation of total accumulated precipitation. The M scheme initialized by GFS025 was the only configuration that captured a two-maxima precipitation pattern, consistent with observations. GFS1 configurations showed a similar temporal evolution, with a heavy precipitation onset at 14:00 UTC but a single maximum at 16:00 UTC. This physics scheme underestimated precipitation with every model configuration, but appeared to be the best performer. The Y scheme was the most variable. It captured very well the total accumulated precipitation with GFS025, but underestimated with GFS1. Also, it produced a single maximum at 15:00 UTC with GFS1 for D1 and D3 (maxima at 13:00 UTC are negligible), a single maximum with D1-GFS025 at 14:00 UTC (showing severe overestimation), and a double maximum with D3-GFS025 at 15:00 and 18:00 UTC. All these LEMD results were consistent with the overall model results already presented.

It is remarkable that the observed data of accumulated precipitation (Figure 6) were sometimes outside the probability distribution function of the ensembles initialized by GFS1 (because observed accumulated precipitation was outside the range between the minimum and maximum simulated accumulated precipitation). This indicates that these ensembles are underdispersive. Although the validation results of simulations initialized by GFS025 were poorer than those of GFS1, by considering these simulations we may increase the ensemble spread, which can be interesting for detecting the risk of heavy precipitation at particular locations.

The temporal behaviour already detailed for each station is reflected in r values (Table 7). The T scheme results are statistically non-significant for every model configuration and the Y scheme values are small. Results for the M scheme were outstanding, with D1-GFS025-M the best performer. Ensemble configurations did not improve M results, but also produced very large values, especially for physics ensembles and D1 configurations. Considering RAEC and RAAC at LEMD (Table 7), it is evident that the D scheme performed very well with GFS1 and the Y scheme with GFS025. The M scheme results with D3-GFS1 were favourable, but overall results were mediocre.

Table 7. LEMD station validation: RAAC, RAEC, and *r* values for a specific station. Only deterministic configurations, physics ensembles, and initial condition ensembles are shown. Values of *r* in parentheses denote a non-significant statistical result. Best three performers for each index are shaded.

		Deterministic				Physics Ensemble	Initial Conditions Ensemble
		D	**T**	**Y**	**M**	**DTYM**	**DTYM**
					RAEC		
D1	GFS025	−0.254	−0.521	0.197	−0.312	−0.222	−0.223
	GFS1	−0.098	−0.375	−0.215	−0.203	−0.223	
D3	GFS025	−0.290	−0.516	−0.123	−0.315	−0.311	−0.261
	GFS1	−0.046	−0.361	−0.261	−0.177	−0.211	
					RAAC		
D1	GFS025	0.274	0.522	0.197	0.313	0.230	0.238
	GFS1	0.198	0.402	0.238	0.214	0.246	
D3	GFS025	0.306	0.517	0.172	0.316	0.317	0.274
	GFS1	0.183	0.392	0.271	0.188	0.231	
					r		
D1	GFS025	0.754	(0.438)	0.809	0.987	0.880	0.896
	GFS1	0.764	(0.460)	0.553	0.938	0.833	
D3	GFS025	0.745	(0.429)	(0.380)	0.979	0.670	0.777
	GFS1	0.774	(0.453)	0.554	0.943	0.843	

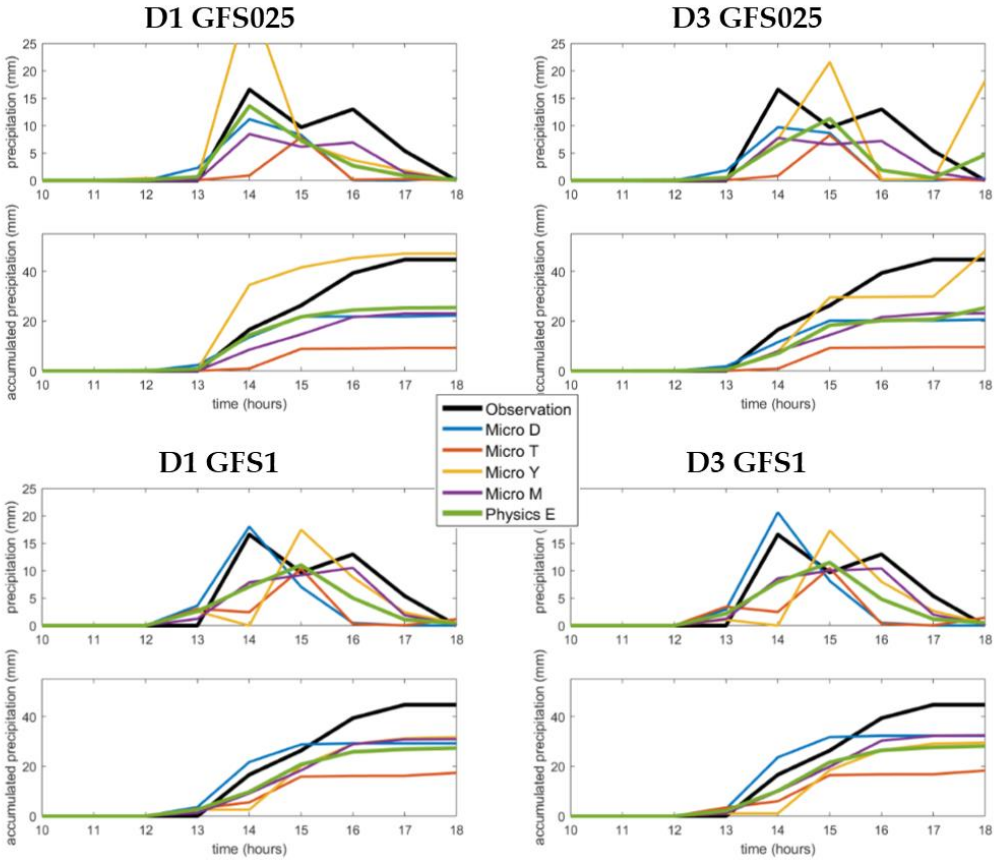

Figure 6. Hourly precipitation (mm, **upper** panels) and accumulated precipitation (mm, **lower** panels) between 10:00 and 18:00 UTC for LEMD station. Each deterministic model configuration is shown with the four microphysics schemes, the physics ensemble for each configuration and observed precipitation.

We must note some factors regarding the favourable performance of the Y scheme with GFS025. It is important to recall that LEMD was the station with the largest observed precipitation values for the event, registering all its accumulated precipitation in just over three hours. This may be linked to a very heavy precipitation cell during that period. As has been mentioned, the Y scheme tended to overestimate overall precipitation and was not the best performer, but its overestimation improved the results of Y for this particular station and event.

The benefits of RAEC and RAAC can be seen by taking as examples the D and M schemes for the D1-GFS1 configuration. Total accumulated precipitation at the end of the validation period was essentially the same for both schemes, resulting in RBias values of −0.346 for D and −0.308 for M. It may seem that both schemes notably underestimated precipitation, but when time was considered, RAEC values showed that D (−0.098) underestimated considerably less than M (−0.203). This is confirmed by the accumulated precipitation behaviour (Figure 6), in which the D scheme overestimated precipitation from 13:00 to 15:00 UTC. The RMAE results were 0.553 for D and 0.493 for M. However, although at the end of the validation period these may be the errors, RAAC confirms that persistence of the error over the period was less for D (0.198) than for M (0.214). This means that the accumulated precipitation curve simulated by D remained closer to the observed curve vs. time, which is evident in the aforementioned figure.

When the error curves were assessed (Figure 7), similar characteristics were found. These curves confirm that the best overall deterministic configurations for this station were D3-GFS1-D and D3-GFS1-M. GFS025 tended to create larger errors than GFS1 and there were almost no differences between domains. However, when the physics ensembles were evaluated it was discovered that the best performer was D1-GFS025, followed by D3-GFS1. This highlights that the improvements may be marginal and are strongly dependent on the exact model configuration.

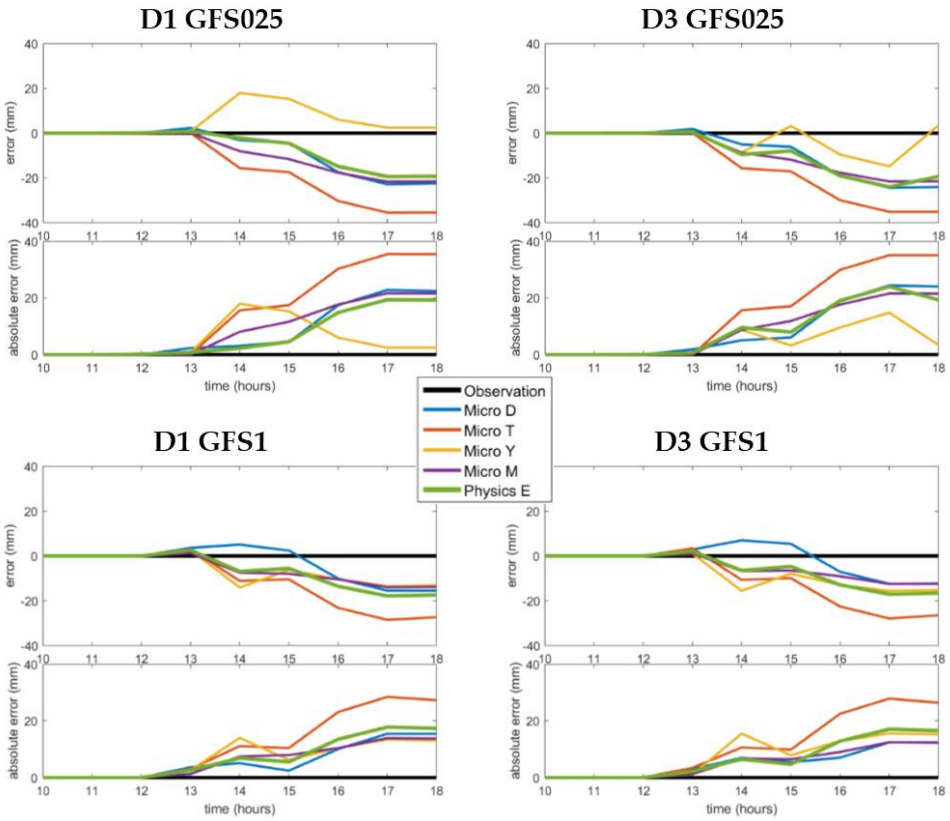

Figure 7. Hourly error (mm, **upper** panels) and absolute error (mm, **lower** panels) between 10:00 and 18:00 UTC at LEMD station. Each deterministic model configuration is shown with the four microphysics schemes, the physics ensemble for each configuration and observed precipitation.

4. Discussion and Conclusions

Considering the physics parameterizations, it is evident that the T scheme was not able to simulate this heavy precipitation event accurately. The results produced by this scheme were always outperformed by some other scheme using any index or configuration. Results of ensembles not considering the T scheme consistently improved the ensembles that did consider it. Thus, we concluded that the T scheme is not apt for simulating this episode. This is consistent with the fact that Thompson et al. [19] designed this parameterization mainly to simulate drizzle conditions. This microphysics scheme produces excessive numbers of small droplets, which are not appropriate for convective precipitation [33]. Nevertheless, the D configuration (which also uses the Thompson microphysics parameterizations) should be considered, although its performance may be the second poorest. This is a clear indication that precipitation simulations depend on several factors and model parameterizations, not only on microphysics. Nonetheless, evaluating only the microphysics, the results for the M physics scheme were clearly the best among the deterministic configurations, although as it consistently underestimated the precipitation. Especially when initialized with the GFS1 resolution, the M scheme produced some of the best results for every validation index. Morrison et al. [22] created a two-moment microphysics scheme specifically designed for storms, and the parameterizations were fine-tuned to simulate stratiform precipitation trailing a squall line. This particular feature explains very well the outstanding results of this scheme for temporal correlation (Tables 5 and 7), and it was the only one that captured the two maxima of precipitation over LEMD (Figure 6). Also, this finding is consistent with the results obtained by García-Ortega et al. [8], who included the M scheme in the best-performing microphysics parameterizations in their analysis of convective precipitation over the Northeastern Iberian Peninsula. Validating the ensemble configurations, the best results are achieved by YM and DYM, with small differences between them. In case a configuration must be selected in future investigations, it should depend on the objective and needs of the study. A YM ensemble would be less computationally demanding, but a DYM ensemble would be more robust and consistent.

Evaluating domain resolution, D3 produced coarser rainfalls than D1, but only minor differences were found in the numerical results. The performance of domain resolution appears to depend on the exact model configuration. Nevertheless, D1 results were better for almost every index for the initial conditions and additional ensembles, but improvements were almost negligible. Schwartz et al. [34] reached this conclusion when they found no statistically significant differences between 4 km and 2 km grid resolutions for severe precipitation forecasting using WRF. Even before this, Kain et al. [35] had already questioned if downscaling from 4 km to 2 km would provide any added value to forecast skills. There are also other important considerations, because short-range simulations of convective weather validated against scarce and non-uniform data have serious challenges. The use of "traditional" validation scores for high-resolution simulations has been extensively questioned by Mass et al. [36] among others, mainly owing to the penalty that timing errors may generate. Pontoppidan et al. [37] concluded that complex terrain adds another source of error because of gravity wave representations, resulting in marginal improvement when downscaling resolution.

After assessing the GFS resolution, our results confirm that mesoscale models have a strong dependence and sensitivity to initial conditions [38]. Also, it is evident that the sensitivity of the model is greater for initial condition resolution than domain resolution. It is very interesting that GFS1 improved GFS025 results for almost every validation index, some being an order of magnitude better. In this case, the GFS1 initial conditions provided a more realistic representation of the rainfall field and precipitation amount than simulations initialized with GFS025. Also, the poor performance of GFS025 appeared to be largely affected by a timing/location error. Given that the majority of observing stations were west of the domain, the simulation of heavier precipitation displaced to the east had a great impact on scoring indices. Similar validation errors have been observed by Mass et al. [36], and timing differences for deep convection between domain resolutions have been described by Weisman et al. [39]. However, to our knowledge, timing errors for different resolutions of initial conditions produced by the same source have not been previously assessed. Nevertheless, such results are in agreement

with those noted by Jee and Kim [17], who obtained better validation results initializing their model with initial conditions with horizontal resolution $1^\circ \times 1^\circ$ than by initial conditions with much higher resolution. This suggests the need for improving data assimilation at the regional scale, especially by additional observational data sources.

As a general conclusion, physics parameterizations controlled the spatial distribution and quantity of precipitation simulated for the event, while initial conditions resolution affect the exact placement and timing of it. The domain resolution, being D1 and D3 having very high resolutions, had no significant effect. Other conclusions can be made. Bias, MAE, RMSE, and r values obtained are comparable to those of other works also simulating heavy precipitation events, e.g., Evans et al. [40] in Australia, García-Ortega et al. [8] in Spain, and Pontoppidan et al. [37] in Norway. Because of the poor validation scores of GFS025, the initial conditions and additional ensembles rarely outperformed the best physics ensemble or deterministic configuration. The only exception to this was the temporal correlation for D1, in which differences between GFS025 and GFS1 were smaller and the performance of the initial conditions and additional ensembles improved.

It is also important that although the GFS1 initial conditions and M physics scheme combination yielded outstanding results, the robustness and consistency produced by ensembles must be taken into account. An increase in ensemble spread may be attained by combining different physics parameterizations and initial conditions [41]. In this way, the underdispersive nature of the ensembles detected in the results can be partially corrected [42]. Therefore, although the best scores from the validation were obtained by the D1-GFS1-M configuration, the use of an ensemble provides additional information about the uncertainty associated with the spatiotemporal evolution of precipitation as well as the accumulated precipitation. Also, because underestimation of precipitation by numerical models is very common during convective episodes [43], a solution for the development of future early warning systems may be the use of ensemble maximum precipitation, in addition to the ensemble mean, with the aim of minimizing the underestimation.

The conclusions in this paper were reached by analysing a particular deep convection event in a specific region. They cannot be directly extrapolated to other regions or episodes. Therefore, we intend to evaluate similar episodes to obtain more robust conclusions about the optimal setup of the WRF model for forecasting this type of event. It was decided to examine this episode because of the serious disruptions it caused around the city of Madrid and especially at the LEMD airport.

We conclude with some other considerations about LEMD. The very heavy rain and gale-force wind gusts produced during the event forced the diversion and cancelation of several flights. As has been mentioned, these phenomena may be related to a microburst that the authors intend to analyse in detail in a later work. It is demonstrated by the present work that when a single location is evaluated, a unique assessment should be made, because model performance may vary greatly. Thus, the validation presented herein should be expanded and completed in future studies. Nevertheless, the results and methodology of the work can be very useful to develop early warning systems for minimizing the adverse effects of similar episodes in the study area.

Author Contributions: F.V. and J.L.S. helped in the project administration and supervision of the paper. A.M. and E.G.-O. collaborated in the design of the methodology. M.L.M. participated in the conceptualization and review of the paper. S.F.-G. supported in the validation and formal analysis. P.B. was the responsible of calculating the results and writing the original draft.

Funding: This research was funded by the Spanish Ministry of Economy, Industry and Competitiveness (MINECO) under the framework of the SAFE-FLIGHT research project (CGL2016-78702-C2-1-R and CGL2016-78702-C2-2-R).

Acknowledgments: This work was supported by research projects METEORISK (RTC-2014-1872-5), PCIN-2014-013-C07-04, PCIN-2016-080 (UE ERANET Plus NEWA Project), SAFE-FLIGHT (CGL2016-78702-C2-1-R and CGL2016-78702-C2-2-R), ESP2013-47816-C4-4-P, CGL2010-15930, CGL2016-81828-REDT, FEI-EU-17-16, and the Instituto de Matemática Interdisciplinar (IMI) of the Universidad Complutense. Special thanks go to Roberto Weigand for computer support, and to Steven Hunter and Analisa Weston for reviewing the English translation. The authors also thank AEMET for providing the observational databases used in the validation.

Conflicts of Interest: The authors declare no conflict of interest. The founding sponsors had no role in the design of the study, nor in the collection, analyses or interpretation of data, in the writing of the manuscript, or in the decision to publish the results.

References

1. Easterling, D.R.; Meehl, G.A.; Parmesan, C.; Changnon, S.A.; Karl, T.R.; Mearns, L.O. Climate Extremes: Observations, Modeling, and Impacts. *Science* **2000**, *289*, 2068–2074. [CrossRef] [PubMed]
2. Cortés, M.; Turco, M.; Llasat-Botija, M.; Carmen Llasat, M. The relationship between precipitation and insurance data for floods in a Mediterranean region (northeast Spain). *Nat. Hazards Earth Syst. Sci.* **2018**, *18*, 857–868. [CrossRef]
3. Santos, J.A.; Reis, M.A.; De Pablo, F.; Rivas-Soriano, L.; Leite, S.M. Forcing factors of cloud-to-ground lightning over Iberia: Regional-scale assessments. *Nat. Hazards Earth Syst. Sci.* **2013**, *13*, 1745–1758. [CrossRef]
4. Hermida, L.; López, L.; Merino, A.; Berthet, C.; García-Ortega, E.; Sánchez, J.L.; Dessens, J. Hailfall in southwest France: Relationship with precipitation, trends and wavelet analysis. *Atmos. Res.* **2015**, *156*, 174–188. [CrossRef]
5. Tapiador, F.J.; Tao, W.K.; Shi, J.J.; Angelis, C.F.; Martinez, M.A.; Marcos, C.; Rodriguez, A.; Hou, A. A comparison of perturbed initial conditions and multiphysics ensembles in a severe weather episode in Spain. *J. Appl. Meteorol. Climatol.* **2012**, *51*, 489–504. [CrossRef]
6. Beguería, S.; Angulo-Martínez, M.; Vicente-Serrano, S.M.; López-Moreno, J.I.; El-Kenawy, A. Assessing trends in extreme precipitation events intensity and magnitude using non-stationary peaks-over-threshold analysis: A case study in northeast Spain from 1930 to 2006. *Int. J. Climatol.* **2011**, *31*, 2102–2114. [CrossRef]
7. Nakamura, I.; Llasat, M.C. Policy and systems of flood risk management: A comparative study between Japan and Spain. *Nat. Hazards* **2017**, *87*. [CrossRef]
8. García-Ortega, E.; Lorenzana, J.; Merino, A.; Fernández-González, S.; López, L.; Sánchez, J.L. Performance of multi-physics ensembles in convective precipitation events over northeastern Spain. *Atmos. Res.* **2017**, *190*, 55–67. [CrossRef]
9. Kyselý, J.; Rulfová, Z.; Farda, A.; Hanel, M. Convective and stratiform precipitation characteristics in an ensemble of regional climate model simulations. *Clim. Dyn.* **2016**, *46*, 227–243. [CrossRef]
10. Fernández-González, S.; Martín, M.L.; García-Ortega, E.; Merino, A.; Lorenzana, J.; Sánchez, J.L.; Valero, F.; Rodrigo, J.S. Sensitivity analysis of the WRF model: Wind-resource assessment for complex terrain. *J. Appl. Meteorol. Climatol.* **2018**, *57*. [CrossRef]
11. Tapiador, F.J.; Turk, F.J.; Petersen, W.; Hou, A.Y.; García-Ortega, E.; Machado, L.A.T.; Angelis, C.F.; Salio, P.; Kidd, C.; Huffman, G.J.; et al. Global precipitation measurement: Methods, datasets and applications. *Atmos. Res.* **2012**, *104–105*. [CrossRef]
12. Merino, A.; Fernández-González, S.; García-Ortega, E.; Sánchez, J.L.; López, L.; Gascón, E. Temporal continuity of extreme precipitation events using sub-daily precipitation: Application to floods in the Ebro basin, northeastern Spain. *Int. J. Climatol.* **2018**, *38*, 1877–1892. [CrossRef]
13. Chai, T.; Draxler, R.R. Root mean square error (RMSE) or mean absolute error (MAE)?—Arguments against avoiding RMSE in the literature. *Geosci. Model Dev.* **2014**, *7*, 1247–1250. [CrossRef]
14. Buytaert, W.; Celleri, R.; Willems, P.; Bièvre, B.D.; Wyseure, G. Spatial and temporal rainfall variability in mountainous areas: A case study from the south Ecuadorian Andes. *J. Hydrol.* **2006**, *329*. [CrossRef]
15. Agencia Estatal de Meteorología. *Climatología Aeronáutica Madrid/Barajas*; Agencia Estatal de Meteorología: Madrid, Spain, 2012.
16. Skamarock, W.C.; Klemp, J.B. A time-split nonhydrostatic atmospheric model for weather research and forecasting applications. *J. Comput. Phys.* **2008**, *227*, 3465–3485. [CrossRef]
17. Jee, J.B.; Kim, S. Sensitivity sudy on high-resolution WRF precipitation forecast for a heavy rainfall event. *Atmosphere* **2017**, *8*. [CrossRef]
18. Mooney, P.A.; Mulligan., F.J.; Fealy, R. Evaluation of the sensitivity of the weather research and forecasting model to parameterization schemes for regional climates of Europe over the period 1990–1995. *J. Clim.* **2013**, *26*, 1002–1017. [CrossRef]

19. Thompson, G.; Field, P.R.; Rasmussen, R.M.; Hall, W.D. Explicit Forecasts of Winter Precipitation Using an Improved Bulk Microphysics Scheme. Part II: Implementation of a New Snow Parameterization. *Mon. Weather Rev.* **2008**, *136*, 5095–5115. [CrossRef]
20. Milbrandt, J.A.; Yau, M.K. A Multimoment Bulk Microphysics Parameterization. Part I: Analysis of the Role of the Spectral Shape Parameter. *J. Atmos. Sci.* **2005**, *62*, 3051–3064. [CrossRef]
21. Milbrandt, J.A.; Yau, M.K. A Multimoment Bulk Microphysics Parameterization. Part II: A Proposed Three-Moment Closure and Scheme Description. *J. Atmos. Sci.* **2005**, *62*, 3065–3081. [CrossRef]
22. Morrison, H.; Thompson, G.; Tatarskii, V. Impact of Cloud Microphysics on the Development of Trailing Stratiform Precipitation in a Simulated Squall Line: Comparison of One- and Two-Moment Schemes. *Mon. Weather Rev.* **2009**, *137*, 991–1007. [CrossRef]
23. Chou, M.; Suarez, M.J. *Technical Report Series on Global Modeling and Data Assimilation a Thermal Infrared Radiation Parameterization for Atmospheric Studies Revised May 2003 I*; NASA: Washington, DC, USA, 2001; p. 19.
24. Tewari, M.; Chen, F.; Wang, W.; Dudhia, J.; LeMone, M.A.; Mitchell, K.; Ek, M.; Gayno, G.; Wegiel, J.; Cuenca, R.H. Implementation and verification of the unified NOAH land surface model in the WRF model. *Bull. Am. Meteorol. Soc.* **2004**, 2165–2170. [CrossRef]
25. Janjić, Z.I. The Step-Mountain Eta Coordinate Model: Further Developments of the Convection, Viscous Sublayer, and Turbulence Closure Schemes. *Mon. Weather Rev.* **1994**, *122*, 927–945. [CrossRef]
26. Dudhia, J. Numerical Study of Convection Observed during the Winter Monsoon Experiment Using a Mesoscale Two-Dimensional Model. *J. Atmos. Sci.* **1989**, *46*, 3077–3107. [CrossRef]
27. Benjamin, S.; Bleck, R.; Brown, J.; Brundage, K.; Devenyi, D.; Grell, G.; Kim, D.; Manikin, G.; Schlatter, T.; Schwartz, B.; et al. Mesoscale Weather Prediction with the RUC Hybrid Isentropic-Sigma Coordinate Model and Data Assimilation System Operational Numerical Weather Prediction. In Proceedings of the 50th Anniversary of Operational Numerical Weather Prediction, College Park, MD, USA, 14–17 June 2004; pp. 495–518.
28. Nakanishi, M.; Niino, H. An improved Mellor-Yamada Level-3 model: Its numerical stability and application to a regional prediction of advection fog. *Bound.-Layer Meteorol.* **2006**, *119*, 397–407. [CrossRef]
29. Fernández-González, S.; Valero, F.; Sánchez, J.L.; Gascón, E.; López, L.; García-Ortega, E.; Merino, A. Numerical simulations of snowfall events: Sensitivity analysis of physical parameterizations. *J. Geophys. Res.* **2015**, *120*, 10130–10148. [CrossRef]
30. Bolgiani, P.; Fernández-González, S.; Martin, M.L.; Valero, F.; Merino, A.; García-Ortega, E.; Sánchez, J.L. Analysis and numerical simulation of an aircraft icing episode near Adolfo Suárez Madrid-Barajas International Airport. *Atmos. Res.* **2018**, *200*, 60–69. [CrossRef]
31. Atlas, D.; Ulbrich, C.W.; Williams, C.R. Physical origin of a wet microburst: Observations and theory. *J. Atmos. Sci.* **2004**, *61*, 1186–1195. [CrossRef]
32. Srivastava, R.C. A simple model of evaporatively driven downdraft—Application to microburst downdraft. *J. Atmos. Sci.* **1985**, *42*, 1004–1023. [CrossRef]
33. Otkin, J.; Huang, H.-L.; Seifert, A. A comparison of microphysical schemes in the WRF model during a severe weather event. In Proceedings of the 7th WRF Users' Workshop, Boulder, CO, USA, 19–22 June 2006; pp. 19–22.
34. Schwartz, C.S.; Kain, J.S.; Weiss, S.J.; Xue, M.; Bright, D.R.; Kong, F.; Thomas, K.W.; Levit, J.J.; Coniglio, M.C. Next-Day Convection-Allowing WRF Model Guidance: A Second Look at 2-km versus 4-km Grid Spacing. *Mon. Weather Rev.* **2009**, *137*, 3351–3372. [CrossRef]
35. Kain, J.S.; Weiss, S.J.; Bright, D.R.; Baldwin, M.E.; Levit, J.J.; Carbin, G.W.; Schwartz, C.S.; Weisman, M.L.; Droegemeier, K.K.; Weber, D.B.; et al. Some Practical Considerations Regarding Horizontal Resolution in the First Generation of Operational Convection-Allowing NWP. *Weather Forecast.* **2008**, *23*, 931–952. [CrossRef]
36. Mass, C.F.; Ovens, D.; Westrick, K.; Colle, B.A. Does increasing horizontal resolution produce more skillful forecasts? The results of two years of real-time numerical weather prediction over the Pacific Northwest. *Bull. Am. Meteorol. Soc.* **2002**, *83*, 407–430. [CrossRef]
37. Pontoppidan, M.; Reuder, J.; Mayer, S.; Kolstad, E.W. Downscaling an intense precipitation event in complex terrain: The importance of high grid resolution. *Tellus Dyn. Meteorol. Oceanogr.* **2017**, *69*, 1271561. [CrossRef]
38. Mittermaier, M.P. Improving short-range high-resolution model precipitation forecast skill using time-lagged ensembles. *Q. J. R. Meteorol. Soc.* **2007**, *133*, 1487–1500. [CrossRef]

39. Weisman, M.L.; Skamarock, W.C.; Klemp, J.B. The Resolution Dependence of Explicitly Modeled Convective Systems. *Mon. Weather Rev.* **1997**, *125*, 527–548. [CrossRef]
40. Evans, J.P.; Ekström, M.; Ji, F. Evaluating the performance of a WRF physics ensemble over South-East Australia. *Clim. Dyn.* **2012**, *39*, 1241–1258. [CrossRef]
41. Jankov, I.; Gallus, W.A.; Segal, M.; Koch, S.E. Influence of Initial Conditions on the WRF–ARW Model QPF Response to Physical Parameterization Changes. *Weather Forecast.* **2007**, *22*, 501–519. [CrossRef]
42. Fernández-González, S.; Martín, M.L.; Merino, A.; Sánchez, J.L.; Valero, F. Uncertainty quantification and predictability of wind speed over the Iberian Peninsula. *J. Geophys. Res. Atmos.* **2017**, 122. [CrossRef]
43. Heath, N.K.; Fuelberg, H.E.; Tanelli, S.; Turk, F.J.; Lawson, R.P.; Woods, S.; Freeman, S. WRF nested large-eddy simulations of deep convection during SEAC4RS. *J. Geophys. Res.* **2017**, *122*, 3953–3974. [CrossRef]

6.4. Microburst: Sensitivity Analysis

Bolgiani, P., Fernández-González, S., Valero, F., Merino, A., García-Ortega, E., Sánchez, J. L., & Martín, M. L. (2020). **Simulation of Atmospheric Microbursts Using a Numerical Mesoscale Model at High Spatiotemporal Resolution**. *Journal of Geophysical Research: Atmospheres*, *125*(4), e2019JD031791.

The following article was published in February 2020 in the JGR Atmospheres journal. This is ranked 17th in the Meteorology & Atmospheric Sciences category as per the 2018 Journal Citation Report. The Journal Impact Factor is 3.633.

JGR Atmospheres

RESEARCH ARTICLE
10.1029/2019JD031791

Simulation of Atmospheric Microbursts Using a Numerical Mesoscale Model at High Spatiotemporal Resolution

Pedro Bolgiani[1], Sergio Fernández-González[2], Francisco Valero[1,5], Andrés Merino[3], Eduardo García-Ortega[3], José Luis Sánchez[3], and María Luisa Martín[4,5]

[1]Department of Earth Physics and Astrophysics, Faculty of Physics, Complutense University of Madrid, Madrid, Spain, [2]State Meteorological Agency (AEMET), Santander, Spain, [3]Atmospheric Physics Group, IMA, University of León, León, Spain, [4]Department of Applied Mathematics, Faculty of Computer Engineering, University of Valladolid, Valladolid, Spain, [5]Interdisciplinary Mathematics Institute, Complutense University of Madrid, Madrid, Spain

Key Points:
- The Weather Research and Forecasting numerical model is able to reproduce high-reflectivity microbursts
- The characteristic variables of the microburst are properly simulated, although some intensities are lower than observations
- Differences are observed between different microphysics and planetary boundary layer parametrizations

Correspondence to:
P. Bolgiani,
pbolgian@ucm.es

Citation:
Bolgiani, P., Fernández-González, S., Valero, F., Merino, A., García-Ortega, E., Sánchez, J. L., & Martín, M. L. (2020). Simulation of atmospheric microbursts using a numerical mesoscale model at high spatiotemporal resolution. *Journal of Geophysical Research: Atmospheres*, *125*, e2019JD031791. https://doi.org/10.1029/2019JD031791

Received 8 OCT 2019
Accepted 31 JAN 2020
Accepted article online 5 FEB 2020

Abstract Atmospheric microbursts are low-level meteorological events that can produce significant damage on the surface and pose a major risk to aircraft flying close to the ground. Studies and ad hoc numerical models have been developed to understand the origin and dynamics of the microburst; nevertheless, there are few researches of the phenomenon using global and mesoscale models. This is mainly due to the limitations in resolution, as microbursts normally span for less than 4 km and 20 min. In this paper, the Weather Research and Forecasting model is used at resolutions of 400 m and 3 min to test if it can properly capture the variables and dynamics of high-reflectivity microbursts. Several microphysics and planetary boundary layer parametrizations are tested to find the best model configuration for the simulation of this kind of episodes. General conditions are evaluated by using thermodynamic diagrams. Surface and vertical wind speed, reflectivity, precipitation, and other variables for each simulated event are compared with observations, and the model's sensitivity to the variables is assessed. The dynamics and evolution of the microburst is evaluated using different plots of a chosen event. The results show that the model is able to reproduce high-reflectivity microbursts in accordance with observations, although there is a tendency to underestimate the intensity of variables, most markedly on the wind vertical velocity. Regarding the microphysics schemes, the Morrison parametrization performs better than the WRF single-moment 6-class scheme. No major differences are found between the Mellor-Yamada-Janjic and the Mellor-Yamada-Nakanishi-Niino planetary boundary layer parametrizations.

1. State of the Art

Atmospheric *downbursts* are first noted in the scientific literature by Fujita (1976) and Fujita and Byers (1977), who describe it as an extremely intense *downdraft*, a negative vertical component of the wind vector (w), near the ground that can generate extensive damage on the surface and pose a risk to aircraft at low altitudes. The authors differentiate the phenomenon from the more common downdrafts generated by heavy precipitating convective cells, noted by Byers and Braham (1949). Then, Fujita and Byers (1977), Fujita (1981b), and Fujita and Wakimoto (1981) define a downburst as an atmospheric event where a strong downdraft in the lower heights of the atmosphere produces an area of damaging surface wind with a divergent pattern, ranging from less than one to tens of kilometers. These surface winds generate a toroidal shaped gust front (Fujita, 1981b; Fujita & Wakimoto, 1983), named outburst at first and *outflow* in the later literature. Fujita also creates a subdivision of downbursts based on the planetary horizontal scale of the outflow (Fujita, 1981b) and the duration of the peak winds (Fujita, 1980). Thus, a *macroburst* is defined by an outflow diameter larger than 4 km with peak winds lasting more than 5 min, while a *microburst* presents an outflow diameter smaller than 4 km and peak winds lasting less than 5 min. Downbursts can also be subdivided considering the amount of precipitation generated and the radar reflectivity of the convective cell (Fujita, 1985; Fujita & Wakimoto, 1981; Wilson et al., 1984). *Low reflectivity* or dry downbursts generate precipitation below 0.25 mm and radar reflectivity below 35 dBZ, while *high reflectivity* or wet downbursts present precipitation over 0.25 mm and radar reflectivity over 35 dBZ.

Microbursts are defined as a major meteorological hazard for aviation and flight safety (Fujita, 1980, 1981a, 1985; Wolfson et al., 1994). The phenomenon draws the attention of the aviation community and the

meteorological science in the decade of 1980, as it is related to several aircraft accidents and incidents. Thus, four major field programs are conducted to characterize the event, in which more than 300 microbursts are studied: the Northern Illinois Meteorological Research On Downbursts project (Fujita, 1985), the Joint Airport Weather Studies project (McCarthy et al., 1982; Wilson et al., 1984), the Federal Aviation Administration—Lincoln Laboratory Operational Weather Studies project (Wolfson et al., 1985), and the Microburst and Severe Thunderstorm (MIST) project (Atkins & Wakimoto, 1991; Dodge et al., 1986). These projects provide most of the information and technical knowledge of the microbursts, and their results have been verified by research in different countries as Japan (Ohno et al., 1996) and Australia (Potts, 1991). Along with the field programs, notable laboratory studies on the buoyancy and vertical acceleration of the air and ad hoc numerical models of the microbursts are developed by Srivastava (1985, 1987) and Proctor (1988, 1989).

Since the nineties the research in microbursts moves towards more practical approaches. McCann (1994) develops the Wind Index, and Pryor and Ellrod (2004) develop the Wet Microburst Severity Index, both forecasting algorithms to be used by operational meteorologists. Atlas et al. (2004) use Doppler radar observations to conclude the concurrence with Srivastava's models and that a narrow distribution of hail meteor sizes produces stronger high-reflectivity microbursts. Ferrero et al. (2014) perform laboratory simulations of microbursts to conclude that the fluid column height and density do not produce remarkable differences to the microburst, although high flow rotation can prevent the event, in contrast to former results. Pryor (2015) produces the Microburst Windspeed Potential Index as a nowcasting algorithm. Burlando et al. (2017) conduce a field study to confirm a high-reflectivity downburst event over Italy and the associated synoptic conditions.

With the development of high-performance computers, numerical models can reach high resolutions, and simulations are used in the research of the microburst. Lin et al. (2007) and Vermeire et al. (2011a) use subcloud idealized simulations to reproduce different microbursts' features generating results concurrent with observations. James and Markowski (2010) perform idealized three-dimensional simulations to find that, contrary to previous findings, dry air aloft is detrimental for downbursts as it reduces the hydrometeors' mass. Vermeire et al. (2011b) use large eddy simulations to model outflows with the conclusion that a cooling source model is better than and impinging jet model in capturing the features of the event. Nevertheless, Orf et al. (2012) perform a three-dimensional cloud simulation to prove that neither the impinging jet nor the cooling source models are sufficient to capture the complete process of downbursts, presenting results concurrent with observations. Oreskovic et al. (2018) also use cloud simulations to evaluate the thermodynamic cooling associated with downbursts. In the field of numerical weather prediction models, few publications are found on the microburst issue. A report by van Dijke et al. (2011) presents a high-resolution Weather Research and Forecasting (WRF) hindcast of a microburst event associated to a bow-echo structure, evaluating the winds and reflectivity of the event. A research by Carroll et al. (2011) shows a hit-or-miss test of four microphysics parametrizations, based on seven case studies, to conclude that the WRF single-moment 6-class scheme (WRF6) is the best performer. To the authors' knowledge, no research has been done to perform a detailed analysis of the variables and structure of the microburst using a mesoscale numerical model. Precisely, the objectives of this paper are to verify if the WRF model is able to reproduce high-reflectivity microbursts and evaluate the simulation of the main variables related. In addition, an assessment of two microphysics and two planetary boundary layer (PBL) parametrizations is performed. The paper is structured as follows: Section 2 presents a technical analysis of the microburst and the observational data used, both necessary to understand the assessment of the simulations, which are described in section 3 along with the evaluation process. Section 4 presents the results of the simulations and discussion of the evaluation, which lead to the conclusions in section 5.

2. The Microburst

Fujita (1985) and Wakimoto (1985) establish a series of conditions on the surface wind intensities to be considered a microburst, being the principal a minimum of 10 m s^{-1} at maximum wind speed (this would generate a radial difference in wind speed of $\Delta V \geq 20$ m s^{-1}). In addition, Wilson et al. (1984) and Hjelmfelt (1988) create the following characterization:

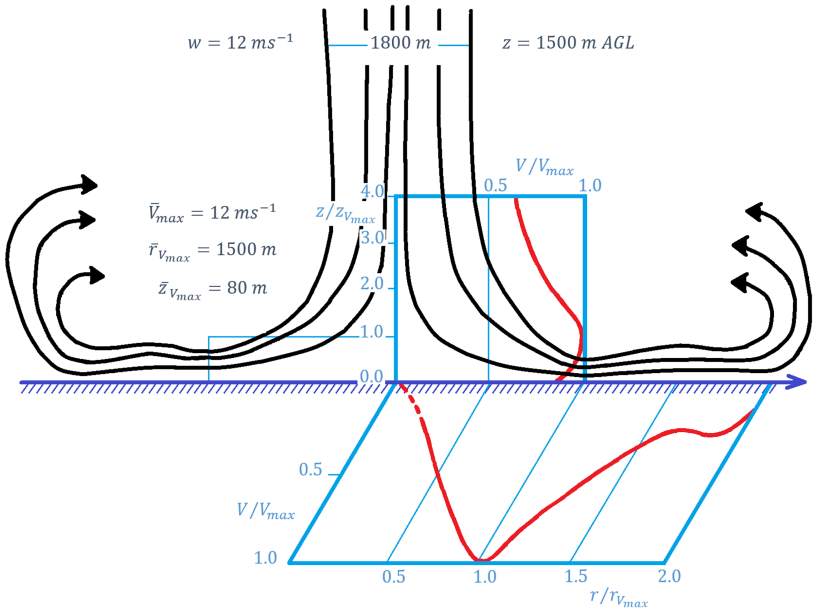

Figure 1. Vertical cross section of the characteristic microburst structure at maximum intensity. Based on a figure from Hjelmfelt (1988). © American Meteorological Society. Used with permission.

- Average maximum radial velocity differential: 24 m s^{-1}. Median: 22 m s^{-1}.
- Average distance of maximum radial velocity differential: 3,100 m.
- Average depth of outflow: 700 m.
- Characteristic lifespan:
- t = −5 min: downburst can be detected at 3.0 km above ground level (AGL) ($-5 \geq w \geq -10$ m s^{-1}).
- t = −2 min: downburst can be detected at 1.5 km AGL.
- t = 0 min: downburst reaches the surface; divergence appears in the surface wind field.
- t = +2.5 min: outflow reaches microburst wind speed ($\Delta V \geq 20$ m s^{-1}, $w \leq -10$ m s^{-1}).
- t = +7 min: outflow reaches maximum wind speed.
- t = +15 min: outflow decays under microburst intensity.

Figure 1 illustrates the characteristic downburst and outflow. Being the wind gust events most common during the summer (Kelly et al., 1985), a diurnal variation is also observed for the microburst, with 91% of occurrences between 10:00 and 21:00 local time (LT) and a peak observed between 14:00 and 16:00 LT (34% of events). Figure 2 presents the temporal frequency observed in the 297 microbursts registered in Northern Illinois Meteorological Research On Downbursts, Joint Airport Weather Studies (Fujita, 1985), and MIST (Atkins & Wakimoto, 1991).

Laboratory studies and numerical models of the microbursts developed by Srivastava (1985, 1987) and Proctor (1988, 1989) show that the microphysical and thermodynamic details are very important in the formation of a downdraft, which is governed by the inviscid vertical momentum equation (Wakimoto, 2001):

$$\frac{d\overline{w}}{dt} = -\frac{1}{\rho}\frac{\partial \overline{p}'}{\partial z} + g\left[\frac{\theta_v'}{\theta_{v0}} - \frac{c_v}{c_p}\frac{p'}{p_0} - (r_c + r_r + r_i)\right], \text{ Eq. (1)}$$

where w is vertical velocity, t is time, ρ is air density, p is pressure, z is height, g is gravity, Θ_v is the virtual potential temperature, c_p is specific heat at constant pressure, c_v is specific heat at constant volume, r_c is the mixing ratio of cloud water, r_r is the mixing ratio of rain water, and r_i is the mixing ratio of ice water. Primes denote differences with height. This makes four terms in the equation: perturbation pressure vertical gradient, thermal buoyancy, perturbation pressure buoyancy, and condensate loading. The vertical gradient of perturbation pressure is generally small and may be only considered in large mesoscale convective

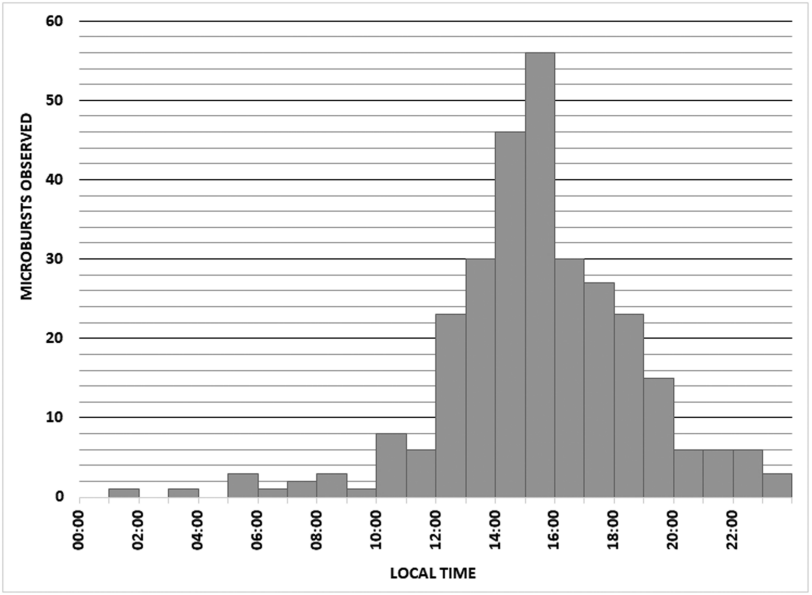

Figure 2. Temporal distribution of observed microbursts. Summation of data from NIMROD, JAWS, and MIST. JAWS = Joint Airport Weather Studies; MIST = Microburst and Severe Thunderstorm; NIMROD = Northern Illinois Meteorological Research On Downbursts.

systems and not for microbursts. The effects of pressure buoyancy are even smaller (Wakimoto, 2001) and should also be disregarded for the present study.

Downbursts usually initiate at midlevel layers, close above the 0 °C level (Proctor, 1989). Thermal buoyancy is the main factor in the downdraft due to the latent cooling generated by phase changes, although downdrafts tend to be notably subsaturated (Proctor, 1989; Srivastava, 1985) and not necessarily present a large negative buoyancy (Wakimoto, 2001). Compared with evaporation, melting and sublimation enhance downdraft speeds due to additional cooling (Proctor, 1988; Srivastava, 1987; Wakimoto et al., 1994); thus, snow conduces to strong low-reflectivity microbursts, and hail generates stronger high-reflectivity microbursts. Smaller drops have a large evaporative potential due to greater curvature, which leads to a larger equilibrium vapor pressure and lower relative humidity (Proctor, 1989; Srivastava, 1985, 1987). Also dependent on atmospheric meteors, condensate loading can initiate the downdraft or maintain it once initiated, in function of drop size, intensity, and downdraft speed (Byers & Braham, 1949; Knupp, 1988; Roberts & Wilson, 1989). Entrainment of environmental dry air at midlevel layers can initiate downdrafts by promoting evaporation. However, this effect may be detrimental at lower levels, where high relative humidity increases virtual ambient temperature, developing stronger downdrafts (Wakimoto, 2001).

Srivastava (1985) considers all these factors to produce a relationship between downburst speeds, temperature lapse rate, and liquid water mixing ratio (Figure 3), both measured at the 0 °C level. This relationship shows that thermal buoyancy (second term in equation 1) is dominant for low-reflectivity microbursts, but condensate loading (fourth term in equation 1) can override it in the initiation of high-reflectivity microbursts. The temperature lapse rate between 700 and 500 hPa is correlated with the occurrence of low-reflectivity microbursts, particularly when this lapse rate is observed to be smaller or equal to −8 °C km^{-1} in the afternoon (Caplan et al., 1990). In the case of high-reflectivity microbursts, the equivalent potential temperature (Θ_e) deficit, defined as the difference between the maximum Θ_e near the ground and the minimum Θ_e at midlevels, is more accurate. Afternoon environments conductive to high-reflectivity microbursts consistently exhibit Θ_e deficits equal or larger than 20 °C (Atkins & Wakimoto, 1991). The characteristic vertical thermodynamic diagrams for high-reflectivity microbursts are defined for temperature, dew point temperature, and Θ_e, as depicted in Figure 4.

Microburst models show that the downdraft accelerates in the lower levels of the atmosphere, reaching the maximum speed between 1,000 and 500 m AGL, thus the subcloud temperature lapse rate has to be less than

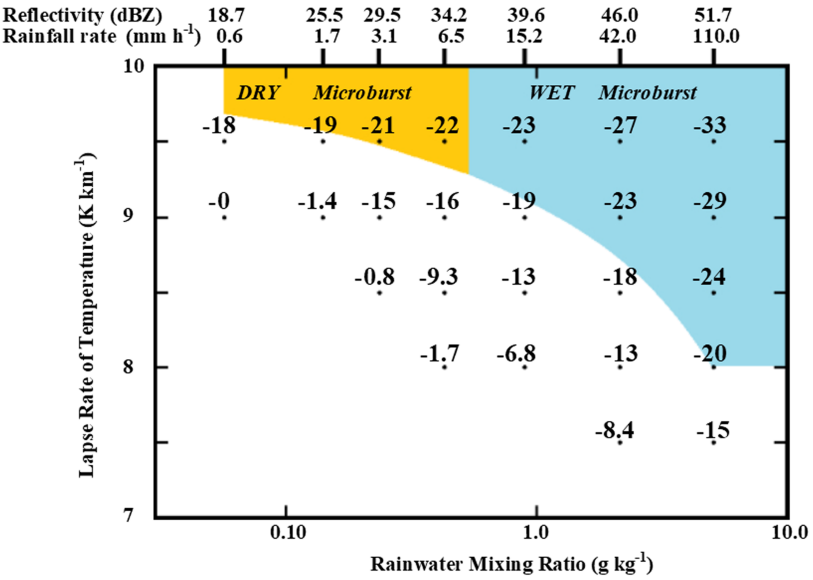

Figure 3. Results of a one-dimensional nonhydrostatic model of a downdraft. Plotted numbers show the vertical air velocity (m s^{-1}) at 3,700 m below the top of the downdraft as a function of environmental temperature lapse rate and liquid water mixing ratio at the top of the downdraft. Scales on top indicate radar reflectivity and precipitation rate at the top of the downdraft. Colored areas indicate microburst intensities as defined by Srivastava, colors differentiate between dry and high-reflectivity microbursts. Based on a figure from Srivastava (1985). © American Meteorological Society. Used with permission.

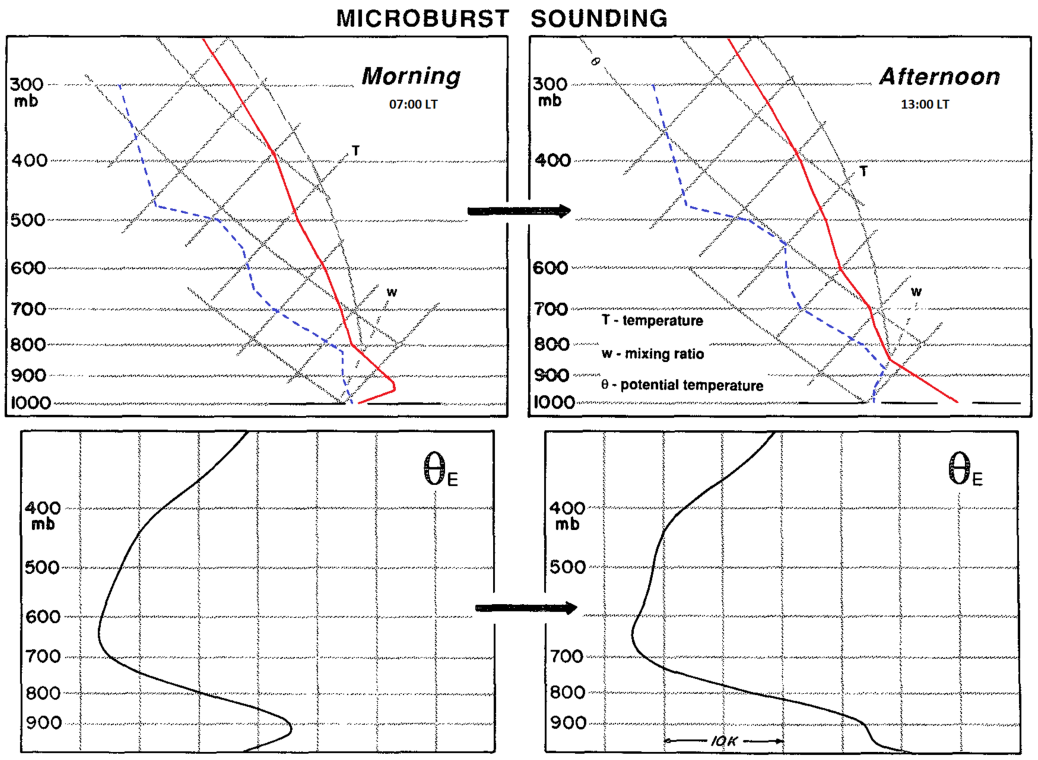

Figure 4. Characteristic thermodynamic diagrams for humid environments conductive to high-reflectivity microbursts. Upper plots depict temperature (red) and dew point temperature (blue). Lower plots depict equivalent potential temperature. Based on a figure from Atkins and Wakimoto (1991). © American Meteorological Society. Used with permission.

−7.5 °C km^{-1} for the evaporative cooling to support the downdraft (Proctor, 1988, 1989; Srivastava, 1985, 1987). It is also remarkable that, despite being one of the elemental components of microbursts, there is not a general agreement for the minimum w speed to the definition of the microburst. Fujita (1976) initially noted a minimum w for the downburst as −3.6 m s^{-1} at 90 m AGL. Hjelmfelt (1988) characterizes the microburst w speed as −12 m s^{-1} at 1,500 m AGL; later Wakimoto (2001) defines it as −20 m s^{-1}, but this is done in base of the arbitrary selection made by Srivastava (1985).

Finally, it has to be considered that microbursts typically develop in environments with weak wind shear (Johns & Doswell, 1992). The convective cells producing microbursts usually present vorticities comparable to the mesocyclones associated to tornadoes (Kessinger et al., 1988), although they show radial convergence aloft. In addition, some results support the concept of microbursts primarily occurring on new convective processes within existing outflow boundaries (Rydell & Ladd, 1991) or interacting with front leading edges (Wolfson, 1990).

2.1. Data: The MIST Project

The observational data used in this paper is gathered in one of the mayor projects performed in the study of microbursts. The MIST project (Atkins & Wakimoto, 1991; Dodge et al., 1986) is conducted in northern Alabama (United States of America) for 61 days during June and July 1986. The project uses an array of 41 surface stations operated by the National Center for Atmospheric Research (NCAR) and 30 stations operated by the Federal Aviation Administration—Lincoln Laboratory Operational Weather Studies. This mesoscalar network covers an area of approximately 40 × 30 km and is complemented with the data from three Doppler radar stations and the radiosonde data from the nearby Marshall Space Flight Center, operated by the National Aeronautics and Space Administration (commonly referred to as Redstone). A total of 62 microbursts were recorded in the project, 33 of them identified by the surface stations network, and 29 identified by the Doppler radar stations beyond the network's area (Atkins & Wakimoto, 1991).

The observations and results gathered during the MIST project become one of the original and main sources for high-reflectivity microburst characterization. Some of those observations are presented here to be used in the validation of the experiment. Particularly three dates have been selected as case studies (Atkins & Wakimoto, 1991), named with the number of microbursts observed:

- 13 July (MB25): This is the most active day in the project with 25 microbursts detected (40.3% of the total recorded by MIST). On this date the following data are observed, which will be used in the evaluation of the results of this paper:
  - Synoptic conditions are relatively stagnant, with a dry air inflow from the west into midlevels.
  - The cumulonimbus producing microbursts have tops reaching the tropopause.
  - Main precipitation cores are mainly composed of ice. They present reflectivities over 55 dBZ and extend between the level of minimum Θ_e and 7 to 10 km AGL.
  - During the descent of the precipitation core of the microbursts, environmental air is dragged into the core, at approximately the level of minimum Θ_e. This enhances negative buoyancy and accelerates the negative w.
  - Average maximum surface wind speed for microbursts: 15.1 m s^{-1}.
  - Average surface temperature difference for microbursts: −4.2 °C.
  - 13 microburst produce surface wind speeds over 15 m s^{-1}, five events reach over 20 m s^{-1}, only one microburst reaches over 25 m s^{-1}.
- 20 July (MB1): On this day a single microburst is observed, which is thoroughly documented and described (Kingsmill & Wakimoto, 1991; Wakimoto & Bringi, 1988).
- 10 June (MB0): This day is recorded as a thunderstorm day with no microbursts detection.

3. Experimental Design

The experiment consists in the numerical modelization of the three aforementioned days selected from the MIST project and the validation of these against the observational data. The simulations are performed with the Advanced Research WRF model version 3.7.1. This is a nonhydrostatic model that has been extensively proven and validated for weather prediction and research (Skamarock et al., 2008; Skamarock & Klemp, 2008). It is possible to fine-tune the model to local conditions using the multiple variables and

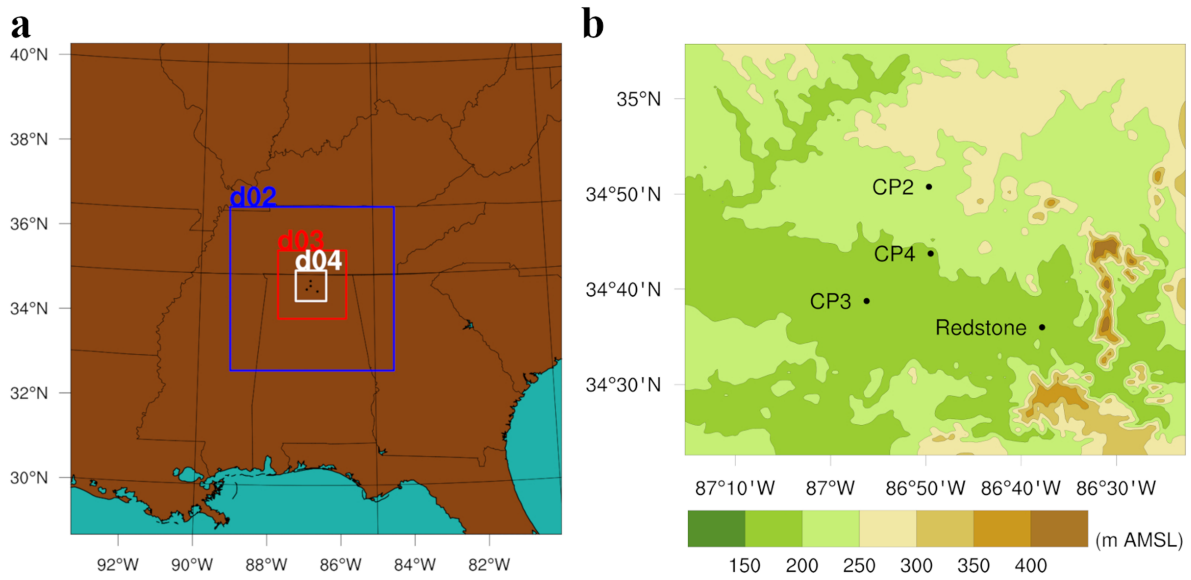

Figure 5. Area of study. (a) Positioning of the four nested domains used for the simulations (outer boundaries correspond to D1). (b) Terrain elevation map for D4. Black circles show the position of the MIST Doppler radar stations (CP2, CP3, and CP4) and the Redstone radiosonde site.

parametrizations available. In this study, two different PBL and two microphysics schemes are used, thus four simulations are presented for each date selected, making a total of 12 simulations.

3.1. Model Configuration and Parametrization

Initial and boundary conditions are taken from the Climate Forecast System Reanalysis developed by the National Center for Environmental Prediction. The reanalysis data is taken at 6-hr intervals with a surface spatial resolution of 0.312°, atmospheric spatial resolution of 0.5° and 37 vertical levels (Saha et al., 2010).

Four domains are allocated for the simulations, named D1, D2, D3, and D4 from outmost to innermost, with a two-way nesting strategy (Figure 5a). One of the challenges of this study is to work with spatial and temporal resolutions adapted to microburst events, so it can be determined if the WRF simulates it properly. The innermost domain (D4) is then configured as a 202 × 202 grid point domain with 400 m spatial grid resolution and 3 min of temporal resolution. D3 is 151 × 151 grid point with 1,200 m spatial resolution and 30 min temporal resolution. Outer domains are both 121 × 121 grid point with resolutions of 3,600 m, 60 min for D2 and 10,800 m, 180 min for D1. For vertical resolution, 60 sigma levels are defined from surface to 50 hPa, with a progressive resolution being greater in the lower levels of the troposphere, and four soil layers are used.

As high-reflectivity microbursts are related to heavy precipitation events (Fujita, 1985; Srivastava, 1985), parametrizations are chosen according to previous work by the authors to validate the model in similar conditions (Bolgiani et al., 2018). Long and short wave radiation scheme are new Goddard (Chou et al., 2001; Chou & Suarez, 1999) (called every 10 min), soil layers scheme (technically, land surface scheme) is unified Noah (Tewari et al., 2004), surface-atmosphere interface scheme (technically, surface layer scheme) is Eta similarity (Janjic, 1994), urban physics are not applied. Cumulus clouds are computed for D3 and D4, while the Grell-Freitas ensemble scheme (Grell & Freitas, 2014) is used for D1 and D2 (called every time step). The model is operated as nonhydrostatic in the four domains, with no w damping. For microphysics two schemes are used, being the moments computed the main difference between them. The Morrison scheme computes two moments (mixing ratio and number concentration of hydrometeors are independently predicted) and is proven to be a good performer in storm and trailing related precipitation (Morrison et al., 2009). The WRF6 scheme is a single-moment scheme (only mixing ratio is predicted) proven suitable for heavy precipitation forecasting (Hong & Lim, 2006). Both consider the same six different hydrometeors types: water vapor, cloud water, rainwater, cloud ice, snow, and graupel. For the PBL two schemes are used (called every time step),

both based on the Mellor-Yamada scheme. The Mellor-Yamada-Janjic (MYJ) scheme is proven suitable for forecasting the development and movement of severe storm (Janjic, 1994). The Mellor-Yamada-Nakanishi-Niino (MYNN) scheme is an improvement on buoyancy, stability, and turbulence kinetic energy formulations (Nakanishi & Niino, 2006). Thus, each date simulated is performed with the following configurations: Morrison-MYJ, WRF6-MYJ, Morrison-MYNN, and WRF6-MYNN. It has to be noted that initially other parametrizations were also tested, although they were discarded from the final experiment due to the poor performance shown in the preliminary results.

3.2. Area and Time of Study

The position of D4 corresponds to the geographical domain selected for this study, which is an 80 × 80-km square area, comprising the MIST Project surface network area and a buffer zone for radar detection beyond (Atkins & Wakimoto, 1991). This is centered near 086°50′W and 34°44′N, located west of the city of Huntsville, east of the city of Athens, and north of the Tennessee River (Figure 5b). The area is mostly a flat valley on a low plateau with elevations ranging from 150 to 300 m above mean sea level. Hills develop to the north and larger elevations to the east, reaching more than 400 m above mean sea level, where the outskirts of the Appalachian Mountains can be found. The climatology corresponds to a humid subtropical climate with hot and humid summers. For June and July the Huntsville International Airport (inside D4) reports the following daily averages: mean temperature 26.7 °C, maximum 32.4 °C, minimum 21.1 °C, wind speed 2.5 m s^{-1}, relative humidity 75%, and precipitation 1.9 mm (NWS, 2019). Thunderstorms are reported an average of 12.5 days per month.

The three case studies selected (see section 2.1) are simulated with a cold start from 01:00 to 01:00 LT the next day. This allows the model to spin up and reach the simulation daytime in stable conditions. It has to be noted that, regarding the diurnal variation of the microburst, local times are predominantly used in this paper, as they are more useful than Universal Time Coordinated (UTC). For the date and place of this study, LT = UTC–5 h.

3.3. Assessment Process and Methods

The evaluation of the simulations is done by steps, first evaluating the atmospheric general conditions, then the characteristic variables and finally the dynamics of the simulation. Data are processed and plotted using the NCAR Command Language software, version 6.6.2 (NCAR, 2019).

The environmental conditions are assessed by comparing the sounding data at 07:00 and 13:00 LT. Temperature, dew point, Θ_e, and Θ_e deficit are evaluated. In addition, the convective condensation level is determined as it is used as a reference height to evaluate microburst variables. After that, a count of microbursts generated by each simulation is performed using the surface wind field. It has to be noted that initially the surface wind divergence was evaluated to establish an objective threshold to define a microburst, but this was not possible due to the diversity of wind flows that can generate the same divergence values. Thus it was decided to perform this task by scanning the surface wind plot, searching for outflow patterns in each time step. Two conditions are required to be considered a microburst: First, a clear divergent wind pattern. Second, wind intensities equal or larger than 10 m s^{-1}, covering at least a 180° arc of the divergent flow ($\Delta V \geq 20$ m s^{-1}) (see example on Figure 9). Attending to the observations and times recorded for each date, the time window evaluated for this count ranges from 10:00 to 22:00 LT for MB0 and MB25, and from 11:00 to 18:00 LT for MB1. The results are evaluated against the number of microbursts observed each day. For comparison with further results, also the time steps which the microbursts span are taken into account; as the average lifetime of the microbursts is larger than the simulation's time step, a single event can be seen in several time steps of the simulation; also, several events can be found in the same time step.

To evaluate the characteristic variables of the microburst, an Eulerian approach is used, as this would be the kind of data recorded by a surface detection station. The grid location for the center of divergence of each simulated microburst is stablished, and over that point a data timeline is recorded for each characteristic variable: surface wind speed and direction (10 m AGL), minimum w between surface and 2,000 m AGL (based on results for the convective condensation level), maximum reflectivity between surface and 2,000 m AGL, temperature lapse rate between surface and 2,000 m AGL, precipitation, and surface temperature (2 m AGL). Every variable timeline is adjusted to the time step where maximum surface wind speed is achieved and a span of ±30 min is taken. Timelines are plotted, averages and standard deviations are

computed for every simulation. These data are used to evaluate the performance of each model parametrization.

In addition, probable wind gusts are calculated to assist in the wind speed evaluation. This is done by using a Weibull cumulative distribution function.

$$CDF(X) = 1 - e^{-\left(\frac{X - X_0}{\beta}\right)^{\alpha}} \quad \text{Eq. (2)}$$

The parameters used for the equation are proved in the estimation of wind gusts by the Air Force Weather Agency (Creighton et al., 2014), being $\alpha = 3.0$, $\beta = X_0^{0.75}$, and X_0 the maximum sustained surface wind speed during the time step considered (a variable computed by the model). The required probability is 0.95.

After this, the sensitivity of the model to the variables is evaluated with an automatic detection script. The script is designed to perform a test on the variables selected and yield a warning on each time step the conditions established are met in any grid point of the domain. In case several variables are requested, the script only yields a warning if every condition is met over some grid point. If every condition is met on the domain but on scattered grid points and no single grid point reunites all the variables, there is no warning. Based on results of the previous evaluation of w, three threshold speed are selected to test minimum w individually: −3, −6, and −9 m s^{-1}. Every other variable is individually tested at the defined characteristic or mean value. Then, variables are combined, using w, reflectivity, and temperature lapse rate to test the downburst and wind speed, surface temperature anomaly, and precipitation to test the outflow.

Finally, a single simulated microburst is used to evaluate the performance of the model on the structure and dynamic of the event against an observed microburst. The observation of MB1 is chosen for this assessment precisely because only one microburst was recorded, and it is properly documented (Kingsmill & Wakimoto, 1991; Wakimoto & Bringi, 1988). Thus, if we did not account for natural variability and other factors, a "perfect" simulation would reproduce a single microburst with similar characteristics. The simulation to evaluate is selected from the best performing parametrizations. The life cycle of the high-reflectivity microburst is systematically plotted with horizontal and cross-section figures showing the evolution of several variables. In this case, a Lagrangian approach is taken following the divergent center as it moves. Three different plots are produced for each time step. A north-south vertical cross section over the divergence center is used to depict the wind flow, w speeds, reflectivity, water, and ice content. A horizontal plot shows the surface wind vectors and speed. Another horizontal plot depicts the wind vectors and contours the fields, where the characteristic variables are met.

4. Results and Discussion

It has to be noted that the results presented in this section do not follow the same order in which they were achieved as described in section 3.3. First, the thermodynamic diagrams are shown, followed by the dynamic evaluation, and then by the characteristic variables and the variables sensitivity. Following this order allows a better understanding of the variables evaluation, as the reader will have a previous example to visualize.

4.1. Thermodynamic Diagrams

Figure 6 shows the simulated skew-T log-P diagrams at 07:00 and 13:00 LT for the four parametrizations on every date. The soundings are simulated over Redstone, as it is performed during the MIST Project. The results for each day are very similar for every simulation at 07:00 LT. The differences that can be noted at 13:00 LT are mainly due to the microphysics parametrization, as the PBL parametrizations only create remarkable differences for the dew point temperature above 700 hPa. In addition, every simulation creates a midlevel temperature inversion, also present at 07:00 LT for MB1 and MB0, not recorded in the observed thermodynamic diagrams for any date (Atkins & Wakimoto, 1991); they also produce a lower relative humidity than recorded near the 0 °C level. This makes the diagrams to perform worse above 700 hPa. It is noteworthy that this inversion is reducing the convective available potential energy, which should hinder

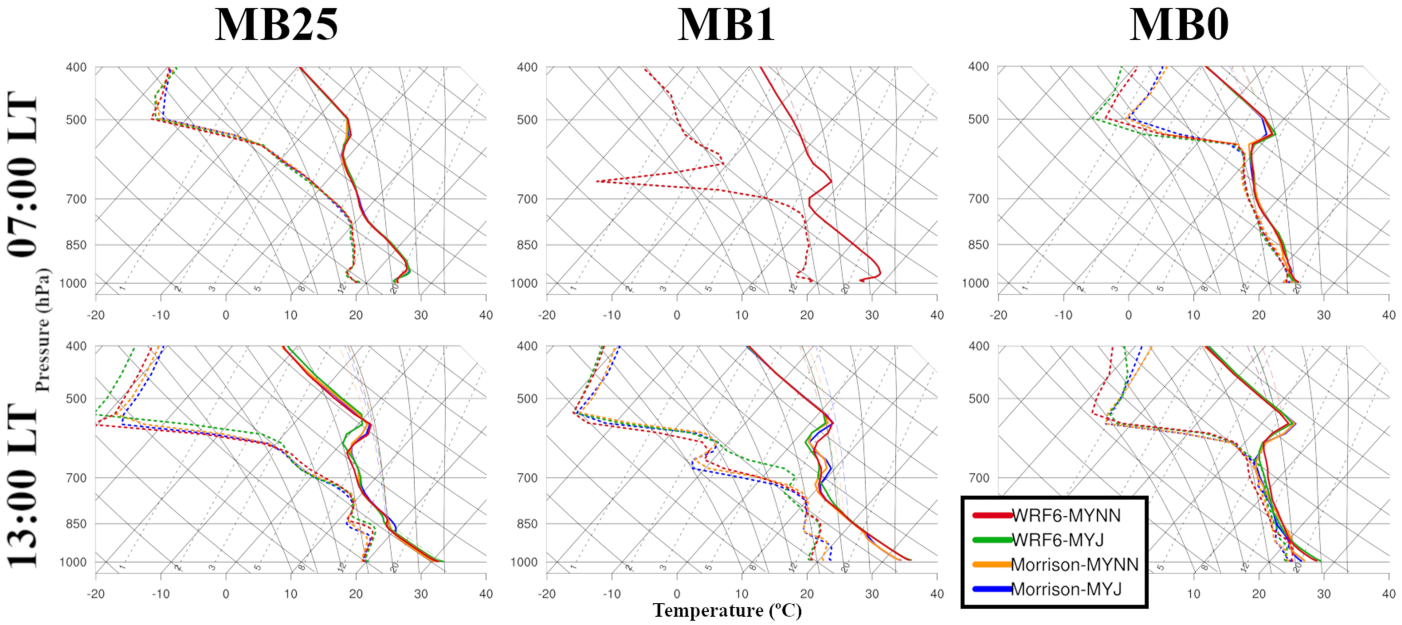

Figure 6. Thermodynamic diagrams for each date at morning and afternoon. Each diagram comprises temperature (solid lines), dew point temperature (short dashed lines), and CAPE (long dashed thin lines) for every parametrization used as per legend.

the generation of microbursts, while at the same time the dry layer is fostering the evaporation, which should enhance latent cooling.

Considering only the lower troposphere, the results for MB25 and MB1 show profiles similar to the characteristic inverted V described as conductive to high-reflectivity microbursts (Figure 4), properly reproducing the low-level temperature inversion in the morning diagram and the subcloud dry-adiabatic layer in the afternoon. The morning inversions are due to radiation and disappear as surface heating promotes convection. The large differences between the morning and afternoon diagrams for MB1 seem to respond to a deep convective situation, that forces the dry midlevel capping to higher levels. The simulations for MB0 also reproduce correctly the thermodynamic diagram in the lower troposphere with very small differences among them; particularly, the Morrison microphysics produces for 07:00 LT a small inversion below 970 hPa similar to the data presented by Atkins and Wakimoto (1991), although at 13:00 LT WRF6 is closer to observations in temperature values near the ground, producing a more accurate temperature lapse rate. The convective condensation level is computed for every date at 13:00 LT, being the highest result approximately 800 hPa. This correlates with a height of 2,000 m, which is used to evaluate *w*, reflectivity, and temperature lapse rate. It has also to be noted that the dry level at 13:00 LT is between 600 and 500 hPa.

Figure 7 shows the Θ_e diagram for the four different simulations at 07:00 and 13:00 LT on every date. The Θ_e diagrams present patterns similar to those described by Atkins and Wakimoto (1991), particularly for MB25 and MB1. It is remarkable that the different parametrizations produce very similar diagrams at 07:00 LT, in fact for MB1 they are exactly the same. Every diagram at 07:00 LT shows the low-level inversion described in the characterization (Figure 4), although most of them produce an unstable layer below 900 hPa not recorded in the observations. On MB0 and MB1 profiles present anomalies in midlevels, rendering the Θ_e deficit value unreliable. The results for 13:00 LT yield a poor performance on low levels. The stability of the layer is not properly reproduced for any day, although the general profile is similar to those recorded by Atkins and Wakimoto (1991). Evaluating the Θ_e deficit at 13:00 LT the WRF6 microphysics yields very similar values for every study case, above the 20 °C characteristic threshold. The Morrison parametrization generates different values for each case, only reaching the defined threshold on MB25 and MB1, in line with what this value is expected to do on microburst conducing situations. Nevertheless, it tends to overestimate the values on MB0 and MB1 for both PBL schemes, according to the profiles observed (Atkins & Wakimoto, 1991).

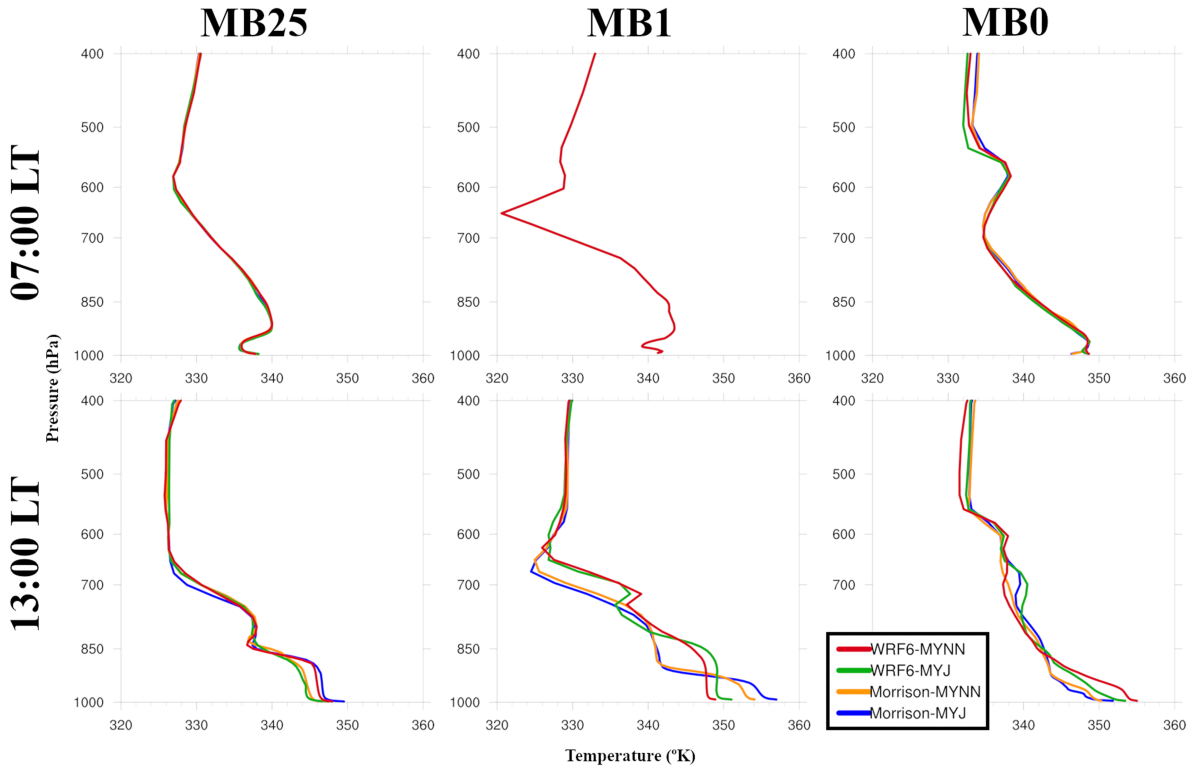

Figure 7. Equivalent potential temperature diagrams for each date at morning and afternoon. Each diagram comprises every parametrization used as per legend.

4.2. Morrison-MYJ Simulation for MB1

The reasons to select the Morrison-MYJ simulation for the dynamics assessment are deducted from results presented in the following subsections. In brief, no definitive conclusions can be taken from the variables assessment, as no one presents a clear difference between parametrizations to select one as best performer. Nevertheless, the Morrison microphysics generally outperforms the WRF6. Then, to choose the best model configuration, we have to use the initial count based on divergence (section 4.3). From these results it is evident that the Morrison-MYJ has to be selected, as the Morrison-MYNN produces no microbursts on MB1.

On MB1, the MIST project records a single high-reflectivity microburst from 14:19 to 14:28 LT, which is extensively documented by radar and direct observation (Kingsmill & Wakimoto, 1991; Wakimoto & Bringi, 1988). The event takes place to the north east of the geographical domain, outside the mesoscalar surface network, but it is detected by the three Doppler radar stations. The Morrison-MYJ simulation produced three different microbursts on MB1, at 12:42, 13:00, and 13:24 LT, all of them in the north east corner of D4. From these, the one simulated at 13:03 LT is chosen, as it is the best defined. Figures 8 and 9 present the life cycle of the simulated high-reflectivity microburst.

The cross sections at 12:51 and 12:54 LT (not shown) display a 50 dBZ core descending from 550 to 700 hPa as it travels south. At 12:57 LT (Figure 8) the nucleus of the convective cell is formed by ice above 600 hPa and water below, which is already initiating precipitation. A strong updraft is present in the upper part of the core, air entrainment is taking place from the north at 700 hPa and the influence of the outflow produced by another microburst can be seen to the north at low levels. At 13:00 LT the precipitation shaft reaches the surface, and the downdraft is properly formed with w below -6 m s^{-1}, pulling down the reflectivity core. The initiation of surface divergence can be seen at low levels, as well as an updraft to the north of the microburst due to the interaction with a former outflow. At 13:03 LT the downdraft attains maximum intensity, with w under -9 m s^{-1} very close to the ground. The cross section shows an approximately 2-km wide precipitation shaft, the 50 dBZ core reaching the ground, divergent winds near the surface, a 4- to 5-km wide outflow and weak updrafts generated by it at both sides. At 13:06 LT the ice over 600 hPa has depleted,

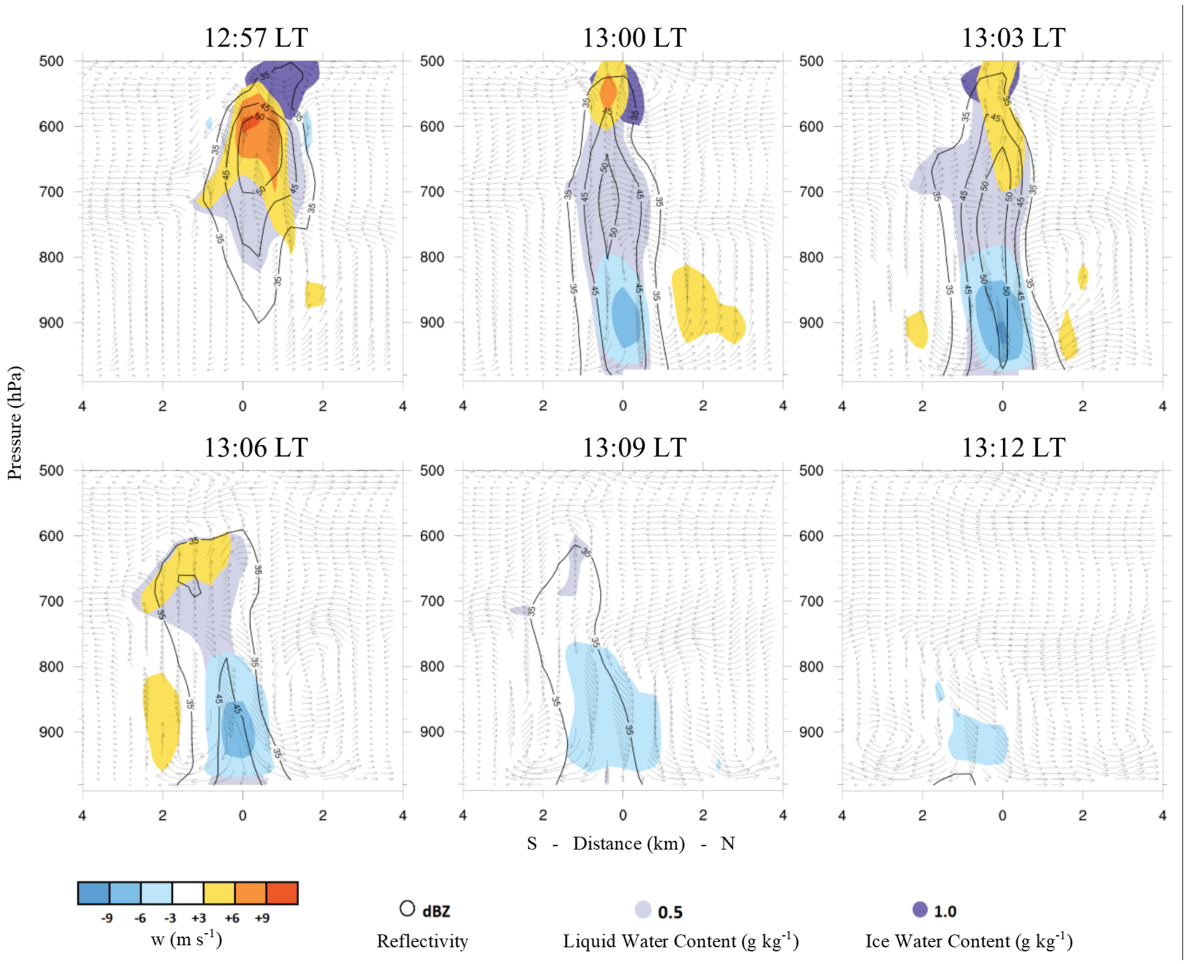

Figure 8. Vertical cross section for a Morrison-MYJ simulated microburst event, at 3-min intervals, depicting wind vectors, *w*, reflectivity, liquid, and ice water content, as per legend. Surface scale is km from the center of divergence. Plots correspond to sections depicted in Figure 9.

the reflectivity core is collapsing, and the *w* is receding back to 6 m s^{-1}. The outflow is approximately 5-km wide and 800-m deep. At 13:09 LT the downdraft is quickly dissipating and the liquid water content is almost zero, with no reflectivity over 45 dBZ. Divergence and outflow are still visible. At 13:12 LT only a few perturbations below 900 hPa remain, although divergence is present in the surface wind.

The plots in Figure 9 depict the surface wind vectors for the Morrison-MYJ simulation on MB1, the wind speed and several contours, properly reproducing the event. At 12:57 LT the temperature lapse rate near the microburst is still below −7.5 °C km^{-1} (no green contours can be seen near the black line). The 35 dBZ core has descended below 2,000 m AGL (orange contour). The outflow produced by another microburst can be seen to the north east. Despite the low-level winds depicted in the cross section (Figure 8), at 13:00 LT divergence cannot be properly seen in the surface wind field. Nevertheless, at this time, precipitation has reached the ground (light blue contour) and a shaft of minimum *w* below −6 m s^{-1} can be seen (dark blue contour). At 13:03 LT the surface wind field properly generates the divergence and the wind speeds of the microburst outflow, with the center of divergence reaching over 15 m s^{-1}. First pools of cold air appear near the microburst center (yellow contour), and this cooling makes the temperature lapse rate to reach above −7.5 °C in some spots (green contour). In addition, the precipitation, reflectivity, and *w* contours widen, which shows an intensification of these variables correlated with the cross section (Figure 8). At 13:06 LT the outflow reaches maximum intensity with wind speeds over 15 m s^{-1} near the microburst divergent center (Figure 9). The pools of cold air near the surface are evident, and the *w* weakens. At 13:09 LT divergence

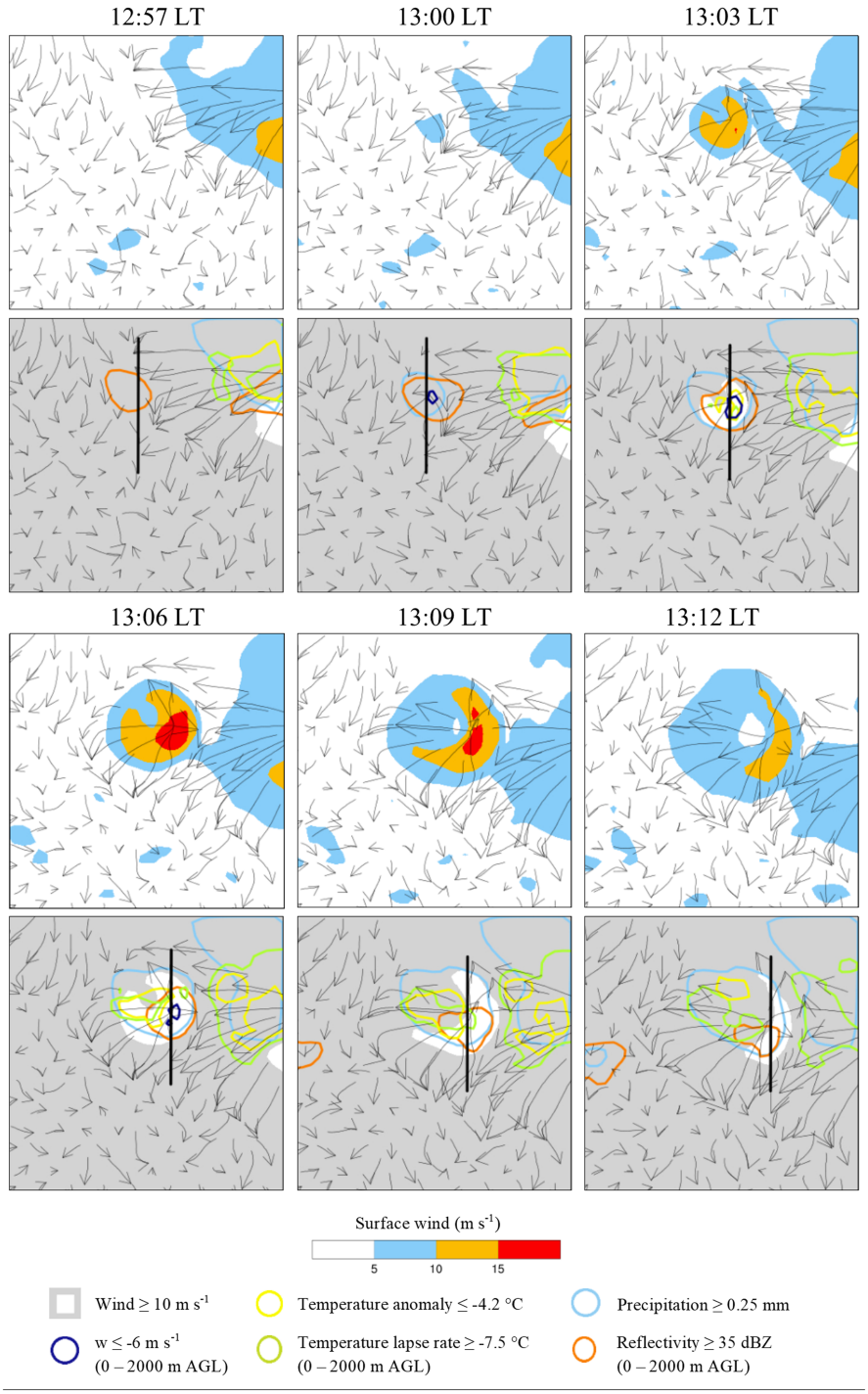

Figure 9. Horizontal plots depicting the surface wind vectors for a Morrison-MYJ simulated microburst event, at 3-min intervals. Top: wind speeds, as per legend. Bottom: contours of areas where each variable meets the defined thresholds, as per legend. The black line depicts the section used for vertical cross section in Figure 8.

and outflow are still visible, but the wind speed intensity is already decreasing, and the minimum w shaft is above -6 m s^{-1}, in correlation with the cross section (Figure 8). At 13:12 LT the divergence is present in the surface wind, but it cannot be considered a microburst anymore as most of the outflow is below 10 m s^{-1} in wind speed.

Table 1
Number of Microbursts Simulated for Each Date by Every Parametrization Used. Note. Time steps comprised by those microbursts and local time window in which they are generated. The name for each study case indicates the number of microbursts observed for that date.

Simulation parameters	Study cases								
	MB25			MB1			MB0		
	Microbursts	Time steps	Local time	Microbursts	Time steps	Local time	Microbursts	Time steps	Local time
Morrison-MYJ	22	35	15:00–19:00	3	9	12:00–14:00	0	/	/
Morrison-MYNN	14	32	15:00–19:00	0	/	/	1	3	20:00–21:00
WRF6-MYJ	75	108	12:00–19:00	97	84	11:00–18:00	12	25	13:00–20:00
WRF6-MYNN	44	68	12:00–18:00	53	72	12:00–17:00	14	54	10:00–19:00

Overall, the WRF model can properly simulate the dynamics of the high-reflectivity microburst. The timing and dimensions correspond to the microburst characterization, the water phases and reflectivity core evolution is according to the described process, midlevel air entrainment can be seen, the acceleration of the downdraft below the cloud base is evident (Figure 8), a well-defined outflow is simulated, reaching $\Delta V \geq 30$ m s^{-1} across the divergent center (Figure 9). It can even be argued if the microburst generates from the flow interaction with the previous outflow boundary.

Comparing with the observations (Kingsmill & Wakimoto, 1991; Wakimoto & Bringi, 1988), the simulation takes place 80 min before the recorded microburst and in the same quadrant of the domain field, although farther from the surface network than registered. It is remarkable that the microburst detected is generated by a convective cell growing next to an older cell, situated north east from it. Despite this older cell does not produce any microburst as the model does, the simulation properly generates both convective systems. The simulation displays a general wind flow similar to the conditions described by Wakimoto and Bringi (1988), and the 0 °C level is close to the observed level at 550 hPa. Although Kingsmill and Wakimoto (1991) show the reflectivity core reaching higher than 10 km AGL, the reflectivity values, timing and heights of the base of the core descending to the ground are very close to the radar data gathered. The *w* values derived from the radar also show large positive intensities above 5 km AGL before the microburst and negative values only below 2.5 km AGL at microburst intensity, as the model depicts.

4.3. Characteristic Variables

Table 1 summarizes the results of the surface wind divergence and speed evaluation. The Morrison-MYJ simulation yields 22 microbursts for MB25, 3 for MB1, and 0 for MB0 (35, 9, and 0 time steps, respectively), very close to the numbers of events observed (Atkins & Wakimoto, 1991). The Morrison-MYNN simulation presents an underestimation for MB25 and MB1, while it simulates a single microburst for MB0. Both WRF6 simulations produce a large overestimation, most notable on MB1 where WRF6-MYJ generates 97 microbursts and WRF6-MYNN simulates 53 events.

These results show a clear difference between microphysics parametrizations, with a marked overestimation for WRF6, which immediately renders this microphysics parametrization as a poor performer for this study. The PBL parametrizations yield more similar results but a tendency of underestimation for MYNN. Morrison-MYNN yields tolerable results overall, and the underestimation presented on MB25 and MB1 would be acceptable but for the fact that it generates one microburst on MB0, where the mesoscale conditions simulated are not conductive to microburst at all. Morrison-MYJ is the best performer, presenting the results most similar to observations. It is remarkable that the simulations generate the microbursts in local time windows very close to those recorded by Atkins and Wakimoto (1991) and in line with Figure 2.

Before evaluating the variables depicted in the following figures, a consideration of the method used for the assessment has to be made. As the selected grid point is approximately the center of the microburst and this may not be the most critical point for every variable, some values may not be properly represented. Even more, some microbursts travel notably during their life span due to the prevailing winds, which alters the results shown over time. Thus, the values produced may not show the complete picture

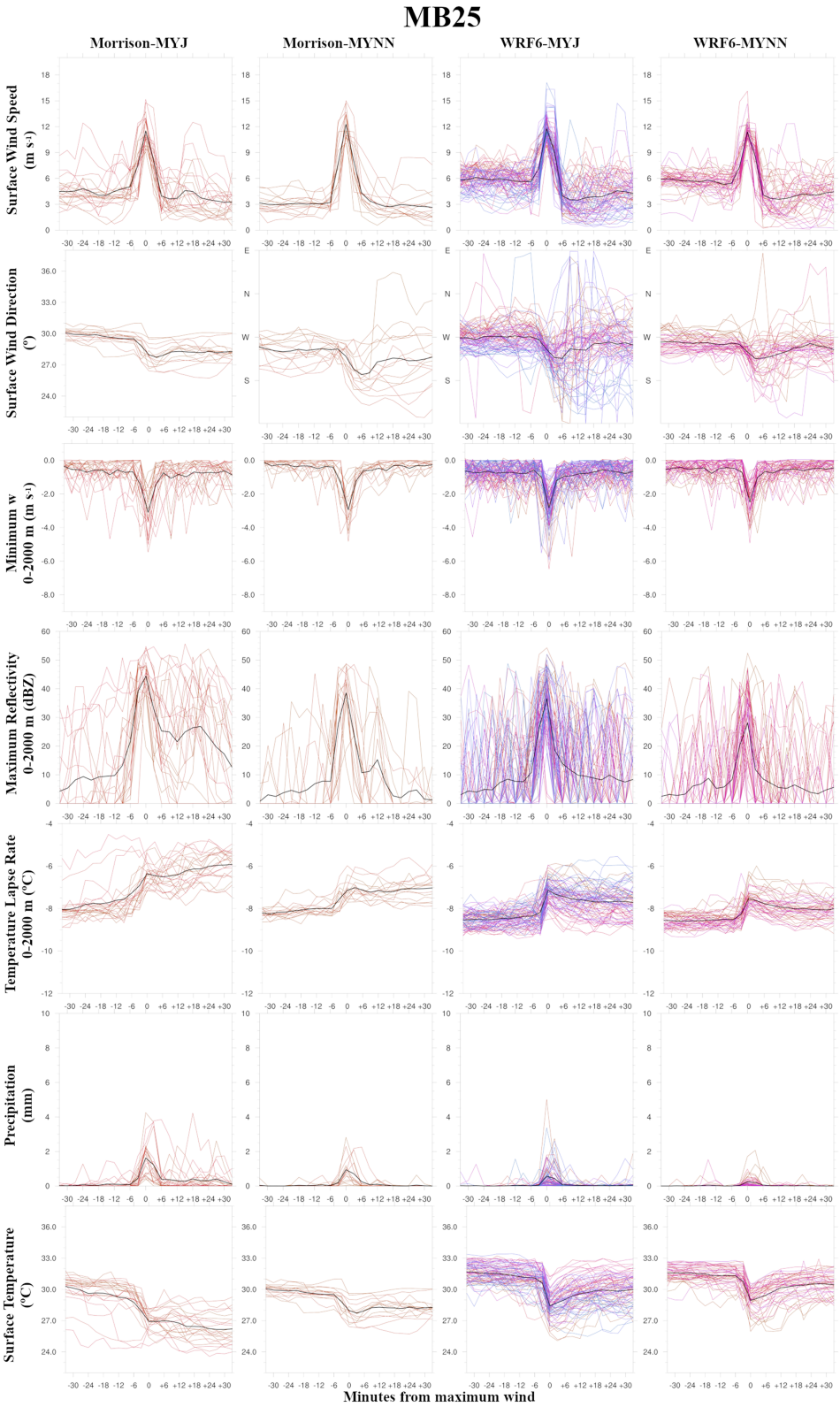

Figure 10. Values for the characteristic variables over the divergence center for each simulated microburst in a ±30 min time window from maximum wind ($t = 0$), for MB25 and every parametrization used. Color lines depict each simulated microburst, black lines depict averages.

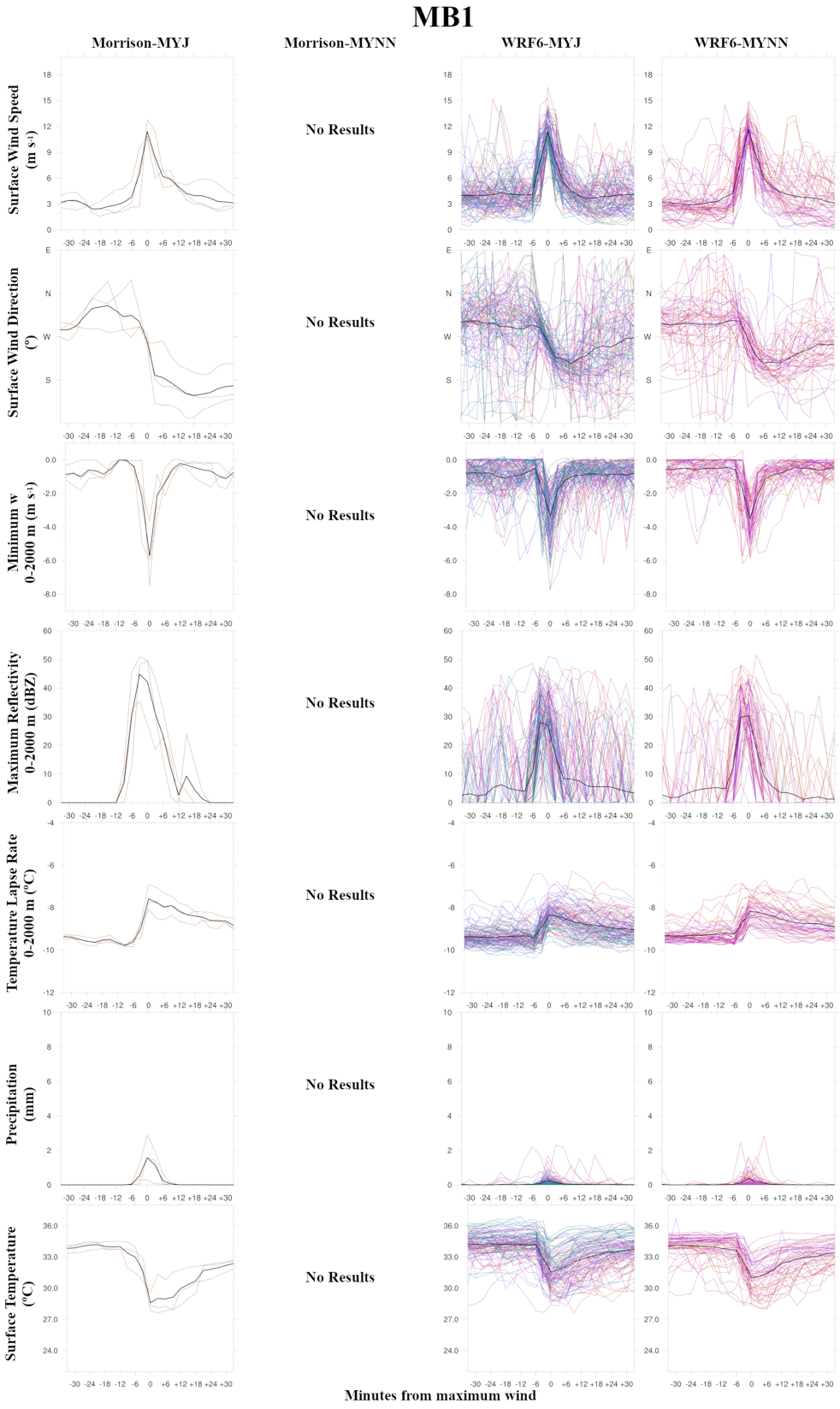

Figure 11. As Figure 10 for MB1.

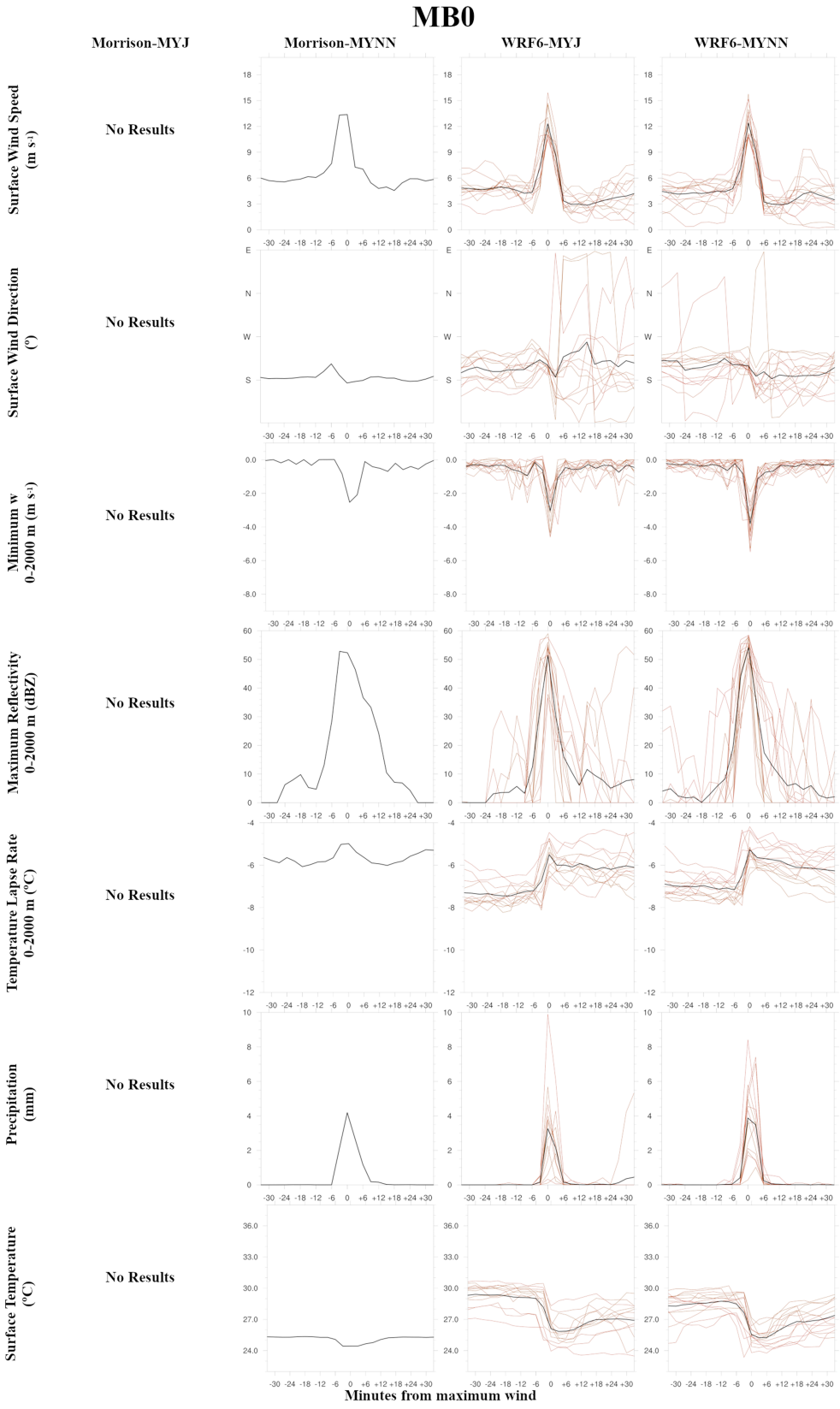

Figure 12. As Figure 10 for MB0.

of the event. Overall, it can be verified in Figures 10, 11, and 12 that the major differences appear between the microphysics parametrizations and not between the PBL parametrizations. In fact, the similarities between the results for WRF6 considering both PBL parametrizations are remarkable. Evaluating the standard deviations for the ±30 min window of each variable (results not shown), it becomes evident that the MYNN PBL parametrization generates a smaller dispersion than the MYJ parametrization, as it yields lower results for the majority of variables and cases. This can be clearly seen in the surface temperature plots for MB25 (Figure 10), where the dispersion values are 0.85 for Morrison-MYNN, 1.00 for WRF6-MYNN, 1.21 for WRF6-MYJ, and 1.47 for Morrison-MYJ. Another example would be the temperature lapse rate for the same date, generating 0.41 for Morrison-MYNN, 0.43 for WRF6-MYNN, 0.55 for WRF6-MYJ, and 0.76 for Morrison-MYJ.

Figure 10 presents the variables for every microburst simulated on MB25. It shows that the average maximum surface wind speed behaves in a pattern similar to the typical process description and complies with the defined wind conditions (Fujita, 1985). The average peak wind speed is approximately 12 m s^{-1}, being this result very consistent for every simulation. The wind speed is more or less stable up to −6 min, returning to approximately the initial speed at +6 min; thus, the event lasts between 6 and 12 min. Both speed and duration are in line with the defined microburst characterization. This would indicate that this variable is properly simulated by the model. Attending to the observations for MB25 (see section 2.1) some discrepancies can be noted. The average maximum wind speed is approximately 3 m s^{-1} lower than the observed speeds, and no simulation shows wind speeds larger than 20 m s^{-1}. To correct the methodical defects stated earlier, the wind gust plots are evaluated for every event and simulation (not shown). The Morrison-MYJ simulation produces two microbursts with gusts over 20 m s^{-1}, while the Morrison-MYNN produces one, the WRF6-MYJ generates nine, and the WRF6-MYNN simulates two. No simulation generates events with wind gusts over 25 m s^{-1} on MB25. Thus, the wind speed variable complies with the characteristics of a microburst but underestimates the maximum intensity. The peak in wind speed is coordinated with a sudden change in wind direction (Figure 10), concurring with the expected microburst process. The rotation is typically less than 90° to a southbound direction from the prevailing western winds. It usually occurs at −3 or 0 min and takes about 15 min to veer back to the original direction. Due to the lack of observations for this variable, it is difficult to evaluate if it is properly simulated.

The minimum negative w component of the wind in the lowest 2,000 m AGL yields mixed results (Figure 10). The sudden onset, timing, and duration of the subsidence are coordinated with the wind speed increase on the surface, reaching the lowest values at 0 min, in line with the genesis of the event (Wilson et al., 1984). Nevertheless, the averages for every simulation are typically over −4 m s^{-1}, and only a few simulated microbursts reach velocities under −6 m s^{-1}. This discrepancy from the characteristic average of −12 m s^{-1} (Hjelmfelt, 1988) makes this variable a weak point for these simulations, which is noteworthy as the w is the main process in the microburst event. Maximum reflectivity for the lowest 2,000 m AGL produces different results for each microphysics parametrization. Every simulation produces a sharp increase in coordination with the maximum wind speed, reaching the maximum reflectivity value at 0 min. This is in accordance with the microburst development and would correspond to the descending reflectivity nucleus (Kingsmill & Wakimoto, 1991; Wakimoto & Bringi, 1988). Averages for the Morrison scheme are above the 35 dBZ threshold. The WRF6 parametrization shows results below the limit, nevertheless, as the variable presents the expected behavior and it is properly coordinated with every other variable, the deficit can be considered negligible.

Temperature lapse rate results (Figure 10) show values below −7.5 °C km^{-1} before the microburst event for every simulation, in agreement with the characterization. A sharp increase of the lapse rate is coincident with the increment of maximum wind speed, and the largest value is typically reached at 0 min, as would expected by the flow of cold air descending from the middle atmosphere (Srivastava, 1985). Afterwards, the variable tends to decrease towards the original value for the WRF6 parametrization but remains the same for the Morrison-MYNN and slightly increases for the Morrison-MYJ. The performance of microphysics parametrizations for precipitation is similar to reflectivity. A maxima is noted at 0 min, as expected per the high-reflectivity microburst development (Srivastava, 1985), Morrison parametrizations clearly exceed the 0.25-mm limit, while the WRF6-MYNN does not reach the minimum. Finally, surface temperature also behaves as expected (Proctor, 1989) although values should be lower. The parcel of air descended from

colder layers of the atmosphere creates a sharp decrease of temperature for almost every simulation, typically around −3 °C, which is above the −4.2 °C average anomaly observed for MB25 (see section 2.1).

The variables for every microburst simulated on MB1 are presented in Figure 11. As evident on Table 1, the Morrison-MYNN simulation produces no microbursts; thus, it generates no results for this case. Evaluating the wind speed, the simulations are very consistent with the results produced for MB25, in behavior, duration of peak winds and wind speed. Wind direction also shows prevailing westerly winds and a change coordinated with the maximum wind speed; although for this case the change is larger than for MB25 (Figure 10), and winds tend to veer back to a more southerly direction than original. The minimum w for the lowest 2,000 m AGL (Figure 11) presents a similar behavior than for MB25, although for MB1 intensities are slightly closer to −4 m s^{-1} for the WRF6 simulations, and the average minimum w is approximately −6 m s^{-1} for the Morrison-MYJ parametrization. Nevertheless, the simulations are far from the characterization, and the variable remains as a weak result for these simulations. Reflectivity once again presents the Morrison-MYN simulations above the 35-dBZ limit, while the WRF6 simulations are below 30 dBZ on average. Temperature lapse rate produces a largely unstable situation for every simulation on MB1, close to being superadiabatic right before the microbursts are simulated. After the event the variable slowly decreases towards its original value. WRF6-MYJ does not comply with the characteristic threshold for precipitation, while the WRF6-MYNN barely reaches it. The surface temperature anomaly behaves similar to reflectivity for MB1. The Morrison-MYJ simulations show a marked drop coordinated to the microburst, close to −6 °C, while the WRF6 simulations present smaller anomalies.

Concerning the variables for MB0, shown on Figure 12, no microburst is simulated by the Morrison-MYJ; thus, it generates no results for the figure. The Morrison-MYNN simulation generates a single microburst with notable differences to the variables described for MB25 (Figure 10) and MB1 (Figure 11). Wind speed and minimum w behave in a similar pattern. Nevertheless, the wind direction shows a southerly flow with a slight change only before the maximum speed, the reflectivity produced is above 50 dBZ, and the precipitation is much larger than for previous cases. At the same time, temperature lapse rate presents a significantly less unstable condition and surface temperature is notably lower; both presenting only slight modifications to the maximum wind speed. All these results show that, despite producing a microburst when none was observed, the simulation is generating a difference in the variables, according to the differences in the thermodynamic situation shown in section 4.1.

The variables for the two WRF6 parametrizations (Figure 12) do not seem to respond in the same way to the changes in the thermodynamic conditions. There are only a few changes from the MB25 and MB1 cases, being the wind direction the most notable. This presents a southerly general flow, seems more chaotic than for the other cases, and does not generate a sharp and coordinated change to the maximum wind speed. Other than that, reflectivities are over 50 dBZ, and surface temperature is slightly lower than the other cases.

4.4. Variables Sensitivity

Table 2 shows the results generated by the detection script (see section 3.3). The assessment of several w intensities (from ground to 2,000 m AGL) once again shows that the model does not reach the characteristic threshold for this variable. As an example, when minimum w is individually tested for MB25, the Morrison-MYJ parametrization produces 0, 43, and 117 warnings for −9, −6, and −3 m s^{-1}, respectively. Imposing a threshold of −6 m s^{-1} yields the best results for this variable, very close to the initial time step count based on divergence for the Morrison-MYJ simulation (Table 1) and once again below the characteristic intensity. However, it has to be considered that the average minimum w for simulated microburst is close to −3 m s^{-1} (Figures 10, 11, and 12), so it can be assumed that most of the times when these w values are detected a microburst is not generated in the surface wind field. This makes this individual variable a poor detection tool.

Evaluating the downburst variables (from ground to 2,000 m AGL), several considerations have to be made. The threshold for w is set at −3 m s^{-1}, as it is the closer value to the average produced by the simulations. It is remarkable the difference between the Morrison and the WRF6 schemes for the temperature lapse rate on MB0. In this case, the Morrison parametrization is performing worse, as the observed thermodynamic diagram shows a low-level instability at 13:00 LT (Atkins & Wakimoto, 1991). It is also notable that, even the temperature lapse rate producing warnings for the majority of time steps, when it is combined with w,

Table 2
Number of Time Steps That Yield Test Warnings as per the Conditions Demanded, for Every Study Case and Parametrization Used

		Downburst (from 0 to 2,000 m AGL)								Outflow					
w (m s^{-1})		≤ −9	≤ −6	≤ −3	—	—	≤ −3	≤ −3	≤ −3						
T Lapse Rate (°C)		—	—	—	≤ −7.5	—	≤ −7.5	—	≤ −7.5						
Reflectivity (dBZ)		—	—	—	—	≥ 35	—	≥ 35	≥ 35						
Wind Speed (m s^{-1})										≥ 10	—	—	≥ 10	≥ 10	≥ 10
T Difference (°C)										—	≤ −4.2	—	≤ −4.2	—	≤ −4.2
Precipitation (mm)										—	—	≥ 0.25	—	≥ 0.25	≥ 0.25
		Positive test results (time steps) for conditions above													
MB25	Morrison-MYJ	0	43	117	185	95	87	87	50	183	43	119	31	80	31
	Morrison-MYNN	0	10	61	190	77	50	60	48	156	7	113	4	49	4
	WRF6-MYJ	0	40	134	202	143	128	127	120	183	116	155	65	122	63
	WRF6-MYNN	0	4	111	223	156	111	103	95	154	50	146	30	73	30
MB1	Morrison-MYJ	1	5	38	140	32	38	25	24	17	17	60	8	15	8
	Morrison-MYNN	0	0	2	140	10	2	1	1	0	0	33	0	0	0
	WRF6-MYJ	7	86	135	140	133	135	124	124	116	109	130	73	81	68
	WRF6-MYNN	5	79	123	140	122	123	113	113	92	83	118	60	77	58
MB0	Morrison-MYJ	0	5	96	0	208	0	84	0	43	0	238	0	16	0
	Morrison-MYNN	0	1	147	0	240	0	125	0	29	0	240	0	19	0
	WRF6-MYJ	0	56	240	161	240	36	236	13	161	119	240	5	156	5
	WRF6-MYNN	0	30	240	124	240	15	240	0	122	85	240	4	121	4

almost no event is detected. This shows that w is governing the sensitivity of the variables. When reflectivity is added to the combination, there are no drastic changes, but the results are improved. The combination of the three variables yields the best detection results for downburst. Assessing the parametrizations, the Morrison-MYNN simulation is the best performer in detecting the downburst, as the results are closer to the number of observed microbursts.

When the outflow variables are analyzed the surface temperature anomaly shows the better sensitivity to detect microbursts. For this variable, Morrison-MYJ shows a good correlation with the thermodynamic situation (see section 4.1) and the initial microburst count (Table 1). The surface wind speed and precipitation tend to reach the characteristic thresholds in many time steps. The combination of variables presents the best results when using the wind speed and temperature anomaly. The precipitation adds no useful information, as almost no difference can be seen when the three variables are combined. Regarding the parametrizations, the Morrison-MYJ performs best in detecting the outflow, as it yields a number of events closer to observations.

5. Conclusions

In this study, several episodes of high-reflectivity microbursts are simulated using the WRF model at spatial resolutions of 400 m and temporal resolutions of 3 min. Different microphysics and PBL parametrizations are tested to find the best model configuration for these events. Every parametrization used seems to capture the thermodynamic diagrams, the diurnal variation, and the characteristic variables of the microburst. The timing and coordination between variables are according to observations and characteristic process. Also the average values are in agreement with the characteristic thresholds, although there is a tendency to underestimate intensities, most notable for w. The dynamics of the microburst are properly reproduced too, with a good simulation of dimensions, time span, and dynamic development of events.

The Morrison microphysics scheme slightly outperforms the WRF6 parametrization in the modeling of the variables, although differences are not remarkable. As variables cannot be used as a definitive discriminator, the total number of microburst simulated remains the main difference between parametrizations. When this is considered, the Morrison parametrization clearly outperforms the WRF6. The sensitivity of the variables and the number of microbursts simulated by the WRF6 microphysics scheme do not seem to present a correlation with the different thermodynamic situation of each day, although these are properly reproduced. The Morrison-MYJ yields better results in the total count and performs better in capturing the outflow

when the variables' thresholds are considered. The Morrison-MYNN produces better results in the simulation of the variables related to the downburst and tends to simulate more uniform events as it has lower dispersion values.

One important issue requiring further study is the simulation of w. The analysis performed in this paper leads to the conclusion that the WRF model largely underestimates the intensity of this variable. Nevertheless, when the scientific literature is reviewed, it can be noted that the fist value proposed is just a mere $-3.6\ \mathrm{m\ s^{-1}}$. Although the characterization of this variable for the microburst is much larger, no study states a specific minimum value. At the light of the results of this paper, with an average w value very close to the aforementioned figure, it may be considered if high-reflectivity microbursts can develop with weaker w intensities than expected by the present knowledge.

Overall, it can be concluded that the WRF properly simulates the variables and dynamics of a high-reflectivity microburst. Although the results may appear to be suboptimal, it has to be considered that the WRF is a mesoscale model, not optimized to simulate microscale events. It has also to be noted that the microburst is a complex event, governed by several microphysics processes and atmospheric variables very sensitive to small changes, and in turn to natural variability, which renders it a meteorological phenomenon very hard to prognosticate in exact time and position even using real time data. When accounting for the internal variability, it cannot be expected for the model to simulate exactly the same number of microbursts, in the exact area and times. Thus, the simulations yielded by the Morrison-MYJ and the Morrison-MYNN parametrizations are close enough to observations to consider them as good performers.

Further research is required to fine-tune the WRF model for microburst detection, which will also depend on the geographical area of study. No specific variable shows the sensitivity required to be used as a prognostic tool. Nevertheless, the authors consider that using the available data and numerical predicting models, forecasting algorithms may already be viable. The application of existing warning indices and forecasting algorithms on numerical prediction models may be studied. From the results of this paper, the sharp variation over short periods of variables as surface wind divergence, temperature lapse rate, w, or Θ_e should be considered as possible precursors. Another possibility is to develop a forecasting algorithm based on different detection phases, which may use several simulations according to the performance of each parametrization for each microburst phase.

Acknowledgments
The authors declare no conflict of interest. The founding sponsors have no participation in the execution of the experiment, the decision to publish the results, nor in the writing of the manuscript. This work is supported by the Interdisciplinary Mathematics Institute of the Complutense University of Madrid and the following research projects: METEORISK (RTC-2014-1872-5), PCIN-2014-013-C07-04, PCIN-2016-080 (UE ERANET Plus NEWA Project), ESP2013-47816-C4-4-P, CGL2010-15930, CGL2016-81828-REDT, FEI-EU-17-16, and SAFEFLIGHT (CGL2016-78702-C2-1-R and CGL2016-78702-C2-2-R). This research is founded by the Spanish Ministry of Economy and Enterprise under the framework of the SAFEFLIGHT research project (CGL2016-78702-C2-1-R and CGL2016-78702-C2-2-R). The data used to support the conclusions of this paper are model outputs mainly. Model configuration scripts, data processing scripts, and processed data are available for further examination (https://doi.10.17632/xfxkpsg4mc.1). As this paper is part of an ongoing research at the time of publication, the dataset may be under a provisional embargo.

References

Atkins, N. T., & Wakimoto, R. M. (1991). Wet microburst activity over the southeastern United States: Implications for forecasting. *Weather and Forecasting*, *6*(4), 470–482. https://doi.org/10.1175/1520-0434(1991)006<0470:WMAOTS>2.0.CO;2

Atlas, D., Ulbrich, C. W., & Williams, C. R. (2004). Physical origin of a wet microburst: Observations and theory. *Journal of the Atmospheric Sciences*, *61*(10), 1186–1195. https://doi.org/10.1175/1520-0469(2004)061<1186:POOAWM>2.0.CO;2

Bolgiani, P., Fernández-González, S., Valero, F., Merino, A., García-Ortega, E., Sánchez, J. L., & Martín, M. L. (2018). Numerical simulation of a heavy precipitation event in the vicinity of Madrid-Barajas International Airport: Sensitivity to initial conditions, domain resolution, and microphysics parameterizations. *Atmosphere*, *9*(9), 24. https://doi.org/10.3390/atmos9090329

Burlando, M., Romanić, D., Solari, G., Hangan, H., & Zhang, S. (2017). Field data analysis and weather scenario of a downburst event in Livorno, Italy, on 1 October 2012. *Monthly Weather Review*, *145*(9), 3507–3527. https://doi.org/10.1175/MWR-D-17-0018.1

Byers, H. R., & Braham, R. R. (1949). *The thunderstorm*. Washington, DC: U.S. Government Printing Office.

Caplan, S. J., Bedard, A. J., & Decker, M. T. (1990). The 700–500 mb lapse rate as an index of microburst probability: An application for thermodynamic profilers. *Journal of Applied Meteorology*, *29*(8), 680–687. https://doi.org/10.1175/1520-0450(1990)029<0680:TMLRAA>2.0.CO;2

Carroll, D., Hollings, E. F., Garrett, G., Carpenter, E., Weather, N., & Jackson, S. (2011). *WRF optimization for forecasting wet microburst potential*. Abstract presented at *American Geophysical Union, Fall Meeting 2011*, A51A-0148.

Chou, M., & Suarez, M. (1999). A solar radiation parameterization (CLIRAD-SW) for atmospheric studies. In *NASA Tech. Memo* (Vol. 10460). Greenbelt, MD.

Chou, M., Suarez, M., Liang, X., & Yan, M. (2001). A thermal infrared radiation parameterization for atmospheric studies. In *NASA Technical Report* (Vol. *19*). Greenbelt, MD.

Creighton, G., Kuchera, E., Adams-Selin, R., McCormick, J., Rentschler, S., & Wickard, B. (2014). AFWA Diagnostics in WRF.

van Dijke, D., Hinssen, Y., & Bijlsma, F. (2011). A 500 m WRF hindcast of a microburst event in The Netherlands. Abstract presented at *European Meteorological Society Annual Meeting*, EMS2011-546-1, 8, 1–4.

Dodge, J., Arnold, J., Wilson, G., Evans, J. P., & Fujita, T. T. (1986). The cooperative Huntsville Meteorological Experiment (COHMEX). *Bulletin of the American Meteorological Society*, *67*(4), 417–419.

Ferrero, E., Mortarini, L., Manfrin, M., Solari, M., & Forza, R. (2014). Physical simulation of atmospheric microbursts. *Journal of Geophysical Research: Atmospheres*, *119*, 6292–6305. https://doi.org/10.1002/2013JD021243

Fujita, T. T. (1976). Spearhead echo and downburst near the approach end of a John F. Kennedy Airport runway. Chicago, IL.

Fujita, T. T. (1980). Downbursts and microbursts, an aviation hazard. *19th Conference on Radar Meteorology*, 8. Miami Beach, FL: American Meteorological Society.
Fujita, T. T. (1981a). Microbursts as an aviation wind shear hazard. *19th Aerospace Sciences Meeting*, 9. St. Louis, MO: American Institute of Aeronautics and Astronautics.
Fujita, T. T. (1981b). Tornadoes and downbursts in the context of generalized planetary scales. *Journal of the Atmospheric Sciences*, *38*(8), 1511–1534. https://doi.org/10.1175/1520-0469(1981)038<1511:TADITC>2.0.CO;2
Fujita, T. T. (1985). The downburst: Microburst and macroburst. In *SMRP Research Papers* (Vol. *210*). Chicago, IL.
Fujita, T. T., & Byers, H. R. (1977). Spearhead echo and downburst in the crash of an airliner. *Monthly Weather Review*, *105*(2), 129–146. https://doi.org/10.1175/1520-0493(1977)105<0129:seadit>2.0.co;2
Fujita, T. T., & Wakimoto, R. M. (1981). Five scales of airflow associated with a series of downbursts on July 16, 1980. *Monthly Weather Review*, *109*(7), 1438–1456. https://doi.org/10.1175/1520-0493(1981)109<1438:FSOAAW>2.0.CO;2
Fujita, T. T., & Wakimoto, R. M. (1983). JAWS microbursts revealed by triple-Doppler radar, aircraft, and PAM data. *13th Conference on Severe Local Storms*, 4.
Grell, G., & Freitas, S. R. (2014). A scale and aerosol aware stochastic convective parameterization for weather and air quality modeling. *Atmospheric Chemistry and Physics*, *14*(10), 5233–5250. https://doi.org/10.5194/acp-14-5233-2014
Hjelmfelt, M. R. (1988). Structure and life cycle of microburst outflows observed in Colorado. *Journal of Applied Meteorology*, *27*(8), 900–927.
Hong, S.-Y., & Lim, J.-O. J. (2006). The WRF single–moment 6–class microphysics scheme (WSM6). *Journal of the Korean Meterological Society*, *42*, 129–151.
James, R. P., & Markowski, P. M. (2010). A numerical investigation of the effects of dry air aloft on deep convection. *Monthly Weather Review*. https://doi.org/10.1175/2009MWR3018.1
Janjic, Z. I. (1994). The step-mountain eta coordinate model: Further developments of the convection, viscous sublayer, and turbulence closure schemes. *Monthly Weather Review*, *122*, 927–945. https://doi.org/10.1175/1520-0493(1994)122<0927:TSMECM>2.0.CO;2
Johns, R. H., & Doswell, C. A. (1992). Severe local storms forecasting. *Weather and Forecasting*, *7*, 588–612.
Kelly, D. L., Schaefer, J. T., & Doswell, C. A. (1985). Climatology of nontornadic severe thunderstorm events in the United States. *Monthly Weather Review*, *113*(11), 1997–2014. https://doi.org/10.1175/1520-0493(1985)113<1997:CONSTE>2.0.CO;2
Kessinger, C. J., Parsons, D. B., & Wilson, J. W. (1988). Observations of a storm containing misocyclones, downbursts, and horizontal vortex circulations. *Monthly Weather Review*, *116*(10), 1959–1982. https://doi.org/10.1175/1520-0493(1988)116<1959:OOASCM>2.0.CO;2
Kingsmill, D. E., & Wakimoto, R. M. (1991). Kinematic, dynamic, and thermodynamic analysis of a weakly sheared severe thunderstorm over northern Alabama. *Monthly Weather Review*, *119*(2), 262–297. https://doi.org/10.1175/1520-0493(1991)119<0262:KDATAO>2.0.CO;2
Knupp, K. (1988). Downdrafts within high plains cumulonimbi. Part II: Dynamics and thermodynamics. *Journal of the Atmospheric Sciences*, *45*(24), 3965–3982. https://doi.org/10.1175/1520-0469(1988)045<3965:DWHPCP>2.0.CO;2
Lin, W. E., Orf, L. G., Savory, E., & Novacco, C. (2007). Proposed large-scale modelling of the transient features of a downburst outflow. *Wind and Structures, An International Journal*, *10*(4), 315–346. https://doi.org/10.12989/was.2007.10.4.315
McCann, D. W. (1994). WINDEX—A new index for forecasting microburst potential. *Weather & Forecasting*, *9*(4), 532–541. https://doi.org/10.1175/1520-0434(1994)009<0532:WNIFFM>2.0.CO;2
McCarthy, J., Wilson, J. W., & Fujita, T. T. (1982). The joint airport weather studies project. *Bulletin of the American Meteorological Society*, *63*(1), 15–22.
Morrison, H., Thompson, G., & Tatarskii, V. (2009). Impact of cloud microphysics on the development of trailing stratiform precipitation in a simulated squall line: Comparison of one- and two-moment schemes. *Monthly Weather Review*, *137*(3), 991–1007. https://doi.org/10.1175/2008MWR2556.1
Nakanishi, M., & Niino, H. (2006). An improved Mellor-Yamada Level-3 model: Its numerical stability and application to a regional prediction of advection fog. *Boundary-Layer Meteorology*, *119*(2), 397–407. https://doi.org/10.1007/s10546-005-9030-8
NCAR (2019). *NCAR command language*. https://doi.org/10.5065/D6WD3XH5
NWS (2019). National Weather Service Monthly Weather Summary for Huntsville Airport. Retrieved February 24, 2019, from https://w2.weather.gov/climate/index.php?wfo=hun
Ohno, H., Suzuki, O., & Kusunoki, K. (1996). Climatology of downburst occurrence in Japan. *18th Conference on Severe Local Storms*, 87–90.
Oreskovic, C., Orf, L. G., & Savory, E. (2018). A parametric study of downbursts using a full-scale cooling source model. *Journal of Wind Engineering and Industrial Aerodynamics*. https://doi.org/10.1016/j.jweia.2018.07.020
Orf, L., Kantor, E., & Savory, E. (2012). Simulation of a downburst-producing thunderstorm using a very high-resolution three-dimensional cloud model. *Journal of Wind Engineering and Industrial Aerodynamics.*. https://doi.org/10.1016/j.jweia.2012.02.020
Potts, R. J. (1991). Microburst observations in tropical Australia. *25th Internation Conference on Radar Meteorology*, J67–J72.
Proctor, F. H. (1988). Numerical simulations of an isolated microburst. Part I: Dynamics and structure. *Journal of the Atmospheric Sciences*, *45*(21), 3137–3160. https://doi.org/10.1175/1520-0469(1988)045<3137:NSOAIM>2.0.CO;2
Proctor, F. H. (1989). Numerical simulations of an isolated microburst. Part II: Sensitivity experiments. *Journal of the Atmospheric Sciences*, *46*(14), 2143–2165. https://doi.org/10.1175/1520-0469(1989)046<2143:NSOAIM>2.0.CO;2
Pryor, K. L. (2015). Progress and developments of downburst prediction applications of GOES. *Weather and Forecasting*, *30*(5), 1182–1200. https://doi.org/10.1175/WAF-D-14-00106.1
Pryor, K. L., & Ellrod, G. P. (2004). WMSI—A new index for forecasting wet microburst severity. *National Weather Association Electronic Journal of Operational Meteorology*, *25*.
Roberts, R. D., & Wilson, J. W. (1989). A proposed microburst nowcasting procedure using single-Doppler radar. *Journal of Applied Meteorology*, *28*, 285–303. https://doi.org/10.1175/1520-0450(1989)028<0285:APMNPU>2.0.CO;2
Rydell, N. N., & Ladd, J. W. (1991). Toward a climatology of south Texas downbursts. *4th International Conference on Aviation Weather Systems*, 169–173. Paris, France.
Saha, S., Nadiga, S., Thiaw, C., Wang, J., Wang, W., Zhang, Q., ... Xie, P. (2010). NCEP Climate Forecast System Reanalysis (CFSR) 6-hourly Products, *January 1979 to December 2010*. https://doi.org/10.5065/D69K487J
Skamarock, W. C., & Klemp, J. B. (2008). A time-split nonhydrostatic atmospheric model for weather research and forecasting applications. *Journal of Computational Physics*, *227*(7), 3465–3485. https://doi.org/10.1016/j.jcp.2007.01.037
Skamarock, W. C., Klemp, J. B., Dudhia, J., Gill, D. O., Barker, D. M., Duda, M. G., ... Powers, J. G. (2008). A description of the advanced research WRF Version 3. *NCAR Technical Note NCAR/TN-475 + STR*, p. 113. https://doi.org/10.5065/D68S4MVH

Srivastava, R. C. (1985). A simple model of evaporatively driven downdraft: Application to microburst downdraft. *Journal of the Atmospheric Sciences*, *42*(10), 1004–1023. https://doi.org/10.1175/1520-0469(1985)042<1004:ASMOED>2.0.CO;2

Srivastava, R. C. (1987). A model of intense downdrafts driven by the melting and evaporation of precipitation. *Journal of the Atmospheric Sciences*, *44*(13), 1752–1773.

Tewari, M., Chen, F., Wang, W., Dudhia, J., LeMone, M. A., Mitchell, K., ... Cuenca, R. H. (2004). Implementation and verification of the unified NOAH land surface model in the WRF model. *20th Conference on Weather Analysis and Forecasting/16th Conference on Numerical Weather Prediction*, 10–15. Seattle, WA: American Meteorological Society.

Vermeire, B. C., Orf, L. G., & Savory, E. (2011a). A parametric study of downburst line near-surface outflows. *Journal of Wind Engineering and Industrial Aerodynamics*, *99*(4), 226–238.

Vermeire, B. C., Orf, L. G., & Savory, E. (2011b). Improved modelling of downburst outflows for wind engineering applications using a cooling source approach. *Journal of Wind Engineering and Industrial Aerodynamics*. https://doi.org/10.1016/j.jweia.2011.03.003

Wakimoto, R. M. (1985). Forecasting dry microburst activity over the high plains. *Monthly Weather Review*, *113*(7), 1131–1143. https://doi.org/10.1175/1520-0493(1985)113<1131:FDMAOT>2.0.CO;2

Wakimoto, R. M. (2001). Convectively driven high wind events. In C. A. Doswell (Ed.), *Severe convective storms* (Vol. 50, pp. 255–298). Boston, MA: American Meteorological Society. https://doi.org/10.1007/978-1-935704-06-5_7

Wakimoto, R. M., & Bringi, V. N. (1988). Dual-polarization observations of microbursts associated with intense convection: The 20 July storm during the MIST project. *Monthly Weather Review*, *116*(8), 1521–1539. https://doi.org/10.1175/1520-0493(1988)116<1521:DPOOMA>2.0.CO;2

Wakimoto, R. M., Kessinger, C. J., & Kingsmill, D. E. (1994). Kinematic, thermodynamic, and visual structure of low-reflectivity microbursts. *Monthly Weather Review*, *122*(1), 72–92. https://doi.org/10.1175/1520-0493(1994)122<0072:KTAVSO>2.0.CO;2

Wilson, J. W., Roberts, R. D., Kessinger, C. J., & McCarthy, J. (1984). Microburst wind structure and evaluation of Doppler radar for airport wind shear detection. *Journal of Climate & Applied Meteorology*, *23*(6), 898–915. https://doi.org/10.1175/1520-0450(1984)023<0898:MWSAEO>2.0.CO;2

Wolfson, M. M. (1990). Understanding and predicting microbursts. Massachusetts Institute of Technology.

Wolfson, M. M., Delanoy, R. L., Forman, B. E., Hallowell, R. G., Pawlak, M. L., & Smith, P. D. (1994). Automated microburst wind-shear prediction. *The Lincoln Laboratory Journal*, *7*(2), 399–426.

Wolfson, M. M., DiStefano, J. T., & Fujita, T. T. (1985). Low-altitude wind shear in the Memphis, TN area based on mesonet and LLWAS data. *14th Conference on Severe Local Storms*, 322–327. Indianapolis, IN: American Meteorological Society.

6.5. Microburst: Effective Resolution

Bolgiani, P., Santos-Muñoz, D., Fernández-González, S., Sastre, M., Valero, F., & Martín, M. L. (2020). **Microburst Detection with the WRF Model: Effective Resolution and Forecasting Indices**. *Journal of Geophysical Research: Atmospheres, 125*(14), e2020JD032883.

The following article was sent for publication in March 2020 to the JGR Atmospheres journal. This is ranked 17th in the Meteorology & Atmospheric Sciences category as per the 2018 Journal Citation Report. The Journal Impact Factor is 3.633. To the date this thesis is finished, the status is: Accepted for Publication, In Production.

JGR Atmospheres

RESEARCH ARTICLE
10.1029/2020JD032883

Microburst Detection With the WRF Model: Effective Resolution and Forecasting Indices

Pedro Bolgiani[1], Daniel Santos-Muñoz[1], Sergio Fernández-González[2], Mariano Sastre[1], Francisco Valero[1,3], and María Luisa Martín[3,4]

[1]Department of Earth Physics and Astrophysics, Faculty of Physics, Complutense University of Madrid, Madrid, Spain, [2]State Meteorological Agency (AEMET), Santander, Spain, [3]Interdisciplinary Mathematics Institute, Complutense University of Madrid, Madrid, Spain, [4]Department of Applied Mathematics, Faculty of Computer Engineering, University of Valladolid, Valladolid, Spain

Key Points:
- The WRF model shows an unrealistic energy spectrum when microscale spatial resolutions are used
- The effective resolution of the simulations casts doubts over the ability to forecast microbursts
- WINDEX, WMSI, and MWPI microburst indices show better forecasting performance than climatology, despite being suboptimal in general terms

Correspondence to:
P. Bolgiani,
pbolgian@ucm.es

Citation:
Bolgiani, P., Santos-Muñoz, D., Fernández-González, S., Sastre, M., Valero, F., & Martín, M. L. (2020). Microburst detection with the WRF model: Effective resolution and forecasting indices. *Journal of Geophysical Research: Atmospheres*, *125*, e2020JD032883. https://doi.org/10.1029/2020JD032883

Received 5 APR 2020
Accepted 14 JUN 2020
Accepted article online 18 JUN 2020

Abstract Microbursts are meteorological phenomena in the lower troposphere which can produce damaging surface winds and pose a severe risk to aircraft flying close to the ground. As these events usually span less than 4 km and 15 min, the spatiotemporal resolution is a challenge for numerical simulations. Although research of microburst using operative mesoscale models is scarce, the Weather Research and Forecasting (WRF) model has been used in the diagnosis of this phenomenon. In this paper, such model is used to simulate several microburst conducive days using two different boundary conditions. The energy spectra of the simulations are computed to evaluate the effective resolution of the model. The results are in line with previous studies and produce no notable differences among the boundary conditions. Nonetheless, the energy spectra show an overenergetic troposphere at microscale resolutions, rendering the effective resolution inadequate for microburst forecasting using the simulated physics variables. Thus, mesoscale indices are analyzed as a prognostic tool. The wind index, the wet microburst severity index and the microburst windspeed potential index do not show high forecasting performances, even though improving the results of climatology. Also, notable differences among the boundary conditions can be seen. The most consistent results are achieved by the wet microburst severity index.

1. Introduction

A *microburst* is a strong downdraft in the lower troposphere, generated by dynamic and thermodynamic effects in the midtroposphere, which produces a divergent pattern of surface wind with a differential speed of, at least, 20 m s^{-1} (Fujita, 1985; Fujita & Byers, 1977; Fujita & Wakimoto, 1981; Wakimoto, 1985). This surface wind forms a toroidal-shaped gust front (*outflow*) prone to producing severe damage, presenting a diameter under 4 km and a lifespan under 15 min (Fujita, 1980, 1981a). The differential wind speed over a relatively small distance produces a severe change in the relative airspeed of an aircraft flying through the outflow, posing a risk for aircraft flying low and slow, as in take off and landing operations. Being the event related to several accidents in the decade of 1980, microbursts are defined as a major meteorological hazard for aviation and flight safety (Fujita, 1980, 1981b; Wolfson et al., 1994). This promoted four major field campaigns, the latest one being the microburst and severe thunderstorm (MIST) project (Atkins & Wakimoto, 1991). Since these, no other major observational research has been performed specifically for microbursts, and thus, there is not much data based on adequate instruments. Srivastava (1987) performed notable studies in laboratory conditions to develop an ideal one-dimensional thermodynamic model, which was then confirmed by Doppler radar observations (Atlas et al., 2004). Proctor (1988) used ad hoc numerical models to gain further insight on the evaporative cooling of rain and hail, and on the dynamics of the outflow. This was later reproduced in idealized runs of numerical models (Lin et al., 2007; Vermeire et al., 2011), also used by James and Markowski (2010) to prove that dry air aloft is detrimental to microburst generation, contrary to previous findings. Some other ideal cloud models have been used for the research of downbursts (Oreskovic et al., 2018; Orf et al., 2012), but not particularly for microbursts. The review on aviation meteorology conducted by Gultepe et al. (2019) shows that research on the topic has been scarce in the last two decades, and that it still remains a very elusive phenomenon for prediction. To the authors' knowledge, the simulations performed by Bolgiani et al. (2020) are the first attempt to evaluate the ability of a mesoscale numerical weather prediction model to capture the characteristic variables of the microburst.

Microbursts can be divided in two categories considering the amount of precipitation generated and the radar reflectivity of the convective cell (Fujita, 1985; Fujita & Wakimoto, 1981; Wilson et al., 1984). Thus, *low-reflectivity* or *dry* microbursts generate less than 0.25 mm of precipitation and a reflectivity below 35 dBZ, while *high-reflectivity* or *wet* microbursts show values above those thresholds. High-reflectivity microbursts are associated with the development of convective cells (Atkins & Wakimoto, 1991), which occur at small spatiotemporal scales (Kunz, 2007), rendering the forecast a challenging task. In this regard, the use of thermodynamic indices can be very useful in the operation forecasting of extreme weather events (Gascón et al., 2015). Previous results by the authors show the ability of the Weather Research and Forecasting (WRF) numerical model to properly capture the variables and dynamics of the high-reflectivity microburst (Bolgiani et al., 2020). The vertical thermodynamic profile, the dimensions, and timing of the event are appropriately reproduced. The simulations show a descending reflectivity core which generates a precipitation shaft, associated with a vertical wind speed minimum and the related surface outflow. Surface and vertical wind speeds, reflectivity, precipitation, temperature lapse rate, and surface temperature are correctly reproduced as well, although a tendency to underestimate their intensity is observed. Nonetheless, the model presents a low sensitivity to the thermodynamic conditions, generating microbursts even when the simulated atmospheric environment is nonconducive to it. This casts doubts on the ability of the WRF model to properly forecast the phenomenon. In turn, the question arises as to whether using microscale spatial resolutions adds value to the simulations or simply forces the model to compute equations without retaining any useful data from the mesoscale and boundary conditions information.

This article is based on the aforementioned results and expands the previous research. The objectives of this study are two. First, to evaluate the effective resolution of the WRF model, used as an operational mesoscale model, in high spatiotemporal resolutions with two different boundary conditions. This is done to establish the ability of the model to forecast microburst events. The second objective is to evaluate different microburst forecasting indices currently used as operational tools. Accordingly, the paper is organized as follows: Section 2 describes the data used, the model configuration, the kinetic energy spectrum, and the microburst forecasting indices. Section 3 presents the assessment methods used, followed by the results and discussion in section 4. Finally, the conclusions are summarized in section 5.

2. Experiment Design

The experiment for this paper consists of the numerical simulation and assessment of two sets of simulations. Each set comprehends 20 days with recorded observations. The data used for validation are the observations of the MIST project (Atkins & Wakimoto, 1991), which is one of the major researches performed in microbursts. This field program was conducted in the northern part of the State of Alabama (USA) during June and July 1986, using a mesoscale array of 71 surface stations and three Doppler radar stations. A total of 62 microbursts are observed in 15 days, and 3 days are described as thunderstorm situations with no microbursts observations. All these days are simulated along with two others, which are randomly chosen among the remaining 43 days with no recorded microbursts nor special observations (Table 1).

2.1. WRF Configuration

The simulations are performed using the nonhydrostatic mesoscale Advanced Research WRF model version 4.0.3, which has been extensively proven and validated (Skamarock et al., 2008; Skamarock & Klemp, 2008). The configuration of the model is based on the best results from previous research by the authors on the same subject and study domain (Bolgiani et al., 2020). Four concentric domains (D1, D2, D3, and D4 from outermost to innermost) are defined with a two-way nesting strategy (Figure 1). The position and area of D4 approximately corresponds to the spatial domain of the MIST project (Atkins & Wakimoto, 1991), centered on 086°50″W 34°44″N. The resolution for each domain is as follows: D4 is 202 × 202 grid points with 400 m spatial and 3 min of output temporal resolution, D3 is 151 × 151 grid points with 1,200 m spatial and 30 min temporal resolution, D2 is 121 × 121 grid points with 3,600 m spatial and 60 min temporal resolution, and D1 is 121 × 121 grid points with 10,800 m spatial and 180 min temporal resolution. The vertical domain is 59 sigma levels from 1,000 to 50 hPa, with resolution decreasing with altitude, and four soil levels. Each day is simulated with a cold start run from 01:00 to 01:00 local time (LT) the next day. This allows for spin

Table 1
Dates Selected for Evaluation and Number of Microbursts Observed During the MIST Project

Date	Observation	Date	Observation	Date	Observation	Date	Observation
3 Jun	3	24 Jun	6	16 Jul	1	4 Jun	TH
7 Jun	6	26 Jun	2	17 Jul	1	10 Jun	TH
8 Jun	3	1 Jul	1	19 Jul	2	28 Jun	TH
17 Jun	5	6 Jul	4	20 Jul	1	10 Jul	NIL
21 Jun	1	13 Jul	25	28 Jul	1	23 Jul	NIL

Note: TH indicates observation of thunderstorms but no microburst, NIL indicates no special observation.

up, reaching the simulation daytime in stable conditions. Please note, LT is Universal Time Coordinated minus 5 hr for this time and location.

As per the parametrizations used, the microphysics scheme is Morrison (Morrison et al., 2009) and the planetary boundary layer (PBL) scheme is Mellor-Yamada-Janjic (Janjic, 1994). Longwave and shortwave radiation schemes are New Goddard called every 10 min (Chou et al., 2001; Chou & Suarez, 1999), soil layers scheme (technically, land surface scheme) is Unified Noah (Tewari et al., 2004), and surface-atmosphere interface scheme (technically, surface layer scheme) is Eta Similarity (Janjic, 1994). Cumulus clouds are computed for D3 and D4, while the Grell-Freitas Ensemble scheme called every time step (Grell & Freitas, 2014) is used for D1 and D2. The model is operated as nonhydrostatic in the four domains, with no w-damping. Please, refer to the data set associated with this paper for the complete model configuration details (see Data Availability Statement).

Two sets of simulations are performed, the only difference being in the boundary conditions used. One is taken from the Climate Forecast System Reanalysis (CFSR) developed by the National Centers for Environmental Prediction (NCEP). This has a surface spatial resolution of 0.312°, atmospheric spatial resolution of 0.5° and 37 vertical levels (Saha et al., 2010). The other conditions used are the European Centre for Medium-Range Weather Forecasts Re-Analysis 5 (ERA5), with a spatial resolution of 0.25° and 37 pressure levels (European Centre for Medium-Range Weather Forecast, 2019). In both cases, the boundary conditions are provided to the model at 6 hr intervals.

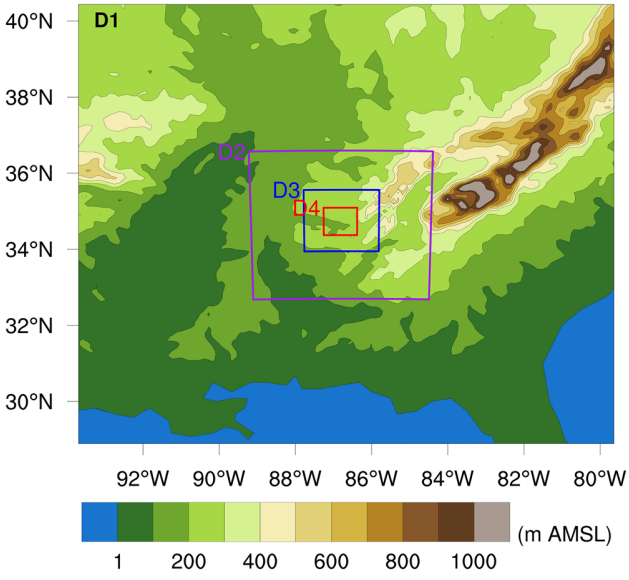

Figure 1. Orographic elevation and configuration of the nested domains used for the experiment.

2.2. Kinetic Energy Spectrum and Model Resolution

Since the numerical simulation of meteorology became a widespread research tool, the increase of spatiotemporal resolutions has been one of the paradigms for improving models and forecasting. As the availability of computational power has made high resolutions possible, the question arose as to what point increasing the model resolution is productive. One simple method of evaluating the effective resolution is to produce a diagram of the kinetic energy spectrum of the model (Skamarock, 2004). The spectral decomposition of the simulated wind produces a curve of the kinetic energy dissipation of the model. When this is compared to the theoretical dissipation curves, the performance of the model can be evaluated. The observations by Nastrom and Gage (1985) confirm that the kinetic energy associated with lower wave numbers (k), namely the planetary and large-scale processes, follows a theoretical dissipation curve proportional to k^{-3}, while the mesoscale (<400 km) atmospheric energy dissipates proportional to $k^{-5/3}$ (Kolmogorov, 1941). These observations of the upper troposphere confirm the theoretical curves down to the microscale limit (≈4 km) and are used by Lindborg (1999, equation 71) to create an equation which describes the energy dissipation. It has to be considered that the kinetic energy spectrum can be altered by synoptic conditions, the geographical region and even the local topography, thus, the domain selected for evaluation can induce

differences in the spectrum curve (Ricard et al., 2013; Skamarock, 2004). On the other hand, it is not noticeably affected by the altitude selected (in the free troposphere) nor by the dimension in which the spectral decomposition is performed (latitude or longitude).

As evident as it may be, mesoscale models are not optimized for microscale events. In consequence, most of the parametrizations schemes are not designed for microscale grid resolutions, and they may limit the competence of the model in these simulations, for example, two-dimensional radiation schemes. Bolgiani et al. (2020) results yield that the model configuration used is able to properly reproduce the microburst, but show no sensitivity of the variables to the thermodynamic conditions conducive to the phenomenon. This may be related to the aforementioned inadequacy. In the case of kinetic energy, turbulence, and wind, the vast majority of operative mesoscale models lack a large eddy simulation process and simply parameterize the energy dissipation (Skamarock et al., 2008), rendering it an unreliable process at high frequencies. There is a limit where the model parameterizations cannot produce a realistic dissipation curve anymore, and the kinetic energy spectrum diverges from the observed curve; this marks the effective resolution of the model. Skamarock (2004) defines the effective resolution as the wavelength where the model's spectrum begins to decay relative to the observed spectrum. He also estimates it to be approximately seven times the grid resolution ($7\Delta x$) down to spatial resolutions of 4,000 m for the WRF model. Any resolution under this limit may be considered inadequate as per the kinetic energy simulated. Even more, the Nyquist-Shannon sampling theorem (Nyquist, 1928) states that to completely reproduce a certain frequency the sampling rate must be at least 2 times the frequency. Thus, the models filter out any wavelengths below $2\Delta x$, marking the minimum resolution (Skamarock & Klemp, 2008). Nevertheless, it is not clear that the model follows the same dissipation behavior as resolution is forced into microscale. In fact, these resolutions are named *terra incognita* by Wyngaard (2004) as they are too coarse for large eddy simulations and too small for the spatial filtering of the equations of motion. For the WRF model the threshold into terra incognita may be ≈1,400 m, as Rai et al. (2017) results show large variations of the wind speed field for higher resolutions. Notwithstanding, finer resolutions can be explored as a better resolved orography and land surface processes can improve the PBL modelization (Skamarock, 2004).

2.3. Microburst Forecasting Indices

The dimensions of the microbursts are a challenge for predictability, not only when using numerical models but also when using real time data. As per the state of the art, the most reliable technique today would be nowcasting high-reflectivity microbursts by observing the descent of the reflectivity core using a Doppler-radar (Roberts & Wilson, 1989). Apart from this, every other forecasting technique relies on mesoscale data; essentially, algorithms trying to condensate the thermodynamic situation conducive to a microburst. There are three principal ad hoc algorithms for microburst forecasting:

McCann (1994) introduced the wind index (WINDEX) as a dimensionless index based on the thermodynamic profiles observed in microburst situations. It is designed to be computed from a regular sounding (it can also be calculated from satellite soundings) and comprehends the data from the ground to the 0°C level, where the microbursts initiate. It is formulated as follows:

$$\mathrm{WINDEX}=2.572\left[H_M R_Q \left(\Gamma^2-30+Q_L-2Q_M\right)\right]^{0.5} \quad (1)$$

where H_M is the height of the 0°C level in (km above the ground), $R_Q = Q_L/12$ but not greater than 1, Γ is the temperature lapse rate from the surface to the 0°C level (°C km^{-1}), Q_L is the average mixing ratio in the lowest 1 km above the surface (g kg^{-1}), and Q_M is the mixing ratio at the 0°C level (g kg^{-1}). Originally, the WINDEX is calibrated to yield a product equal to knots, but here the scaling factor is 2.572 to estimate the index in m s^{-1}. Typical values for this index would be the same as for the wind speed associated with the microburst.

Pryor and Ellrod (2004) produced the wet microburst severity index (WMSI). This dimensionless index considers convection to summarize the thermodynamic profile and precipitation formation, and the equivalent potential temperature deficit from the ground to the midtroposphere as an indicator of evaporative cooling and the generation of negative buoyancy. It is designed to be computed from satellite data. It is defined as follows:

$$\mathrm{WMSI}=\mathrm{CAPE}\ (\Theta e_{\max}-\Theta e_{\min})/1,000 \tag{2}$$

where CAPE is the surface based convective available potential energy (J kg^{-1}), Θe_{max} is the maximum value of equivalent potential temperature at the surface, and Θe_{min} is the minimum value of equivalent potential temperature in the midlevels of the troposphere. The scaling factor of 1,000 J kg^{-1} is applied based on observations. Typical values for this index would be ≈50 for a 18 m s^{-1} wind gust or 80 for a 26 m s^{-1} wind gust.

Pryor (2015) then developed the microburst windspeed potential index (MWPI). This is another dimensionless index, formulated as an improvement of the previous one. It considers updated knowledge on the role of relative humidity in the troposphere and is designed to consider both high and low reflectivity microbursts. It is composed as follows:

$$\mathrm{MWPI}=\mathrm{CAPE}/1,000+\Gamma/5+\left[(T-T_d)_{850}-(T-T_d)_{670}\right]/5 \tag{3}$$

where Γ is the temperature lapse rate from 850 to 670 hPa (°C km^{-1}), T is temperature (°C) and T_d is dewpoint temperature (°C), both at 850 and 670 hPa. The scaling factors of 1,000 J kg^{-1}, 5°C km^{-1} and 5°C are applied based on observations. Typical values for this index would be ≈2 for a 19 m s^{-1} wind gust or 4 for a 23 m s^{-1} wind gust.

Most of the data used to compute these products are derived from satellite instruments such as the Infrared Atmospheric Sounder Interferometer (Menzel et al., 2018), which provides a vertical resolution of 1 km in the lower troposphere, a horizontal resolution of 25 km, and an accuracy of 1 °K. This instrument is currently operating in polar orbiting satellites and is planned to be onboard the geostationary Meteosat Third Generation (Serio et al., 2012). As a consequence of the resolutions provided, none of these indices can produce a spatiotemporal accurate prognostic, although they are useful tools to identify meso-beta conditions.

3. Assessment Methodology

The software used to perform the evaluation are the R programming language (R Core Team, 2020) version 3.4.4 and the National Center for Atmospheric Research Command Language (NCAR, 2019) version 6.6.2. Please refer to the data set associated with this paper for the script details (see Data Availability Statement).

The methodology used for producing the kinetic energy spectrum is based on the procedure described by Skamarock (2004) and Abdalla et al. (2013). Wind speed is calculated (using u, v, and w components) at hourly intervals from 07:00 to 24:00 LT. This time window allows for a spin up time of 6 hr while spanning the complete diurnal variation of microbursts recorded by Atkins and Wakimoto (1991). The anomalies are computed by removing the average wind speed, and the time series is detrended before calculating the energy. The spectral decomposition of the energy is performed longitudinal-wise (at each latitudinal grid point) using single vertical (sigma) levels. The resulting energy spectra are averaged over latitude and then over every day simulated. Thus, hourly energy spectra for each set of simulations are derived. These are plotted together with the total average. The plots are redimensioned into wave number and energy density for easier understanding. The Lindborg (1999, equation 71) energy dissipation curve is added to ease the assessment. The wind speed at 1,000 hPa is selected for evaluation, as the closest level to the ground, where the microburst's outflow takes place. It is worth mentioning that, as we are evaluating the energy on a single level and a relatively small domain, the potential energy differences can be overlooked and the kinetic energy can be considered the total of the system.

To test the aforementioned microburst indices, a dichotomous validation is performed (Nurmi, 2003). This is computed using many thresholds for each index, thus assessing the sensitivity of the algorithm. As the observational data available (Atkins & Wakimoto, 1991) does not provide location or timing of the microbursts (only the number observed each day), the validation needs to be performed for the complete domain in daily time windows. To achieve this, the indices are calculated at every grid point for D2, D3, and D4, from 07:00 to 24:00 LT at each output time. To equate the assessment area, D2 and D3 are cropped to match D4. Considering that the microburst downdraft requires ≈10 min to reach the surface (Srivastava, 1987), and an average microburst outflow lifespan of 15 min (Hjelmfelt, 1988), the domain maxima are then selected every 30 min (as D2 has a temporal resolution of 60 min, results are linearly interpolated). This yields 34

maximum values for each index at each day. To create the daily contingency tables, a threshold is selected for the index in question, and any value reaching that threshold is considered a hit. When the number of hits does not reach the number of daily observations, the remainder are considered misses. When the daily hits exceed the number of observations, the surplus are considered false alarms. If there are no hits and no observations, a correct negative is considered. Following the previous procedure, contingency tables are computed for various threshold values: WINDEX from 0 to 29 at single-unit increases, WMSI from 0 to 290 at 10-unit increases, and MWPI from 0 to 14.5 at 0.5-unit increases. The resulting tables are used to calculate the probability of detection (POD) and probability of false detection (POFD) of each threshold and domain resolution. These are then averaged over every day creating a POD and a POFD for each index threshold considered, which can be compared in a receiver operating characteristic (ROC) curve plot. In addition, the area under the curve (AUC) for each index are computed (Nurmi, 2003) using a trapezoidal integration. Finally, to establish a reference for comparison, the climatology ROC curve is also plotted. The climatology is defined as the daily average from the summation of the three major microburst field programs (Atkins & Wakimoto, 1991; McCarthy et al., 1982; Wolfson et al., 1985), considering every day of study and conforming the data to the MIST domain area. Thus, the climatology results in an average of 1.5 microbursts per day in the MIST domain and a standard deviation (σ) of 3.7. The aforementioned procedure is followed to create the contingency tables for climatology, although in this case the thresholds are computed using $\pm 3\sigma$ increases from the average.

4. Results and Discussion

As the spectra are affected by the amount of energy in the system, before evaluating the overall energy spectrum for the simulations, it is worth to previously consider the response it shows to several factors. With this objective, different days at 18:00 LT are evaluated against the thermodynamic diagram and the synoptic situation in Figure 2. Three days are selected, each one representing a different situation: 6 July is a day with four microburst observations, 10 June is a day with thunderstorms but no microbursts observations, and 23 July is a typical summer day with no thunderstorm nor microburst observations. As the results are very similar for both boundary conditions, only those for ERA5 are shown, based on the better resolution provided by these conditions. The 6 July day presents a characteristic high-reflectivity microburst thermodynamic diagram associated with deep convection (Atkins & Wakimoto, 1991) and showing an almost superadiabatic dry layer below the cloud base (850 hPa). These mesoscale conditions are in contrast with the low energetic synoptic conditions, which show small pressure gradients and wind speeds for D1. Thus, the spectrum for D1 falls below the expected curve, in line with previous results (Ricard et al., 2013; Skamarock, 2004). It should also be considered that the theoretical curve (Lindborg, 1999) is estimated for the upper troposphere and these spectra are computed at 1,000 hPa. At finer resolutions, higher amounts of energy are captured by the model (Rai et al., 2017; Skamarock & Klemp, 2008), hence the parallel shifting to lower wavelengths in smaller domains, which can also be appreciated in Skamarock (2004) results. This is most evident for D4, which produces an unrealistically overenergized spectrum as a consequence of the model trying to resolve microscale winds affected by convection and orographic forcing. To illustrate this, the average wind speed over the D4 area is computed on 6 July at 18:00 LT. The results for each resolution are 1.25 m s^{-1} for 10,800 m, 1.28 m s^{-1} for 3,600 m, 1.30 m s^{-1} for 1,200 m, and 1.83 m s^{-1} for 400 m.

The 10 June day presents a more humid thermodynamic diagram with a deep conditionally unstable layer reaching above the 0°C level, at ≈600 hPa (Figure 2). The atmospheric pattern highlights an energetic situation, with a low-pressure system on the west generating a considerable gradient and wind speeds in agreement with a front passage. As a result, the dissipation curves are steeper and yield larger amounts of energy for every domain, most noticeable for D3. D4 yields an unrealistic result again and D1 comes closer to the expected curve, correcting the low-energy situation of 6 July but still penalized by the lower-energy content of near-surface winds. The results for 23 July show a low-energy stable atmospheric pattern with unstable local conditions. These are evident in the thermodynamic diagram and the wind speed "spots," probably generated by mesoscale convective systems. Thus, D1 and D2 present a somewhat mixed state between the previous two situations, while D3 shows a curve very similar to 6 July most probably due to local instability. These three spectra seem to converge into a general spectrum, as they also do for 6 July. Nevertheless, D4 is an outlier once more, generating an unrealistic level of energy, even this being the lowest of the three days evaluated.

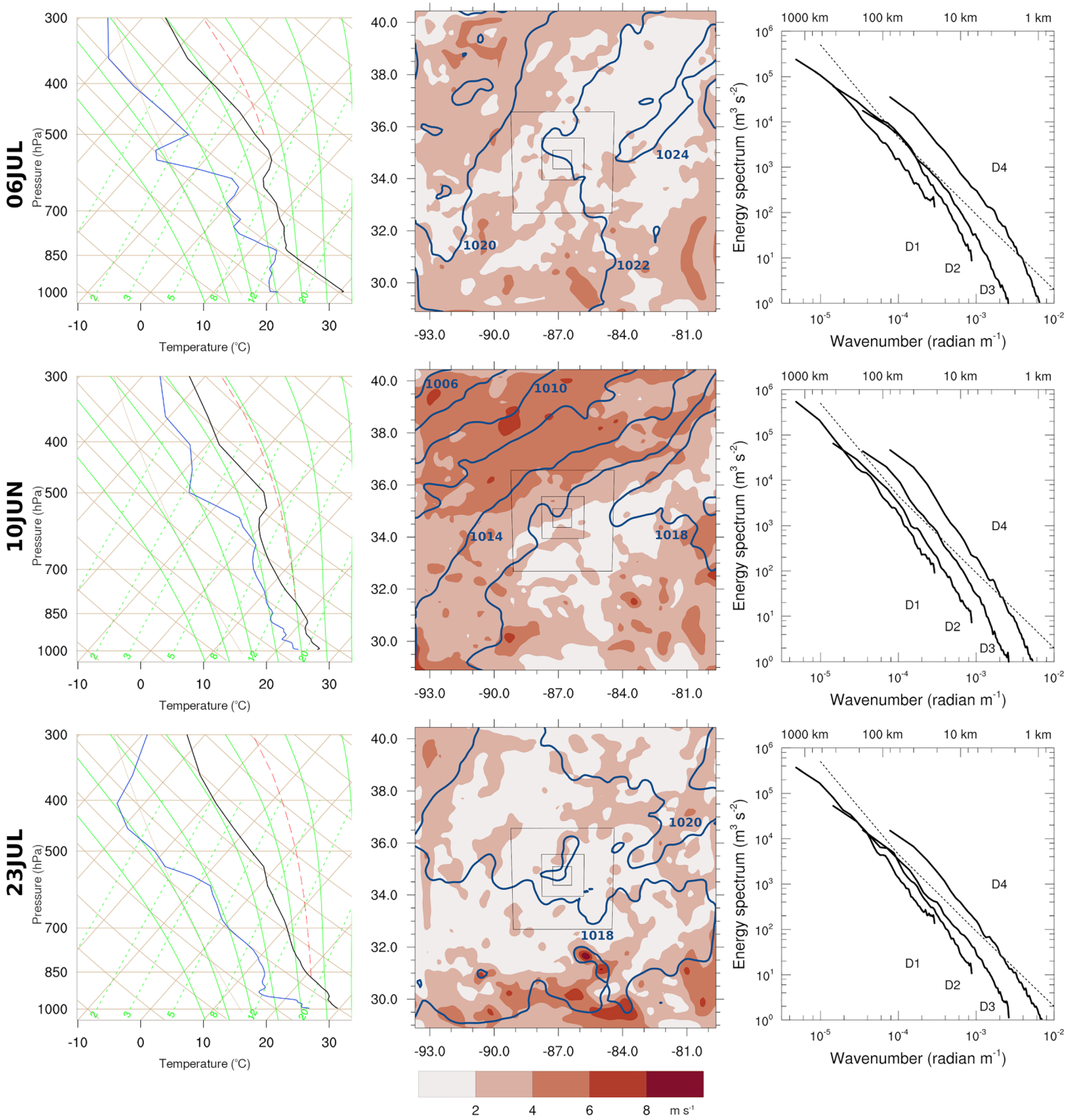

Figure 2. Synoptic analysis for ERA5 simulations at 18:00 LT for 6 Jul (four microbursts observed), 10 Jun (thunderstorms observed), and 23 Jul (no significant weather observed): (left column) Thermodynamic diagram at the center of the domain; black line is temperature, blue line is dew point temperature. (middle column) Sea level pressure (hPa) and wind speed at 1,000 hPa; black squares represent inner domains as per Figure 1. (right column) Wind kinetic energy spectra at 1,000 hPa; dashed line represents dissipation rates as per Lindborg (1999, equation 71).

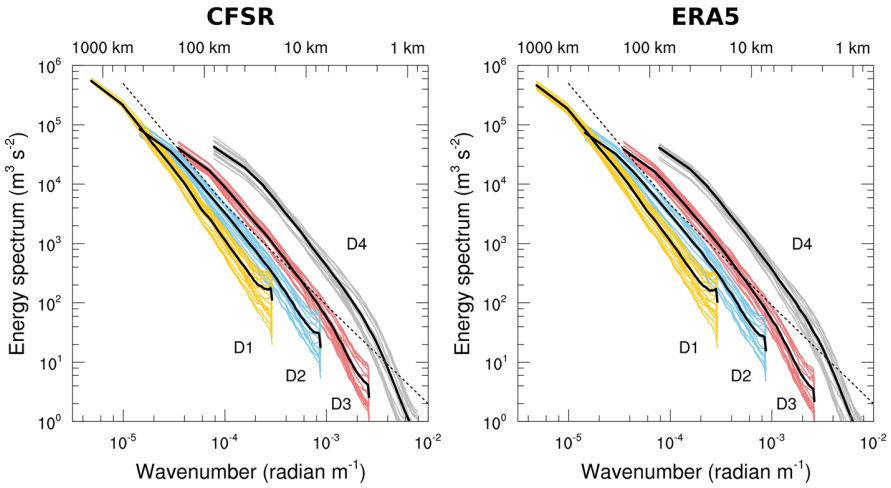

Figure 3. Wind kinetic energy spectra at 1,000 hPa for each domain and set of simulations: (left) CFSR; (right) ERA5. Black curves correspond to the spectral average. Dashed line corresponds to dissipation rates as per Lindborg (1999, equation 71).

4.1. Energy Spectrum

When evaluating the total average kinetic energy spectra for each set of simulations (Figure 3), the first results to consider are the differences among them. The spectra are very similar for CFSR and ERA5, although CFSR inputs a slightly larger amount of energy in the simulations, most noticeable in the smaller wave numbers at D1 and D2. This is consistent with the fact that both boundary conditions are taken from smooth reanalyses, which contribute little energy to the mesoscale spectrum. Nevertheless, the different energy content can also be appreciated in the mesoscale wave numbers, as the spin up time allows the energy to be transmitted downstream from large-scale wave numbers, generating fine-scale structures (Skamarock, 2004). Notwithstanding the previous considerations, the similarity of the spectra renders the influence of boundary conditions negligible. The maximum resolution of each spectra equals the domain size, as this acts as a filter for larger wavelengths. The decay of the curves when reaching the upper energy limits is related to the fact that they are computed at 1,000 hPa, removing the planetary-scale waves present in the upper troposphere (Skamarock, 2004). The minimum resolution for the curves follows the $2\Delta x$ rule as expected (Nyquist, 1928). The spectra also produce a decaying tail with a small upturn before the minimum resolution, proving only that a small aliasing of larger wave numbers is being generated, in accordance with the typical limited-area model behavior described by Skamarock (2004). The dispersion generated for each domain is created by the hourly spectra, and thus represents the average daily variability. As the majority of days simulated can be considered highly convective (Table 1), the variability is large and more pronounced in the smaller wavelengths. The convective activity is also responsible for part of the energy overestimation in the smaller wavelengths of the spectra. Nevertheless, similar to previous results, D4 produces a highly improbable overenergetic curve. In consequence, 400 m should be considered an unreliable resolution to simulate the meteorological conditions of the days selected. The same consideration should be done with the resolution of 1,200 m, as D3 also shows a large part of the curve above the expected energy level. This is consistent with the results of Rai et al. (2017) which establish the spatial resolution of 1,400 m as the beginning of terra incognita for the WRF model. On the other hand, the curve for D1 adjusts reasonably well to the expected dissipation rate for the larger wavelengths, as the energy deficit observed may be attributed to low-energy synoptic situations and the near-surface wind speeds. D2, with 3,600 m resolution, is the best performing domain. This is in line with the fact that WRF is a mesoscale model, not optimized to use microscale resolutions.

In addition, even if the spectra do not show a marked decay (Figure 3), an effective resolution can be established. A drop of the spectrum is clearly visible at a wavelength of ≈3 km for D4 and at ≈9 km for D3. The decay is still observable for D2 around 30 km. These effective resolutions are about $8\Delta x$, not far from the behavior described by Skamarock (2004). This has important implications for the simulation of

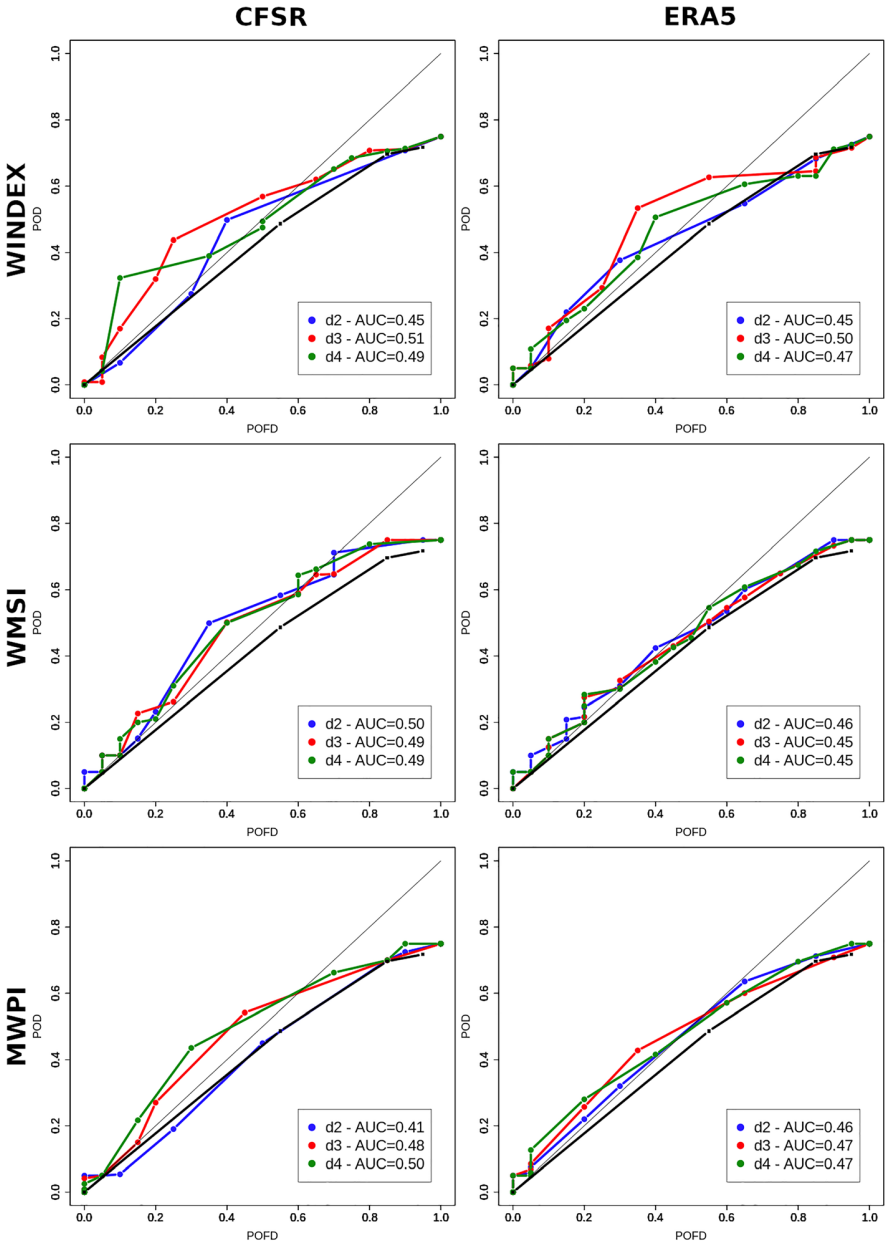

Figure 4. Average ROC curves and AUC for (top row) WINDEX, (middle row) WMSI, and (bottom row) MWPI tested at each domain and set of simulations: (left) CFSR; (right) ERA5. The black curve in each plot corresponds to the climatology ROC.

microbursts with WRF, as these cannot be considered appropriate resolutions for this kind of event. Bolgiani et al. (2020) results prove that the model is able to diagnose the microburst, properly simulating the characteristic variables and dynamics of the event, although when the physical variables' sensitivity are tested, they show no ability for forecasting. The results here produced for the energy spectrum are in line with these conclusions: as per the uncertainty introduced, no forecasting ability can be expected from the simulation of the microscale physical variables of a microburst. However, most of the variables considered by the microburst forecasting indices are mesoscale-related conditions (see section 2.3), therefore, these are worth to be evaluated.

4.2. Microburst Forecasting Indices

Figure 4 depicts the ROC curves for the three indices considered at both sets of simulations. Before evaluating the indices, it is worth analyzing the climatology curve. The forecast based on the climatological data yields a poor performance, even a negative predictive ability, as evident by a curve clearly below the nondiscrimination diagonal (this would represent a zero skill, random guess forecasting). These results are understandable when taking into account the large variability of the event, as highlighted by Table 1 and the first- and second-order moments of the climatology (1.5 and 3.7, respectively). In addition, as microbursts observations with the appropriate equipment are so scarce, the available climatological data yield a large uncertainty, making it a poor forecasting tool. Another feature to take into account is the behavior of the curve when reaching the maximum POFD. The curve reaches an inflection point, rapidly increasing the POFD for marginal increases of POD, which may be related to the contingency table for 13 July, as on this date 25 microbursts are observed. When the threshold used to compute the contingency table is decreased to a minimum, with the objective of reaching the 25 hits on this date, the number of false alarms rises dramatically for every other date. Thus, the average POFD reaches the maximum value before reaching a POD of 0.8. This feature is reproduced in every other curve in the figure.

When the ROC curves for the indices are evaluated (Figure 4), the results show that every one of them improves the results of the climatology forecast. Nevertheless, none shows an outstanding performance as no curve largely separates from the diagonal. Also, AUC values are hindered by the aforementioned inflection near the maximum POFD. Comparing the results for each boundary condition, CFSR performs better than ERA5 at every index. Even if the total energetic input is practically the same for both, that energy may be distributed in dissimilar spatial patterns or atmospheric variables. These variations will yield different energy expressions when downscaled and, in turn, the model will compute different values for a given variable. This effect is stronger for variables which are postprocessed from simpler ones, like CAPE or convection triggering. Although the different indices' results are not optimal, there is a clear added value against the climatology for the CFSR simulations. For the ERA5 set, only the WINDEX shows a forecasting ability (with slightly worse AUC than for CFSR), the WMSI and the MWPI being close to a random forecast.

Regarding the results for the CFSR (Figure 4), the WMSI yields the most robust ones, as every domain produces a similar curve with a maximum around 0.50 POD and 0.35 POFD. The AUC values reflect the same behavior, with very consistent results close to 0.49. The WINDEX at D3 produces the best AUC (0.51), nonetheless, each domain generates a different curve reflecting a less coherent forecast. The MWPI shows similar curves for D3 and D4, although D2 is a very poor performer, close to the climatology. The differences shown by the indices are in part related to the variables they consider and the complexity of the algorithm. This is evident for WINDEX, which presents a large variability among the different resolutions as it contemplates variables verging the microscale. The WMSI, on the other hand, only accounts for CAPE and Θe, which are variables indicative of the mesoscale behavior. It also may be tempting to conclude that the WINDEX at D3 presents the best AUC and therefore is the best performer, but here the energy spectrum results should be taken into account. The uncertainty and the effective resolution produced by microscale grid resolutions demand to take with care any other result on these domains and give priority to the most consistent ones.

5. Conclusions

In this study, several days with observed microbursts activity are simulated using the WRF model at high spatiotemporal resolutions and two different boundary conditions. The energy spectra of the simulations are evaluated to establish the minimum and effective resolutions of the model. These prompt the use of mesoscale forecasting indices for microbursts. According to the results, we can yield the following conclusions:

1. The kinetic energy quantity and dissipation rate simulated by the WRF model responds adequately to the different large-scale and mesoscale conditions evaluated.
2. The total input of energy by the CFSR and ERA5 reanalyses is practically identical.
3. The energy spectra fit reasonably well the observations in meso-beta resolutions. Nonetheless, when the model is forced into finer resolutions it produces an overenergetic troposphere.

4. Due to the unrealistic energy spectrum, the resolutions of 400 m (D4) and 1,200 m (D3) should be considered unreliable. Thus, considering the grid spacing of 3,600 m (D2), the minimum resolution for the simulations is 7.2 km and the effective resolution is approximately 30 km.
5. As per the aforementioned conclusion, the WRF simulation of microbursts is not reliable in atmospheric energy terms. This would partly explain the poor sensitivity of the characteristic variables shown by the authors in previous results (Bolgiani et al., 2020).
6. The forecasting ability of microburst climatology is very poor, most probably due to the very rare scientific observations.
7. When microburst forecasting indices based on mesoscale variables are applied, these show an improvement over a prognostic based on climatology.
8. CFSR boundary conditions show better prognostic results for the forecasting indices than ERA5.
9. The WMSI produces the most robust results, consistently achieving a POD of 0.50 against a POFD of 0.35 for every domain evaluated. Nevertheless, the WINDEX and the MWPI indices yield similar AUC values in some domains.

In summary, it can be concluded that the WRF model performs an adequate diagnosis of the microburst, although it does not present a high performance in the forecasting of the event. Nevertheless, the results show an added value over statistical data, indicating that it may be viable to achieve a reliable forecasting tool. Further research is required to improve the microburst detection using the WRF model, by fine-tuning the parametrizations, the model configuration, or developing new forecasting indices adapted to mesoscale numerical simulations.

Data Availability Statement

The model configuration files, data processing scripts, and processed data used to support the conclusions of this paper are available for further examination (https://doi.org/10.17632/fv6tg9n2jh.1).

Acknowledgments

The authors declare no conflict of interest. The funding sponsors have no participation in the execution of the experiment, the decision to publish the results, nor the writing of the manuscript. This work is supported by the Interdisciplinary Mathematics Institute of the Complutense University of Madrid and funded by the Spanish Ministry of Economy and Enterprise under the following research projects: PCIN-2014-013-C07-04, PCIN-2016-080 (UE ERANET Plus NEWA Project), CGL2016-81828-REDT, FEI-EU-17-16, SAFEFLIGHT (CGL2016-78702-C2-1-R and CGL2016-78702-C2-2-R), PID2019-105306RB-I00. This work is also supported by the ECMWF special projects SPESMART and SPESVALE.

References

Abdalla, S., Isaksen, L., Janssen, P., & Wedi, N. (2013). Effective spectral resolution of ECMWF atmospheric forecast models. *ECMWF Newsletter*, *137*, 19–22. https://doi.org/10.21957/rue4o7ac

Atkins, N. T., & Wakimoto, R. M. (1991). Wet microburst activity over the Southeastern United States: Implications for forecasting. *Weather and Forecasting*, *6*(4), 470–482. https://doi.org/10.1175/1520-0434(1991)006<0470:WMAOTS>2.0.CO;2

Atlas, D., Ulbrich, C. W., & Williams, C. R. (2004). Physical origin of a wet microburst: Observations and theory. *Journal of the Atmospheric Sciences*, *61*(10), 1186–1195. https://doi.org/10.1175/1520-0469(2004)061<1186:POOAWM>2.0.CO;2

Bolgiani, P., Fernández-González, S., Valero, F., Merino, A., García-Ortega, E., Sánchez, J. L., & Martín, M. L. (2020). Simulation of atmospheric microbursts using a numerical mesoscale model at high spatiotemporal resolution. *Journal of Geophysical Research: Atmospheres*, *125*, 1–23. https://doi.org/10.1029/2019JD031791

Chou, M., & Suarez, M. (1999). A solar radiation parameterization (CLIRAD-SW) for atmospheric studies. In *NASA Tech. Memo* (Vol. 10460).

Chou, M., Suarez, M., Liang, X., & Yan, M. (2001). A thermal infrared radiation parameterization for atmospheric studies. In *NASA Technical Report* (Vol. 19, Issue May 2003).

European Centre for Medium-Range Weather Forecast. (2019). ERA5 reanalysis (0.25 degree latitude-longitude grid). https://doi.org/10.5065/BH6N-5N20.

Fujita, T. T. (1980). Downbursts and microbursts, an aviation hazard. *19th Conference on Radar Meteorology*, 8.

Fujita, T. T. (1981a). Tornadoes and downbursts in the context of generalized planetary scales. *Journal of the Atmospheric Sciences*, *38*(8), 1511–1534. https://doi.org/10.1175/1520-0469(1981)038<1511:TADITC>2.0.CO;2

Fujita, T. T. (1981b). Microbursts as an aviation wind shear hazard. *19th Aerospace Sciences Meeting*, 9.

Fujita, T. T. (1985). In *The downburst: Microburst and macroburst*, *SMRP Research Papers* (Vol. 210, pp. 1–128). Chicago, Illinois, USA: University of Chicago.

Fujita, T. T., & Byers, H. R. (1977). Spearhead echo and downburst in the crash of an airliner. *Monthly Weather Review*, *105*(2), 129–146. https://doi.org/10.1175/1520-0493(1977)105<0129:seadit>2.0.co;2

Fujita, T. T., & Wakimoto, R. M. (1981). Five scales of airflow associated with a series of downbursts on July 16, 1980. *Monthly Weather Review*, *109*(7), 1438–1456. https://doi.org/10.1175/1520-0493(1981)109<1438:FSOAAW>2.0.CO;2

Gascón, E., Merino, A., Sánchez, J. L., Fernández-González, S., García-Ortega, E., López, L., & Hermida, L. (2015). Spatial distribution of thermodynamic conditions of severe storms in southwestern Europe. *Atmospheric Research*, *164-165*, 194–209. https://doi.org/10.1016/j.atmosres.2015.05.012

Grell, G., & Freitas, S. R. (2014). A scale and aerosol aware stochastic convective parameterization for weather and air quality modeling. *Atmospheric Chemistry and Physics*, *14*(10), 5233–5250. https://doi.org/10.5194/acp-14-5233-2014

Gultepe, I., Sharman, R., Williams, P. D., Zhou, B., Ellrod, G. P., Minnis, P., et al. (2019). A review of high impact weather for aviation meteorology. *Pure and Applied Geophysics*, *176*(5), 1869–1921. https://doi.org/10.1007/s00024-019-02168-6

Hjelmfelt, M. R. (1988). Structure and life cycle of microburst outflows observed in Colorado. *Journal of Applied Meteorology*, *27*(8), 900–927. https://doi.org/10.1175/1520-0450(1988)027<0900:SALCOM>2.0.CO;2

James, R. P., & Markowski, P. M. (2010). A numerical investigation of the effects of dry air aloft on deep convection. *Monthly Weather Review*, *138*(1), 140–161. https://doi.org/10.1175/2009MWR3018.1

Janjic, Z. I. (1994). The step-mountain eta coordinate model: Further developments of the convection, viscous sublayer, and turbulence closure schemes. *Monthly Weather Review*, *122*(5), 927–945. https://doi.org/10.1175/1520-0493(1994)122<0927:TSMECM>2.0.CO;2
Kolmogorov, A. N. (1941). The local structure of turbulence in incompressible viscous fluid for very large Reynolds numbers. *Doklady Akademii Nauk*, *434*(1890), 9–13. https://doi.org/10.1098/rspa.1991.0075
Kunz, M. (2007). The skill of convective parameters and indices to predict isolated and severe thunderstorms. *Natural Hazards and Earth System Sciences*, *7*(2), 327–342. www.nat-hazards-earth-syst-sci.net/7/327/2007/, https://doi.org/10.5194/nhess-7-327-2007
Lin, W. E., Orf, L. G., Savory, E., & Novacco, C. (2007). Proposed large-scale modelling of the transient features of a downburst outflow. *Wind and Structures, An International Journal*, *10*(4), 315–346. https://doi.org/10.12989/was.2007.10.4.315
Lindborg, E. (1999). Can the atmospheric kinetic energy spectrum be explained by two-dimensional turbulence? *Journal of Fluid Mechanics*, *388*, 259–288. https://doi.org/10.1017/S0022112099004851
McCann, D. W. (1994). WINDEX—A new index for forecasting microburst potential. *Weather & Forecasting*, *9*(4), 532–541. https://doi.org/10.1175/1520-0434(1994)009<0532:WNIFFM>2.0.CO;2
McCarthy, J., Wilson, J. W., & Fujita, T. T. (1982). The joint airport weather studies project. *Bulletin of the American Meteorological Society*, *63*(1), 15–22. https://doi.org/10.1175/1520-0477(1982)063<0015:TJAWSP>2.0.CO;2
Menzel, W. P., Schmit, T. J., Zhang, P., & Li, J. (2018). Satellite-based atmospheric infrared sounder development and applications. *Bulletin of the American Meteorological Society*, *99*(3), 583–603. https://doi.org/10.1175/BAMS-D-16-0293.1
Morrison, H., Thompson, G., & Tatarskii, V. (2009). Impact of cloud microphysics on the development of trailing stratiform precipitation in a simulated squall line: Comparison of one- and two-moment schemes. *Monthly Weather Review*, *137*(3), 991–1007. https://doi.org/10.1175/2008MWR2556.1
Nastrom, G. D., & Gage, K. S. (1985). A climatology of atmospheric wavenumber spectra of wind and temperature observed by commercial aircraft. *Journal of the Atmospheric Sciences*, *42*(9), 950–960. https://doi.org/10.1175/1520-0469(1985)042<0950:ACOAWS>2.0.CO;2
NCAR. (2019). NCAR command language (6.6.2). UCAR/NCAR/CISL/TDD. https://doi.org/10.5065/D6WD3XH5
Nurmi, P. (2003). Recommendations on the verification of local weather forecasts. In *ECMWF Technical Memorand*. https://doi.org/10.21957/y1z1thg5l
Nyquist, H. (1928). Certain topics in telegraph transmission theory. *Transactions of the American Institute of Electrical Engineers*, *47*(2), 617–644. https://doi.org/10.1109/T-AIEE.1928.5055024
Oreskovic, C., Orf, L. G., & Savory, E. (2018). A parametric study of downbursts using a full-scale cooling source model. *Journal of Wind Engineering and Industrial Aerodynamics*, *180*, 168–181. https://doi.org/10.1016/j.jweia.2018.07.020
Orf, L., Kantor, E., & Savory, E. (2012). Simulation of a downburst-producing thunderstorm using a very high-resolution three-dimensional cloud model. *Journal of Wind Engineering and Industrial Aerodynamics*, *104-106*, 547–557. https://doi.org/10.1016/j.jweia.2012.02.020
Proctor, F. H. (1988). Numerical simulations of an isolated microburst. Part I: Dynamics and structure. *Journal of the Atmospheric Sciences*, *45*(21), 3137–3160. https://doi.org/10.1175/1520-0469(1988)045<3137:NSOAIM>2.0.CO;2
Pryor, K. L. (2015). Progress and developments of downburst prediction applications of GOES. *Weather and Forecasting*, *30*(5), 1182–1200. https://doi.org/10.1175/WAF-D-14-00106.1
Pryor, K. L., & Ellrod, G. P. (2004). WMSI—A new index for forecasting wet microburst severity. *National Weather Association Electronic Journal of Operational Meteorology*, *25*, ■■■. http://citeseerx.ist.psu.edu/viewdoc/download?doi=10.1.1.510.9871&rep=rep1&type=pdf
R Core Team. (2020). R: Language and environment for statistical computing (3.4.4). R Foundation for Statistical Computing. https://www.r-project.org
Rai, R. K., Berg, L. K., Kosović, B., Mirocha, J. D., Pekour, M. S., & Shaw, W. J. (2017). Comparison of measured and numerically simulated turbulence statistics in a convective boundary layer over complex terrain. *Boundary-Layer Meteorology*, *163*(1), 69–89. https://doi.org/10.1007/s10546-016-0217-y
Ricard, D., Lac, C., Riette, S., Legrand, R., & Mary, A. (2013). Kinetic energy spectra characteristics of two convection-permitting limited-area models AROME and meso-NH. *Quarterly Journal of the Royal Meteorological Society*, *139*(674), 1327–1341. https://doi.org/10.1002/qj.2025
Roberts, R. D., & Wilson, J. W. (1989). A proposed microburst nowcasting procedure using single-Doppler radar. *Journal of Applied Meteorology*, *28*(4), 285–303. https://doi.org/10.1175/1520-0450(1989)028<0285:APMNPU>2.0.CO;2
Saha, S., Nadiga, S., Thiaw, C., Wang, J., Wang, W., Zhang, Q., et al. (2010). NCEP climate forecast system reanalysis (CFSR) 6-hourly products, January 1979 to December 2010. Research Data Archive at the National Center for Atmospheric Research, Computational and Information Systems Laboratory. https://doi.org/10.5065/D69K487J
Serio, C., Amoroso, M., Masiello, G., Venafra, S., Calbet, X., Stuhlmann, R., et al. (2012). Expected profiling retrieval performance of the Meteosat Third Generation infrared sounder. In D. Cimini, P. Di Girolamo, F. S. Marzano, & V. Rizi (Eds.), *Proceedings of the 9th International Symposium on Tropospheric Profiling*. L'Aquila, Italy: CETEMPS. http://cetemps.aquila.infn.it/istp/proceedings/
Skamarock, W. C. (2004). Evaluating mesoscale NWP models using kinetic energy spectra. *Monthly Weather Review*, *132*(12), 3019–3032. https://doi.org/10.1175/MWR2830.1
Skamarock, W. C., & Klemp, J. B. (2008). A time-split nonhydrostatic atmospheric model for weather research and forecasting applications. *Journal of Computational Physics*, *227*(7), 3465–3485. https://doi.org/10.1016/j.jcp.2007.01.037
Skamarock, W. C., Klemp, J. B., Dudhia, J., Gill, D. O., Barker, D. M., Duda, M. G., et al. (2008). A description of the advanced research WRF version 3. In *Technical Report*. https://doi.org/10.5065/D6DZ069T
Srivastava, R. C. (1987). A model of intense downdrafts driven by the melting and evaporation of precipitation. *Journal of the Atmospheric Sciences*, *44*(13), 1752–1774. https://doi.org/10.1175/1520-0469(1987)044<1752:AMOIDD>2.0.CO;2
Tewari, M., Chen, F., Wang, W., Dudhia, J., LeMone, M. A., Mitchell, K., et al. (2004). Implementation and verification of the unified NOAH land surface model in the WRF model. 20th Conference on Weather Analysis and Forecasting/16th Conference on Numerical Weather Prediction, 10–15.
Vermeire, B. C., Orf, L. G., & Savory, E. (2011). Improved modelling of downburst outflows for wind engineering applications using a cooling source approach. *Journal of Wind Engineering and Industrial Aerodynamics*, *99*(8), 801–814. https://doi.org/10.1016/j.jweia.2011.03.003
Wakimoto, R. M. (1985). Forecasting dry microburst activity over the high plains. *Monthly Weather Review*, *113*(7), 1131–1143. https://doi.org/10.1175/1520-0493(1985)113<1131:FDMAOT>2.0.CO;2
Wilson, J. W., Roberts, R. D., Kessinger, C. J., & McCarthy, J. (1984). Microburst wind structure and evaluation of Doppler radar for airport wind shear detection. *Journal of Climate & Applied Meteorology*, *23*(6), 898–915. https://doi.org/10.1175/1520-0450(1984)023<0898:MWSAEO>2.0.CO;2

Wolfson, M. M., Delanoy, R. L., Forman, B. E., Hallowell, R. G., Pawlak, M. L., & Smith, P. D. (1994). Automated microburst wind-shear prediction. *The Lincoln Laboratory Journal*, *7*(2), 399–426.

Wolfson, M. M., DiStefano, J. T., & Fujita, T. T. (1985). Low-altitude wind shear in the Memphis, TN area based on mesonet and LLWAS data. 14th Conference on Severe Local Storms, 322–327.

Wyngaard, J. C. (2004). Toward numerical modeling in the "Terra Incognita." *Journal of the Atmospheric Sciences*, *61*(14), 1816–1826. https://doi.org/10.1175/1520-0469(2004)061<1816:TNMITT>2.0.CO;2

7. DISCUSSION

The publications presented in the results section give answers to the partial objectives of this doctoral thesis. However, the principal objective is to improve the knowledge on the model when applied to aeronautical meteorology as a broad field, not in particular events. Thence, before addressing an integrated discussion, the principal results of each of the publications need to be summarised to set a base to build on:

Mountain wave icing

- The WRF model properly captures mountain waves and the associated aircraft icing and in-flight turbulence conditions. The meteorological variables evaluated are in line with the literature of the phenomenon and in situ observations.
- Vertical wind speed and supercooled liquid water content may be used as predicting variables, providing a considerable forecasting lead time.
- Numerical simulations and satellite images may notably improve the short-term forecasting and nowcasting of the phenomenon in question.

Low visibility

- Both, the HARMONIE-AROME and the WRF models are able to capture the mesoscale conditions of the fog episodes evaluated. Nevertheless, WRF results are hindered by the underestimation and poor correlation of wind speed, thereby the overall results are better for the HARMONIE-AROME models.
- The results for the visibility estimation algorithms confirm the better performance of the HARMONIE-AROME model, proving a satisfactory method for short-term forecasting of low visibility episodes. The threshold categorical validation shows the overestimation of the WRF model, which generates a large amount of false alarms. In addition, the less restrictive thresholds used produce the best results, but the use of medium restrictive thresholds is encouraged due to the rate of misses being lower.
- Data shows that no single method can be used in numerical simulations to properly forecast poor visibility. A combination of information may be more useful as it provides a certain measure of the uncertainty of the prediction.
- Satellite images can be helpful, providing information about moisture in the lower troposphere, although a complete nowcasting cannot be derived from these products due to the very local dimension of the phenomenon evaluated.

Deep convective precipitation

- The WRF model simulations are consistent with the observations and the general structure of the convective system, although most of the parametrizations systematically underestimate precipitation. The performance of the simulation depends on several factors of the model configuration.
- Data suggests that physics parametrizations control the spatial distribution and quantity of precipitation. As expected, microphysics is a major factor in the simulation, and schemes designed for convective precipitation perform better in the simulation of this event.
- At microscale levels, the resolution of the simulations presents a negligible role in the outcome. Higher resolutions show more realistic depictions, even though the numerical scores are only marginally better.
- The resolution of initial and boundary conditions are a factor in the results. The relatively coarse resolution chosen for this study improves the results of the higher resolution. Data suggest that the initial and boundary conditions affect the placement and timing of the simulated precipitation.
- Configuration ensembles provide only marginal improvements to the results. Despite this, they might add more consistency to the forecast and yield information on its uncertainties.

Microbursts: sensitivity analysis

- The WRF model is able to capture microburst events at microscale resolutions. The characteristics of the phenomenon are properly reproduced, even if there seems to be a systematic underestimation of the vertical wind speed simulated.
- The microphysics parametrizations evaluated seem to be decisive in the number of microburst simulated for each day, according to the results of the surface wind field analysis. Additionally, the data suggests that the planetary boundary layer scheme plays a role in the simulation of the structure of the event.
- The simulated microburst variables yield a very low sensitivity to the mesoscale conditions, rendering them ineffective as discriminators for forecasting.

Microbursts: effective resolution

- The WRF model kinetic energy content shows sensitivity to different synoptic conditions. The input of energy by the reanalyses evaluated is very similar.
- The energy spectra fit reasonably well the observations in meso-beta resolutions (as per Fujita scale). When the model is forced into microscale resolutions, it simulates an over-energetic atmosphere.
- The uncertainties in the energy spectra renders the microscale resolutions unreliable. The effective resolution of the simulations performed is approximately 30 *km*. As per evident reasons, this is not adequate for microburst simulation. These results explain the poor sensitivity of the microburst variables to mesoscale conditions.
- Mesoscale forecasting indices, adequate to the effective resolution of the model, present an improvement over climatology in the forecasting of microbursts, yet none of them are very

good performers. Differences can be observed in the results of the forecasting indices. Besides, these are affected by the initial and boundary conditions selected.

7.1. Integrated Analysis

Setting aside the particularities of each meteorological phenomenon, some interesting issues arise from the integration of the publications. The relevancy of numerical weather prediction models for aeronautical meteorology is profusely proved by the amount of research on the topic (Gultepe et al., 2019), and some of the usual questions can be addressed with the results of this thesis.

Initial and boundary conditions are a large factor in numerical simulations, in accordance with previous literature (Jankov et al., 2007; Mittermaier, 2007). These are usually derived from global models, therefore the resolution of the conditions fed becomes an issue in the simulations. The relatively low resolution of the typical reanalyses is questioned as adequate for high spatiotemporal resolutions (Gultepe et al., 2019), as local phenomena may be very sensitive to mesoscale conditions (Kücken et al., 2012; Nance & Durran, 1997; Selz & Craig, 2015). Nonetheless, Jee and Kim (2017) have found better simulation results for lower-resolution initial and boundary conditions. Likewise, this is the case in this thesis. When the model is initialised with GFS data at 1^{o} resolution, the simulations for deep convection yield better results than the initialised with the same data at 0.25^{o} of resolution. Thence, other factors are interceding in the process. The results also show that the initial and boundary conditions can produce a shift in the timing and location of the simulated phenomena. Similar errors have been noticed in deep convective events due to the resolution of the model (Mass et al., 2002; Weisman et al., 1997), but in this case the determinant factor is the resolution of the initialization data. The result of microburst forecasting suggests that the aforementioned errors may be related with the atmospheric energy distribution of the initial and boundary conditions. The wind kinetic energy spectra for microburst forecasting present almost negligible differences between the CFSR and ERA5 reanalyses. The dissimilarities are small when the synoptic situation is depicted as well. In spite of it, the results show that these slight differences are enough to produce large variations in the performance of the microburst forecasting indices. This is in line with Carvalho et al. (2014), who already noticed that different reanalyses produce variations in surface wind speed. All these facts point to relatively large variations induced by the process of downscaling from synoptic to microscale features in the model. Which may be only a remainder of the already well known internal variability of the numerical systems (Giorgi & Bi, 2000; Vukicevic, 1991; Vukicevic & Errico, 1990) and the natural variability of the atmosphere (Lorenz, 1969).

A partial solution to the initial and boundary conditions problem may come from the assimilation of observations. This represents a whole other problem by itself, as the quality and distribution of the observations, and the adaptation of the data to a standardised grid may generate several errors (Kalnay et al., 1996; Langland et al., 1999). Even so, the advantages are obvious (Dee et al., 2011) and most current operational models make use of it. This asset may be a factor in the better performance of the HARMONIE-AROME model against the WRF when simulating very local fog events. The HARMONIE-AROME is usually fed with satellite assimilated data among other observations. Furthermore, the results presented for low visibility and mountain wave show that satellite observations can be a very useful nowcasting tool, in line with other results (Gultepe et al., 2019). The ability to discern the phase of the cloud in question is helpful

in the identification of mountain waves and aircraft icing conditions (Lensky & Rosenfeld, 2008). Cloud types, precipitable water or cloud top altitudes are competent products in the case of low level clouds deteriorating visibility (Rípodas et al., 2016). Even the WMSI and MWPI microburst forecasting indices are derived from satellite data (Pryor, 2007). Furthermore, satellite constellations provide global coverage. Thus is a logical consequence that observations assimilation can improve numerical weather models. Integrating all the possible observations, apart from satellites, should continue to be improved. Many operational models already take advantage of this, yet they usually lack the flexibility provided by the WRF as a research model. This also explains the efforts to provide close-to-real-time reanalyses (European Centre for Medium-Range Weather Forecast, 2019; Saha et al., 2014).

Another distinction between operational and research models may be the initialisation process. A cold start of the model presents no major issues in research, nonetheless, it must be properly considered. Literature points to the fact that there are only small differences in the kinetic energy spectrum development between 6 and 12 *h* spin up times (Skamarock, 2004). Notwithstanding, as aforementioned, the results of two almost identical energy spectra show very significant variations in the performance of the microburst forecasting indices. Consequently, the scale of the phenomenon to evaluate should be considered in the spin up, as finer structures require larger times to develop. When dealing with high resolution simulations, the undue extension of the spin up is not an option either, as Rai et al. (2017) show that some meteorological variables become unstable and oscillatory when microscale resolutions are used. And this necessarily takes us to a core issue of this thesis: spatial resolution.

From the beginning of this thesis, the local aspect of the phenomena in study has been emphasised as a problem for forecasting. The five publications presented use microscale horizontal resolutions in the simulations, being 1 *km* the smallest grid size for mountain waves, fog and convective precipitation, and 400 *m* for microbursts. These seem adequate for the phenomena in question. In fact, the results present a good performance in the simulation of mountain waves and the associated aircraft icing and in-flight turbulence conditions, the structure and general features of deep convective systems are correctly captured, the cloud representation in low visibility events is adequate, and the mesoscale and thermodynamic conditions conducive to microbursts are satisfactorily simulated. The competence to capture meso-beta scale phenomena is clear, in accordance with many other publications, as presented in the review made by Gultepe et al. (2019). From the microburst simulation results it can be argued that the model can reproduce microscale features as well, with a proper diagnosis of the variables. In fact, the dynamics and thermodynamics of the microburst are undoubtedly well reproduced, as presented in the case study evaluated. However, the kinetic energy spectrum analysis proves that these simulations are conditioned by a large uncertainty. The results are in line with the findings of Rai et al. (2017) and Wyngaard (2004), and suggest that these resolutions are stepping into *terra incognita*. Albeit the outputs of the model may seem adequate, they must be taken with care, as the data presents an unrealistic simulation of the atmospheric kinetic energy. This may be the consequence of forcing the model to resolve microscale wind structures, as finer resolutions generate higher amounts of energy (Skamarock, 2004; Skamarock & Klemp, 2008). Zhou et al. (2014) also describe a grid resolution dependence of convective boundary layers simulated in the range of *terra incognita*, producing an unrealistic behaviour. When the PBL is dominated by convection, most kinetic features have length scales on the same order of the PBL depth. The uncertainties introduced in the energy spectrum at microscale resolutions cast doubts on the

competence of reproducing the scale of this convection. This may partially explain the poor scoring results in the microburst forecasting, as these indices are very dependant on convection. It may also be a reason behind the timing and placement errors in deep convective events, further than initial and boundary conditions resolution.

As per Nyquist (1928) theory, the minimum wavelength captured by a numerical model is $2\Delta x$. But Skamarock (2004) shows that to avoid the kinetic energy uncertainties, the effective resolution of the WRF model is about $7\Delta x$, while Abdalla et al. (2013) found an $8\Delta x$ effective resolution for a spectral global model. The results in this thesis are in line with those. Taking into consideration that Rai et al. (2017) results show 1.4 *km* as the beginning of *terra incognita* for the WRF, the effective resolution would be about 10 *km*, given a proper model configuration. This confirms that the model can resolve meso-beta features. At the same time, it shows that very local events may be subject to large uncertainties, *e.g.*, errors in deep convective precipitation and low visibility events, or the low sensitivity of the microburst characteristic variables. In spite of this, microscale resolutions should not be dismissed. Surface-atmosphere interphase processes and PBL variables subject to orographic forcing can notably benefit from a more detailed terrain and land use resolution (Pontoppidan et al., 2017; Skamarock, 2004). Some authors defend that deep convection may be possible to capture with *ad hoc* parametrizations specifically developed for microscale resolutions (Zhou et al., 2014). Also, the uncertainties introduced may be used as information, rendering a deterministic product into a stochastic one, reflecting some of the internal variability (Skamarock & Klemp, 2008).

To summarise the resolution issue, the data suggest that the model is adequate for the meteorological phenomena in study. At the same time, it suggests that there is improvement plausible, as adapting the model to allow an integration of the mesoscale and the microscale may be possible. This would represent a great advance for aeronautical meteorology forecasting. However, it leads to new issues to discuss. One of these is the election between deterministic or probabilistic forecasting. Both approaches have been extensively taken in aeronautical meteorology. The plethora of research performed using a deterministic approach is a confirmation of its benefits *per se* (Gultepe et al., 2019). A properly configured experiment avoids losing information about maxima and minima, and smoothing out possible hazards, which is very important when dealing with extreme events. At the same time, the results for deep convective precipitation show that the amount of precipitation is underestimated by most of the microphysics parametrizations evaluated. A similar problem is found with the estimation of wind vertical speed in the simulation of microbursts, and an underestimation is likewise described for surface wind speed in the low visibility events, for both WRF and HARMONIE-AROME models. These biases are not easily removed from the models and are a representation of the difficulty in fine-tuning every parametrization even for a single phenomenon. When the myriad of possible model configurations offered by the WRF is considered (W. Wang et al., 2019), the scale of the problem is comprehended.

On the other hand, the results for deep convective precipitation show that the possible ensembles add little information and would indeed flatten the spatial distribution of precipitation. Ensemble prediction systems rely on the statistical probability of an event to occur, and hence smoothens out the intensities of events, yet this problem can be avoided with an adequate management of information. The deterministic results are not lost, as extreme percentiles of the distribution still represent the maxima and minima of the event. At the same time, very valuable

information for an operational forecast can be assessed, as dispersion and uncertainties, which can be also derived from the results of this thesis. Furthermore, as many deterministic configurations are evaluated, the chances of missing a particular event are reduced. Up to date, the ensemble technique is very successful in the prediction of synoptic scale features, and many efforts are focused on its improvement to address forecasting uncertainties. Notwithstanding, the ability to predict meso-beta and microscale phenomena is far from perfect (Yano et al., 2018), and some problems related with underdispersion and overconfidence of the predictions have yet to be solved (Fernández-González et al., 2017).

Another topic to consider would be the validation scores. Observations are of paramount importance not only for improving the models, but for validating them as well, which in turn is vital for a proper parametrization development. In addition, observations improve the knowledge on natural variability, allowing for the assessment of the internal variability of the numerical model (Ralph et al., 2013). However, obtaining properly instrumented observations of microbursts, as an example, is very challenging and requires bespoke field campaigns as those set up by Fujita (1985). In the case the observations are available, the adequate skill score must be selected, taking into consideration that typical skill scores may not be optimal for high resolution simulations, as questioned by Mass et al. (2002). Additionally, specific phenomena may require a validation through multiple methods, as shown for the low visibility events.

To conclude the discussion of this doctoral thesis, some specific results should be addressed. In the first place, it may be noted that despite some of the research presented here being performed on particular study cases, the physics processes are simple enough to allow the extension of the results to other similar events. On the topic of low visibility, an effective and operational tool was developed. This has already been implemented and is available for operational forecasters in the Spanish national meteorology agency (Agencia Estatal de Meteorología). For the publication on deep convective precipitation two validation indices were developed. The idea of these is to use the area under the curve of error and absolute error to have information on the temporal behaviour of the model. Traditionally, numerical weather models are evaluated at several lead times, while these indices provide an integrated value for the temporal performance. Similar validation scores may exist, yet this is a simple proposal which may be useful. And finally, on the topic of the microbursts, the publications presented are somewhat noteworthy. To the author's knowledge, these are the first publications in which microbursts are simulated and evaluated in detail using non-ideal model runs. In fact, the review performed by Gultepe et al. (2019) shows that operational models are currently used only to assist the observational nowcasting of microbursts. These remain one of the most elusive aviation related meteorological hazards to forecasting. Therefore, the results yielded by these simulations may prove the potential of high spatiotemporal resolutions for increasing the forecasting lead times. And this leads this study to the conclusions to follow.

8. CONCLUSIONS

From all the aforementioned discussion, some integrated conclusions can be reached:

- Proper model configuration is paramount for the simulation of fine scale phenomena. This should be performed considering the particular characteristics of the event. Additionally, deviations and errors may arise from multiple factors, *e.g.*, initial and boundary conditions, parametrizations, resolution or internal variability. Therefore, an integrative and multiple-view approach should be taken for the research of these phenomena.
- At meso-beta scale and microscale, each specific phenomenon requires a particular set of parametrizations. Microphysics and PBL schemes are proven to be determinant for the events evaluated in this study. Biases and systematic errors are not uncommon and the improvement of parametrizations is required to reduce these. And more importantly, an overall, general-purpose model able to capture every phenomena affecting aviation is not possible as per the state of the art.
- The effective resolution of the model needs to be considered for every fine scale phenomena. Internal and natural variabilities in the system can create large deviations in the simulations, and the uncertainties induced in the simulations should be assessed for better high resolution simulations.
- Better observations are required for the study of extremely local phenomena. This would help to reduce deviations, to evaluate variabilities and provide better tools for validation of the model.
- As per the state of the art, *ad hoc* forecasting techniques based in numerical weather models are possible. Any operational forecasting tool to be developed would require observations assimilation. Warm starting should be considered as well. Configuration ensembles and a statistical approach may contribute to further insight into possible forecasting algorithms.

In summary, it can be concluded that there still is much room for improvement in aeronautical meteorology numerical forecasting. The potential of some of the techniques here presented is clear, and many results are promising. Moreover, there are currently large efforts on the improvement of microscale resolution simulations, which produces an optimistic future for the issue.

9. FUTURE RESEARCH

The outlook for the research of meteorological hazards to aviation is certainly promising. From the results of this thesis and recent reviews on the topic, it seems clear that there is still a large improvement possible. Numerical weather prediction models may provide new abilities to operational forecasting, and lead times may be notably increased with the improvement of computational capabilities. Nevertheless, this does not mean there are no challenges ahead. Parametrizations need to be adapted and, most probably, core functions of the models will need to be further developed to integrate them into the microscale. The role of observations is unquestionable. Local observations need to be improved as an input to mesoscale models, and the integration of every available system should be further pursued. And the last, in the author's view, is the most important issue for future developments.

The amount of data available today has become almost unmanageable. This needs to be addressed promptly, as it would provide the chance of a technological leap. The benefits of Artificial Intelligence and Big Data Analysis are already proven, and may entail the next step in weather forecasting. Deterministic fine-tuned models, fed with assimilated observations and integrated in an ensemble prediction system are a reality. To take the statistical process of the system one step further and implement an artificial intelligence diagnosis based on the vast amount of real time data available is only natural. An additional note on the integration of data is that, due to several issues, a lot of very valuable information is lost. Surprisingly, the Aircraft Meteorological Data Relay project (World Meteorological Organization, 2020) is only participated by 40 airlines. In addition, the aircraft are relaying temperature, wind, pressure and turbulence data. Nonetheless, all of these aircraft are equipped with an on-board meteorological radar, which is left out of the system.

As per what is directly relevant to aviation safety, airport based specialised models are already feasible and, in fact, a reality in some cases. Airport operators and aeronautical providers should invest in the development of *ad hoc* forecasting systems. Operational models specifically configured for aviation hazards, and running particular forecasting algorithms, would provide all the benefits derived from research directly to the users. These systems should not be independent from larger meteorological networks, even so, there is a gap between research developments and the operative application of those that needs to be reduced. Users with such specific needs should have more concrete information than that provided by the major, synoptic and mesoscale focused models.

Finally, adding onto the idea of integrating global information to provide very local forecasting, another line of development can be thought of. The computational capability of a modern airliner aircraft is very large. Industry professionals estimate that the lines of software processed by a modern-era airliner ten-folds each decade. A state of the art airliner monitors more

than 50000 sensors in the airframe, computing thousands of software scripts and storing more than 100 *GB* of data per hour of flight. This proves that computing power would not be a problem to develop on-board numerical simulation systems. An *ad hoc* numerical model, with initial and boundary conditions provided before the flight, assimilating on-board observations and other relaid data, may be able to produce real time nowcasting. The domains to simulate would not be large, as only a few minutes lead times would be required to take preventive actions. Providing each flight crew with a bespoke prediction for the next minutes would be an excellent improvement on safety.

Personal note on the future of aeronautical meteorology

On a personal view as a professional and recreational pilot there is something I would like to highlight. It has already been stated in the previous sections, however sometimes it is surprising how far apart authorities are from the research community, and these from the industry. A well trained and skilled pilot has enough meteorological information to perform the duty safely. But if you want to get that information, you will have to browse over four or five different sources, some of those not official. Aviation meteorological reports are usually incomplete or inaccurate, information is scattered all around, and it is shocking how authorities do not seem to understand the information needs of the industry. Even worse, as a meteorology researcher I know that some national agencies have developed many useful and informative products, even so, these are not released to the public. Advanced products, expensive to develop and produce, which detail the conditions on critical parts of the flight, are routinely generated yet hidden from the industry. Meanwhile, the reports released are based on decades old techniques. Consequently, some airlines need to create a meteorological office and some pilots choose to perform our own meteorological assessment, improving the official one with non-regulated information. However not every airline has this capacity, nor does every pilot have the skill for doing this, especially the recreational pilots. In consequence, many flights take off with unreliable information and without a proper idea of the meteorological conditions. Authorities, industry and research community should learn to work together, providing adequate feedback and addressing the real needs of each other. Many improvements, already feasible, could be produced with a well oriented culture and an integrative point of view.

References

Abdalla, S., Isaksen, L., Janssen, P., & Wedi, N. (2013). Effective spectral resolution of ECMWF atmospheric forecast models. *ECMWF Newsletter*, *137*, 19--22. https://doi.org/10.21957/rue4o7ac

Ahrens, C. D. (2009). *Meteorology today: an introduction to weather, climate, and the environment* (Brooks/Cole (Ed.); 9th ed.). CengageLearning.

American Meteorological Society. (2020). *Glossary of Meteorology*. http://glossary.ametsoc.org/wiki/Main_Page

Atkins, N. T., & Wakimoto, R. M. (1991). Wet Microburst Activity over the Southeastern United States: Implications for Forecasting. *Weather and Forecasting*, *6*(4), 470–482. https://doi.org/10.1175/1520-0434(1991)006<0470:WMAOTS>2.0.CO;2

Aviation Safety Network. (2020). *Statistics*. https://aviation-safety.net/statistics/

Bengtsson, L., Andrae, U., Aspelien, T., Batrak, Y., Calvo, J., de Rooy, W., Gleeson, E., Hansen-Sass, B., Homleid, M., Hortal, M., Ivarsson, K.-I., Lenderink, G., Niemelä, S., Nielsen, K. P., Onvlee, J., Rontu, L., Samuelsson, P., Muñoz, D. S., Subias, A., … Køltzow, M. Ø. (2017). The HARMONIE–AROME Model Configuration in the ALADIN–HIRLAM NWP System. *Monthly Weather Review*, *145*(5), 1919–1935. https://doi.org/10.1175/MWR-D-16-0417.1

Carvalho, D., Rocha, A., Gómez-Gesteira, M., & Silva Santos, C. (2014). WRF wind simulation and wind energy production estimates forced by different reanalyses: Comparison with observed data for Portugal. *Applied Energy*, *117*, 116–126. https://doi.org/10.1016/j.apenergy.2013.12.001

Dee, D. P., Uppala, S. M., Simmons, A. J., Berrisford, P., Poli, P., Kobayashi, S., Andrae, U., Balmaseda, M. A., Balsamo, G., Bauer, P., Bechtold, P., Beljaars, A. C. M., van de Berg, L., Bidlot, J., Bormann, N., Delsol, C., Dragani, R., Fuentes, M., Geer, A. J., … Vitart, F. (2011). The ERA-Interim reanalysis: configuration and performance of the data assimilation system. *Quarterly Journal of the Royal Meteorological Society*, *137*(656), 553–597. https://doi.org/10.1002/qj.828

Dusek, U., Frank, G. P., Hildebrandt, L., Curtius, J., Schneider, J., Walter, S., Chand, D., Drewnick, F., Hings, S., Jung, D., Borrmann, S., & Andreae, M. O. (2006). Size Matters More Than Chemistry for Cloud-Nucleating Ability of Aerosol Particles. *Science*, *312*(5778), 1375–1378. https://doi.org/10.1126/science.1125261

Eick, D. (2014). *Turbulence Related Accidents & Incidents*. https://ral.ucar.edu/sites/default/files/public/events/2014/turbulence-impact-mitigation-workshop-2/docs/eick-turbulencerelatedaccidents.pdf

European Centre for Medium-Range Weather Forecast. (2019). *ERA5 Reanalysis (0.25 Degree Latitude-Longitude Grid)*. https://doi.org/10.5065/BH6N-5N20.

European Centre for Medium-Range Weather Forecast. (2020). *Anomaly correlation of ECMWF 500hPa height forecasts*. https://www.ecmwf.int/en/forecasts/charts/catalogue/plwww_m_hr_ccaf_adrian_ts?facets=undefined&time=2020051100

European Union Aviation Safety Agency. (2019). *Annual Safety Review 2019*. https://doi.org/10.2822/098259

Federal Aviation Administration. (2016a). *Advisory Circular 00-6B: Aviation Weather*. https://doi.org/AFS-800 AC 91-97

Federal Aviation Administration. (2016b). Pilot ’s Handbook of Aeronautical Knowledge. In *Pilot’s Handbook of Aeronautical Knowledge*. United States Department of Transportation. https://doi.org/10.1016/S0740-8315(86)80070-5

Fernández-González, S. (2016). *Análisis de engelamiento y nevadas en la Península Ibérica mediante modelos numéricos* [Universidad Complutense de Madrid]. https://eprints.ucm.es/41987/

Fernández-González, S., Martín, M. L., Merino, A., Sánchez, J. L., & Valero, F. (2017). Uncertainty quantification and predictability of wind speed over the Iberian Peninsula. *Journal of Geophysical Research: Atmospheres*, *122*(7), 3877–3890. https://doi.org/10.1002/2017JD026533

Fujita, T. T. (1981). Tornadoes and downbursts in the context of generalized planetary scales. *Journal of the Atmospheric Sciences*, *38*(8), 1511–1534. https://doi.org/10.1175/1520-0469(1981)038<1511:TADITC>2.0.CO;2

Fujita, T. T. (1985). The Downburst: microburst and macroburst. In *SMRP Research Papers* (Vol. 210).

Gent, R. W., Dart, N. P., & Cansdale, J. T. (2000). Aircraft icing. *Philosophical Transactions of the Royal Society A: Mathematical, Physical and Engineering Sciences*, *358*(1776), 2873–2911. https://doi.org/10.1098/rsta.2000.0689

Giorgi, F., & Bi, X. (2000). A study of internal variability of a regional climate model. *Journal of Geophysical Research: Atmospheres*, *105*(D24), 29503–29521. https://doi.org/10.1029/2000JD900269

González, B. (2005). *Meteorología Aeronáutica* (1st ed.). Actividades Varias Aeronáuticas.

Gultepe, I., Sharman, R., Williams, P. D., Zhou, B., Ellrod, G. P., Minnis, P., Trier, S., Griffin, S., Yum, S. S., Gharabaghi, B., Feltz, W., Temimi, M., Pu, Z., Storer, L. N., Kneringer, P., Weston, M. J., Chuang, H. ya, Thobois, L., Dimri, A. P., … Neto, F. L. A. (2019). A Review of High Impact Weather for Aviation Meteorology. *Pure and Applied Geophysics*, *176*(5), 1869–1921. https://doi.org/10.1007/s00024-019-02168-6

Hjelmfelt, M. R. (1988). Structure and life cycle of microburst outflows observed in Colorado. *Journal of Applied Meteorology*, *27*(8), 900–927.

Huffman, G. J., & Norman, G. A. (1988). The Supercooled Warm Rain Process and the Specification of Freezing Precipitation. *Monthly Weather Review*, *116*(11), 2172–2182. https://doi.org/10.1175/1520-0493(1988)116<2172:TSWRPA>2.0.CO;2

International Air Transport Association. (2019). *Annual Review 2019*. https://www.iata.org/en/publications/annual-review/

International Civil Aviation Organization. (2016). *Annex 3 to the Convention on International Civil Aviation: Meteorological Service for International Air Navigation*.

International Civil Aviation Organization. (2020). *Data Plus*. https://data.icao.int/newDataPlus/

Jankov, I., Gallus, W. A., Segal, M., & Koch, S. E. (2007). Influence of Initial Conditions on the WRF–ARW Model QPF Response to Physical Parameterization Changes. *Weather and Forecasting*, *22*(3), 501–519. https://doi.org/10.1175/WAF998.1

Jeck, R. K. (2001). A History and Interpretation of Aircraft Icing Intensity Definitions and FAA Rules for Operating in Icing Conditions. In *FAA Report*.

Jee, J.-B., & Kim, S. (2017). Sensitivity Study on High-Resolution WRF Precipitation Forecast for a Heavy Rainfall Event. *Atmosphere*, *8*(12), 96. https://doi.org/10.3390/atmos8060096

Kalnay, E., Kanamitsu, M., Kistler, R., Collins, W., Deaven, D., Gandin, L., Iredell, M., Saha, S., White, G., Woollen, J., Zhu, Y., Chelliah, M., Ebisuzaki, W., Higgins, W., Janowiak, J., Mo, K. C., Ropelewski, C., Wang, J., Leetmaa, A., … Joseph, D. (1996). The NCEP/NCAR 40-year reanalysis project. *Bulletin of the American Meteorological Society*. https://doi.org/10.1175/1520-0477(1996)077<0437:TNYRP>2.0.CO;2

Kücken, M., Hauffe, D., & Österle, H. (2012). A high-resolution simulation of the year 2003 for Germany using the regional model COSMO. *Journal of Applied Meteorology and Climatology*. https://doi.org/10.1175/JAMC-D-11-0186.1

Lamb, D., & Verlinde, J. (2011). *Physics and Chemistry of Clouds*. Cambridge University Press. https://doi.org/10.1017/CBO9780511976377

Langland, R. H., Toth, Z., Gelaro, R., Szunyogh, I., Shapiro, M. A., Majumdar, S. J., Morss, R. E., Rohaly, G. D., Velden, C., Bond, N., & Bishop, C. H. (1999). The North Pacific Experiment (NORPEX-98): Targeted Observations for Improved North American Weather Forecasts. *Bulletin of the American Meteorological Society*. https://doi.org/10.1175/1520-0477(1999)080<1363:TNPENT>2.0.CO;2

Lauritzen, P., Jablonowski, C., Taylor, M., & Nair, R. (Eds.). (2011). *Numerical Techniques for Global Atmospheric Models* (Vol. 80). Springer Berlin Heidelberg. https://doi.org/10.1007/978-3-642-11640-7

Ledesma, M., & Baleriola, G. (2007). *Meteorología Aplicada a la Aviación* (13th ed.). ITES - Paraninfo. https://doi.org/9788428329422

Lee, R. E., Lee, M. R., & Strong-Gunderson, J. M. (1993). Insect cold-hardiness and ice nucleating active microorganisms including their potential use for biological control. *Journal of Insect Physiology*, *39*(1), 1–12. https://doi.org/10.1016/0022-1910(93)90011-F

Lensky, I. M., & Rosenfeld, D. (2008). Clouds-Aerosols-Precipitation Satellite Analysis Tool (CAPSAT). *Atmospheric Chemistry and Physics*, *8*(22), 6739–6753. https://doi.org/10.5194/acp-8-6739-2008

List, R., Fung, C., & Nissen, R. (2009). Effects of Pressure on Collision, Coalescence, and Breakup of Raindrops. Part I: Experiments at 50 kPa. *Journal of the Atmospheric Sciences*, *66*(8), 2190–2203. https://doi.org/10.1175/2009JAS2863.1

Lorenz, E. N. (1969). The predictability of a flow which possesses many scales of motion. *Tellus*, *21*(3), 289–307. https://doi.org/10.1111/j.2153-3490.1969.tb00444.x

Mass, C. F., Ovens, D., Westrick, K., & Colle, B. A. (2002). Does increasing horizontal resolution produce more skillful forecasts? The results of two years of real-time numerical weather prediction over the Pacific Northwest. *Bulletin of the American Meteorological Society*, *83*(3), 407-430+341. https://doi.org/10.1175/1520-0477(2002)083<0407:DIHRPM>2.3.CO;2

McElroy, M. B. (2002). *The Atmospheric Environment: Effects of Human Activity* (Princeton University Press (Ed.)).

Mittermaier, M. P. (2007). Improving short-range high-resolution model precipitation forecast skill using time-lagged ensembles. *Quarterly Journal of the Royal Meteorological Society*, *133*(627), 1487–1500. https://doi.org/10.1002/qj.135

Nance, L. B., & Durran, D. R. (1997). A Modeling Study of Nonstationary Trapped Mountain Lee Waves. Part I: Mean-Flow Variability. *Journal of the Atmospheric Sciences*, *54*(18), 2275–2291. https://doi.org/10.1175/1520-0469(1997)054<2275:AMSONT>2.0.CO;2

National Aeronautics and Space Administration. (2020). *In-Flight Icing: Ice Gallery*. https://aircrafticing.grc.nasa.gov/1_2_8_1.html

National Oceanic and Atmospheric Administration. (2020). *Deep/Shallow Convection*. 1999. https://www.wpc.ncep.noaa.gov/international/training/deep/sld003.htm

Nyquist, H. (1928). Certain Topics in Telegraph Transmission Theory. *Transactions of the American Institute of Electrical Engineers*, *47*(2), 617–644. https://doi.org/10.1109/T-AIEE.1928.5055024

Peter Thompson. (2015). *Higgins Storm Chasing*. https://higginsstormchasing.com/what-are-microbursts/

Pontoppidan, M., Reuder, J., Mayer, S., & Kolstad, E. W. (2017). Downscaling an intense precipitation event in complex terrain: the importance of high grid resolution. *Tellus A: Dynamic Meteorology and Oceanography*, *69*(1), 1271561. https://doi.org/10.1080/16000870.2016.1271561

Proctor, F. H. (1988). Numerical simulations of an isolated microburst. Part I: dynamics and structure. *Journal of the Atmospheric Sciences*, *45*(21), 3137–3160. https://doi.org/10.1175/1520-0469(1988)045<3137:NSOAIM>2.0.CO;2

Proctor, F. H. (1989). Numerical simulations of an isolated microburst. Part II: sensitivity experiments. *Journal of the Atmospheric Sciences*, *46*(14), 2143–2165. https://doi.org/10.1175/1520-0469(1989)046<2143:NSOAIM>2.0.CO;2

Pryor, K. L. (2007). *The GOES Microburst Windspeed Potential Index*. *2004*, 15. http://edberry.com/SiteDocs/PDF/Pryor GOES Microburst Windspeed Potential.pdf

Rai, R. K., Berg, L. K., Kosović, B., Mirocha, J. D., Pekour, M. S., & Shaw, W. J. (2017). Comparison of Measured and Numerically Simulated Turbulence Statistics in a Convective Boundary Layer Over Complex Terrain. *Boundary-Layer Meteorology*, *163*(1), 69–89. https://doi.org/10.1007/s10546-016-0217-y

Ralph, F. M., Intrieri, J., Andra, D., Atlas, R., Boukabara, S., Bright, D., Davidson, P., Entwistle, B., Gaynor, J., Goodman, S., Jiing, J.-G., Harless, A., Huang, J., Jedlovec, G., Kain, J., Koch, S., Kuo, B., Levit, J., Murillo, S., … Weiss, S. (2013). The Emergence of Weather-Related Test Beds Linking Research and Forecasting Operations. *Bulletin of the American Meteorological Society*, *94*(8), 1187–1211. https://doi.org/10.1175/BAMS-D-12-00080.1

Rauber, R. M., & Tokay, A. (1991). An Explanation for the Existence of Supercooled Water at the Top of Cold Clouds. *Journal of the Atmospheric Sciences*, *48*(8), 1005–1023. https://doi.org/10.1175/1520-0469(1991)048<1005:AEFTEO>2.0.CO;2

Rípodas, P., Legleau, H., Kerdraon, G., Moisselin, J. M., Autones, F., García, J., Martínez, M. Á., Marcos, C., Jann, A., Wirth, A., Calbet, X., Alonso, Ó., & Ariza, C. (2016). NWCSAF GEO v2016 : new products, changes and improvements. *EUMETSAT Meteorological Satellite Conference*, 7. http://hdl.handle.net/20.500.11765/7271

Rogers, D. C. (1993). Measurements of natural ice nuclei with a continuous flow diffusion chamber. *Atmospheric Research*, *29*(3–4), 209–228. https://doi.org/10.1016/0169-8095(93)90004-8

Saha, S., Moorthi, S., Wu, X., Wang, J., Nadiga, S., Tripp, P., Behringer, D., Hou, Y.-T., Chuang, H., Iredell, M., Ek, M., Meng, J., Yang, R., Mendez, M. P., van den Dool, H., Zhang, Q., Wang, W., Chen, M., & Becker, E. (2014). The NCEP Climate Forecast System Version 2. *Journal of Climate*, *27*(6), 2185–2208. https://doi.org/10.1175/JCLI-D-12-00823.1

Schmetz, J., Pili, P., Tjemkes, S., Just, D., Kerkmann, J., Rota, S., & Ratier, A. (2002). An Introduction to Meteosat Second Generation (MSG). *Bulletin of the American Meteorological Society*, *83*(7), 977–992. https://doi.org/10.1175/1520-0477(2002)083<0977:AITMSG>2.3.CO;2

Selz, T., & Craig, G. C. (2015). Upscale error growth in a high-resolution simulation of a summertime weather event over Europe. *Monthly Weather Review*. https://doi.org/10.1175/MWR-D-14-00140.1

Skamarock, W. C. (2004). Evaluating Mesoscale NWP Models Using Kinetic Energy Spectra. *Monthly Weather Review*, *132*(12), 3019–3032. https://doi.org/10.1175/MWR2830.1

Skamarock, W. C., & Klemp, J. B. (2008). A time-split nonhydrostatic atmospheric model for weather research and forecasting applications. *Journal of Computational Physics*, *227*(7), 3465–3485. https://doi.org/10.1016/j.jcp.2007.01.037

Skamarock, W. C., Klemp, J. B., Dudhia, J., Gill, D. O., Barker, D. M., Duda, M. G., Huang, X.-Y., Wang, W., & Powers, J. G. (2008). A Description of the Advanced Research WRF Version 3. In *Technical Report*. https://doi.org/10.5065/D6DZ069T

Srivastava, R. C. (1985). A simple model of evaporatively driven downdraft: application to microburst downdraft. *Journal of the Atmospheric Sciences*, *42*(10), 1004–1023. https://doi.org/10.1175/1520-0469(1985)042<1004:ASMOED>2.0.CO;2

Srivastava, R. C. (1987). A model of intense downdrafts driven by the melting and evaporation of precipitation. *Journal of the Atmospheric Sciences*, *44*(13), 1752–1773.

Tafferner, A., Hauf, T., Leifeld, C., Hafner, T., Leykauf, H., & Voigt, U. (2003). ADWICE: Advanced diagnosis and warning system for aircraft icing environments. *Weather and Forecasting*, *18*(2), 184–203. https://doi.org/10.1175/1520-0434(2003)018<0184:AADAWS>2.0.CO;2

Vukicevic, T. (1991). Nonlinear and Linear Evolution of Initial Forecast Errors. *Monthly Weather Review*, *119*(7), 1602–1611. https://doi.org/10.1175/1520-0493(1991)119<1602:NALEOI>2.0.CO;2

Vukicevic, T., & Errico, R. M. (1990). The Influence of Artificial and Physical Factors upon Predictability Estimates Using a Complex Limited-Area Model. *Monthly Weather Review*, *118*(7), 1460–1482. https://doi.org/10.1175/1520-0493(1990)118<1460:TIOAAP>2.0.CO;2

Wakimoto, R. M. (1985). Forecasting dry microburst activity over the High Plains. *Monthly Weather Review*, *113*(7), 1131–1143. https://doi.org/10.1175/1520-0493(1985)113<1131:FDMAOT>2.0.CO;2

Wakimoto, R. M. (2001). Convectively Driven High Wind Events. In C. A. Doswell (Ed.), *Severe Convective Storms* (Vol. 50, pp. 255–298). American Meteorological Society. https://doi.org/10.1175/0065-9401-28.50.255

Wang, P. K. (2013). *Physics and Dynamics of Clouds and Precipitation*. Cambridge University Press.

Wang, W., Bruyère, C., Duda, M., Dudhia, J., Gill, D., Kavulich, M., Werner, K., Chen, M., Lin, H.-C., Michalakes, J., Rizvi, S., Zhang, X., Berner, J., Munoz-Esparza, D., Reen, B., Ha, S., Fossell, K., Beezley, J., Coen, J., & Mandel, J. (2019). *Weather Research & Forecasting Model, User´s Guide* (Issue January). https://www2.mmm.ucar.edu/wrf/users/docs/user_guide_V4/WRFUsersGuide.pdf

Weisman, M. L., Skamarock, W. C., & Klemp, J. B. (1997). The Resolution Dependence of Explicitly Modeled Convective Systems. *Monthly Weather Review*, *125*(4), 527–548. https://doi.org/10.1175/1520-0493(1997)125<0527:TRDOEM>2.0.CO;2

Wolfson, M. M., Delanoy, R. L., Forman, B. E., Hallowell, R. G., Pawlak, M. L., & Smith, P. D. (1994). Automated microburst wind-shear prediction. *The Lincoln Laboratory Journal*, *7*(2), 399–426.

World Meteorological Organization. (2019a). *Aerodrome Reports and Forecast*.

World Meteorological Organization. (2019b). *Manual on Codes International Codes Volume I.1 Annex II to the WMO Technical Regulations Part A-Alphanumeric Codes*.

World Meteorological Organization. (2020). *AMDAR Participating Airlines*. https://www.wmo.int/pages/prog/www/GOS/ABO/AMDAR/AMDAR_Airlines.html

Wyngaard, J. C. (2004). Toward numerical modeling in the "Terra Incognita." *Journal of the Atmospheric Sciences*, *61*(14), 1816–1826. https://doi.org/10.1175/1520-0469(2004)061<1816:TNMITT>2.0.CO;2

Yano, J.-I., Ziemiański, M. Z., Cullen, M., Termonia, P., Onvlee, J., Bengtsson, L., Carrassi, A., Davy, R., Deluca, A., Gray, S. L., Homar, V., Köhler, M., Krichak, S., Michaelides, S., Phillips, V. T. J., Soares, P. M. M., & Wyszogrodzki, A. A. (2018). Scientific Challenges of Convective-Scale Numerical Weather Prediction. *Bulletin of the American Meteorological Society*, *99*(4), 699–710. https://doi.org/10.1175/BAMS-D-17-0125.1

Zhou, B., Simon, J. S., & Chow, F. K. (2014). The convective boundary layer in the terra incognita. *Journal of the Atmospheric Sciences*, *71*(7), 2545–2563. https://doi.org/10.1175/JAS-D-13-0356.1

AGRADECIMIENTOS

Algunas frases me han acompañado a lo largo de esta tesis. Porque hace años aprendí que a ciertos ojos les basta con ver que «el sol está entrando en tormenta» para pronosticar mejor que cualquier supercomputador. Luego, cuando me decidí a dedicar cuatro años a algo que poco tiene que ver con mi profesión, recordé que «todo suma». Y cuando la carga de trabajo me sacó canas, una voz inolvidable me decía «no se aflija, m'ijo».

Gracias a Paco, Marisa y Sergio por todo el ánimo, el cariño, la paciencia y el conocimiento. Gracias a Lara, Javi, Dani y Mariano por aguantarme y ayudarme, por enfadar a los jefazos de la AEMET y por hacerme un hueco en su oficina (literalmente).

Gracias a Jorge y al Negro por enseñarme a mirar las nubes. Y muy especialmente por enseñarme a volar.

Gracias al Mullallo, al Moreno, a Pablus y a Xavi por la fuerza, las charlas, las risas, los viajes, los asados y los aviones.

Gracias a la Rubia por los tangos, los abrazos y tanto amor.

Gracias a mis abuelos, tíos y primas por estar cerca incluso con un océano de por medio.

Gracias a Ale, Tade y Tom, y a Cin, Patri, Charito, Matu, Luqui, Dani y Saimon, por quererme a pesar del mal humor y hacerme saber que tengo una familia allá donde vaya.

Y gracias eternas a mis padres. Por hacerme quien soy, por empujarme a mejorar, por enseñarme el mundo y por darme una vida feliz.

«*¡Yogurtu! Ven aquí astuto sobrino mío. Te enseñaré a invocar a los dioses para que nos envíen lluvias*».

− Les Luthiers,
Cartas de Color

«*He venido al sepelio del rey*».

− Gabriel García Márquez,
Cien Años de Soledad

This thesis was finished in Madrid on 09 September 2020.
The meteorological conditions reported at the time were:
LEMD 091000Z 22004KT 190V280 CAVOK 22/07 Q1024 NOSIG